

**Quantum dynamics of ultracold atoms
in inhomogeneous magnetic fields**

*** * ***

From ground state atoms to Rydberg atoms

Referees: Prof. Dr. Peter Schmelcher
Prof. Dr. Jochen Schirmer

Dissertation
submitted to the
Combined Faculties for the Natural Sciences
and for Mathematics
of the Ruperto-Carola University of Heidelberg,
Germany
for the degree of
Doctor of Natural Science

presented by
Dipl.-Phys. Igor Lesanovsky
born in Grevesmühlen (Germany)
Oral examination: April 26th 2006

Zusammenfassung

Quantendynamik ultrakalter Atome in inhomogenen Magnetfeldern

Gegenstand dieser Arbeit ist die Untersuchung der Quantendynamik ultrakalter Atome in Gegenwart von inhomogenen Magnetfeldern. Wir studieren das Verhalten von Grundzustandsatomen, die näherungsweise als neutrale spinbehaftete Punktteilchen aufgefasst werden können, in typischen, auf Quadrupolfeldern basierenden, Magnetfallenkonfigurationen. Insbesondere analysieren wir das Resonanzspektrum und die Zustandsdichte von fermionischen und bosonischen Atomen. Wir zeigen die Existenz von quasi-gebundenen Zuständen die eine näherungsweise analytische Beschreibung erlauben. Weiterhin widmen wir uns dem Studium quantenmechanischer Zustände von ultrakalten und zugleich elektronisch hoch angeregten Atomen, so genannter Rydbergatome, in Magnetfallen. In einem ersten Schritt untersuchen wir deren interne Dynamik unter Annahme eines unendlich schweren und räumlich fixierten Atomkerns. Im Rahmen dieser Näherung werden spektrale Eigenschaften sowie Eigenschaften des Elektronenspins und elektromagnetische Übergänge berechnet. Schließlich stellen wir einen adiabatischen Zugang vor, der die umfassende Beschreibung der quantisierten Elektronen- und Schwerpunktdynamik ermöglicht. Wir demonstrieren die Möglichkeit des Fangens von elektronisch hoch angeregten Atomen und präsentieren neuartige Quantenzustände, in denen die Schwerpunktswellenfunktion stärker lokalisiert ist als die der Elektronenbewegung. Dies zeigt, dass Rydbergatome in Gegenwart von inhomogenen Magnetfeldern, im Gegensatz zu Grundzustandsatomen, nicht mehr als punktförmige Teilchen betrachtet werden können.

Abstract

Quantum dynamics of ultracold atoms in inhomogeneous magnetic fields

Subject of this thesis is the investigation of the quantum dynamics of ultracold atoms in the presence of external inhomogeneous magnetic fields. We discuss the behavior of ground state atoms inside typical magnetic field configurations. Such atoms can be approximately treated as neutral point-like particles which carry a certain spin. In particular we analyze the resonance spectrum and the density of states of both fermionic and bosonic atoms. We point out the existence of so-called quasi-bound states whose wave functions can be approximately calculated analytically. Moreover, we focus on studying quantum mechanical states of ultracold but electronically highly excited atoms - so-called Rydberg atoms - inside magnetic traps. In a first step we explore their internal dynamics by employing a fixed-nucleus approximation. The latter assumes the atomic nucleus to be fixed in the magnetic field minimum. Within this framework we analyze spectral properties as well as properties of the electronic spin and calculate electromagnetic transitions. Finally we present an adiabatic approach which allows for a thorough description of the coupled center of mass and electronic dynamics. We highlight ways to magnetically trap highly excited atoms and present novel quantum states in which the center of mass and the electronic wave function are equal in size. This finding shows that Rydberg atoms even in inhomogeneous fields with moderate gradients cannot be considered point-like.

Contents

1. Introduction	5
1.1. Objective of this work	6
I. Magnetic field configurations and numerical toolkit	9
2. Inhomogeneous magnetic fields - Magnetic traps	11
2.1. A three-dimensional quadrupole field generated by coils	11
2.2. A two-dimensional quadrupole field created by a sideguide configuration	12
2.3. The Ioffe-Pritchard trap	13
2.4. The atom chip	14
3. Numerical tools	17
3.1. The linear variational principle	17
3.1.1. The Hylleraas-Undheim theorem	18
3.1.2. Convergence of the eigenvalues	19
3.2. Arnoldi decomposition and shift-and-invert method	19
3.2.1. The Arnoldi decomposition	19
3.2.2. The shift-and-invert method	20
3.3. Grid-based eigenvalue solver	20
3.4. The complex scaling method	21
II. Dynamics of point particles in inhomogeneous magnetic fields	25
4. Introductory remarks	27
5. Neutral fermions and bosons in a magnetic quadrupole field	29
5.1. The system - Hamiltonian and scaling properties	29
5.2. Symmetries and degeneracies	30
5.3. Numerical treatment	31
5.4. Energies and decay widths of resonance states	32
5.4.1. Relation between energy and momentum of an eigenstate	32
5.4.2. The resonance spectrum of spin $\frac{1}{2}$ fermions	32
5.4.3. Resonance spectrum and density of states of spin 1 bosons	33
5.5. Quasi-bound states	34
5.5.1. Spin $\frac{1}{2}$ fermions	34
5.5.2. Spin 1 bosons	38
5.6. Resonances of magnetically trapped alkali metal atoms	39
5.7. Summary	40

6. Fermions and bosons in a magnetic quadrupole guide and a Ioffe-Pritchard trap	43
6.1. The System - Hamiltonian and scaling properties	43
6.2. Symmetries and Degeneracies	44
6.2.1. Symmetries and degeneracies in the absence of a Ioffe field	44
6.2.2. Symmetries in the presence of a Ioffe field	46
6.3. Numerical treatment	46
6.3.1. Spin $\frac{1}{2}$ fermions - cartesian basis set	46
6.3.2. Spin 1 bosons - cylindrical basis set	47
6.4. Energies and decay widths of resonance states	48
6.4.1. Relation between energy and momentum of an eigenstate	48
6.4.2. The resonance spectrum of spin $\frac{1}{2}$ fermions	49
6.4.3. The resonance spectrum of spin 1 bosons	51
6.5. Angular momentum of the resonance states	51
6.5.1. Resonances of spin $\frac{1}{2}$ fermions and their dependence on their Λ_z eigenvalue	51
6.5.2. Resonances of spin 1 bosons and their dependence on their Λ_z eigenvalue	53
6.6. Quasi-bound states	54
6.6.1. Quasi-bound states of spin $\frac{1}{2}$ fermions in the magnetic guide ($\gamma = 0$)	54
6.6.2. Quasi-bound states of spin $\frac{1}{2}$ fermions in the Ioffe-Pritchard trap ($\gamma \neq 0$) - Comparison to the adiabatic approximation	56
6.6.3. Quasi-bound states of spin 1 bosons in a Ioffe-Pritchard trap ($\gamma \neq 0$)	59
6.7. Resonances of magnetically trapped alkali metal atoms	61
6.8. Summary	62
III. Electronic structure of atoms in high gradient magnetic fields	65
7. Introductory remarks	67
8. Electronic structure of atoms in a three-dimensional quadrupole field	69
8.1. The Hamiltonian	69
8.2. Symmetries and conserved quantities	70
8.3. Numerical treatment	71
8.4. The energy spectrum	72
8.5. Ellipsoidal states	73
8.6. Properties of the electronic spin	75
8.6.1. Expectation value	75
8.6.2. Spin polarization	76
8.7. Electric dipole transitions	78
8.8. Magnetic field induced electric dipoles	80
8.9. Summary	81
9. Electronic structure of atoms in a magnetic guide	85
9.1. The Hamiltonian	85
9.2. Symmetries and degeneracies	86
9.2.1. Degeneracies in the energy spectrum of spin $\frac{1}{2}$ systems in magnetic quadrupole fields	87
9.2.2. Symmetry properties - eigenstates and expectation values	88
9.2.3. Symmetries in the presence of a Ioffe field	89
9.3. Numerical treatment	89
9.4. Spectral properties	91
9.5. Properties of the electronic spin in the absence of a Ioffe field	92

9.5.1. Expectation value	92
9.5.2. Spin polarization	92
9.6. Electric dipole transitions in the absence of a Ioffe field	93
9.7. Properties of the electronic spin in the presence of a Ioffe field	95
9.7.1. The expectation value of S_z	95
9.7.2. Spin polarization	96
9.8. Electric dipole transitions for in the presence of a Ioffe field	96
9.9. Summary	97
IV. Coupled electronic and center of mass dynamics of Rydberg atoms in an inhomogeneous magnetic field	99
10. Quantum states of electronically excited atoms in a magnetic quadrupole trap	101
10.1. Introductory remarks	101
10.2. The Hamiltonian of an excited atom exposed in a linear magnetic field configuration	102
10.3. The magnetic quadrupole field: Hamiltonian and symmetries	104
10.3.1. Symmetries and degeneracies	104
10.3.2. Unitary and scaling transformations	105
10.4. Moving Rydberg atoms in the magnetic quadrupole field	106
10.5. The adiabatic approximation	107
10.5.1. The angular momentum barrier and the avoided crossings near the Z -axis . .	109
10.5.2. The regime of local homogeneity	110
10.5.3. The regime being dominated by the electronic energy	111
10.6. Quantized center of mass motion	111
10.6.1. Confined quantum states of the center of mass motion	113
10.6.2. Properties of the combined quantized center of mass and Rydberg states . . .	115
10.6.3. Radiative decay of trapped atoms	117
10.7. Summary	119
11. Conclusion and outlook	121
A. Vector potential of a magnetic field in a source-free region	125
B. Atomic Units	127
C. Matricelements	129
C.1. Spin $\frac{1}{2}$ Fermions in a magnetic guide - cartesian basis set	129
C.2. Spin 1 Bosons in a magnetic guide - cylindrical basis set	129
D. Danksagung	131

1. Introduction

Tremendous progress has been accomplished in the field of ultracold atomic physics during the past two decades. Laser and evaporative cooling of ground state atoms below temperatures of one micro-Kelvin have become well-established experimental techniques. In conjunction with the application of magnetic and/or electric fields this has granted an outstandingly precise control over the external atomic degrees of freedom. Eventually, this paved the way for the experimental observation of such fascinating phenomena like Bose-Einstein-Condensation (BEC) [23, 29, 79] as well as the formation of degenerate Fermi gases [96] - effects which had been theoretically predicted decades ago. The preparation of these degenerate quantum gases is currently an experimental standard procedure which is performed in countless experiments.

In the course of exploring their properties the potential of ultracold atomic gases for modeling solid state systems was quickly recognized. In contrast to the particles or quasi-particles which are present within solids degenerate quantum gases, made of ultracold atoms, are directly accessible and can be easily probed and manipulated. Periodic potentials which are usually found in crystalline matter can be mimicked by optical lattices [37]. Gauge potentials which are reminiscent of electromagnetic field couplings can be introduced into the many-body Hamiltonian by rotating the atomic gas [6]. Moreover, the capability of adjusting the two-body interaction strengths by means of Feshbach resonances [54] allows for the preparation of very defined and clean physical conditions. In this way virtually any kind of many-particle Hamiltonian can be modeled. The possibility of gaining an unprecedented precise control over the properties of many-body systems has opened a new window for studying and understanding of solid state physics. This enables one to study many-body phenomena like quantum phase transitions [37, 102], the quantum Hall effect [16, 6] or the BEC-BCS crossover [84]. The latter phenomenon takes place in gases of fermionic atoms which, depending on their mutual interaction, either form tightly bound molecules that can condense (BEC) or strongly correlated Cooper pairs (BCS-regime) - a regime which can also be found within superconductors where it is hidden from the view of the outside world.

Apart from these enthralling phenomena which can be observed in gases of ground state atoms there has always been a vivid interest in examining the properties of excited atoms. A special class of them is represented by the so-called Rydberg atoms [34, 32] whose properties are almost solely determined by their single active electron. The most prominent member of this family is hydrogen. Its spectral lines can be grouped into different series named after their discoverers, e.g. Lyman, Balmer, Paschen, Brack, Pfund and Hymphreys. Theoretically the positions of these lines were predicted by the famous Rydberg formula which was deduced by J. Rydberg in 1888. A rigorous theoretical derivation of it, however, was firstly achieved in the framework of the Bohr model of the atom in 1913. Unfortunately this model failed to explain the fine-structure of the spectral lines and the spectrum of complex multi-electron atoms which eventually could be unraveled by modern quantum mechanics. Apart from hydrogen also the spectrum of alkali metal atoms can be described by the Rydberg formula. The occurrence of inner closed electron shells, however, requires the introduction of a quantum defect which accounts for differences from the hydrogen spectrum. The magnitude of this quantum defect strongly depends on the degree of electronic excitation of the atom and for a large degree of excitation an almost unperturbed Rydberg series is encountered. Rydberg atoms occur naturally in star formation, nebula, the boundary between the solar wind and comets but their simple level structure makes them also interesting for earthbound experimental studies.

But only since the availability of small bandwidth and tunable laser sources [89] the controlled realization of Rydberg states up to principal quantum numbers of $n = 100$ and beyond became feasible also in the laboratory. Such highly excited atoms exhibit remarkable features which result from the high density of quantum mechanical states. Essentially this is the reason why describing the interaction of such atoms with strong external magnetic fields requires more sophisticated methods [32, 94] than for ground state atoms. However, it is this complexity which at the same time gives rise to beautiful often unexpected properties.

For small field strengths as they are usually utilized in the laboratory, perturbative approaches are sufficient to understand the magnetized Rydberg spectrum. In homogeneous magnetic fields the degeneracy of states with different angular momentum projections on the field axis is lifted. A special class of quantum states is then constituted by so-called circular states whose angular momentum projection is maximal. G. Raithel and his co-workers analyzed the properties of this kind of Rydberg states in homogeneous magnetic fields. Lifetimes of the order of many milliseconds were predicted [40, 39]. Very recently these results have been backed up by experimental observations [20].

Besides single atom physics the exploration of many-body effects in ultracold Rydberg gases has moved more and more into the focus of experimental and theoretical research [80, 67, 68, 69]. Most of the exciting physics arises from the long ranged Rydberg-Rydberg interaction which is a consequence of the multipole interaction between the electronic clouds [72, 73, 15] - a mechanism which plays no role for ground state atoms. C. Greene *et al.* predicted the existence of long-range homonuclear but polar molecular Rydberg states. The associated wave functions show an extremely peculiar nodal structure which has inspired the authors to refer to them as Trilobite states [36]. Recently the behavior of this exceptional molecular species inside a homogeneous magnetic field has been explored [61]. It was shown that the potential energy surfaces are significantly altered, resulting in the transition of a rotational degree of freedom into a vibrational one. This mechanism allows for the alignment of these molecules and therefore represents a step forward to gain control over this fragile species. Several authors have investigated the properties of so-called frozen Rydberg gases (for example see ref. [77]). In such gases the timescale on which the inter-atomic interactions take place is much faster than the one related to the translational motion of the individual atoms. Here evidence for the formation of long-range Rydberg molecules was found [30], and a plethora of new many-body effects is expected to emerge [80, 81]. Even the existence of a new form of matter so-called Rydberg-matter has been predicted [71, 104]. The strong inter-atomic interaction results in such remarkable features like the dipole blockade mechanism which has been investigated both theoretically [70] and experimentally [106, 100]. In ref. [70, 88] the use of Rydberg atoms as a tool for quantum information processing has been suggested: Provided one finds a mechanism to trap two atoms regardless of their degree of electronic excitation at spatially separated sites one could take advantage of the state dependent atom-atom interaction. While two ground state atoms would not interact there was an interaction established if one or both of the atoms were excited to Rydberg states. Achieving an entangled state by means of this mechanism seems possible.

Altogether, these days - 118 years after J. Rydberg posed his formula - Rydberg physics undergoes a vivid revival with lots of exciting work being done on the theoretical as well as the experimental side.

1.1. Objective of this work

In this work we aspire a thorough investigation and exploration of the quantum dynamics of ground state and Rydberg atoms which are exposed to inhomogeneous magnetic fields. So far comparatively little research has been carried out into this direction.

Unlike this the properties of atoms being exposed to weak homogeneous or quasi-homogeneous magnetic fields are topic of any introductory class in atomic physics. Such quasi-homogeneous fields

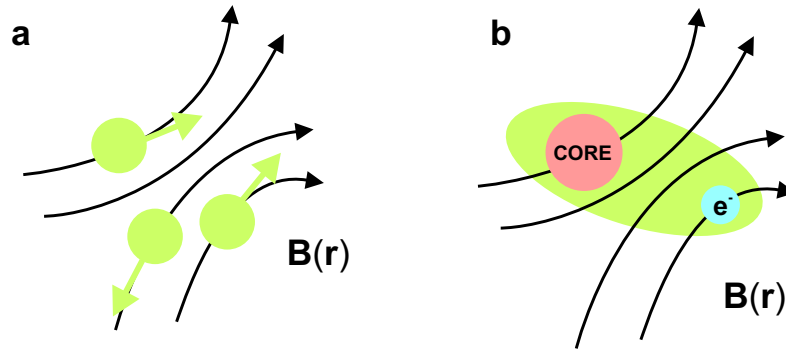


Figure 1.1.: **a:** For small degrees of electronic excitation the atomic size is much smaller than the length scale of the magnetic field variations. In this regime and for weak fields an atom can be regarded as a point-like particle which couples only through its total angular momentum (usually a fine-structure component) to the external field. Effectively the atoms can be treated as if it was a structure-less boson or fermion. **b:** For strongly inhomogeneous fields and/or highly excited atoms, e.g. Rydberg atoms, the internal atomic structure cannot be neglected. Here the couplings of the individual atomic constituents to the external field and the interactions among them have to be taken into account.

exhibit comparatively small spatial variations and can be considered homogeneous over the size of an atom (see figure 1.1a). In this case the appearance of the energy spectrum can be rather easily understood by means of angular momentum couplings and first-order perturbation theory [98]. For large magnetic field strengths or high degrees of excitations, however, this picture breaks down since both the electrostatic and the magnetic interaction become comparable in strength. Such systems cannot be solved by analytical means but require the application of powerful numerical methods. One of the probably best-known and most extensively studied systems of this type is certainly hydrogen in a homogeneous magnetic field. Most of the work regarding this problem was carried out in the 1980's and the beginning of the 1990's [33, 32, 19, 94]. On the one hand this was motivated by the experimental accessibility of highly excited Rydberg atoms [46, 48]. But, on the other hand, also the spectroscopy of astronomical objects such as magnetic white dwarfs possessing an atmosphere that contains significant amounts of hydrogen had demanded for theoretical investigations [87]. Moreover, the progress of developing new numerical techniques made it possible to address regimes where the competition of the Coulomb and diamagnetic interaction leads to unusual and complex properties and phenomena. Apart from the vivid interest in magnetized structures the hydrogen atom also served, and still serves, as a paradigm of a nonseparable and nonintegrable system possessing major impact with respect to the development of several fields such as quantum chaos, semiclassics of nonintegrable systems and nonlinear dynamics in general (see [33, 32, 94, 19] and refs. therein). Besides hydrogen also the exploration of the structure of more complex many-electron atoms exposed to strong and ultra-strong magnetic field has been and still is a vivid and progressing field of research. In particular Helium [8, 7, 2] but also other light atoms like Lithium [4] and Beryllium [3] been extensively studied.

These days inhomogeneous fields find its application in ultracold atomic physics for the purpose of trapping and confinement. While for ground state atoms the assumption of a quasi-homogeneous is in general justified this is not necessarily the case if excited atoms are considered. In strongly nonuniform fields one could think of a scenario where the size of the atom is comparable to or even exceeds the length scale of the spatial magnetic field variations (see figure 1.1b). Here the internal structure of the atom requires to be taken into account.

In this thesis we cover both the quasi-homogeneous as well as the regime where atoms cannot be considered point-like. The work consists of four parts each of which presents a dedicated topic in complete and self-contained form:

- Part I is dedicated to give an overview of the inhomogeneous magnetic field configurations

which are commonly used to trap atoms. Moreover, we briefly outline their experimental realization by means of macroscopic and microscopic wire configurations. Furthermore, we present numerical methods and techniques which will be employed in the course of this work to extract the bound and resonance spectrum of the Schrödinger equation of several quantum mechanical systems. This part can be skipped by the reader who is familiar with magnetic traps and numerical methods for solving large-scale eigenvalue problems.

- In part II we present an analysis of the quantum dynamics of ground state atoms in magnetic quadrupole fields. The internal atomic structure is not resolved and consequently the atoms can be treated as if they were neutral fermions or bosons. The interaction with the external field is solely established via the coupling of total atomic spin to the field. We will see that such systems in general exhibit a resonance rather than a bound spectrum whose properties are explored.
- In part III we focus on the opposite regime. Here we neglect the external (center of mass) dynamics and account only for the internal electronic motion. Thereby the atomic nucleus is assumed to be fixed in the magnetic field minimum. Although this approximation is rather crude it nevertheless illuminates the plethora of features which are expected to occur if highly excited atoms are subjected to inhomogeneous magnetic fields.
- Part IV is certainly the most elaborate part of the present work. Here we coalesce the expertise which has been gained in the previous parts in order to describe the fully quantized motion of an electronically excited atom in a magnetic quadrupole field. To tackle this system in feasible manner the main idea is to decouple the electronic and the center of mass motion adiabatically. We will analyze the peculiar properties of the combined quantum states and investigate whether it is possible to achieve magnetically trapped Rydberg atoms.

We conclude this thesis by summarizing its main results and providing an outlook to future work in a dedicated chapter.

Part I.

**Magnetic field configurations and
numerical toolkit**

2. Inhomogeneous magnetic fields - Magnetic traps

In a large number of present experiments which deal with ultracold atoms inhomogeneous magnetic field are employed for the purpose of trapping. Atoms interact via their total angular momentum with the magnetic field. Depending on the actual projection of the angular momentum vector onto the direction of the magnetic field this gives rise to either confining or nonconfining potentials (see part II of this thesis). Maxwell's equation do not permit the occurrence of magnetic field maxima but only minima in a source-free region. Thus in order to ensure trapping one has to focus on such atomic states for which the underlying potential grows with increasing magnetic field strength. Atoms in such states are referred to as low-field seekers [31].

In the following sections we introduce three magnetic field configurations which exhibit a local field minimum and are therefore suited to trap low-field seeking atoms: We present the three-dimensional quadrupole field realized by two coils being operated in an anti-Helmholtz configuration, a two dimensional quadrupole guide (sideguide) and the so-called Ioffe-Pritchard trap. For each setup we provide approximations of both the magnetic field strength $\mathbf{B}(\mathbf{r})$ and the vector potential $\mathbf{A}(\mathbf{r})$. Finally we outline how all these field configuration can be realized in a very elegant and highly integrated manner by using an atom chip.

2.1. A three-dimensional quadrupole field generated by coils

Probably the most prominent inhomogeneous field configuration is constituted by the three-dimensional quadrupole field. Such field finds its application in virtually any ultracold atom experiment as it is a main element of a magneto-optical trap [75]. The three-dimensional quadrupole field can be generated by two coils of radius R being axially aligned within a distance of $2D_C$ with respect to each other. Both coils are flown through by counter-propagating currents of equal magnitude I_C . Due to the symmetry of this setup there is a single zero of the magnetic field right in the

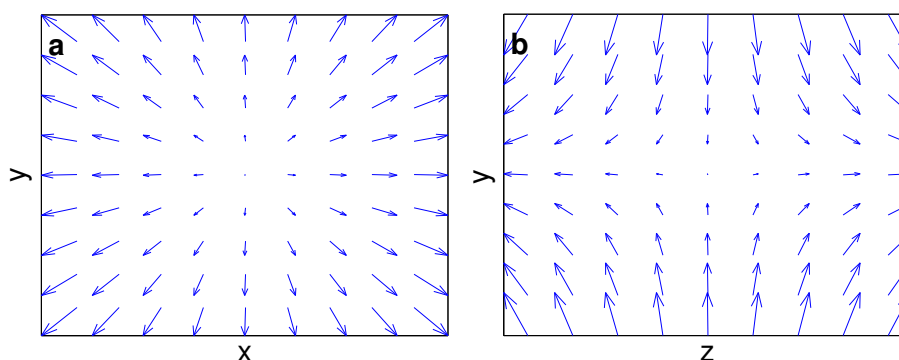


Figure 2.1.: Vectorial plots of intersections through the magnetic quadrupole field (2.1). The intersections are the $x-y$ -plane for $z=0$ (a) and the $y-z$ -plane for $x=0$ (b). The quadrupolar shape and the rotational invariance around the z -axis are clearly visible.

center between the two coils [55]. The position of the field minimum shall be denoted by $\mathbf{r}_0 = 0$. By solving Biot-Savart's law [99] one obtains the following leading order expansion of the magnetic

field

$$\mathbf{B}_{3D}(\mathbf{r}) = \frac{3}{2} \frac{\mu_0 I_C R^2}{(D_C^2 + R^2)^{\frac{5}{2}}} \begin{pmatrix} x \\ y \\ -2z \end{pmatrix} = b \begin{pmatrix} x \\ y \\ -2z \end{pmatrix}. \quad (2.1)$$

This expression is valid in the vicinity of $\mathbf{r}_0 = 0$ up to second order in the spatial coordinates. The field (2.1) depends solely on the parameter b which is referred to as the magnetic field gradient. It is rotationally symmetric around the z -axis and invariant under the z -parity operation. In figure 2.1 we present intersections through the magnetic field for $z = 0$ and $x = 0$, correspondingly.

When considering the coupling of charged particles to a magnetic field one requires a vector-potential which obeys $\nabla \times \mathbf{A}(\mathbf{r}) = \mathbf{B}(\mathbf{r})$. A vector potential which satisfies the Coulomb gauge condition ($\nabla \cdot \mathbf{A}(\mathbf{r}) = 0$) is given by

$$\mathbf{A}_{3D}(\mathbf{r}) = \frac{1}{3} [\mathbf{B}_{3D}(\mathbf{r}) \times \mathbf{r}] = b \begin{pmatrix} yz \\ -xz \\ 0 \end{pmatrix}. \quad (2.2)$$

This expression can either be obtained by a direct integration of $\nabla \times \mathbf{A}(\mathbf{r}) = \mathbf{B}(\mathbf{r})$ or more elegantly by performing the procedure outlined in appendix A.

2.2. A two-dimensional quadrupole field created by a sideguide configuration

The three-dimensional quadrupole field grants confinement in all three spatial directions. A quadrupole field which only allows for a two-dimensional confinement is formed by a so-called sideguide configuration. It consists of a current carrying wire whose 'circular' magnetic field (figure 2.2a) is superimposed by an external homogeneous bias-field of strength B_B . Its field vector is oriented perpendicular to the direction of the current flow. Consequently the magnetic field vanishes

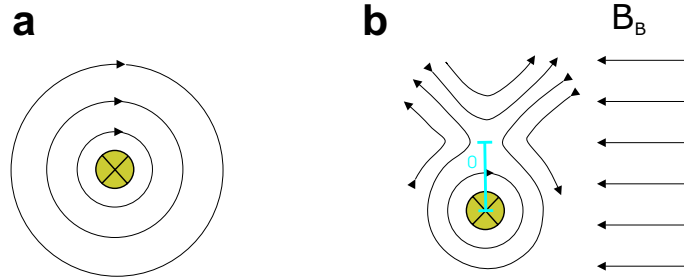


Figure 2.2.: **a:** Magnetic field of a current carrying wire. The magnetic field lines form concentric circles around the wire axis [99]. **b:** Superimposing a homogeneous magnetic field perpendicular to the current flow results in the formation of a two-dimensional quadrupole field at a distance ρ_0 above the wire.

along a line parallel to the wire at a distance $\rho_0 = \frac{\mu_0 I}{2\pi B}$. This distance is completely determined by the current I that is sent through the wire and the bias-field strength B_B (see figure 2.2b). Using Biot-Savart's law the Taylor expansion of the magnetic field in the vicinity of ρ_0 is given according to

$$\mathbf{B}(\mathbf{r}) \approx \frac{B_B}{\rho_0} \begin{pmatrix} x \\ -y \\ 0 \end{pmatrix} + \frac{B_B}{\sqrt{2}\rho_0^2} \begin{pmatrix} -x^2 + 2xy + y^2 \\ x^2 + 2xy - y^2 \\ 0 \end{pmatrix} + \frac{B_B}{\rho_0^3} \begin{pmatrix} y(y^2 - 3x^2) \\ -x(x^2 - 3y^2) \\ 0 \end{pmatrix}. \quad (2.3)$$

These terms represent the quadrupole, hexapole and octopole components of the inhomogeneous field. Neglecting the higher order terms and keeping only the quadrupole term should represent a

good approximation for sufficiently large values of ρ_0 . In this case one obtains

$$\mathbf{B}_{2D}(\mathbf{r}) = b \begin{pmatrix} x \\ -y \\ 0 \end{pmatrix} \quad (2.4)$$

Here, reminiscent of the three-dimensional quadrupole field, b is the magnetic field gradient which determines the linear growth of the field strength with increasing distance from the line of zero field. Its magnitude depends on the field strength B_B of the bias-field and the current I according to

$$b = \frac{B_B}{\rho_0} = \frac{2\pi B_B^2}{\mu_0 I}. \quad (2.5)$$

In figure 2.3 we show two vectorial plots which are made along cuts through the field. The cut

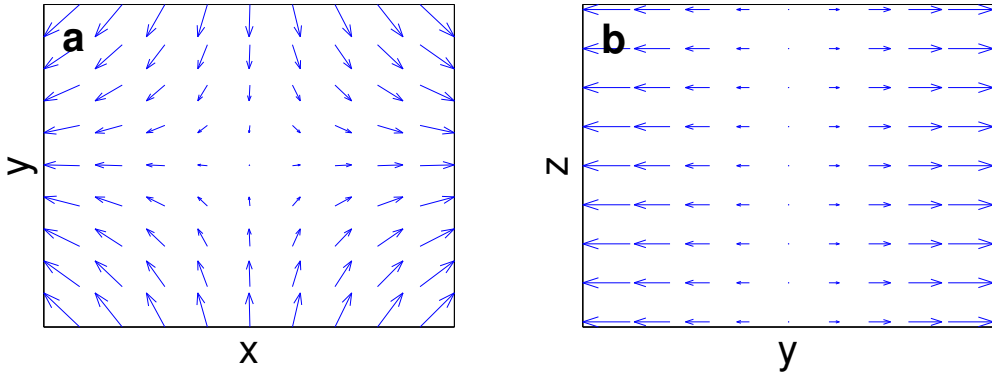


Figure 2.3.: Vectorial plots of the two-dimensional magnetic quadrupole field according to equation (2.4). **a:** Intersection for $z = 0$. The quadrupolar shape of the field is clearly recognized. **b:** The intersection made at $x = 0$ reveals the invariance of the field with respect to translations parallel to the z -axis.

through the $x - y$ -plane immediately reveals the quadrupolar shape. The translational invariance along the z -axis can be easily observed in figure 2.3b. A vector potential of (2.4) which satisfies the Coulomb gauge is given by

$$\mathbf{A}_{2D}(\mathbf{r}) = b \begin{pmatrix} 0 \\ 0 \\ xy \end{pmatrix}. \quad (2.6)$$

This expression can be received by following the procedure outlined in appendix A.

2.3. The Ioffe-Pritchard trap

Another setup which can be utilized to generate a two-dimensional quadrupole field is presented in figure 2.4. In this so-called Ioffe-Pritchard setup the quadrupole field is generated by four straight wires or rods - the Ioffe bars. Each of them carries the same current I_B but with alternating directions of the current flow, as indicated in the figure. Assuming the bars to be placed at the corners of a square of width D_B the magnetic field in vicinity of $(x_0, y_0) = 0$ reads approximately

$$\mathbf{B}_{2D}(\mathbf{r}) = b \begin{pmatrix} x \\ -y \\ 0 \end{pmatrix} = \frac{4\mu_0 I_B}{\pi D_B^2} \begin{pmatrix} x \\ -y \\ 0 \end{pmatrix} \quad (2.7)$$

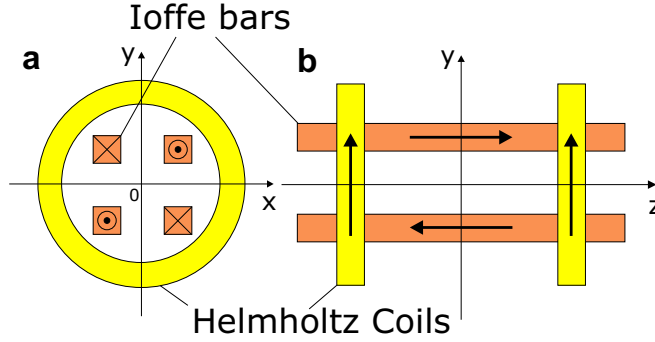


Figure 2.4.: Sketch of a setup that gives rise to a so-called Ioffe-Pritchard trap (**a**: axial view, **b**: longitudinal view). A two-dimensional quadrupole field is created by counter propagating currents that flow through the Ioffe bars. The so-called Ioffe field perpendicular to the quadrupole is created by two coils running parallel currents (Helmholtz-configuration).

To avoid the line of zero field strength the setup additionally incorporates two circular coils of diameter R being axially aligned with a displacement of $2D_C$ centered at $z_0 = 0$. Provided that both coils carry the same current I_C the Taylor expansion of the magnetic field up to second order around $\mathbf{r}_0 = 0$ reads

$$\mathbf{B}_C(\mathbf{r}) = \frac{\mu_0 I_C R^2}{(D_C^2 + R^2)^{\frac{3}{2}}} \begin{pmatrix} 0 \\ 0 \\ 1 \end{pmatrix} + \frac{3\mu_0 I_C R^2 (R^2 - 4D_C^2)}{2(D_C^2 + R^2)^{\frac{7}{2}}} \begin{pmatrix} xz \\ yz \\ \frac{1}{2}(x^2 + y^2 - 2z^2) \end{pmatrix}. \quad (2.8)$$

For $R = 2D_C$ the second term vanishes. This particular setup is then known as the Helmholtz configuration. In this case the total field of the Ioffe-Pritchard trap approximately reads

$$\mathbf{B}_{IP}(\mathbf{r}) = \begin{pmatrix} bx \\ -by \\ B_I \end{pmatrix} \quad \text{with} \quad B_I = \frac{\mu_0 I_C R^2}{(D_C^2 + R^2)^{\frac{3}{2}}}. \quad (2.9)$$

In this context B_I is denoted as the Ioffe field strength. In practise the inhomogeneity of the magnetic field given by equation (2.8) is usually exploited to establish a confinement of, for instance, an atomic cloud in the longitudinal (z -)direction. However, throughout this work we will not consider such inhomogeneity.

Finally we provide the vector potential of the field generated by the Ioffe-Pritchard trap. According to the considerations of appendix A it is given by

$$\mathbf{A}_{IP}(\mathbf{r}) = \frac{B_I}{2} \begin{pmatrix} -y \\ x \\ 0 \end{pmatrix} + \mathbf{A}_{2D}(\mathbf{r}). \quad (2.10)$$

2.4. The atom chip

In the previous sections we have considered macroscopic setups which involved coils or broad wires in order to generate specific types of inhomogeneous fields. In practice, however, such setups are bulky and therefore inflexible. Consequently - as a result of the growing effort for miniaturization and integration - the so-called atom chip was developed [31, 85]. Here the field generating wires are mounted on a surface (see figure 2.5a). These structures are extremely robust although the typical

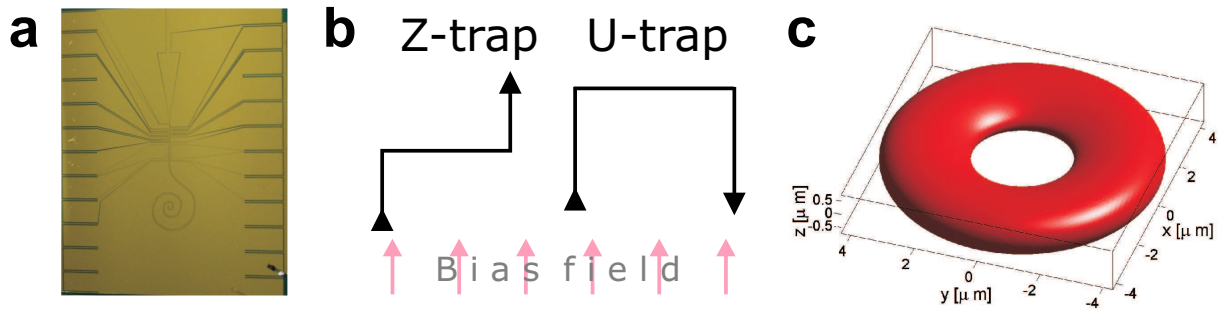


Figure 2.5.: **a:** Photograph of an atom chip. The wires are formed by gold being evaporated onto a silicon surface. Virtually any wire geometry can be realized by this method. Even spiral shaped structures are possible this way. **b:** Wire traps. A current running through a Z-shaped wire results in a Ioffe-Pritchard type field configuration. A three-dimensional quadrupole field is achieved by using a U-shaped wire. **c:** By not only using static magnetic fields but combining them with electric or time-dependent magnetic fields outstandingly versatile trapping configurations can be achieved. Here a ring-shaped potential is shown which is arises by coupling the magnetic hyperfine-states of an alkali metal atom by a radio frequency field.

wire widths is only about a few micrometers. Due to its small structure size the atom chip has the capability to generate extremely high gradient fields that are necessary for the realization of very tightly confining traps with typical ground state sizes of a few 10 nanometers [59].

Since the field generating structures can be almost designed at will there seems in principle to be a total freedom in designing magnetic field 'landscapes': Bent wires can be used to create the quadrupole field configuration which were discussed in the previous sections: A U-shaped wire is utilized to create a three-dimensional quadrupole field. Z-shaped wires give rise to a Ioffe-trap. Both kinds of wire traps are depicted in figure 2.5b. However, by generating static magnetic fields of arbitrary shape the full potential of the atom chip is by far not tapped entirely. By using an external laser source, standing light waves can be established right above the reflecting chip surface. The resulting optical dipole potentials can be utilized to carry out further manipulation on trapped atomic clouds [35]. Moreover, the number of possible potential shapes can be diversified by introducing electric potentials by charging appropriate areas of the chip surface [52] or running AC currents through the wires which create oscillating magnetic fields. In particular the latter gives rise to so-called dressed adiabatic potentials that allow for a most simple and elegant implementation of a plethora of atom optical elements such as beamsplitters and interferometers [97, 66]. Even more sophisticated configurations such as rings (see figure 2.5c) can be achieved by this method.

3. Numerical tools

3.1. The linear variational principle

The quantum mechanical problems discussed in this work require the solution of the stationary Schrödinger equation

$$H |\Psi_j\rangle = E_j |\Psi_j\rangle \quad (3.1)$$

where H is the Hamiltonian of the system under consideration. A powerful tool which allows for solving this, in general, infinitely dimensional eigenvalue problem is the linear variational principle [105]. Here a set of basis functions $\{|\beta\rangle\}$ is employed to construct the trial function

$$|\Psi\rangle = \sum_{\beta} c_{\beta} |\beta\rangle \quad (3.2)$$

with the expansion coefficients c_{β} serving as variational parameters. The basis functions $|\beta\rangle$ shall be normalized, i.e. $\langle\beta|\beta\rangle = 1$, but need not necessarily to be orthogonal with respect to each other. Moreover, $|\Psi\rangle$ shall be normalized which leads to the requirement

$$1 = \langle\Psi|\Psi\rangle = \sum_{\beta\beta'} c_{\beta}^* c_{\beta'} \langle\beta|\beta'\rangle = \sum_{\beta\beta'} c_{\beta}^* c_{\beta'} \mathcal{S}_{\beta\beta'} = \mathbf{c}^{\dagger} \mathcal{S} \mathbf{c}. \quad (3.3)$$

\mathcal{S} is the so-called overlap matrix, which is unity in case of an orthonormal set of basis functions. The expectation value of the Hamiltonian H in the functions (3.2) reads

$$\langle H \rangle = \langle\Psi|H|\Psi\rangle = \sum_{\beta\beta'} c_{\beta}^* c_{\beta'} \langle\beta|H|\beta'\rangle = \sum_{\beta\beta'} c_{\beta}^* c_{\beta'} \mathcal{H}_{\beta\beta'} = \mathbf{c}^{\dagger} \mathcal{H} \mathbf{c}. \quad (3.4)$$

According to the variational principle the optimal set of expansion coefficients c_{β} is that which minimizes this expectation value. In order to find this set we have to minimize the following expression

$$L = \sum_{\beta\beta'} c_{\beta}^* c_{\beta'} \mathcal{H}_{\beta\beta'} - \chi \left[\sum_{\beta\beta'} c_{\beta}^* c_{\beta'} \mathcal{S}_{\beta\beta'} - 1 \right]. \quad (3.5)$$

Here the second term accounts for the constraint of the state $|\Psi\rangle$ to be normalized and χ is the corresponding Lagrange parameter. Evaluating the derivative of equation (3.5) with respect to c_{β} and putting it equal to zero we obtain an equation whose solution yields the optimal expansion coefficients c_{β} :

$$\frac{\partial L}{\partial c_{\beta}^*} = \sum_{\beta'} [\mathcal{H}_{\beta\beta'} - \chi \mathcal{S}_{\beta\beta'}] c_{\beta'} = 0 \quad (3.6)$$

It can be written more compactly as

$$\mathcal{H} \mathbf{c} = \chi \mathcal{S} \mathbf{c} \quad (3.7)$$

and is now immediately recognized as a generalized algebraic eigenvalue equation. In order to illuminate the actual meaning of the eigenvalues χ we consider the matrix element

$$\langle \Psi_i | H | \Psi_j \rangle = \mathbf{c}_i^\dagger \mathcal{H} \mathbf{c}_j = \chi_j \mathbf{c}_i^\dagger \mathcal{S} \mathbf{c}_j = \chi_j \delta_{ij}. \quad (3.8)$$

Apparently χ_j is the energy expectation value of the state $|\Psi_j\rangle$. Hence, the eigenvalues χ_j can be considered to be the energy eigenvalues E_j of the system described by the Hamiltonian H . Using infinitely many basis functions the χ_j would even represent the exact eigenenergies. However, since in practice any computation can involve only a finite set of basis functions the χ_j constitute only upper bounds of the exact eigenvalues. The latter statement is known as the Hylleraas-Undheim theorem whose prove is outlined in the following section.

3.1.1. The Hylleraas-Undheim theorem

For proving the Hylleraas-Undheim theorem we follow ref. [78]. We consider a $N \times N$ Matrix \mathcal{M} of the form

$$\mathcal{M} = \begin{pmatrix} & & & \mathcal{M}_{1N} \\ & \mathcal{M}' & & \mathcal{M}_{2N} \\ & & & \vdots \\ \mathcal{M}_{N1} & \mathcal{M}_{N2} & \cdots & \mathcal{M}_{NN} \end{pmatrix}. \quad (3.9)$$

with \mathcal{M}' being a hermitian $(N-1) \times (N-1)$ matrix which possesses the eigenvalues λ'_i . It is now always possible to find a basis in which \mathcal{M}' becomes diagonal with its eigenvalues occupying the main diagonal in ascending order, i.e. $\lambda'_i \leq \lambda'_{i+1}$. The eigenvalues λ_i of the matrix \mathcal{M} are the zeros of the determinant

$$\begin{aligned} f(\lambda) &= \det(\mathcal{M} - \lambda \mathcal{I}) = \begin{vmatrix} \lambda'_1 - \lambda & 0 & \cdots & \mathcal{M}_{1N} \\ 0 & \lambda'_2 - \lambda & \cdots & \mathcal{M}_{2N} \\ \vdots & \vdots & \ddots & \vdots \\ \mathcal{M}_{N1} & \mathcal{M}_{N2} & \cdots & \mathcal{M}_{NN} - \lambda \end{vmatrix} \\ &= (\mathcal{M}_{NN} - \lambda) \prod_{n=1}^{N-1} (\lambda'_n - \lambda) - \sum_{m=1}^{N-1} |\mathcal{M}_{mN}|^2 \prod_{n \neq m}^{N-1} (\lambda'_n - \lambda). \end{aligned} \quad (3.10)$$

Evaluating $f(\lambda)$ at $\lambda = \lambda'_k$ one obtains

$$f(\lambda'_k) = -|\mathcal{M}_{kN}|^2 \prod_{n \neq k}^{N-1} (\lambda'_n - \lambda'_k) = \begin{cases} \leq 0 & k \text{ odd} \\ \geq 0 & k \text{ even} \end{cases} \quad (3.11)$$

One then finds the following limiting behavior for $f(\lambda)$:

$$\begin{aligned} f(\lambda) &\rightarrow +\infty & \text{if} & \lambda \rightarrow -\infty \\ f(\lambda) &\rightarrow (-)^N \infty & \text{if} & \lambda \rightarrow +\infty \end{aligned}$$

From (3.11) we conclude $f(\lambda)$ to have an odd number of zero between two distinct eigenvalues λ'_i of \mathcal{M}' . Since $f(\lambda)$ must have N real zeros λ_n the λ'_i have to be ordered according to

$$\lambda_1 \leq \lambda'_1 \leq \lambda_2 \leq \lambda'_2 \leq \cdots \leq \lambda'_{N-1} \leq \lambda_N \quad (3.12)$$

Hence, the eigenvalues of \mathcal{M}' constitute upper bounds for the eigenvalues of \mathcal{M} .

3.1.2. Convergence of the eigenvalues

We now know the eigenvalues obtained from the linear variational principle to constitute upper bounds of the exact energy eigenvalues. For a specific calculation it is now important to have a criterion which determines how well an exact energy eigenvalue is actually approximated. To obtain a measure of the convergence behavior of the eigenvalues we perform the following procedure:

At first we calculate a number of eigenvalues $E_i^{G_1}$ for a given basis set size G_1 . Thereafter the basis size is significantly increased to a value G_2 . This larger basis set should for instance cover a larger spatial region, involve higher angular momentum states or include basis functions belonging to a different symmetry subspace. Now, using this enlarged basis, the energies are recalculated yielding the new set of eigenvalues $E_i^{G_2}$. As a measure of convergence we now define the quantity

$$K_i = \left| \frac{E_i^{G_1} - E_i^{G_2}}{E_i^{G_1} - E_{i-1}^{G_1}} \right| \quad (3.13)$$

where the difference of the same eigenvalue for the two basis sizes G_1 and G_2 is divided by the distance to the next lower eigenvalue. For any calculation performed in this thesis we have considered the i -th eigenvalue $E_i^{G_2}$ to be well converged if $K_i \leq 0.01$.

3.2. Arnoldi decomposition and shift-and-invert method for solving sparse eigenvalue problems

By employing the variational principle the stationary Schrödinger equation is mapped onto an ordinary or generalized eigenvalue problem. The associated matrices are usually of large dimension but sparsely occupied.

In this section we want to briefly introduce the Arnoldi method which is particularly suited for obtaining numerical solutions of such eigenvalue problems. The gist of the Arnoldi method is that the large-scale eigenvalue problem is reduced to one with a significantly lower dimension which is then soluble with comparatively little effort. In conjunction with this method we utilize the so-called shift-and-invert procedure which allows for the calculation of eigenenergies lying in almost arbitrary regions of the spectrum without the need to calculate the entire spectrum bottom up. For the numerical implementation of both, the Arnoldi decomposition and the shift-and-invert method, we have utilized the routines provided by the ARPACK software package [101]. This package demands for a routine capable of efficiently solving an inhomogeneous system of equations. For this purpose we have utilized the SUPERLU software package [24].

3.2.1. The Arnoldi decomposition

We now briefly outline the fundamentals of the Arnoldi method: The Arnoldi decomposition of a matrix \mathcal{A} is obtained by representing it in the so-called Krylov-space which is defined as

$$K_k := \text{span}\{\mathbf{v}, \mathcal{A}\mathbf{v}, \dots, \mathcal{A}^{k-1}\mathbf{v}\}. \quad (3.14)$$

Here \mathbf{v} can be any nonzero complex vector possessing the same dimension as \mathcal{A} . The Arnoldi decomposition of the matrix $\mathcal{A} \in \mathbb{C}^{n \times n}$ reads

$$\mathcal{A}\mathcal{V}_k = \mathcal{V}_k\mathcal{H}_k + \mathbf{f}_k\mathbf{e}_k^T \quad (3.15)$$

Here the matrix $\mathcal{V}_k \in \mathbb{C}^{n \times k}$ is composed of orthonormal column vectors which obey $\mathcal{V}_k^T \mathbf{f}_k = 0$. The matrix $\mathcal{H}_k \in \mathbb{C}^{k \times k}$ is an upper Hessenberg matrix with nonnegative entries below the main diagonal. In case of \mathcal{A} being hermitian \mathcal{H}_k is reduced to a real, symmetric and tri-diagonal matrix. In this

case (3.15) is referred to as Lanczos factorization. Now be \mathbf{y} a vector satisfying the eigenvalue equation

$$\mathcal{H}_k \mathbf{y} = \eta \mathbf{y}, \quad (3.16)$$

then the vector $\mathbf{x} = \mathcal{V}_k \mathbf{y}$ satisfies the equation

$$\|\mathcal{A}\mathbf{x} - \eta\mathbf{x}\| = \|(\mathcal{A}\mathcal{V}_k - \mathcal{V}_k\mathcal{H}_k)\mathbf{y}\| = \|\mathbf{f}_k\| |\mathbf{e}_k^T \mathbf{y}|. \quad (3.17)$$

Here (\mathbf{x}, η) is denoted as a Ritz pair representing an approximate solution of the eigenvalue problem of the matrix \mathcal{A} . The quality of this approximation is measured by the magnitude of the so-called Ritz estimate $\|\mathbf{f}_k\| |\mathbf{e}_k^T \mathbf{y}|$. In practice the value of the Ritz estimate is controlled through the modulus of the vector

$$\mathbf{r}(\mathbf{x}) = \mathcal{A}\mathbf{x} - \mathbf{x}\eta. \quad (3.18)$$

If $\|\mathbf{r}(\mathbf{x})\| = \|\mathbf{f}_k\| |\mathbf{e}_k^T \mathbf{y}|$ drops below a certain threshold (commonly machine precision), the pair (\mathbf{x}, η) is considered converged. If necessary the value of k has to be increased to establish convergence.

In practise the value of k is much smaller than the dimension of the matrix \mathcal{A} whose eigenvalue problem is being solved. As a result only the eigenvalues and eigenvectors of a k -dimensional Hessenberg matrix have to be calculated for which efficiently working algorithms are available. The method converges firstly for those eigenvalues of \mathcal{A} that are largest or smallest in magnitude. Hence, the method is most efficiently used for finding the extremal eigenvalues of \mathcal{A} .

3.2.2. The shift-and-invert method

For some physical problems it is impractical to have only good approximations of the extremal eigenvalues of the matrix representation of the Hamiltonian. This is in particular the case if one is interested in calculating highly excited electronic states. Here the maximal eigenvalues of the Hamilton matrix are dominated by numerical artifacts arising from the finite number of used basis functions. Thus one had to calculate the entire spectrum bottom up. However, this is impossible due to the high dimensionality of the problem. The solution for this dilemma is to transform the initial Hamilton matrix such that the extremal eigenvalues of the transformed matrix are just the ones one is interested in. Assume we want to find all eigenenergies lying closely to the energy σ . For this purpose we perform the transformation:

$$\mathcal{H}\mathbf{c} = E\mathcal{S}\mathbf{c} \quad \longrightarrow \quad (\mathcal{H} - \sigma\mathcal{S})^{-1}\mathcal{S}\mathbf{v} = \lambda\mathbf{v} \quad (3.19)$$

The old eigenvalues E_i are related to the new ones λ_i by

$$E_i = \sigma + \frac{1}{\lambda_i} \quad (3.20)$$

Hence, eigenvalues lying close to σ are the eigenvalues of the operator $(\mathcal{H} - \sigma\mathcal{S})^{-1}\mathcal{S}$ being largest in magnitude and will thus converge first.

3.3. Grid-based eigenvalue solver

Although extremely powerful the application of the variational method might be simply overdone at some occasions. Especially if one is interested in the eigenstates of a Hamiltonian whose potential $V(x)$ is already given on a low-dimensional grid with the sampling points $\{x_0, x_1, \dots, x_N\}$. We will encounter such kind of problem for instance in part IV of this thesis where the quantum states of the atomic center of mass motion on a two-dimensional energy surfaces will be calculated. Once one

knows the sampled potential one can construct the representation of the kinetic energy operator $T = -\frac{\hbar^2}{2m} \sum_i \frac{\partial^2}{\partial x_i^2}$ on the grid by discretizing the second derivative [83]. This becomes most simple on an equidistant grid with grid spacing Δx . In the one-dimensional case a five-point differencing scheme of the second derivative is given by

$$\frac{\partial^2 \Psi(x)}{\partial x^2} = -\frac{1}{(\Delta x)^2} \left[\frac{1}{12} \Psi(x_{n-2}) - \frac{4}{3} \Psi(x_{n-1}) + \frac{5}{2} \Psi(x_n) - \frac{4}{3} \Psi(x_{n+1}) + \frac{1}{12} \Psi(x_{n+2}) \right]. \quad (3.21)$$

This expression is exact up to fourth order in Δx . Now the stationary Schrödinger equation (3.1) can be written as a matrix equation of the form

$$[\mathcal{T} + \mathcal{V}] \mathbf{v} = E \mathbf{v} \quad (3.22)$$

with the kinetic energy matrix \mathcal{T} and the potential matrix

$$\mathcal{V} = \text{diag}(V(x_0), V(x_1), \dots, V(x_N)). \quad (3.23)$$

These matrices act on the grid representation of the eigenstate $\Psi(x)$ which is given by the vector

$$\mathbf{v} = (\Psi(x_0), \Psi(x_1), \dots, \Psi(x_N))^T. \quad (3.24)$$

In the present case the $(N+1) \times (N+1)$ matrix $\mathcal{T} + \mathcal{V}$ is penta-diagonal and its eigenvalue problem can be efficiently solved for instance by diagonalization routines provided by the NAG or LAPACK library. This scheme can be easily extended to higher dimensions or higher accuracy. For the latter the five-point rule has to be replaced by a higher order approximation of the second derivative. In case of a higher dimensional coordinate space each coordinate requires the introduction of an additional index. To obtain a matrix equation of the form (3.22) these indices have to be combined to a superindex granting a two-dimensional arrangement of the matrix elements.

3.4. The complex scaling method

There are countless physical systems that exhibit a resonance rather than a bound spectrum. According to ref. [76] a resonance state is defined as a long-lived state which has sufficient energy to break up into two or more subsystems. Such system can be an ionized atom decaying into an electron and a nucleus or a radioactive nucleus braking apart into fragments. The latter can be

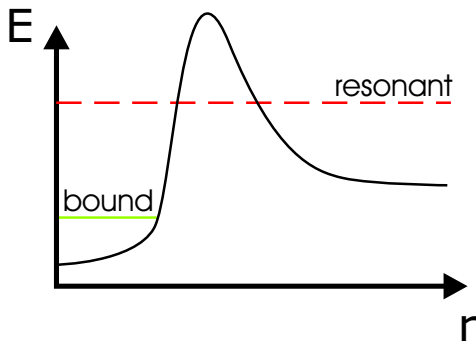


Figure 3.1.: Potential that exhibits both, bound and resonance states. The resonance state is - for a sufficiently long lifetime - localized inside the well before it decays.

effectively considered as a particle being trapped inside a potential barrier of finite height (see figure 3.1). The resonance state is trapped for a considerably long time inside the well until it

tunnels through the barrier within a specific lifetime τ . Such state is not a stationary solution of the Schrödinger equation but can be regarded as a superposition of continuum states for which the probability of finding the particle on the left hand side of the barrier is close to unity at the initial time.

Resonances are nonsquare-integrable eigenfunctions of the Hamiltonian whose eigenvalues have the appearance

$$\varepsilon = E - i\frac{\Gamma}{2}. \quad (3.25)$$

They are complex valued since the Hamiltonian is only hermitian, and has thus real eigenvalues, if it acts on bounded functions, which is not the case here. From the decay width Γ the associated lifetime τ can be calculated according to $\tau = \Gamma^{-1}$. A time-dependent solutions of the underlying Schrödinger equation can be written as

$$\Psi_{\text{res}}(\mathbf{r}, t) = \Phi_{\text{res}}(\mathbf{r})e^{-i\varepsilon t} \quad (3.26)$$

and consequently the probability density

$$|\Psi_{\text{res}}(\mathbf{r}, t)|^2 = |\Phi_{\text{res}}(\mathbf{r})|^2 e^{-\Gamma t} \quad (3.27)$$

decays to zero with a specific decay time $\tau = \Gamma^{-1}$. Most numerical algorithms for solving quantum mechanical problems have been developed for hermitian Hamilton operators. The linear variational principle, for instance, relies on square-integrable eigenfunctions which can be expanded in a given basis set also consisting of square-integrable functions. However, the variational principle can be made applicable to nonhermitian resonance Hamiltonians by performing a similarity transformation S referred to as the complex scaling transformation

$$S^{-1}HSS^{-1}\Phi_{\text{res}} = \left(E - i\frac{\Gamma}{2}\right)S^{-1}\Phi_{\text{res}} \quad (3.28)$$

such that $S^{-1}\Phi_{\text{res}} \rightarrow 0$ as $r \rightarrow \infty$. Such similarity transformation is for instance given by

$$S = e^{-i\theta\mathbf{r}\partial_{\mathbf{r}}}. \quad (3.29)$$

Consider the spatial representation of a Hamiltonian exhibiting a resonance spectrum. The operator S performs a rotation of the spatial coordinates into the complex plane: $\mathbf{r} \rightarrow \mathbf{r}e^{i\theta}$ which then yields the 'rotated' Hamiltonian $H(\mathbf{r}e^{i\theta})$. Unlike the bound states only continuum states are affected by the complex scaling procedure. The scattering states are rotated into the lower half of the complex plane and in particular resonances do now correspond to square-integrable functions. The complex resonance energies ε will in general depend on the value of the rotation angle θ . Continuum states are rotated by 2θ into the lower half of the complex plane whereas energies of resonance states - once revealed - are independent of the angle θ (see figure 3.2). Since the complex scaling procedure transforms resonance states into square-integrable wave functions one can apply the linear variational principle in order to compute the associated resonance energies.

To this end one also uses the ansatz (3.2) for the trial wave function which gives rise to an algebraic eigenvalue problem. However, since the complex scaled Hamiltonian is complex symmetric rather than hermitian one has to carefully distinguish between right hand side \mathbf{c}_R and left hand side eigenvectors \mathbf{c}_L . They obey

$$\mathcal{H}\mathbf{c}_R = \chi\mathcal{S}\mathbf{c}_R \quad (3.30)$$

$$\mathbf{c}_L\mathcal{H} = \chi\mathbf{c}_L\mathcal{S}. \quad (3.31)$$

This so-called c-variational principle is thoroughly discussed in ref. [76]. In figure 3.2 we present

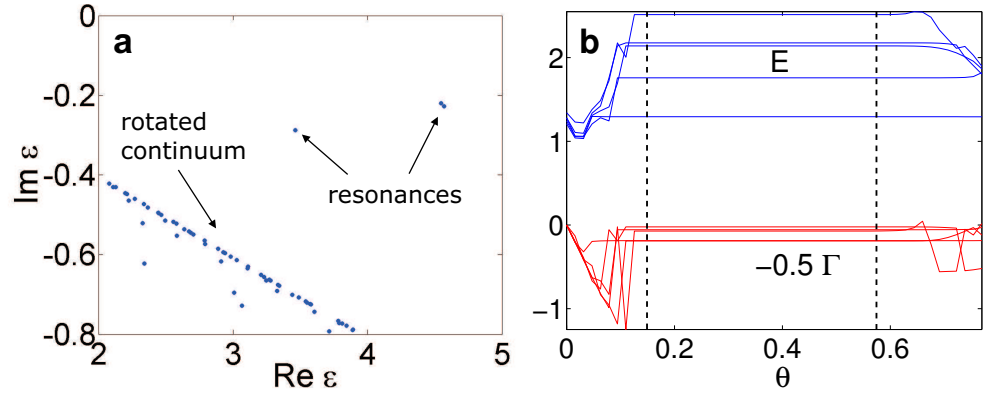


Figure 3.2.: **a:** Rotated continuum and resonances. **b:** Dependence of the resonance energies (upper part) and decay widths (lower part) on the complex scaling angle θ as observed in the numerical calculations. The stationary region is located in-between the dashed lines.

the resonance energy and the decay width of a typical complex scaling calculation with the scaling angle varied over the interval $0 \leq \theta \leq \frac{\pi}{4}$. As expected the resonance positions remain constant after the scaling angle surpasses a certain value (left dashed vertical line). However, there is a second value of θ beyond which this stationarity disappears again. This is an effect of the finite size of the basis set that was used to perform the calculation.

Just like in the hermitian case the eigenstates of the complex scaled Hamiltonian can be used to calculate the expectation of physical quantities. However, this requires the introduction of a modified scalar product. This so-called c-scalar product is defined by

$$(\Psi | \Phi) = \int d^3\mathbf{r} \Psi(\mathbf{r})\Phi(\mathbf{r}) = \mathbf{c}_L^T \mathbf{c}_R. \quad (3.32)$$

The expectation value of a quantity/observable O is now computed according to

$$\langle O \rangle = \frac{(\Psi | S^{-1} O S | \Psi)}{(\Psi | \Psi)} = \frac{\mathbf{c}_L^T O \mathbf{c}_R}{\mathbf{c}_L^T \mathbf{c}_R}. \quad (3.33)$$

For evaluating the latter expression one has to ensure, that $(\Psi | \Psi) = \mathbf{c}_L^T \mathbf{c}_R \neq 0$. Unlike for the hermitian scalar product this conditions is namely not necessarily fulfilled as the c-scalar product is not positive-definite. The diverging expectation value is the consequence of a linear dependence of eigenvectors of the complex scaled Hamiltonian that occurs only for a finite number of complex scaling angles. To overcome this problems in practice usually only a slight variation of θ is needed to reestablish their linear independence.

Part II.

Dynamics of point particles in inhomogeneous magnetic fields

4. Introductory remarks

Magnetic traps are widely used in order to confine and manipulate ultra cold atomic ensembles. With the availability of efficient cooling techniques such as laser and evaporative cooling [75] even the occupation of the lowest quantum levels in such traps became possible. This enabled the exploration of regimes of degeneracy for both bosons (Bose-Einstein-Condensation (see ref. [79] and refs. therein)) and fermions (degenerate Fermi gases [96]).

In order to gain insights into the dynamics of atoms and also neutrons at ultracold temperatures several magnetic field configurations have been subject to theoretical investigations. There exist studies regarding the three-dimensional quadrupole field [10], the wire trap [9, 42, 17, 13] and the magnetic guide and the Ioffe-Pritchard trap [45, 44, 82, 56]. Except for the wire trap none of these field configurations allows for strictly bound states. For the latter even analytical results can be obtained if one restricts oneself to spin $\frac{1}{2}$ particles being trapped in the vicinity of an infinitely thin wire. In the context of cold neutron physics such solutions were obtained for the first time by Blümel and Dietrich by solving a fourth-order Hamburger equation [13]. Further investigations regarding the wire trap have been undertaken by Vestergaard Hau *et al.* [42] who have pursued a supersymmetric approach in order to obtain the Rydberg series of bound states. Particles of higher spin trapped by wires of a finite thickness have been investigated in the work by Burke *et al.* [17].

As already indicated the occurrence of stable states is rather the exception than the rule. For the majority of field configurations one observes a spectrum of states of more or less pronounced resonance character. In refs. [45, 44] Hinds and Eberlein analyze resonances of particles with spin $\frac{1}{2}$ and 1 in a magnetic guide by determining the phase shift of scattered waves. Potvliegé and Zehnle calculated widths and positions of the resonances utilizing the complex scaling method (see ref. [82]). The dynamics of neutral spin particles in the three-dimensional quadrupole field has already been issue of former investigations (see ref. [10]). Here Bergeman *et al.* have calculated about two dozens of resonances, i.e. the resonance energies and decay widths of spin $\frac{1}{2}$ particles. Their numerical method also relied on determining the phase shift of scattered waves.

In this part we study the dynamics of neutral spin $\frac{1}{2}$ and spin 1 particles exposed to three- and two-dimensional quadrupole fields. Each of these two field configuration is dealt with in a separate chapter. In either of them we provide hundreds of resonances which have been calculated by utilizing the complex scaling method. This is why we can, in contrast to previous works, conclude upon global properties of the distribution of the resonance positions. We systematically analyze how the lifetime of the resonances depends on the angular momentum of the quantum states. Thereby we are lead to quasi-bound states which possess extremely long lifetimes. We will derive an approximate Schrödinger equation in order to elucidate the nature of these states. Moreover, we compare the energies of the quasi-bound states to those which are obtained by using the adiabatic approximation [31]. Finally, we demonstrate how our results can be applied to calculate resonance properties of magnetically trapped alkali metal atoms.

5. Spectral properties and lifetimes of neutral fermions and bosons in a magnetic quadrupole field

In this chapter we explore the quantum mechanical resonance states of neutral spin particles which are exposed to a three-dimensional magnetic quadrupole field. Thereby we proceed as follows: In section 5.1 we present the derivation of the Hamiltonian describing our system. Section 5.2 contains a detailed discussion of the corresponding symmetry properties. The structure of the underlying symmetry group leads to degeneracies in the energy spectrum which are deduced. The numerical approach which is pursued in order to calculate the resonance energies and lifetimes is outlined in section 5.3. Sections 5.4 to 5.6 contain a discussion of our results: We present the resonance spectrum of spin $\frac{1}{2}$ and spin 1-particles. Moreover, we show and discuss the properties of the density of states. An exploration of the relation between the lifetime and the angular momentum of the resonance states is provided and a Schrödinger equation providing an approximate description of so-called quasi-bound states is presented. The results are compared to those one would obtain when applying the commonly used adiabatic approximation. Finally we apply our results to the case of ${}^6\text{Li}$ and ${}^{87}\text{Rb}$ atoms being trapped in a hyperfine ground state. The chapter closes with section 5.7 that contains a brief summary of the results.

5.1. The system - Hamiltonian and scaling properties

The Hamiltonian describing the motion of a point-like particle of mass M with the magnetic moment $\boldsymbol{\mu}$ inside a magnetic field $\mathbf{B}(\mathbf{r})$ reads

$$H' = \frac{\mathbf{p}^2}{2M} - \boldsymbol{\mu} \cdot \mathbf{B}(\mathbf{r}). \quad (5.1)$$

Inserting the quadrupole field (2.1) and taking into account that the magnetic moment relates to the particles spin \mathbf{S} by $\boldsymbol{\mu} = -\frac{g}{2}\mathbf{S}$ the Hamiltonian becomes

$$H' = \frac{1}{2M} [\mathbf{p}^2 + b g M (x S_x + y S_y - 2z S_z)] \quad (5.2)$$

with g being the g -factor of the particle. Performing the scale transformation $\bar{x}_i = (bgM)^{\frac{1}{3}} x_i$ and $\bar{p} = (bgM)^{-\frac{1}{3}} p_i$ and omitting the bars one obtains

$$M (bgM)^{-\frac{2}{3}} H' = H = \frac{1}{2} (\mathbf{p}^2 + x S_x + y S_y - 2z S_z) \quad (5.3)$$

which represents this chapter's working Hamiltonian. It does not contain any system related parameters which makes the obtained results generally applicable. Equation (5.3) implies the energy level spacing to scale according to $\frac{1}{M} (bgM)^{\frac{2}{3}}$.

5.2. Symmetries and degeneracies

Before we tackle the problem of finding solutions to the stationary Schrödinger equation we first want to analyze the symmetry properties of the Hamiltonian. In the course of this thesis it will turn out that such - often tedious - analysis is often extremely helpful. It helps to elucidate specific features of the energy spectrum such as degeneracies without the need to solve the Schrödinger equation. Moreover, knowledge of the symmetries allows to make valuable predictions about the magnitude of certain expectation values or (transition) matrix elements.

Analyzing the symmetry properties of the Hamiltonian (5.3) we could identify 16 discrete operations of both unitary and antiunitary character. Antiunitary operators involve the conventional time-reversal operator T . A list of the discrete symmetries can be found in table 5.1. Each one is composed of a number of elementary operations which are listed in table 5.2.

$\Sigma_x = D_1 P_y P_z$	$\Sigma_y = P_x D_2 P_z$	$\Sigma_z = P_x P_y D_3$	1
$P_x P_y P_z I_{xy} D_4$	$P_z I_{xy} D_4^*$	$P_y I_{xy} D_5$	$P_x I_{xy} D_5^*$
$T D_1 P_z$	$T P_x P_y D_2 P_z$	$T P_x D_3$	$T P_y$
$T P_x P_z I_{xy} D_4$	$T P_y P_z I_{xy} D_4^*$	$T I_{xy} D_5$	$T P_x P_y I_{xy} D_5^*$

Table 5.1.: Discrete symmetries of the Hamiltonian (5.3). Each symmetry is composed of a number of elementary symmetries which are listed in table 5.2

Operator	Operation
P_{x_i}	$x_i \rightarrow -x_i$
I_{xy}	$x \rightarrow y \quad y \rightarrow x \quad z \rightarrow z$
T	$A \rightarrow A^*$ (conventional time reversal)
$D_1 = e^{iS_x \pi}$	$S_x \rightarrow S_x \quad S_y \rightarrow -S_y \quad S_z \rightarrow -S_z$
$D_2 = e^{iS_y \pi}$	$S_x \rightarrow -S_x \quad S_y \rightarrow S_y \quad S_z \rightarrow -S_z$
$D_3 = e^{iS_z \pi}$	$S_x \rightarrow -S_x \quad S_y \rightarrow -S_y \quad S_z \rightarrow S_z$
$D_4 = e^{iS_z \frac{\pi}{2}} e^{iS_x \pi}$	$S_x \rightarrow -S_y \quad S_y \rightarrow -S_x \quad S_z \rightarrow -S_z$
$D_5 = e^{-iS_z \frac{\pi}{2}}$	$S_x \rightarrow -S_y \quad S_y \rightarrow S_x \quad S_z \rightarrow S_z$

Table 5.2.: Set of discrete operations out of which all discrete symmetry operations of the Hamiltonian (5.3) can be composed.

Although the symmetry operations shown in the table 5.1 formally possess the same decomposition in terms of elementary operations for both fermions and bosons both underlying symmetry groups possess structural differences. For instance one finds $\{\Sigma_i, \Sigma_j\} = 0$ in case of fermions but $[\Sigma_i, \Sigma_j] = 0$ if bosons are considered.

Apart from the discrete symmetries there is a continuous symmetry group generated by $J_z = L_z + S_z$ which is the z -component of the total angular momentum. This is a consequence of the rotational invariance of the system around the z -axis of the coordinate system. Because of $[J_z, H] = 0$ one can construct energy eigenfunctions which are simultaneously eigenfunctions of J_z . For a spin s particle they read in the spatial representation

$$|m\rangle^{(s)} = \sum_{m_s=-s}^s c_{m_s} e^{i(m-m_s)\phi} |m_s\rangle \quad (5.4)$$

where the states $|m_s\rangle$ obey

$$S_z |m_s\rangle = m_s |m_s\rangle. \quad (5.5)$$

Exploiting the discrete symmetries of the system one can prove the occurrence of degeneracies in the energy spectrum of the Hamiltonian (5.3). Let us consider $|E, m\rangle$ to be an energy eigenstate and at the same time an eigenstate of J_z . Using the anti-commutator $\{J_z, \Sigma_x\} = 0$ we have

$$J_z \Sigma_x |E, m\rangle = -\Sigma_x J_z |E, m\rangle = -m \Sigma_x |E, m\rangle \quad (5.6)$$

Thus the state $\Sigma_x |E, m\rangle$ can be identified with $|E, -m\rangle$. In case of a spin $\frac{1}{2}$ particle it follows from equation (5.6) that any energy level exhibits a two-fold degeneracy.¹ In case of spin 1 the situation is different. Here for $m = 0$ the states $|E, m\rangle$ and $\Sigma_x |E, m\rangle$ do not form a degenerate pair since they are located in the same J_z -subspace. However, for $m \neq 0$ there is a two-fold degeneracy also in the spin 1 case.

5.3. Numerical treatment

The Hamiltonian (5.3) does not support bound states [10]. In order to calculate the energies and decay widths of the scattering wave functions we employ the complex scaling method in conjunction with the linear variational principle. To this end it is convenient to transform the Hamiltonian (5.3) into spherical coordinates:

$$H = \frac{1}{2} \left[-\frac{\partial^2}{\partial r^2} - \frac{2}{r} \frac{\partial}{\partial r} + \frac{L^2}{r^2} + r \sin \theta \mathcal{K}^{(s)} - 2r \cos \theta S_z^{(s)} \right] \quad (5.7)$$

Explicit representations of the matrix \mathcal{K} for spin $\frac{1}{2}$ and spin 1 particles are given through

$$\mathcal{K}^{(\frac{1}{2})} = \frac{1}{2} \begin{pmatrix} 0 & e^{-i\phi} \\ e^{i\phi} & 0 \end{pmatrix} \quad \text{and} \quad \mathcal{K}^{(1)} = \frac{1}{\sqrt{2}} \begin{pmatrix} 0 & e^{-i\phi} & 0 \\ e^{i\phi} & 0 & e^{-i\phi} \\ 0 & e^{i\phi} & 0 \end{pmatrix}, \quad (5.8)$$

respectively. According to section 3.4 the radial coordinate is rotated into the complex plane by the transformation $r \rightarrow r e^{i\eta}$. Then the complex scaled Hamiltonian arising from equation (5.7) reads

$$H(\eta) = \frac{1}{2} \left[-e^{-i2\eta} \frac{\partial^2}{\partial r^2} - e^{-i2\eta} \frac{2}{r} \frac{\partial}{\partial r} + e^{-i2\eta} \frac{L^2}{r^2} + e^{i\eta} r \sin \theta \mathcal{K}^{(s)} - 2e^{i\eta} r \cos \theta S_z^s \right]. \quad (5.9)$$

The eigenvalue problem of this Hamiltonian is solved by utilizing the variational principle. To this end we employ a so-called Sturmian basis set of the form

$$|n, l, m_s\rangle_m = |n\rangle |l, m_s\rangle_m = R_n^{(\zeta)}(r) Y_l^{m-m_s}(\theta, \phi) |m_s\rangle. \quad (5.10)$$

Here $Y_l^m(\theta, \phi)$ denote the spherical harmonics. For fixed m the functions $|n, l, m_s\rangle_m$ are constructed such that the eigenstates of the Schrödinger equation are a priori eigenstates of the J_z operator. The radial part of the orbitals used for the expansion reads

$$R_n^{(\zeta)}(r) = \zeta^{\frac{3}{2}} e^{-\frac{\zeta r}{2}} L_n(\zeta r) \quad (5.11)$$

with $L_n(r)$ being the Laguerre polynomials. By appropriately tuning the parameter ζ an optimal convergence behavior in different parts of the spectrum can be established. ζ possesses the dimension of an inverse length and therefore has to be adapted such that $1/\zeta$ corresponds to the typical length scale of the desired wave functions. The functions $R_n^{(\zeta)}(r)$ form a complete functional set in r -space. They are nonorthogonal which results to an overlap-matrix different from unity. The

¹For a detailed discussion see also section 9.2.1.

basis set (5.10) is complete in r -, θ - and spin space. Utilizing the basis set (5.10) the expansion of an energy eigenstate according to equation (3.2) reads

$$|E, m\rangle = \sum_{n=0, m_s=-s, l=|m-m_s|}^{n < N, l < L, m_s \leq s} c_{n,l,m_s} |n, l, m_s\rangle_m \quad (5.12)$$

It gives rise to the generalized spinor eigenvalue problem $\mathcal{H}(\eta)\mathbf{c} = E\mathcal{S}\mathbf{c}$, where $\mathcal{H}(\eta)$ and \mathcal{S} are the corresponding matrix representation of the Hamiltonian (5.9) and the overlap matrix, respectively:

$$\mathcal{H}(\eta) = \langle n, l, m_s | H(\eta) | n', l', m'_s \rangle_m \quad \mathcal{S} = \langle n, l, m_s | n', l', m'_s \rangle_m \quad (5.13)$$

Using the basis set (5.10) all entries of the matrices (5.13) can be computed analytically by exploiting recurrence identities for the spherical harmonics and the Laguerre polynomials [1, 86], respectively. The expressions for the matrix elements of the individual parts of the Hamiltonian can be found in [55]. The matrices \mathcal{H} and \mathcal{S} possess a particular sparse appearance, e.g. \mathcal{S} is penta-diagonal. This has enabled us to go to large basis set dimensions still being able to compute the spectrum within an agreeable period of time.

5.4. Energies and decay widths of resonance states

5.4.1. Relation between energy and momentum of an eigenstate

We are now going to derive an expression for the mean squared momentum for particles inside a quadrupole trap. For an energy eigenstates apparently the relation $\langle [\mathbf{x} \cdot \mathbf{p}, H] \rangle = 0$ holds. Calculating the commutator explicitly one finds

$$\langle x S_x \rangle = 2 \langle p_x^2 \rangle \quad (5.14)$$

$$\langle y S_y \rangle = 2 \langle p_y^2 \rangle \quad (5.15)$$

$$\langle z S_z \rangle = - \langle p_z^2 \rangle. \quad (5.16)$$

By inserting these expressions into the Hamiltonian one obtains

$$E = \langle H \rangle = \frac{3}{2} [\langle p_x^2 \rangle + \langle p_y^2 \rangle + \langle p_z^2 \rangle] = \frac{3}{2} \langle p^2 \rangle. \quad (5.17)$$

For the sake of comparison we remark that in case of a three-dimensional harmonic oscillator one finds $\langle H \rangle = \langle p^2 \rangle$.

5.4.2. The resonance spectrum of spin $\frac{1}{2}$ fermions

By using the numerical method outlined above we have calculated hundreds of resonances. In figure 5.1 we present this resonance spectrum for a neutral spin $\frac{1}{2}$ particle. The smallest amount of angular momentum is carried by particles which reside in the $m = \frac{1}{2}$ state. In this case the resonances occupy an triangular shaped area in the $E - \Gamma$ plane. The resonances are placed on a series of diagonal lines with negative slope. The pattern becomes increasingly distorted, i.e. irregular, when approaching high resonance energies and large decay widths. Qualitatively the same behavior is observed in the next higher angular momentum subspace, i.e. $m = \frac{3}{2}$. Compared to the previous case here the maximum line width Γ has decreased by approximately half an order of magnitude. This trend continues when approaching even higher angular momenta but at the same time the shape of the resonance pattern suffers significant alteration. Still a triangular shape is observed, however the triangle is flipped such that its hypotenuse now possesses a positive slope. Moreover, the resonances arrange in an increasingly regular way. Let us now investigate how

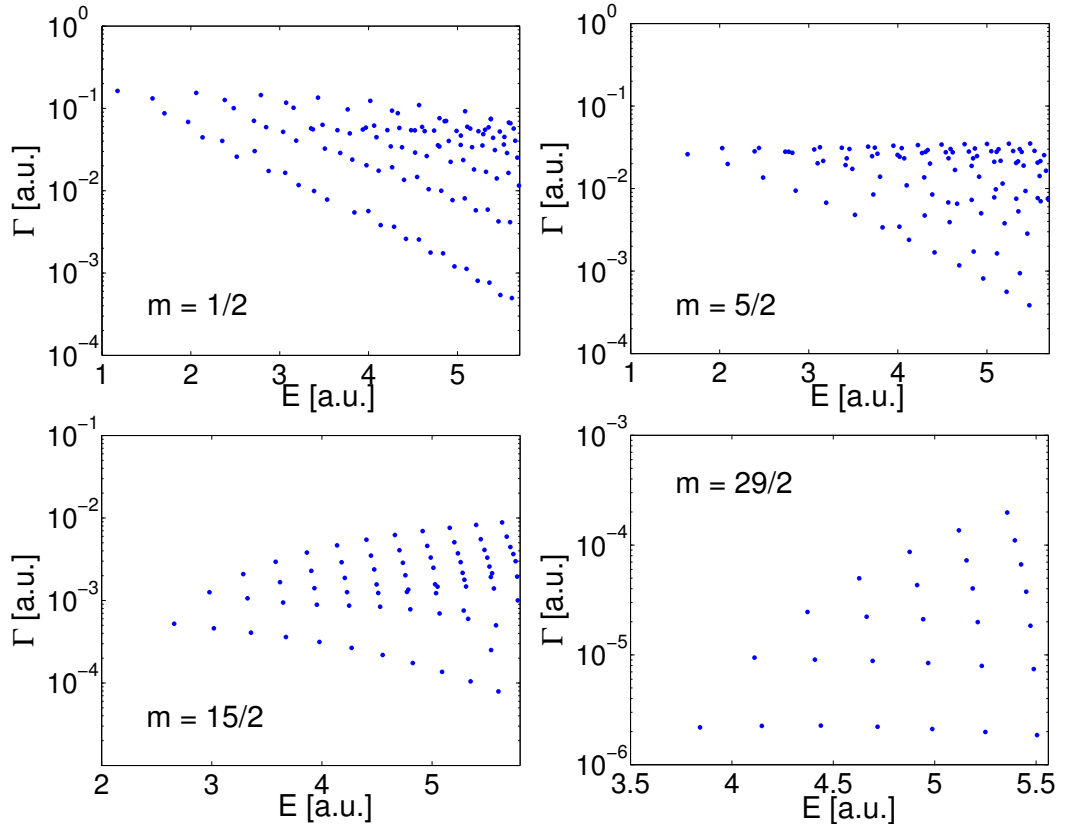


Figure 5.1.: Energies E and decay widths Γ (logarithmic scale) of resonances in the magnetic quadrupole trap for four different values of the J_z quantum number. The structure of the resonance energy pattern is significantly altered as the quantum number m increases. The triangular distribution reverses and at the same time a transition to a more regular pattern is observed.

the decay width of a resonance state is related to its actual angular momentum value. For this purpose we consider the width of the energetically lowest resonance in the different J_z subspaces (see figure 5.2). One immediately notices that a linearly increasing value of the angular momentum results in an exponential decrease of the decay width. Performing an exponential fit we find the dependence $\Gamma \approx 0.2 e^{-0.79|m|}$. The larger the angular momentum of a state the farther it will be located from the center of the trap. Later on we will see that this is the region where transitions from bound to unbound states take place. With increasing angular momentum the wave functions avoid contact with the trap center and therefore the states become more stable. Resonances of spin $\frac{1}{2}$ particles have already been calculated in the work by Bergeman *et al.* [10]. These authors consider J_z subspaces up to $m = \frac{11}{2}$. Since altogether about two dozens of resonance positions were obtained by their numerical approach the authors were not in the position to comment on the global structure of the resonance spectrum. Our results agree well with those by Bergeman *et al.* except for some larger discrepancies in the $m = \frac{1}{2}$ subspace. It seems that the authors of [10] had difficulties of resolving resonances with overlapping decay widths. This limitation arises from their numerical approach where the resonance positions are obtained from a fit to the phase shift of scattered waves.

5.4.3. Resonance spectrum and density of states of spin 1 bosons

In figure 5.3 the resonance positions for a spin 1 particle in a magnetic trap are shown. Qualitatively we observe the same behavior as for the spin $\frac{1}{2}$ case in figure 5.1. Again we find a triangular shaped distribution for low angular momenta. Compared to the spin $\frac{1}{2}$ case the overall distribution in

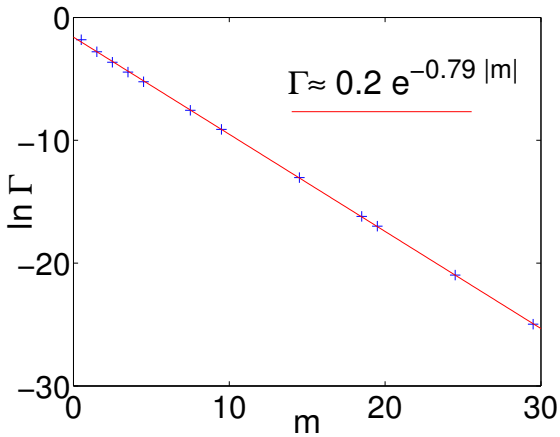


Figure 5.2.: Decay width of the energetically lowest resonance shown as a function the quantum number m (spin $\frac{1}{2}$ particle). An exponential decrease of the decay width is observed. The increased stability of high m states originates from a localization of such states far away from the center of the trap such that transitions to unbound states are inhibited.

the $E - \Gamma$ -plane seems to be more irregular. Approaching higher m values we encounter again a transition to a regular pattern. In figure 5.4 we present the decay width of the energetically lowest resonance in each J_z subspace plotted against the quantum number m . Similar to the spin $\frac{1}{2}$ case the decay width declines with increasing angular momentum. Performing an exponential fit we find $\Gamma \approx 0.68 e^{-0.56|m|}$.

Since we now know the resonance energies and their respective decay width we are able to calculate the density of states (DOS). The DOS measures the fraction of states dN that occupy the energy interval dE and is usually a function of the energy itself: $\frac{dN}{dE}(E)_i$. For a resonance state the DOS profile is determined according to ref. [76] by

$$\frac{dN}{dE}(E)_i = \frac{\Gamma_i}{\pi} \frac{1}{\Gamma_i^2 + (E - E_i)^2}. \quad (5.18)$$

The total density of states is obtained via

$$\frac{dN}{dE}(E) = \sum_i \frac{dN}{dE}(E)_i. \quad (5.19)$$

In figure 5.5 we present the DOS for four selected values of the quantum number m . For $m = 0$ we observe broad peaks. Their positions are determined by the resonance states with the smallest decay width. The high background level is formed by short lived states. For $m = 5$ the energetically lowest resonance is well separated from the others. At the same time a substructure becomes visible for energetically higher peaks. This substructure becomes manifest for $m = 10$ and is even more evident for $m = 15$, where extremely sharp peaks are formed. These sharp resonances are an indication for almost stable states with respect to decay from the quadrupole trap. The peaks form clearly separated groups with the number of subpeaks in adjacent groups differing by one.

5.5. Quasi-bound states

5.5.1. Spin $\frac{1}{2}$ fermions

For sufficiently large values of the angular momentum the wave functions become localized far away from the center of the trap. They form concentric circles around the z -axis. Since transitions to continuum states mainly occur in the center this results in a significant increase of the lifetimes of the states. Thus one could expect such states to be approximately describable as bound states of a certain effective Schrödinger equation. In order to obtain such an equation it is sensible to write

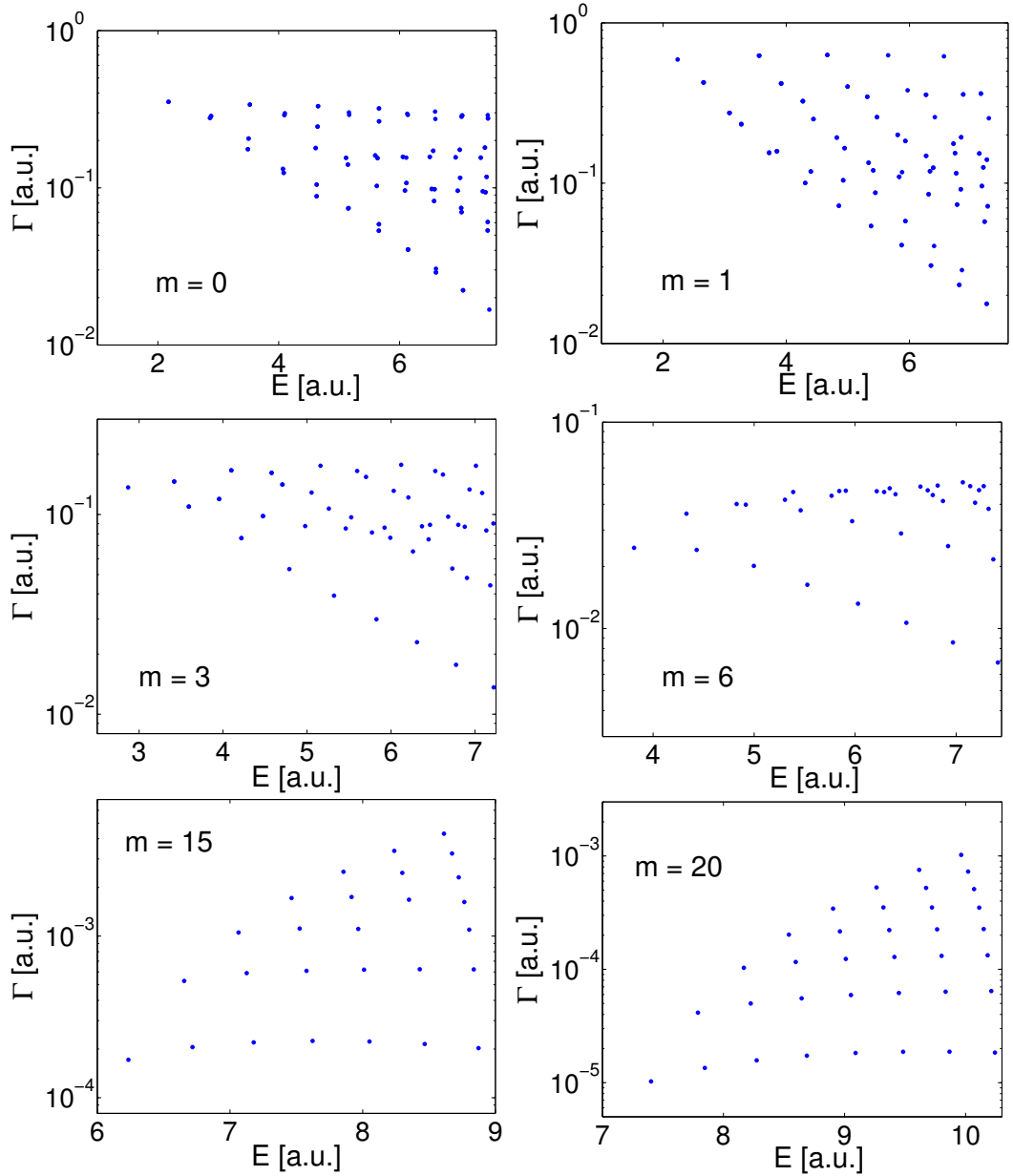


Figure 5.3.: Energies E and decay widths Γ (logarithmic scale) of resonances in the magnetic quadrupole trap for four values of the J_z quantum number (spin 1 particle). The structure of the resonance energy pattern undergoes a significant alteration with increasing values of the quantum number m .

the Hamiltonian (5.3) in cylindrical coordinates and apply the unitary transformation

$$U_1 = e^{-iS_z\phi}. \quad (5.20)$$

This yields

$$\tilde{H} = U_1^\dagger H U_1 = \frac{1}{2} \left[-\frac{\partial^2}{\partial \rho^2} - \frac{1}{\rho} \frac{\partial}{\partial \rho} + \frac{1}{\rho^2} (L_z - S_z)^2 - \frac{\partial^2}{\partial z^2} + \rho S_x - 2z S_z \right]. \quad (5.21)$$

In this frame any explicit dependence on the azimuthal angle ϕ is removed. Hence now L_z instead of J_z constitutes a conserved quantity, because of

$$U_1^\dagger J_z U_1 = L_z. \quad (5.22)$$

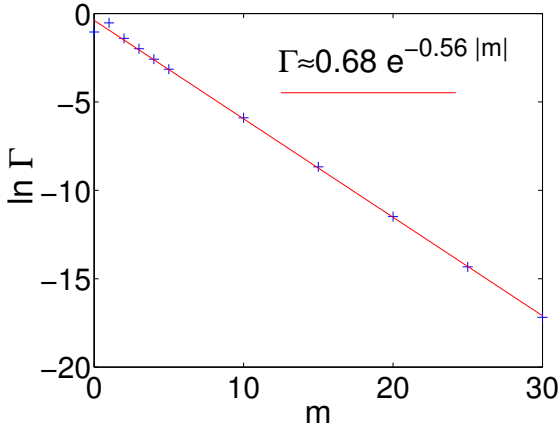


Figure 5.4.: Decay width of the energetically lowest resonance of a spin 1 boson plotted against the quantum number m . An exponential decrease of the decay width is observed. The increased stability of high m states originates from a localization of such states far away from the center of the trap.

Hence we can replace L_z by its quantum number m and consider each L_z subspace separately. At this point we have to emphasize that due to the unitarity of U_1 the quantum number m retains its half-integer character if spin $\frac{1}{2}$ particles are considered and remains integer in case of spin 1. Also, we want to remark that equation (5.21) holds independently of the spin of the particle since the explicit appearance of \mathbf{S} did not enter the calculation yet. The spatially dependent unitary transformation

$$U_2 = e^{-iS_y\beta} \quad (5.23)$$

with $\sin\beta = \frac{\rho}{\sqrt{\rho^2+4z^2}}$ and $\cos\beta = \frac{-2z}{\sqrt{\rho^2+4z^2}}$ diagonalizes the spin-field interaction term of (5.21), i.e.

$$U_2^\dagger (\rho S_x - 2z S_z) U_2 = \sqrt{\rho^2 + 4z^2} S_z. \quad (5.24)$$

The derivatives result in additional terms, e.g.

$$U_2^\dagger \frac{\partial^2}{\partial \rho^2} U_2 = U_2^\dagger U_2'' + 2U_2^\dagger U_2' \frac{\partial}{\partial \rho} + \frac{\partial^2}{\partial \rho^2}, \quad (5.25)$$

which gives rise to additional off-diagonal couplings. However, these terms are proportional to powers of z^{-1} as $\rho \rightarrow 0$ and ρ^{-1} as $z \rightarrow 0$. Thus they become important only in the vicinity of the center of trap, where they lead to transitions between bound and unbound solutions. We now explicitly focus on spin $\frac{1}{2}$ particles. We neglect the off-diagonal terms of the transformed Hamiltonian and considering only the component of $U_2^\dagger \tilde{H} U_2$ which allows for bound solutions that we denote as $|\Psi_{qb}\rangle$. Thereby we obtain the Schrödinger equation

$$\frac{1}{2} \left[-\frac{\partial^2}{\partial \rho^2} - \frac{\partial^2}{\partial z^2} + \frac{m^2}{\rho^2} + \frac{2mz}{\rho^2 \sqrt{\rho^2 + 4z^2}} + \frac{\rho^2 + z^2}{(\rho^2 + 4z^2)^2} + \frac{1}{2} \sqrt{\rho^2 + 4z^2} \right] |\Phi_{qb}\rangle = E_{qb} |\Phi_{qb}\rangle \quad (5.26)$$

which we will in the following referred to as quasi-bound Schrödinger equation. Note that we have introduced the wave function $|\Psi_{qb}\rangle = \rho^{-\frac{1}{2}} |\Phi_{qb}\rangle$.

The traditional approach in order to obtain a Schrödinger equation describing bound states is to employ the so-called adiabatic approximation. In this picture one assumes the projection of the atomic spin onto the local direction of the magnetic field to be conserved. Thus the coupling of the magnetic moment to the field is crudely simplified to read $g\mu_B m_s |\mathbf{B}(\mathbf{r})|$ with m_s being the projection of the spin onto the local field direction. In this approximation the Hamiltonian becomes

$$H_{ad} = \frac{1}{2} \left[\mathbf{p}^2 + m_s \sqrt{\rho^2 + 4z^2} \right] \quad (5.27)$$

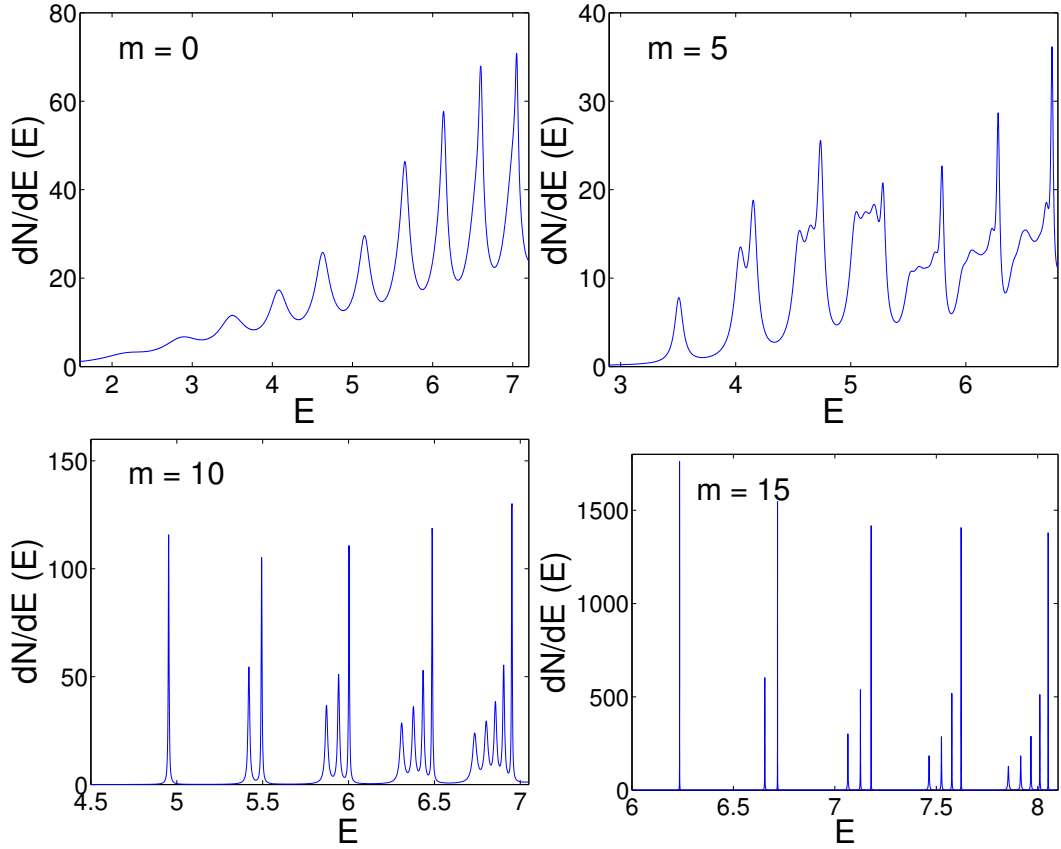


Figure 5.5.: Density of states for four selected values of the quantum number m . For small angular momentum the DOS is dominated by the longest living resonances which emerge from the high background level. Increasing angular momentum leads to a general decline of the decay width. Thus more peaks appear as the angular momentum increases. At the same time the background level decreases. At $m = 15$ one finds extremely narrow resonances which indicate extremely long living states.

thereby having employed scaled coordinates (see section 5.1). Considering $m_s = \frac{1}{2}$ which allows for bound solutions unlike $m_s = -\frac{1}{2}$ and introducing the wave function $|\Psi_{ad}\rangle = \rho^{-\frac{1}{2}} |\Phi_{ad}\rangle$ the corresponding adiabatic Schrödinger equation becomes

$$\frac{1}{2} \left[-\frac{\partial^2}{\partial \rho^2} - \frac{\partial^2}{\partial z^2} + \frac{l^2 - \frac{1}{4}}{\rho^2} + \frac{1}{2} \sqrt{\rho^2 + 4z^2} \right] |\Phi_{ad}\rangle = E_{ad} |\Phi_{ad}\rangle. \quad (5.28)$$

Here l is the quantum number of the operator L_z which is conserved due to the rotational invariance of the system around the z -axis in coordinate space. Note that unlike m the quantum number l is integer-valued. In order to solve equations (5.26) and (5.28) we have utilized the FEMLAB software package which employs the finite element method for solving differential equations. Table 5.3 contains a comparison of the adiabatic eigenvalues E_{ad} and the exact resonance energies as well as the energies of the quasi-bound states E_{qb} . The quantum numbers l and m are chosen such that $l = m - \frac{1}{2}$. For all m eigenvalues E and E_{qb} are in remarkably good agreement. The angular momentum term $\frac{m^2}{\rho^2}$ together with the two consecutive terms in equation (5.26) constitute a potential barrier which prevents a particle from entering the vicinity around the center of the trap. We have already stated that the off-diagonal elements of $U_2^\dagger \tilde{H} U_2$ involve inverse powers of the spatial coordinates. Thus the matrix element for transitions between bound and unbound solutions becomes only significant if there is a sufficiently large overlap of the wave function with the central region of the trap. This explains why the quasi-bound approach performs better and better with

		0	1	2	3	4	5
	E	1.1748	1.5687	1.7023	1.9694	2.0604	2.1314
$m = \frac{1}{2}$	E_{qb}	1.1539	1.5635	1.6757	1.9703	2.0442	2.1069
$l = 0$	E_{ad}	0.9347	1.4652	1.4808	1.8986	1.9194	1.9375
	E	1.4086	1.8101	1.8922	2.1903	2.2503	2.3075
$m = \frac{3}{2}$	E_{qb}	1.3795	1.7814	1.8678	2.1655	2.2251	2.2868
$l = 1$	E_{ad}	1.1192	1.6655	1.6933	2.0748	2.1122	2.1150
	E	2.0707	2.4287	2.4756	2.7664	2.8084	2.8440
$m = \frac{9}{2}$	E_{qb}	2.0597	2.4159	2.4649	2.7531	2.7965	2.8341
$l = 4$	E_{ad}	1.9324	2.3090	2.3457	2.6581	2.6990	2.7164
	E	3.8427	4.1115	4.1475	4.3729	4.4092	4.4384
$m = \frac{29}{2}$	E_{qb}	3.8410	4.1095	4.1456	4.3707	4.4072	4.4365
$l = 14$	E_{ad}	3.7575	4.0298	4.0651	4.2942	4.3305	4.3582
	E	5.9227	6.1399	6.1708	6.3540	6.3851	6.4126
$m = \frac{59}{2}$	E_{qb}	5.9221	6.1393	6.1702	6.3533	6.3845	6.4119
$l = 29$	E_{ad}	5.8569	6.0755	6.1064	6.2908	6.3220	6.3493

Table 5.3.: Comparison of the resonance energies to the approximate energies E_{qb} and E_{ad} obtained from equations (5.26) and (5.28), respectively. The first six resonance energies E for five selected values of the quantum number m are provided. The quantum numbers l have been chosen such that $l = m - \frac{1}{2}$.

increasing values of the quantum number m . For $m = \frac{59}{2}$ we find a very good agreement between E and E_{qb} . Here the relative discrepancy is less than 0.01%. From the data listed in table 5.3 it is apparent that the adiabatic approach essentially fails for $l = 0$. The spin of particles being in such states can certainly not be considered to couple adiabatically to the external field. For larger values of the angular momentum the adiabatic approximation works reasonably well. However, the quality of the quasi-bound energies E_{qb} is never reached by the adiabatic energies E_{ad} .

We will now discuss the origin of the regular pattern formed by the resonance positions which emerges for high values of the m quantum number (see figure 5.1). For high m values the minimum and the associate well of the effective potential in the Schrödinger equation (5.26) becomes more and more pronounced. The minimum is approximately located at the position $(z_0 = 0, \rho_0 = (2m)^{\frac{2}{3}})$. The system now becomes almost integrable, and consequently the states can be characterized by their number of nodes in ρ - and z -direction which we designate by n_ρ and n_z , respectively. This is illustrated in figure 5.6 which shows data obtained from the complex scaling calculation. The energies are approximately those of an anisotropic harmonic oscillator in the ρ - z plane. States with higher number of nodes in ρ -direction possess larger widths. This is easily understood considering that such states are elongated in the ρ -direction and the particles therefore possess higher oscillation frequencies in that direction. Hence these states possess a higher probability to penetrate the angular momentum barrier and undergo a transition to unbound solutions. Unlike that, states with small n_ρ are mainly elongated along the z -direction (see right hand side of figure 5.6) and thus avoid contact with the trap center.

5.5.2. Spin 1 bosons

Like for spin $\frac{1}{2}$ particles one can derive a quasi-bound Schrödinger equation for spin 1 particles as well. Neglecting the off-diagonal terms of $U_2^\dagger \tilde{H} U_2$ and considering only the component which

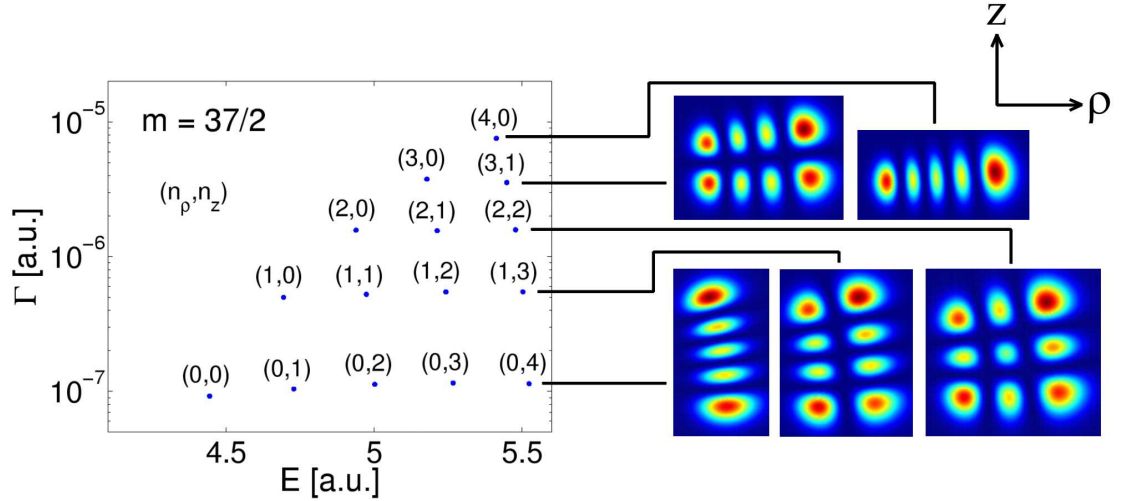


Figure 5.6.: Resonances in the $m = \frac{37}{2}$ subspace. The resonance states can be characterized by the two quantum numbers (n_ρ, n_z) which denote the number of nodes in the ρ - and z -direction, respectively. The right hand side shows the probability density of the wave functions $|\Phi_{qb}\rangle$. The wave functions are approximately centered at the coordinates $(z_0 = 0, \rho_0 = (2m)^{\frac{2}{3}})$.

allows for bound solutions one obtains the following equation:

$$\frac{1}{2} \left[-\frac{\partial^2}{\partial \rho^2} - \frac{\partial^2}{\partial z^2} + \frac{m^2 + \frac{3}{4}}{\rho^2} + \frac{4mz}{\rho^2 \sqrt{\rho^2 + 4z^2}} - \frac{1}{2(\rho^2 + 4z^2)} + \frac{2(\rho^2 + z^2)}{(\rho^2 + 4z^2)^2} + \sqrt{\rho^2 + 4z^2} \right] |\Phi_{qb}\rangle = E_{qb} |\Phi_{qb}\rangle. \quad (5.29)$$

Like in section 5.5.1 we have introduced the wave function $|\Psi_{qb}\rangle = \rho^{-\frac{1}{2}} |\Phi_{qb}\rangle$. Following the derivation of section 5.5.1 the adiabatic Schrödinger equation becomes

$$\frac{1}{2} \left[-\frac{\partial^2}{\partial \rho^2} - \frac{\partial^2}{\partial z^2} + \frac{l^2 - \frac{1}{4}}{\rho^2} + \sqrt{\rho^2 + 4z^2} \right] |\Phi_{ad}\rangle = E_{ad} |\Phi_{ad}\rangle. \quad (5.30)$$

Since we are now dealing with spin 1 particles we have set $m_s = 1$ in equation (5.27). In table 5.4 we present a comparison of the exact resonance energies to the quasi-bound and adiabatic energies E_{qb} and E_{ad} . The data show again a breakdown of the adiabatic approximation for low values of l . The quasi-bound approximation here performs significantly better than the adiabatic approximation but not quite as good as it did for the spin $\frac{1}{2}$ case. For $m = 0$ one finds deviations up to almost 8%. This is most likely due to the fact that there exist two unbound channels instead of a single one like in the spin $\frac{1}{2}$ case. Both, the adiabatic and the quasi-bound approach, perform better when reaching higher values of the angular momentum. However, the quasi-bound approach is still superior with deviations of less than 0.1% for $m = 20$ and greater.

5.6. Resonances of magnetically trapped alkali metal atoms

The results given in this chapter can be directly applied to calculate the resonance energies and lifetimes of magnetically trapped alkali atoms. If the hyperfine-splitting is much larger than the magnetic field induced splitting of the hyper-fine sublevels one can consider each hyper-fine manifold

		0	1	2	3	4	5
	E	2.1759	2.8639	2.8810	3.4898	3.5011	3.5233
$m = 0$	E_{qb}	2.0219	2.7252	2.7402	3.3725	3.3866	3.3900
$l = 0$	E_{ad}	1.4863	2.32789	2.3528	3.0156	3.0490	3.0776
	E	2.2381	2.6590	3.0786	3.2702	3.5605	3.7222
$m = 1$	E_{qb}	2.0715	2.6180	2.9294	3.2149	3.4236	3.6123
$l = 1$	E_{ad}	1.8929	2.6440	2.6880	3.2937	3.3531	3.3576
	E	3.5061	4.0377	4.1537	4.5472	4.6497	4.7384
$m = 5$	E_{qb}	3.4482	3.9775	4.0965	4.4890	4.5885	4.6856
$l = 5$	E_{ad}	3.4086	3.9768	4.0359	4.5090	4.5733	4.6055
	E	4.9525	5.4197	5.4939	5.8715	5.9421	6.0028
$m = 10$	E_{qb}	4.9317	5.3955	5.4718	5.8450	5.9171	5.9806
$l = 10$	E_{ad}	4.9135	5.3889	5.4472	5.8462	5.9067	5.9487
	E	7.4025	7.7894	7.8463	8.1685	8.2252	8.2742
$m = 20$	E_{qb}	7.3957	7.7818	7.8390	8.1602	8.2172	8.2666
$l = 20$	E_{ad}	7.3878	7.7767	7.8296	8.1573	8.2111	8.2555

Table 5.4.: Comparison of the resonance energies to the approximate energies E_{qb} and E_{ad} obtained from equation (5.29) and (5.30), respectively. The first six resonance energies E for 5 selected values of the quantum number m are provided.

separately, i.e. the operator $\mathbf{F}^2 = (\mathbf{J} + \mathbf{I})^2$ can be treated as if it was approximately conserved (for illustration see figure 5.7). Here \mathbf{J} and \mathbf{I} are the total electronic spin and the nuclear spin operator, respectively. As instructive examples we choose the following two species: ${}^6\text{Li}$ being in the hyperfine ground state $2S_{\frac{1}{2}}$, $I = 1$, $F = \frac{1}{2}$ and ${}^{87}\text{Rb}$ being in the hyperfine ground state $5S_{\frac{1}{2}}$, $I = \frac{3}{2}$, $F = 1$. Here I and F denote the quantum numbers of \mathbf{F}^2 and \mathbf{I}^2 , respectively. Since both ${}^6\text{Li}$ and ${}^{87}\text{Rb}$ possess a single valence electron carrying spin $\frac{1}{2}$ the nuclear spin exclusively decides upon whether the species is of fermionic or bosonic character. For the hyperfine states given above we find ${}^6\text{Li}$ to behave like a spin $\frac{1}{2}$ fermion with g-factor $g = \frac{2}{3}$ and mass $M = 10964.67 m_e$ whereas ${}^{87}\text{Rb}$ behaves like a spin 1 boson with $g = \frac{1}{2}$ and $M = 155798.23 m_e$. In table 5.5 we provide the

	mass [m_e]	g_F	energy unit [neV]	length unit [nm]	E_{gs} [neV]	τ_{gs} [μs]
${}^6\text{Li}$	10964.67	$\frac{3}{2}$	0.745	96.55	87.52	5.42
${}^{87}\text{Rb}$	155798.23	$\frac{1}{2}$	0.254	43.87	55.25	7.36

Table 5.5.: Mass, g-factor, energy unit, length unit as well as energy and lifetime of the ground state resonance for ${}^6\text{Li}$ ($2S_{\frac{1}{2}}$, $F = \frac{1}{2}$) and ${}^{87}\text{Rb}$ ($5S_{\frac{1}{2}}$, $F = 1$) at a gradient $b = 100 \frac{T}{m}$.

energy and length unit as well as the energy E_{gs} and lifetime τ_{gs} of the ground state resonance at a gradient $b = 100 \frac{T}{m}$. For this rather high gradient the lifetimes are in the order of μs . As we have pointed out in this work the lifetime of trapped states can be significantly prolonged if the atom is prepared in states of high angular momentum. In case of ${}^{87}\text{Rb}$ being prepared in the $m = 25$ subspace the minimum lifetime evaluates to 433.5s !

5.7. Summary

This chapter was devoted to the investigation of the motion of neutral point-like particles in a three-dimensional magnetic quadrupole field. We have focussed on fermions and bosons, carrying spin $\frac{1}{2}$ and 1, respectively. We have introduced a scaling transformation which removes any system related parameters from the Hamiltonian. Our results are therefore generally applicable. Energies

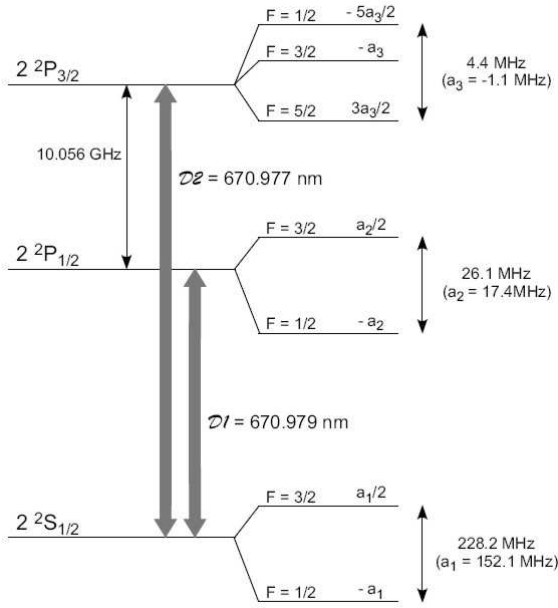


Figure 5.7.: Term scheme of ${}^6\text{Li}$. For sufficiently small magnetic field strength each of the hyperfine manifolds can be treated separately, i.e. F can be considered to be an approximately good quantum number.

and decay widths of resonance states of the Schrödinger equation have been calculated by employing the complex scaling method together with the linear variational principle. For the latter we have utilized a Sturmian basis set which enabled us to converge hundreds of resonances.

The analysis of the underlying Hamiltonian revealed a large number of symmetries. We have identified 16 discrete symmetries of both unitary and anti-unitary character. In addition there is a continuous unitary symmetry generated by the conserved quantity $J_z = L_z + S_z$. A deeper exploration of the underlying symmetry group revealed a two-fold degeneracy of any energy level in case of spin $\frac{1}{2}$ particles. In case of spin 1 such a degeneracy is found in all but the $m = 0$ symmetry subspaces.

We have calculated the resonance energies for a wide range of values of the quantum number m and discussed the distribution of the resonance positions in the $E - \Gamma$ plane. For low m values we have found a triangular shaped pattern exhibiting both regular and irregular regions. For large angular momenta a transition to a pattern of regularly distributed resonance position is observed. In the latter regime the system becomes almost integrable. Here states can be characterized by the quantum numbers n_ρ and n_z which correspond to the number of nodes of the wave function in the respective spatial direction.

We have further shown that there is an exponential increase in the lifetimes of the resonance states with increasing angular momentum. We have shown the transitions between bound and unbound solutions to take place only in vicinity of the trap center. They are therefore highly suppressed for large angular momentum states. Such quasi-bound states which possess long lifetimes can be very well described by a scalar radial Schrödinger equation. Its approximate eigenenergies are in good agreement with the resonance energies obtained from the complex scaling calculation and become exact in the limit of high m quantum numbers. However, for spin $\frac{1}{2}$ particles even for low angular momenta an astonishingly good agreement is achieved. A comparison of the quasi-bound to the commonly used adiabatic description of trapped states has been presented as well. We have found for both spin $\frac{1}{2}$ and spin 1 particles the quasi-bound solutions to be in significantly better agreement to the numerically exact results.

Most of the results presented in this chapter are published in refs. [62, 59].

6. Spectral properties and lifetimes of neutral fermions and bosons in a magnetic quadrupole guide and a Ioffe-Pritchard trap

The last chapter was dedicated to a thorough discussion of the resonance spectrum of spin particles exposed to a three-dimensional quadrupole field. We now turn to an equally important field configuration - the magnetic quadrupole guide or Ioffe-Pritchard trap. In contrast to the previous case this configuration can provide only a two-dimensional confinement of the atomic motion. Moreover, the underlying equations of motion depend parametrically on the Ioffe field strength which, as we will show, has a major impact on the appearance of the resonance spectrum. In detail this chapter is structured as follows: In section 6.1 we present the underlying Hamiltonian which effectively is two-dimensional and does depend solely on a single parameter involving both the gradient of the inhomogeneous field and the Ioffe field strength. The system exhibits a plethora of unitary as well as anti-unitary symmetries. The effects of this intricate symmetry properties and in particular a resultant two-fold degeneracy of the resonance energies are discussed in section 6.2. In section 6.3 we briefly outline the numerical approach we pursue in order to obtain the resonance energies and decay width which is based on the complex scaling method. Section 6.4 to 6.7 are devoted to a discussion of our results. We analyze the resonance spectrum for several values of the Ioffe field strength. Furthermore we investigate how the energies and lifetimes of the resonance states depend on their angular momentum. The properties of so-called quasi bound states are addressed. We provide a radial Schrödinger equation whose eigenenergies are very good approximations of the true resonance energies. A comparison to the commonly used adiabatic approximation is also performed. Finally the results are applied to the experimentally important cases of ${}^6\text{Li}$, ${}^7\text{Li}$ and ${}^{87}\text{Rb}$ in a Ioffe-Pritchard trap. In section 6.8 we provide a brief summary of the results.

6.1. The System - Hamiltonian and scaling properties

The general Hamiltonian of a neutral particle with the magnetic moment $\boldsymbol{\mu}$ and the mass M in the presence of a magnetic field $\mathbf{B}(\mathbf{r})$ reads is given by equation (5.1). After inserting the Ioffe-Pritchard field configuration (2.9) this Hamiltonian does not contain an explicit dependence on the z -coordinate. Hence the z -component of the momentum operator \mathbf{p} is conserved, i.e. $[H', p_z] = 0$. In order to decouple the dynamics in the z -direction we use plain waves $|k_z\rangle$ which obey $p_z |k_z\rangle = k_z |k_z\rangle$. One now obtains an effectively two-dimensional Hamiltonian by performing the projection

$$H_{2D} = \langle k_z | H' | k_z \rangle - \frac{k_z^2}{2M} = \frac{1}{2M} [p_x^2 + p_y^2 + gM (b x S_x - b y S_y + B_I S_z)]. \quad (6.1)$$

Here atomic units (see appendix B) have been adopted. We also assume the relation between the magnetic moment $\boldsymbol{\mu}$ and the spin \mathbf{S} to be $\boldsymbol{\mu} = -\frac{g}{2}\mathbf{S}$ with g being the particle's g -factor. After performing the scale transformation $\bar{x}_i = (bgM)^{\frac{1}{3}} x_i$ and $\bar{p}_i = (bgM)^{-\frac{1}{3}} p_i$ and omitting the bars thereafter we finally obtain the working Hamiltonian

$$M (bgM)^{-\frac{2}{3}} H_{2D} = H = \frac{1}{2} [p_x^2 + p_y^2 + x S_x - y S_y + \gamma S_z] \quad (6.2)$$

with $\gamma = B_I \left(\frac{qM}{b^2} \right)^{\frac{1}{3}}$. For $\gamma = 0$ the gradient b does not explicitly appear in equation (6.2). In this case the energy level spacing scales according to $\frac{1}{M} (bgM)^{\frac{2}{3}}$ exactly as for the three-dimensional quadrupole field.

6.2. Symmetries and Degeneracies

We will now be analyzing the symmetry properties of the system to gain insights into the structure of the resonance spectrum. Before doing so we first introduce some elementary symmetry operations:

The operations

$$R_j = \exp \left[-iS_k \frac{\pi}{2} \right] \exp [-iS_l \pi] \quad \text{cyclic permutations of } j, k, l \quad (6.3)$$

$$\bar{R}_j = \exp \left[-iS_k \frac{\pi}{2} \right] \exp [-iS_l \pi] \quad \text{anti - cyclic permutations of } j, k, l \quad (6.4)$$

$$D_j = \exp [-iS_j \pi] \quad (6.5)$$

exclusively act on the spin space which in case of a spin 1 particle is spanned by the matrices

$$S_x = \frac{1}{\sqrt{2}} \begin{pmatrix} 0 & 1 & 0 \\ 1 & 0 & 1 \\ 0 & 1 & 0 \end{pmatrix} \quad S_y = \frac{1}{\sqrt{2}} \begin{pmatrix} 0 & -i & 0 \\ i & 0 & -i \\ 0 & i & 0 \end{pmatrix} \quad S_z = \begin{pmatrix} 1 & 0 & 0 \\ 0 & 0 & 0 \\ 0 & 0 & -1 \end{pmatrix} \quad (6.6)$$

and the unit matrix. For spin $\frac{1}{2}$ we chose the usual representation of the spin operator in terms of the Pauli-matrices. The elementary symmetry operations (6.3) - (6.5) obey

$$\bar{R}_j R_k = R_k \bar{R}_j = D_l \quad j, k, l \text{ cyclic} \quad (6.7)$$

$$D_j D_k = D_k D_j = D_l \quad (6.8)$$

$$[D_j, D_k] = 0 \quad (6.9)$$

$$R_i R_i = \bar{R}_i \bar{R}_i = D_i D_i = 1. \quad (6.10)$$

Apart from these spin space operations we specify a few operations acting exclusively on the spatial coordinates: These are the common parity operations P_x, P_y (reflections at the x and y axis, respectively) as well as the rotation around the z -axis by an angle $\frac{\pi}{2}$: $G = \exp [i\frac{\pi}{2} L_z]$. Together with the anti-unitary operator of the conventional time reversal T we have now founded the basis for the following symmetry analysis.

6.2.1. Symmetries and degeneracies in the absence of a Ioffe field

We are now able to construct the symmetry operations of the Hamiltonian (6.2), i.e. operations leaving the shape of the Hamiltonian invariant. Since the discrete unitary transformations in real space G, P_x, P_y do not commute with the Hamiltonian they have to be combined with additional spin space operators in order to create symmetries of the Hamiltonian. In total we have identified 16 (including unity) discrete unitary transformations U being composed of real space as well as spin space operators such that $U^\dagger H U = H$. They are listed in table 6.1. At this point we remark that all symmetries of the system described by the Hamiltonian (6.2) hold independently of the dimensionality of the spin space, provided that the spin matrices (6.6) are replaced accordingly by their higher or lower dimensional representations. In any case the algebra of the underlying symmetry group possesses a rich structure which strongly depends on whether spin $\frac{1}{2}$ or spin 1 particles are considered: For instance the operators $\Sigma_x^{(1)}, \Sigma_y^{(1)}$ and $\Sigma_z^{(1)}$ are generating an Abelian subgroup in the spin 1 case (the upper index of the operators indicates the particle's spin). This does

$GP_x R_x$	$\Sigma_z = P_x P_y D_z$	$\Sigma_y = P_x D_y$	$\Sigma_x = P_y D_x$
$GP_y R_y$	$GR_y D_x$	$GP_x P_y R_y D_y$	1
TGR_x	$TP_x D_z$	$TP_x P_y D_y$	TD_x
$TGP_x P_y R_y$	$TGP_x R_y D_x$	$TGP_y R_y D_y$	TP_y

Table 6.1.: Symmetry operations of the Hamiltonian (6.2) for $\gamma = 0$. Top part: unitary symmetries. Bottom part: anti-unitary symmetries.

not hold for spin $\frac{1}{2}$ particles. Here one rather finds the operators $\Sigma_i^{(\frac{1}{2})}$ to generate a non-Abelian subgroup while obeying the algebra $[\Sigma_i^{(\frac{1}{2})}, \Sigma_j^{(\frac{1}{2})}] = 2\epsilon_{ijk}\Sigma_k^{(\frac{1}{2})}$ reminiscent of angular momentum operators.

Additionally to the discrete symmetries there is also continuous one. The generator of the underlying symmetry group is $\Lambda_z = L_z - S_z$ which was already revealed for spin $\frac{1}{2}$ systems by Eberlein and Hinds in ref. [44]. The operator Λ_z obeys the eigenvalue equation

$$\Lambda_z |m\rangle = m |m\rangle \quad (6.11)$$

with (half-)integer quantum numbers m . The corresponding states $|m\rangle$ read in the spatial representation

$$|m\rangle = \sum_{m_s} \alpha_{m_s} e^{i(m+m_s)\phi} |m_s\rangle \quad (6.12)$$

with ϕ being the polar angle and $|m_s\rangle$ being the eigenstates of the spin operator's z -component S_z . The symmetries listed in table 6.1 together with Λ_z allow one to pick several sets of commuting operators. In the present work we pick H , Σ_z and Λ_z but also other combinations are thinkable.

Calculating the eigenvalue of a Λ_z eigenstate with respect to the Σ_z operator one finds

$$\Sigma_z |m\rangle = \sum_{m_s} \alpha_{m_s} e^{-im_s\pi} e^{i(m+m_s)(\phi+\pi)} |m_s\rangle = e^{im\pi} |m\rangle = (-1)^m |m\rangle = \tilde{\kappa} |m\rangle. \quad (6.13)$$

Depending on whether m is integer or half-integer one finds real or complex values of $\tilde{\kappa}$. In order to have an always real-valued quantum number we introduce $\kappa = e^{-is\pi}\tilde{\kappa}$ with s being the spin of the respective particle. Consequently the resonance states can be classified according to the three quantum numbers E , m and κ : $|E, m, \kappa\rangle$.

Like for a three-dimensional quadrupole trap we encounter degeneracies in the resonance spectrum. In the present case this is shown as follows: The operations Λ_z and Σ_x anti-commute, i.e. they obey $\{\Lambda_z, \Sigma_x\} = 0$. Let $|E, m\rangle$ be an energy eigenstate and at the same time an eigenstate of Λ_z with

$$\Lambda_z |E, m\rangle = m |E, m\rangle. \quad (6.14)$$

Employing the above anti-commutator one finds

$$\Lambda_z \Sigma_x |E, m\rangle = -\Sigma_x \Lambda_z |E, m\rangle = -m \Sigma_x |E, m\rangle \quad (6.15)$$

Hence, the state $\Sigma_x |E, m\rangle$ can be identified with $|E, -m\rangle$. Thus except for $m = 0$ there is always an orthogonal pair of states possessing the same energy namely $|E, m\rangle$ and $|E, -m\rangle$.

$\Sigma_z = P_x P_y D_z$	$GR_y D_x$	$GP_x P_y R_y D_y$	1
$TP_x D_z$	$TGP_x R_y D_x$	$TGP_y R_y D_y$	TP_y

Table 6.2.: Discrete symmetry operations of the Hamiltonian (6.2) for a finite Ioffe field strength B , i.e. $\gamma \neq 0$. Top part: unitary symmetries. Bottom part: anti-unitary symmetries.

6.2.2. Symmetries in the presence of a Ioffe field

For $\gamma \neq 0$, i.e. in the presence of a Ioffe field, the conserved quantity Λ_z persists but only 8 (including unity) of the discrete symmetries which were presented for $\gamma = 0$ remain (see table 6.2). These operations obey a non-Abelian algebra. In contrast to the group operations of table 6.1 there are no two anti-commuting operators. Hence it is not possible to construct pairs of degenerate energy eigenstates using the above argument. The operation Σ_x which have been used previously to construct the degenerate pairs of states for $\gamma = 0$ now has the property

$$\Sigma_x H(\gamma) \Sigma_x = H(-\gamma), \quad (6.16)$$

i.e. is reversed the sign of the scaled Ioffe field strength γ in the Hamiltonian (6.2). The above relation equally holds if Σ_x is replaced by any operator in table 6.1 which represents no symmetry operation in the case $\gamma \neq 0$. We emphasize that even for $\gamma \neq 0$ the operators H , Σ_z and Λ_z form a commuting set of operators.

6.3. Numerical treatment

Our goal is now to calculate the resonance spectrum of the system. For this purpose we again adopt the complex scaling method (see section 3.4) in combination with the linear variational method (see section 3.1). We employ different basis sets for calculating the resonance spectrum of the two spin species. For the spin $\frac{1}{2}$ fermions we use two-dimensional harmonic oscillator functions in the cartesian coordinate space. The spin 1 resonances are computed utilizing the eigenfunctions of a cylindrically symmetric harmonic oscillator. Either of these approaches will turn out to deliver reliable results.

6.3.1. Spin $\frac{1}{2}$ fermions - cartesian basis set

We perform a rotation of the spatial coordinates into the complex plane: $x_i \rightarrow x_i e^{i\theta}$ which yields the rotated Hamiltonian

$$H(\theta) = \frac{1}{2} \left(p_x^2 e^{-i2\theta} + p_y^2 e^{-i2\theta} + x e^{i\theta} S_x - y e^{i\theta} S_y + \gamma S_z \right). \quad (6.17)$$

Since the complex scaling procedure transforms resonance states into square-integrable wave functions one can apply the linear variational principle in order to compute the wave functions and resonance energies. We utilize an orthonormal basis set of the form

$$|k, n, m_s\rangle = |k, n\rangle |m_s\rangle \quad (6.18)$$

where the functions $|k, n\rangle$ are the eigenfunctions of a two-dimensional harmonic oscillator in cartesian coordinates

$$|k, n\rangle = \frac{\sqrt[4]{\omega_x \omega_y}}{\sqrt{2^{k+n} \pi k! n!}} e^{-\frac{1}{2}(\omega_x x^2 + \omega_y y^2)} H_k(\sqrt{\omega_x} x) H_n(\sqrt{\omega_y} y). \quad (6.19)$$

The frequencies ω_x and ω_y can be regarded as nonlinear variational parameters which can be adapted in order to gain an optimal convergence behavior. To cover the spin space dynamics we

utilize the spinor-orbitals $|m_s\rangle$, respectively. The matrix elements of the Hamiltonian (6.17) are provided in the appendix C.1.

Performing the linear variational principle the solutions $|E\rangle$ of the stationary Schrödinger equation are expanded in a finite set of the functions (6.19):

$$|E\rangle = \sum_{knm_s} c_{knm_s} |k, n, m_s\rangle \quad (6.20)$$

From our knowledge of the symmetry properties we can choose a more specific appearance of this expansion. Requiring the states $|E\rangle$ to be eigenstates with respect to Σ_z we make use of the properties

$$\Sigma_z |k, n, \uparrow\rangle = (-1)^{k+n} |k, n, \uparrow\rangle \quad (6.21)$$

$$\Sigma_z |k, n, \downarrow\rangle = (-1)^{k+n+1} |k, n, \downarrow\rangle. \quad (6.22)$$

Thus the expansions for the two κ subspaces read

$$|E, \kappa = +1\rangle = \sum_{k+n=\text{even}} a_{kn} |k, n, \uparrow\rangle + \sum_{k+n=\text{odd}} b_{kn} |k, n, \downarrow\rangle \quad (6.23)$$

$$|E, \kappa = -1\rangle = \sum_{k+n=\text{odd}} a_{kn} |k, n, \uparrow\rangle + \sum_{k+n=\text{even}} b_{kn} |k, n, \downarrow\rangle. \quad (6.24)$$

Since $[\Lambda_z, \Sigma_z] = 0$ one can also demand the states to be a priori eigenfunctions of Λ_z as well. However, the basis functions (6.19) are not particularly well suited to construct eigenfunctions to Λ_z . We therefore abstain from putting this constraint onto the above expansion. Nevertheless, the resulting diagonalization of the Hamiltonian matrix guarantees that our numerically obtained energy and Σ_z -eigenfunctions are also eigenfunctions to Λ_z . The determination of the optimal expansion coefficients a_{kn} and b_{kn} gives rise to an ordinary complex algebraic eigenvalue problem $\mathcal{H}(\theta) \mathbf{v}(\theta) = \varepsilon(\theta) \mathbf{v}(\theta)$, where \mathcal{H} is the matrix representation of the Hamiltonian (6.17). The vector \mathbf{v} contains the coefficients a_{kn} and b_{kn} (see section 3.1).

6.3.2. Spin 1 bosons - cylindrical basis set

In a second approach we want to explicitly exploit the conservation of Λ_z as this allows us to remove one degree of freedom in the underlying Schrödinger equation. For this we project the Hamiltonian onto a given m subspace. However, since the quantity Λ_z does not explicitly occur in the Hamiltonian (6.2) this cannot be done straight-forwardly. At first we therefore transform the Hamiltonian to polar coordinates (ρ, ϕ) yielding

$$H = \frac{1}{2} \left[-\frac{\partial^2}{\partial \rho^2} - \frac{1}{\rho} \frac{\partial}{\partial \rho} + \frac{L_z^2}{\rho^2} + \rho (\cos \phi S_x - \sin \phi S_y) + \gamma S_z \right]. \quad (6.25)$$

Secondly we perform the unitary transformation

$$U = e^{iS_z \phi} \quad (6.26)$$

which gives rise to

$$U^\dagger H U = \bar{H} = \frac{1}{2} \left[-\frac{\partial^2}{\partial \rho^2} - \frac{1}{\rho} \frac{\partial}{\partial \rho} + \frac{(L_z + S_z)^2}{\rho^2} + \rho S_x + \gamma S_z \right]. \quad (6.27)$$

Apparently this Hamiltonian does not explicitly depend on the polar angle ϕ . Thus one finds $[L_z, \bar{H}] = 0$. By transforming back to the initial frame one immediately recognizes that the conservation of L_z originates from the conservation of Λ_z back in the initial frame:

$$U L_z U^\dagger = \Lambda_z \quad (6.28)$$

Consequently, the projection of \bar{H} onto a given m -subspace is now simply done by replacing L_z by the corresponding quantum number m of the operator Λ_z :

$$H_m = \langle m | \bar{H} | m \rangle = \frac{1}{2} \left[-\frac{\partial^2}{\partial \rho^2} - \frac{1}{\rho} \frac{\partial}{\partial \rho} + \frac{(m + S_z)^2}{\rho^2} + \rho S_x + \gamma S_z \right]. \quad (6.29)$$

During the complex scaling procedure the radial coordinate is rotated ($\rho \rightarrow \rho e^{i\theta}$) which gives rise to the Hamiltonian

$$H_m(\theta) = \frac{1}{2} \left[e^{-i2\theta} \left(-\frac{\partial^2}{\partial \rho^2} - \frac{1}{\rho} \frac{\partial}{\partial \rho} + \frac{(m + S_z)^2}{\rho^2} \right) + e^{i\theta} \rho S_x + \gamma S_z \right]. \quad (6.30)$$

To tackle its eigenvalue problem we utilize an orthonormal basis set of the form

$$|n, m_s, m\rangle = \frac{1}{\rho_0} \sqrt{\frac{n!}{\pi(n + |m + m_s|)!}} \left(\frac{\rho}{\rho_0} \right)^{|m+m_s|} e^{-\frac{\rho^2}{2\rho_0^2}} L_n^{|m+m_s|} \left(\frac{\rho^2}{\rho_0^2} \right) e^{i(m+m_s)\phi} |m_s\rangle. \quad (6.31)$$

Here the functions $L_n^{|m+m_s|} \left(\frac{\rho^2}{\rho_0^2} \right)$ are the associated Laguerre polynomials and ρ_0 is a parameter defining the typical length scale of the system. The latter can be adapted in order to gain an optimal convergence behavior of the numerically obtained wave functions. Again the spin space dynamics is covered by utilizing the spinor-orbitals $|m_s\rangle$. The spatial part of the basis functions (6.31) is nothing but the eigenfunctions of the two-dimensional isotropic harmonic oscillator with the oscillator length ρ_0 . This choice is convenient as it allows for an analytical calculation of the Hamiltonian's matrix elements (see appendix C.2). Moreover, these particular basis functions allow for a simple construction of approximate analytical solution of the Hamiltonian (6.2) (see section 6.6.3). The basis functions (6.31) - by construction - are eigenfunctions of Λ_z . We are going to use them to find the resonance spectrum of the system. According to Hinds and Eberlein [45] spin 1 bosons might exhibit a class of bound states which diverge logarithmically at the origin ($\rho \rightarrow 0$). Albeit this divergence the corresponding states are still square-integrable. However, since the basis functions (6.31) are regular for $\rho \rightarrow 0$ it would take infinitely many of them to properly describe a logarithmically diverging state. Hence, as all numerical computations incorporate only a finite basis size, it is impossible to recover the bound states found in ref. [45].

Performing the linear variational principle the solutions $|E, m\rangle$ of the stationary Schrödinger equation are expanded according to

$$|E, m\rangle = \sum_{nm_s} c_{nm_s} |n, m_s; m\rangle \quad (6.32)$$

which again gives rise to an ordinary complex algebraic eigenvalue problem whose solution are the optimal expansion coefficients c_{nm_s} .

6.4. Energies and decay widths of resonance states

6.4.1. Relation between energy and momentum of an eigenstate

Similar to the three-dimensional quadrupole field one also finds in the case a quadrupole guide simple relation between the mean momentum and the mean energy of an eigenstate. By exploiting $\langle [\mathbf{x} \cdot \mathbf{p}, H] \rangle = 0$ one obtains

$$E = \langle H \rangle = \frac{3}{2} [\langle p_x^2 \rangle + \langle p_y^2 \rangle] + \frac{\gamma}{2} \langle S_z \rangle. \quad (6.33)$$

Thus, for $\gamma = 0$ one again recovers equation (5.17).

6.4.2. The resonance spectrum of spin $\frac{1}{2}$ fermions

In figure 6.1 we present the energies and decay widths of the resonances of a spin $\frac{1}{2}$ particle trapped inside a magnetic guide. Without Ioffe field, i.e. for $\gamma = 0$, the resonances are arranged in regular

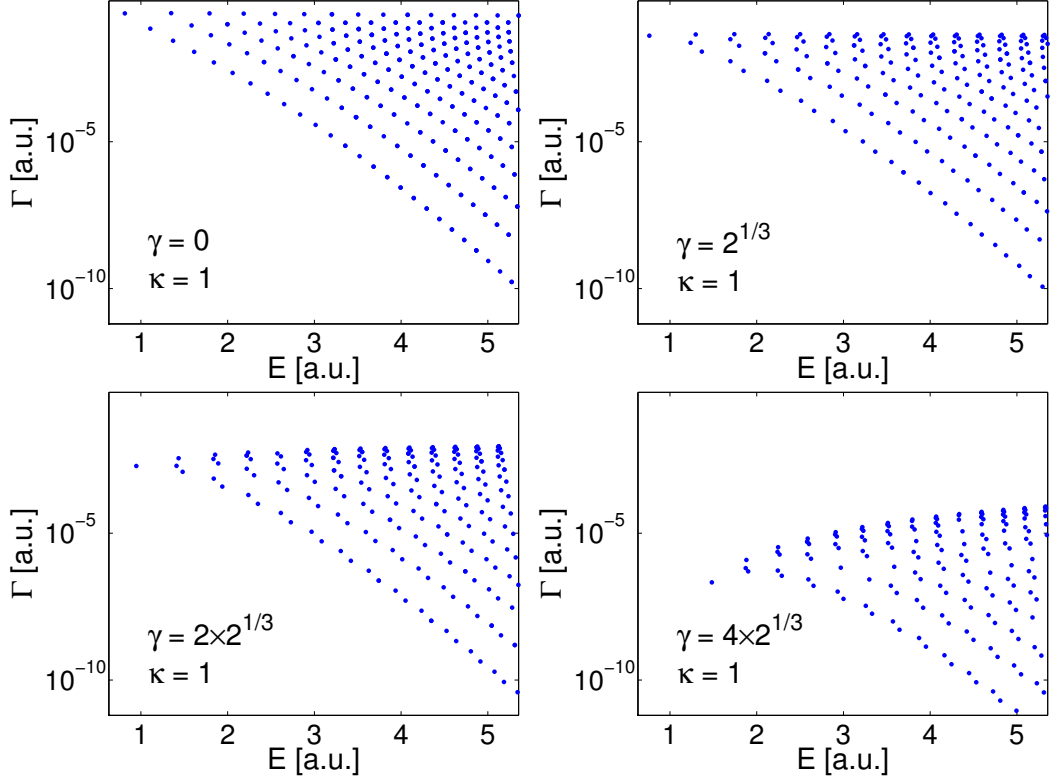


Figure 6.1.: Energies E and decay widths Γ (logarithmic scale) for resonances of a spin $\frac{1}{2}$ particle in the $\kappa = 1$ subspace. An increasing Ioffe field strength leads to a global decrease of the decay widths and therefore has a stabilizing effect. At the same time the resonance pattern becomes distorted and a regrouping of the resonances into pairs is observed.

manner across the complex energy plane. More concrete, they assemble on straight lines in the semi-logarithmic representation. This eventually implies that the decay width of a given state decreases exponentially as its energy increases. The decay width of the lowest (and thus also broadest) resonance evaluates to $\Gamma_{\min}^{\gamma=0} = 0.236$. Applying a homogeneous Ioffe field and then increasing the value of γ results in a distortion of the regular pattern. One observes the formation of vertical lines together with a regrouping of the resonances into pairs for larger γ (see in particular figure 6.1 for $\gamma = 4 \times 2^{\frac{1}{3}}$). Here states with large decay widths are affected more strongly than long lived states. Overall we encounter a decrease of the decay widths if γ increases. Hence the additional Ioffe field has a stabilizing effect. For the decay widths of the lowest resonance state our calculation yields the data listed in table 6.3. These values suggest an exponential decrease of Γ if γ increases. This

γ	0	$2^{\frac{1}{3}}$	$2 \times 2^{\frac{1}{3}}$	$\gamma = 4 \times 2^{\frac{1}{3}}$	$5 \times 2^{\frac{1}{3}}$
Γ	0.236	6.677×10^{-2}	7.794×10^{-3}	1.418×10^{-5}	2.524×10^{-7}

Table 6.3.: Decay width of the energetically lowest resonance for several values of the scaled Ioffe field strength γ . The data suggest an exponential increase of the lifetime.

agrees with the results by Sukumar and Brink who have also found an exponential decrease of Γ by performing an analytical estimation [103].

In section 6.2 we have proven the degeneracy of the $\kappa = 1$ - and $\kappa = -1$ -subspaces in the absence of a Ioffe field. For $\gamma \neq 0$, however, these degeneracies are expected to be lifted since the symmetry properties of the system are altered. Figure 6.2 shows the resonances for $\gamma = 1$. States belonging to the $\kappa = 1$ or $\kappa = -1$ subspaces are indicated by a dot or cross, respectively. Each state is closely

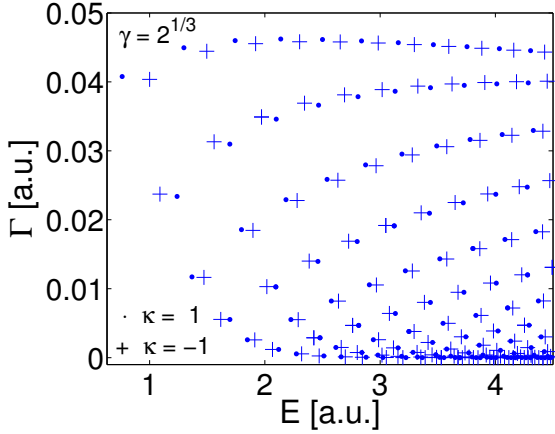


Figure 6.2.: Resonance energies and decay widths of a spin $\frac{1}{2}$ fermion in the $\kappa = 1$ - or $\kappa = -1$ -subspaces at $\gamma = 1$ (linear scale plot). Due to the finite Ioffe field formally degenerate pairs split up. States with negative quantum number m are shifted towards higher resonance energies and vice versa. The splitting decreases with decreasing decay width.

accompanied by its formally degenerate partner. Long lived states are energetically less split than short lived one. In the following we will find that a long lifetime is equipollent with a large Λ_z eigenvalue of the respective state. These high angular momentum states are mainly localized far away from the center of the guide. Here the quadrupole field dominates the homogeneous Ioffe field and therefore determines the appearance of the spectrum. Hence these states become less affected by the Ioffe field which is reflected in a decrease of the energy splitting.

We now perform a comparison of our results to the ones obtained by Hinds and Eberlein in ref. [44]. In table 6.4 we present the resonance energies and decay widths of the first three states of the

	$m = \frac{1}{2}$		$m = \frac{3}{2}$	
	E	Γ	E	Γ
0	0.8150	0.2355	1.1082	0.0707
	0.832	0.214	1.112	0.069
1	1.3484	0.2386	1.5840	0.0910
	1.339	0.214	1.588	0.095
2	1.7915	0.2347	1.9977	0.1004
	1.770	0.214	1.997	0.113

Table 6.4.: Comparison between our results (bold face) and those obtained by Hinds and Eberlein for the ground state and the first two excited resonances in the $m = \frac{1}{2}$ and $m = \frac{3}{2}$ subspaces.

$m = \frac{1}{2}$ and $m = \frac{3}{2}$ subspaces. Both results agree within a few percent. The difference might originate from the rather complicated way Hinds and Eberlein pursued to locate the resonance energies. Their method relies on determining the phase-shift of scattered waves from which they extract the resonance energies and decay widths by a fitting procedure. Complex scaling calculations of Potvliege and Zehnlé [82] have shown similar discrepancies with respect to the results given in ref. [45]. Unfortunately the results in both publications are based on the wrong assumption that the quantum number m is integer-valued [44].

6.4.3. The resonance spectrum of spin 1 bosons

The resonance spectrum of a spin 1 particle in the absence of a Ioffe field, i.e. $\gamma = 0$, is depicted in figure 6.3. The resonances form a regular pattern and, like in the spin $\frac{1}{2}$ case, states with opposite m quantum numbers form a degenerate pair. The energetically lowest lying states of each m -manifold assemble on an approximately straight diagonal line. The same holds for the next neighbored

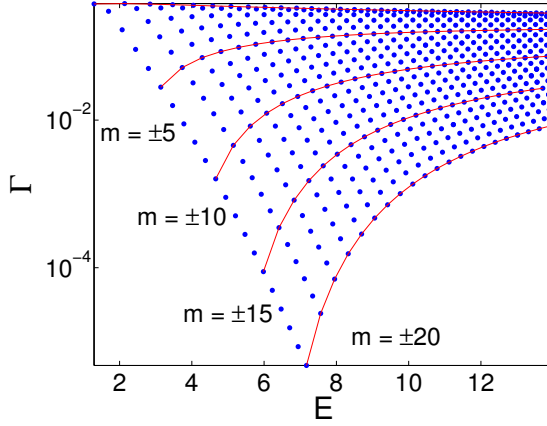


Figure 6.3.: Resonance energies and decay widths in the absence of a Ioffe field. The red lines connect resonances belonging to the same m -manifold.

excited states, so that finally a regular pattern consisting of diagonal lines is formed. In order to guide the eye of the reader resonances belonging to the same m -manifold have been connected by red lines. This has been done for $m = 0, \pm 5, \pm 10, \pm 15, \pm 20$. If now a Ioffe field is applied the resonance pattern undergoes a significant alteration as seen in figure 6.4 where the resonance positions for three different values of γ are presented. Like in the spin $\frac{1}{2}$ case the degeneracy of opposite m -states is lifted and the associated energy splitting is determined by the Ioffe field strength and the magnitude of m : High angular momentum states exhibit a smaller splitting than those with small m . For very large $|m|$ the spectrum becomes increasingly similar to the case of $\gamma = 0$. Apart from lifting the degeneracies the application of the Ioffe field also results in a global prolongation of the resonance lifetimes. For the ground state resonance this behavior is presented in figure 6.5. Although the decay width changes considerably the energy of the states is weakly affected by the Ioffe field. Calculating the decay rate of the ground state resonance up to $\gamma = 10$ we found the lifetime τ and scaled Ioffe field strength to approximately follow $\tau = 1.92 \times e^{0.30\gamma^2 + 0.68\gamma}$. For $\gamma = 0$ the minimal decay width in any m -subspace decreases monotonously with increasing resonance energy, i.e. the left flank of the distribution presented in figure 6.3 descends monotonously with growing E . This changes in the instant at which the Ioffe field is applied. Here the formation of a maximum (see figure 6.4) rather than a monotonous behavior is observed. Hence the ground state is now more stable than the next few excited states. For instance at $\gamma = 7$ the decay width of the first excited state is more than three times larger than the one of the ground state resonance. This remarkable property could be potentially useful for preparing an ensemble of noninteracting atoms in the trap ground state: Starting with a thermal distribution at a sufficiently low temperature the relative occupation number of the ground state would automatically increase by and by, since all other states are shorter lived.

6.5. Angular momentum of the resonance states

6.5.1. Resonances of spin $\frac{1}{2}$ fermions and their dependence on their Λ_z eigenvalue

In this section we analyze how the energies and decay widths of the resonances are related to the eigenvalues of the angular momentum operator Λ_z . Although Λ_z is a conserved quantity we have

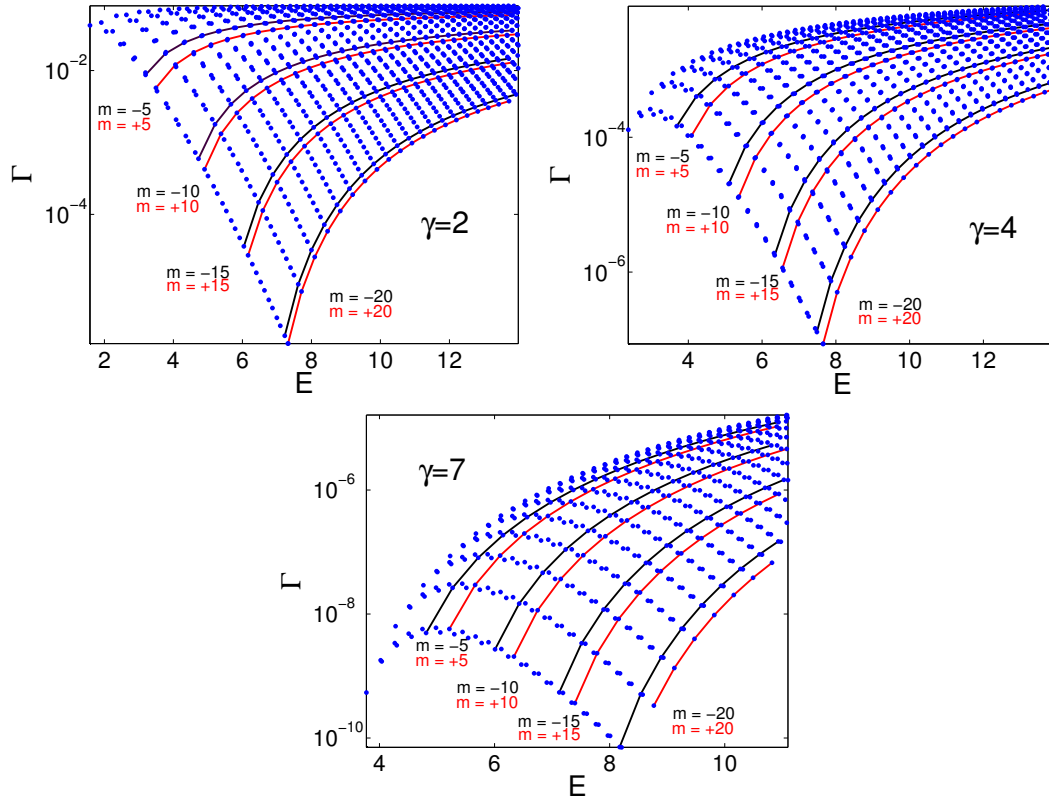


Figure 6.4.: Resonance distribution of a spin 1 boson for three different values of the Ioffe field parameter γ . Compared to the $\gamma = 0$ case the pattern is significantly altered. The formally degenerate states are now energetically separated with the respective splitting being determined by the Ioffe field parameter γ . The higher the modulus of m the smaller the energetic splitting becomes. Additionally high m states are less affected by the Ioffe field.

employed a set of basis functions which do not respect this fact. Thus we need to calculate the matrix element $m = \frac{\langle E, \kappa | \Lambda_z | E, \kappa \rangle}{\langle E, \kappa | E, \kappa \rangle}$ to receive the Λ_z -eigenvalues of the resonances. In order to do this one has to respect the nonhermitian character of the Hamiltonian (6.30) which requires a complex symmetric scalar product (see section 3.4).

In figure 6.6 we have plotted the energies E against the Λ_z eigenvalue of the resonances. For $\gamma = 0$ one observes each state to possess a degenerate counterpart, i.e. a state with opposite m . This results in the formation of a symmetric pyramid-like distribution where the maximum Λ_z eigenvalue depends approximately linearly on the resonance energy E . With increasing γ the resonance energies in general are shifted towards larger values (this can hardly be seen in figure 6.6 for $\gamma = 1$). Thereby, states with positive m acquire a larger energetic shift than states with negative values of the quantum number m . Due to this asymmetric energy shift the distribution becomes eventually asymmetric with respect to $m \rightarrow -m$. Here energies of states having the same κ quantum number form continuous, nearly horizontal, lines whereas we observe the resonance energies for $\gamma = 0$ to arrange on broken horizontal lines. In section 6.6.2 we will show that in the limit of $\frac{\rho^2}{\gamma^2} \rightarrow 0$ one finds a pattern of equidistant straight horizontal lines formed by the resonance energies. Subsequent lines belong to states with opposite Σ_z quantum number.

With increasing m values the states become less affected by the Ioffe field. Their wave functions become localized farther away from the center of the guide. In this region the strength of the linearly increasing quadrupole field outweighs the effects of the Ioffe field. In figure 6.7 the dependence of the decay widths on the Λ_z eigenvalue is presented. The linear slope in the logarithmically scaled graph suggests an exponential decrease of the minimal decay widths with increasing modulus of m .

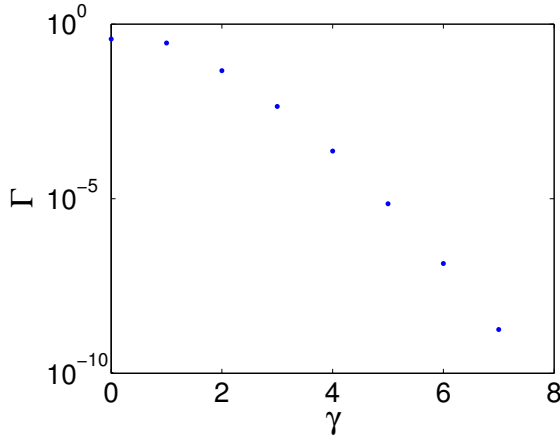


Figure 6.5.: Decay width of the ground state resonance of a spin 1 boson for selected values of the scaled Ioffe field strength γ . Apparently the Ioffe field has a stabilizing effect on the trapped states.

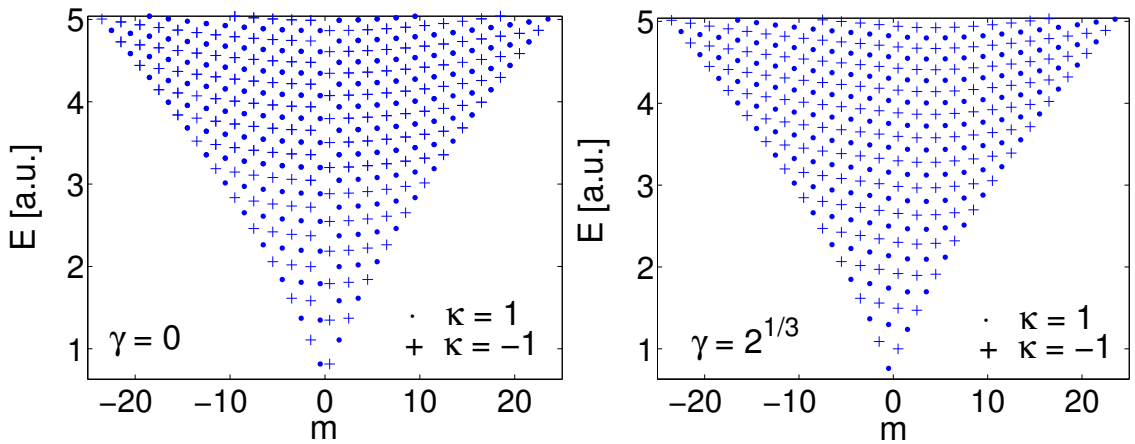


Figure 6.6.: Resonance energies and Λ_z eigenvalues of resonances for $\gamma = 0$ (left picture) and $\gamma = 1$ (right picture) in case of a spin $\frac{1}{2}$ particle. For $\gamma = 0$ the energies of the resonances form a symmetric pyramid-like pattern. For finite Ioffe field strength the pattern becomes asymmetric.

6.5.2. Resonances of spin 1 bosons and their dependence on their Λ_z eigenvalue

In figure 6.8 we show the dependence of the decay width Γ on the m quantum number for the energetically lowest resonance in each m -subspace without Ioffe field. A fit to the data yields $\Gamma \approx 0.490 \times e^{-0.575|m|}$. This curve appears to constitute a fundamental limit for the maximal achievable lifetime in a given m -subspace. Again we observe a higher amount of angular momentum to enhance the stability of the trapped states. For large m states even approximately stable solutions can be obtained analytically. These so-called quasi-bound states are subject of the discussion of section 6.6.

We now turn to the investigation of the dependence of the resonance energy on the eigenvalue of Λ_z . For $\gamma = 0$ and $\gamma = 4$ the corresponding plot is presented in figure 6.9. Apparently there is some connection between the lowest energy in a given m -subspace E_0^m and the actual value of m . This is not surprising since a certain magnitude of angular momentum has to be always associated with a certain amount of energy. Figure 6.9 suggests an approximately linear dependence of E_0^m on the modulus of m . As expected the pattern emerging for $\gamma = 0$ is mirror symmetric with respect to the $m = 0$ axis. By switching on the Ioffe field the distribution shifts to the left hand side and is now approximately symmetric with respect to reflections at $m = -1$. Moreover, the Ioffe field leads to an overall increase of the energies. The global ground state of the system for $\gamma = 0$ possesses the energy $E_0 = 1.29$ whereas one finds $E_0 = 3.77$ for $\gamma = 7$.

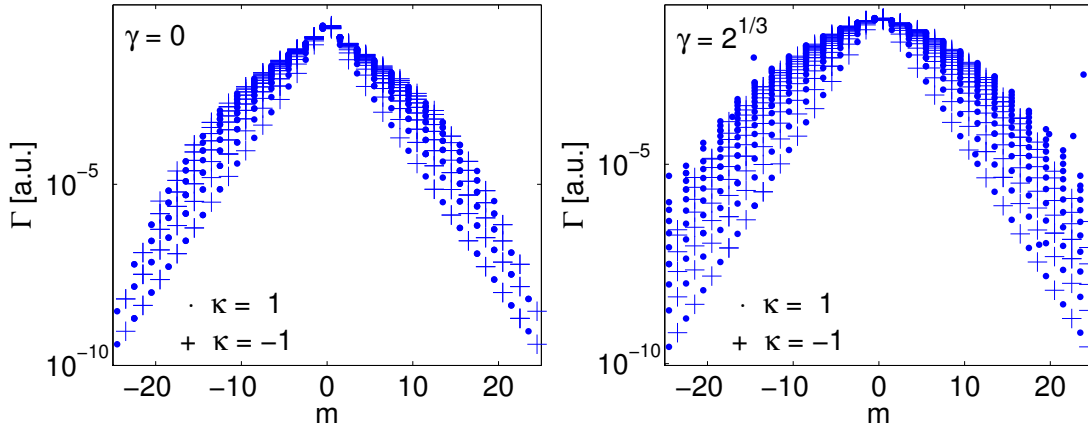


Figure 6.7.: Decay width plotted against the Λ_z eigenvalue of a spin $\frac{1}{2}$ particle for $\gamma = 0$ (left picture) and $\gamma = 2^{\frac{1}{3}}$ (right picture). The minimal decay width of a resonance in a given m -subspace decreases exponentially with increasing modulus of m . If the Ioffe field strength increases one observes an overall decrease of the decay widths and a widening of the distribution.

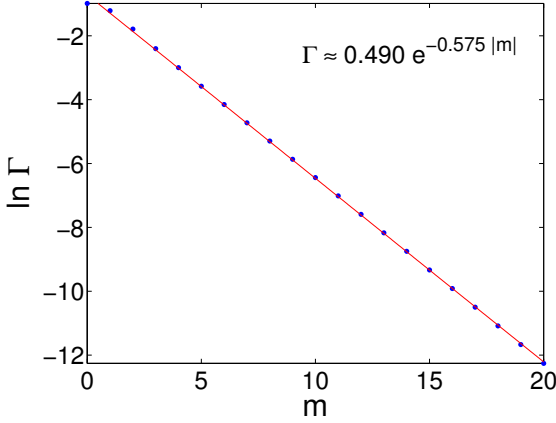


Figure 6.8.: Dependence of the decay width of the ground state resonance of a spin 1 boson on the Λ_z -eigenvalue m for $\gamma = 0$. An exponential decrease of the decay width is observed if m is increased. An exponential fit (red curve) yields $\Gamma \approx 0.490 \times e^{-0.575|m|}$.

6.6. Quasi-bound states

Although in the strict sense there are no bound states we have observed resonance states that carry a high amount of angular momentum to possess extremely long lifetimes / small decay widths. We will now try elucidating the nature of these so-called quasi-bound states. We will thereby be lead to an approximate Schrödinger equation whose stationary solutions represent a good approximation to the quasi-bound states. We will compare these results to the ones one would obtain by employing the commonly used adiabatic approximation [31].

6.6.1. Quasi-bound states of spin $\frac{1}{2}$ fermions in the magnetic guide ($\gamma = 0$)

We start by using Hamiltonian (6.29), where the conservation of Λ_z has been already exploited, and firstly put $\gamma = 0$. The Hamiltonian then depends parametrically on the quantum number m and therefore governs the dynamics of a spin particle inside a particular Λ_z subspace. We now apply the spin space transformation R_x that is defined through equation (6.3). In order to simplify the radial kinetic energy we introduce the spinor $|\Psi\rangle = \rho^{-\frac{1}{2}} |\Phi\rangle$ which gives rise to the Schrödinger

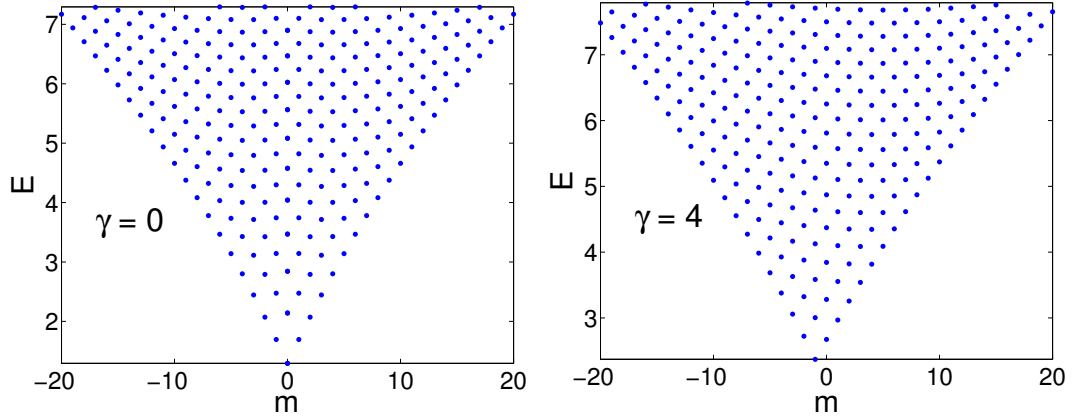


Figure 6.9.: Resonance energies vs. Λ_z eigenvalue m in case of a spin 1 boson. The minimal resonance energy in the different m -subspaces increases approximately linearly with $|m|$. For $\gamma = 0$ the global ground state is located in the $m = 0$ subspace whereas for $\gamma = 4$ it is found in the $m = -1$ subspace.

equation

$$\frac{1}{2} \left[-\frac{\partial^2}{\partial \rho^2} + \frac{m^2 + m\sigma_x}{\rho^2} + \frac{\rho}{2}\sigma_z \right] |\Phi\rangle = E |\Phi\rangle. \quad (6.34)$$

Here the σ_i are the Pauli matrices in their common notation. The transformation R_x diagonalizes the $\boldsymbol{\mu} \cdot \mathbf{B}$ interaction term but leads to off-diagonal elements in the angular momentum term. In the limit of large m we assume that this coupling between the up and down components of $|\Phi\rangle$ can be neglected. This is equivalent to performing the replacement

$$\frac{m^2 + m\sigma_x}{\rho^2} \rightarrow \frac{m^2}{\rho^2} \quad (6.35)$$

which results in

$$\frac{1}{2} \left[-\frac{\partial^2}{\partial \rho^2} + \frac{m^2}{\rho^2} + \rho S_z \right] |\Phi\rangle = E_{qb} |\Phi\rangle. \quad (6.36)$$

By construction this radial Schrödinger equation (6.36) does not couple the up- and down-component of the spinor wave function $|\Phi\rangle$. The lower component is unbound since the corresponding effective potential is $V^-(\rho) = \frac{m^2}{2\rho^2} - \frac{1}{4}\rho$. The potential for the upper component is $V^+(\rho) = \frac{m^2}{2\rho^2} + \frac{1}{4}\rho$ and therefore bound solutions are allowed. We will identify the corresponding states as the quasi-bound states $|\chi\rangle = (\chi(\rho), 0)^T$. Such states are solutions of the Schrödinger equation

$$\frac{1}{2} \left[-\chi'' + \frac{m^2}{\rho^2}\chi + \frac{\rho}{2}\chi \right] = E_{qb}\chi. \quad (6.37)$$

Here a prime denotes the derivative with respect to ρ . In order to solve equation (6.37) we have utilized the FEMLAB software package which employs the finite element method for solving differential equations. To our knowledge there is no analytic solution of equation (6.37). However, for $\rho \rightarrow 0$ the solutions become cylindrical Bessel-functions whereas for $\rho \rightarrow \infty$ they behave like Airy-functions.

In table 6.5 the resonance energies E obtained from the complex scaling calculation are compared to the approximate energies E_{qb} resulting from equation (6.36). Even for $m = \frac{1}{2}$ we find a remarkable good agreement between E and E_{qb} although the validity of the replacement (6.35) is hard to justify since the off-diagonal coupling terms are of the same order of magnitude as the diagonal ones. With increasing m the discrepancy of E and E_{qb} decreases as suggested by equation

		0	1	2	3	4	5
$m = \frac{1}{2}$	E	0.8150	1.3484	1.7915	2.1852	2.5462	2.8833
	E_{qb}	0.8082	1.3410	1.7843	2.1783	2.5397	2.8770
	%	0.83	0.55	0.40	0.31	0.26	0.22
$m = \frac{11}{2}$	E	2.0575	2.4198	2.7590	3.0798	3.3855	3.6785
	E_{qb}	2.0500	2.4100	2.7474	3.0669	3.3717	3.6640
	%	0.36	0.41	0.42	0.42	0.41	0.39
$m = \frac{21}{2}$	E	3.0142	3.3154	3.6053	3.8852	4.1563	4.4196
	E_{qb}	3.0115	3.3121	3.6014	3.8807	4.1513	4.4140
	%	0.09	0.10	0.11	0.12	0.12	0.13
$m = \frac{31}{2}$	E	3.8400	4.1078	4.3684	4.6223	4.8703	5.1128
	E_{qb}	3.8386	4.1061	4.3664	4.6202	4.8679	5.1101
	%	0.04	0.04	0.04	0.05	0.05	0.05
$m = \frac{41}{2}$	E	4.5855	4.8311	5.0715	5.3071	-	-
	E_{qb}	4.5845	4.8300	5.0703	5.3058	5.5368	5.7636
	%	0.02	0.02	0.02	0.02	-	-

Table 6.5.: Comparison of the resonance energies of a spin $\frac{1}{2}$ fermion to the approximate energies E_{qb} obtained from equation (6.36). The first six resonance energies E for 5 selected values of the quantum number m are provided. The rows labeled by '%' show the relative difference between E and E_{qb} in percent.

(6.35). The surprisingly good quality of the approximation can be illuminated by looking at how the bound solution $|\chi\rangle = (\chi(\rho), 0)^T$ and the unbound wave function $|\zeta\rangle = (0, \zeta(\rho))^T$ are coupled by the Schrödinger equation (6.34):

$$\frac{m}{2} \langle \chi | \frac{\sigma_x}{\rho^2} | \zeta \rangle = \frac{m}{2} \int d\rho \chi^*(\rho) \frac{1}{\rho^2} \zeta(\rho) \quad (6.38)$$

From this expression it becomes immediately apparent that transitions from the bound state $|\chi\rangle$ to the unbound state $|\zeta\rangle$ are going to happen essentially at the center of the guide. However, since m can only adopt half-integer values the centrifugal barrier in equation (6.36) always persists. Thus both wave functions $|\chi\rangle$ and $|\zeta\rangle$ vanish for $\rho \rightarrow 0$. But this is the only region where the operator $\frac{1}{\rho^2}$ contributes significantly and hence we have $\langle \chi | \frac{\sigma_x}{\rho^2} | \zeta \rangle \ll 0$. Hence there is only a small coupling between the bound and unbound solution and therefore the resonance states are very well described by the solutions $|\chi\rangle$ of equation (6.37). This is also the explanation for the extraordinary long lifetime of high m states. Here the large angular momentum barrier prevents the coupling between the bound and unbound channel. Accordingly, the particle is then located between the classical turning points of the potential $V_{qb}(\rho) = \frac{m^2}{2\rho^2} + \frac{1}{2}\rho$ at a distance of approximately $\rho_{\min} = m^{\frac{2}{3}}$. Performing a harmonic approximation of the potential $V^+(\rho)$ around its minimum at ρ_{\min} yields a useful expression for the energy of the lowest resonance in each Λ_z subspace

$$E_{\text{lr}} = \frac{\sqrt{3}}{4} m^{-\frac{2}{3}} + \frac{3}{2} m^{\frac{2}{3}}. \quad (6.39)$$

These energies represent a very good approximation. Their discrepancy to the exact ones is less than 0.05%. Figure 6.10 shows the energy spectrum obtained from equation (6.39). For large m values the level spacing scales according to $m^{-\frac{1}{3}}$.

6.6.2. Quasi-bound states of spin $\frac{1}{2}$ fermions in the Ioffe-Pritchard trap ($\gamma \neq 0$) - Comparison to the adiabatic approximation

Now we investigate the class of quasi-bound states that occur in the presence of a Ioffe field. Again we use the Hamiltonian (6.29) as the starting point and consider the spinor wave function

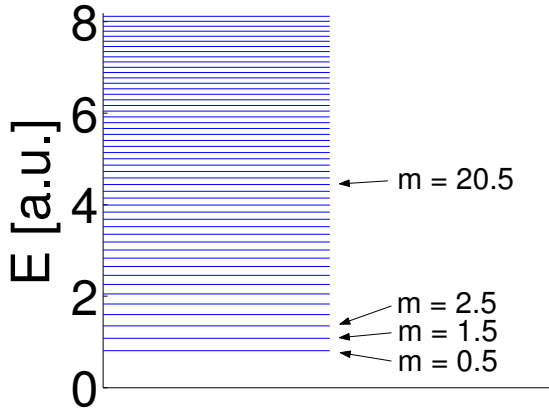


Figure 6.10.: Energies E_{1r} of the lowest resonances in each m subspace of a spin $\frac{1}{2}$ fermion calculated by using equation (6.39). Their accuracy is higher than the resolution of the plot.

$|\Psi\rangle = \rho^{-\frac{1}{2}}|\Phi\rangle$. After applying the unitary transformation

$$U = \frac{1}{\sqrt{2}} \begin{pmatrix} \sqrt{1+\alpha} & \sqrt{1-\alpha} \\ \sqrt{1-\alpha} & -\sqrt{1+\alpha} \end{pmatrix} \quad (6.40)$$

with $\alpha = \frac{\gamma}{\sqrt{\gamma^2 + \rho^2}}$ the corresponding Schrödinger equation becomes

$$\frac{1}{2} \left[-\frac{\partial^2}{\partial \rho^2} + \frac{m^2}{\rho^2} + \frac{m\alpha}{\rho^2} \sigma_z + \frac{\gamma}{2\alpha} \sigma_z + \frac{\alpha^4}{4\gamma^2} - i \left(\frac{\alpha^2}{\gamma} \frac{\partial}{\partial \rho} - \rho \frac{\alpha^4}{\gamma^3} \right) \sigma_y + \frac{m\alpha}{\gamma\rho} \sigma_x \right] |\Phi\rangle = E |\Phi\rangle \quad (6.41)$$

Similar to the $\gamma = 0$ case the operator (6.40) turns the $\boldsymbol{\mu} \cdot \mathbf{B}$ -coupling term diagonal. However, unlike the transformation (6.3) U in equation (6.40) depends explicitly on the coordinate ρ . Therefore the transformation of the derivative results in additional terms:

$$U^\dagger \frac{\partial^2}{\partial \rho^2} U = U^\dagger U'' + 2U^\dagger U' \frac{\partial}{\partial \rho} + \frac{\partial^2}{\partial \rho^2}. \quad (6.42)$$

By neglecting the off-diagonal coupling terms in equation (6.41) one obtains

$$\frac{1}{2} \left[-\frac{\partial^2}{\partial \rho^2} + \frac{m^2}{\rho^2} + \frac{m\alpha}{\rho^2} \sigma_z + \frac{\gamma}{2\alpha} \sigma_z + \frac{\alpha^4}{4\gamma^2} \right] |\Phi\rangle = E_{qb} |\Phi\rangle \quad (6.43)$$

Here similar to equation (6.36) only the upper component of the spinor $|\Phi\rangle$ is bound. It obeys the Schrödinger equation

$$\frac{1}{2} \left[-\frac{\partial^2}{\partial \rho^2} + \frac{m^2}{\rho^2} + \frac{1}{2} \sqrt{\gamma^2 + \rho^2} + \frac{m\gamma}{\rho^2 \sqrt{\gamma^2 + \rho^2}} + \frac{\gamma^2}{4(\gamma^2 + \rho^2)^2} \right] \chi = E_{qb} \chi. \quad (6.44)$$

In table 6.6 we compare the resonance energies E obtained for $\gamma = 2^{\frac{1}{3}} \times 5$ to the eigenvalues E_{qb} calculated by solving the scalar radial Schrödinger equation (6.44). Apart from $m = -\frac{1}{2}$ the agreement is excellent with discrepancies smaller than 0.05 %. This is again the result of a localization of the particle's wave function away from center of the guide which is the only region where the off-diagonal coupling terms are remarkable. However, for $m = -\frac{1}{2}$ the effective potential of the Schrödinger equation (6.44) does not possess a centrifugal barrier. Here the wave function has nonzero contributions in the vicinity of the center of the guide. Hence the off-diagonal coupling terms of equation (6.41) become important. Considering the fact that the equation (6.44) here becomes certainly invalid the energies E and E_{qb} still agree surprisingly well (see table 6.6).

		0	1	2	3	4	5
$m = -\frac{1}{2}$	E	1.7742	2.1405	2.4828	2.8063	3.1143	3.4095
	E_{qb}	1.7936	2.1590	2.5004	2.8230	3.1304	3.4250
	%	1.08	0.86	0.70	0.59	0.51	0.45
$l = 0$	E_{ad}	1.7883	2.1548	2.4968	2.8200	3.1277	3.4225
	%	0.79	0.66	0.56	0.48	0.43	0.38
$m = \frac{11}{2}$	E	2.8136	3.1202	3.4143	3.6976	3.9716	4.2372
	E_{qb}	2.8126	3.1192	3.4131	3.6964	3.9703	4.2359
	%	0.03	0.03	0.04	0.03	0.03	0.03
$l = 6$	E_{ad}	2.8321	3.1370	3.4296	3.7118	3.9847	4.2495
	%	0.65	0.54	0.45	0.38	0.33	0.29
$m = \frac{31}{2}$	E	4.3174	4.5697	4.8162	5.0573	5.2934	5.5249
	E_{qb}	4.3167	4.5690	4.8154	5.0565	5.2926	5.5240
	%	0.02	0.02	0.02	0.02	0.02	0.02
$l = 16$	E_{ad}	4.3495	4.6004	4.8455	5.0854	5.3203	5.5508
	%	0.74	0.67	0.60	0.55	0.51	0.47

Table 6.6.: Comparison of the resonance energies of a spin $\frac{1}{2}$ fermion to the approximate energies E_{qb} and adiabatic energies E_{ad} for $\gamma = 2^{\frac{1}{3}} \times 5$. The first six resonance energies E for 5 selected values of the m quantum number are given. The rows labeled by '%' show the relative difference between E and E_{qb} or E_{ad} , respectively, in percent.

We now compare the results of the approximate Schrödinger equation (6.44) to those one would obtain within the so called adiabatic approximation [31]. In this picture one assumes the projection of the atomic spin onto the local direction of the magnetic field to be conserved. Thus the coupling of the magnetic moment to the field simply reduces to $g\mu_B m_S |\mathbf{B}(\mathbf{r})|$ with m_S being the projection of the spin onto the local field direction. In case of a spin $\frac{1}{2}$ particle in the magnetic guide the corresponding Hamiltonian becomes

$$H_{ad} = \frac{1}{2} \left[p_x^2 + p_y^2 \pm \frac{1}{2} \sqrt{\gamma^2 + x^2 + y^2} \right] \quad (6.45)$$

with having employed scaled coordinates (see section 6.1). Considering only the positive sign (which allows for bound solutions) and introducing the wave function $|\Psi_{ad}\rangle = \rho^{-\frac{1}{2}} |\Phi_{ad}\rangle$ the corresponding Schrödinger equation becomes

$$\frac{1}{2} \left[-\frac{\partial^2}{\partial \rho^2} + \frac{l^2 - \frac{1}{4}}{\rho^2} + \frac{1}{2} \sqrt{\gamma^2 + \rho^2} \right] |\Phi_{ad}\rangle = E_{ad} |\Phi_{ad}\rangle. \quad (6.46)$$

Here l is the quantum number of the operator L_z (z-component of the orbital angular momentum) which is conserved due to the rotational invariance of the system around the z -axis. Note that unlike m the quantum number l is integer-valued. Table 6.6 shows a comparison of the adiabatic eigenvalues E_{ad} to the exact resonance energies as well as the energies of the quasi-bound states E_{qb} . The quantum numbers l and m are chosen such that $l = m + \frac{1}{2}$. Only for $l = 0$ or $m = -\frac{1}{2}$ the adiabatic energies E_{ad} are in better agreement to the exact ones than the quasi-bound energies E_{qb} . One has to note that in contrast to E_{ad} the energies E_{qb} become exact in the limit of high m quantum numbers. Moreover we have to emphasize that only the Schrödinger equation (6.44) which yields the quasi-bound states reproduces the correct degeneracies of the system. Unlike this the equation which relies on the (crude) adiabatic approximation shows a two-fold degeneracy of the states $|l\rangle$ and $|-l\rangle$ for any value of γ . We now investigate how the different approximations perform at different Ioffe field strengths γ . In figure 6.11 the energies obtained from each of the

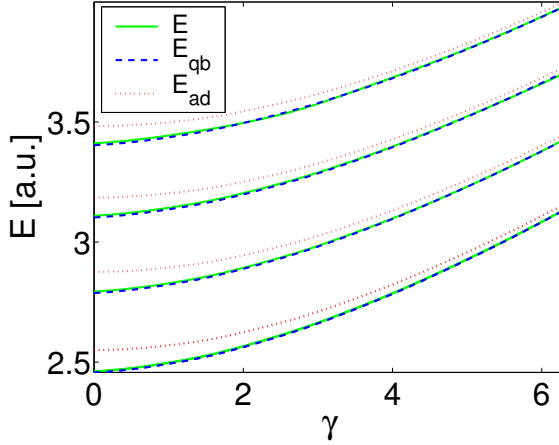


Figure 6.11.: Comparison of the quasi-bound energies E_{qb} and adiabatic energies E_{ad} to the exact energies E . The figure shows the energies of the lowest four states in the $m = \frac{15}{2}$ and $l = 8$ subspace, respectively. The discrepancy between E and E_{qb} is hardly visible throughout the complete γ -interval shown.

three methods (exact, quasi-bound, adiabatic) are depicted for the 4 energetically lowest resonances in the $m = \frac{15}{2}$ and $l = 8$ subspace, respectively. One observes a remarkably good agreement of E and E_{qb} throughout the complete γ -interval. In contrast to that severe discrepancies between the adiabatic and exact energies are revealed for small values of γ . This shows the extremely good performance of the quasi-bound approximation independently of the value of γ . Figure 6.11 also shows that if γ becomes large the adiabatic approximation performs increasingly better.

In the limit $\frac{\rho^2}{\gamma^2} \ll 1$ equation (6.46) can be further simplified. A series expansion of the potential term up to first order in $\frac{\rho^2}{\gamma^2}$ yields

$$\frac{1}{2} \left[-\frac{\partial^2}{\partial \rho^2} + \frac{l^2 - \frac{1}{4}}{\rho^2} + \frac{\rho^2}{4\gamma} + \frac{\gamma}{2} \right] |\Phi_{ad}\rangle = E_{ad} |\Phi_{ad}\rangle. \quad (6.47)$$

This is the Schrödinger equation of a radial harmonic oscillator. The corresponding eigenenergies are given by

$$E_{nl} = \frac{\gamma}{4} + \frac{1}{2\sqrt{\gamma}} (2n + |l| + 1). \quad (6.48)$$

Introducing the frequency $\omega = \frac{1}{2\sqrt{\gamma}}$ together with the substitution $l = m + \frac{1}{2}$ one arrives at the formula

$$E_{nm} = \frac{\gamma}{4} + \omega \left(2n + \left| m + \frac{1}{2} \right| + 1 \right). \quad (6.49)$$

Figure 6.12 shows a plot of the energies E_{nm} . The corresponding Σ_z -eigenvalues are calculated using equation (6.13). The resultant pattern is similar to the one we have already observed in figure 6.6 ($\gamma = 2^{\frac{1}{3}}$). We find alternating equidistant horizontal lines of energies belonging to states of the two different Σ_z -subspaces.

6.6.3. Quasi-bound states of spin 1 bosons in a Ioffe-Pritchard trap ($\gamma \neq 0$)

With now having thoroughly discussed the quasi-bound states of spin $\frac{1}{2}$ particles we now turn to spin 1 bosons. We now want to pursue a more general approach which allows us to calculate quasi-bound states of particles of arbitrary spin. To this end we again perform a unitary transformation of the Hamiltonian (6.29) which diagonalizes the spin-field interaction part. It reads

$$U_S = e^{iS_y\beta} \quad (6.50)$$

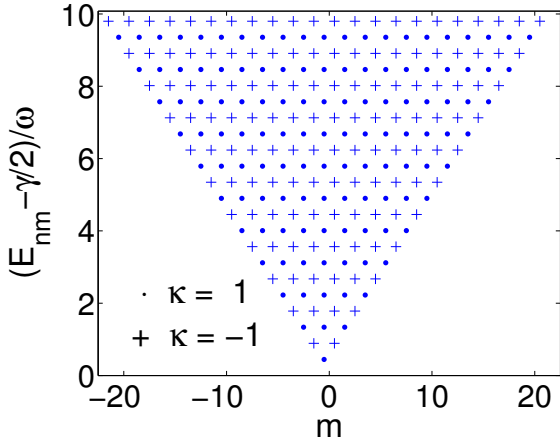


Figure 6.12.: Graphical representation of the eigenenergies (6.49). The values of the quantum number κ are calculated using equation (6.13). A pattern of equidistant horizontal lines with alternating κ values is formed.

with $\cos \beta = \gamma |\mathbf{G}(\mathbf{r})|^{-1}$, $\sin \beta = -\rho |\mathbf{G}(\mathbf{r})|^{-1}$ and the scaled magnetic field $\mathbf{G}(\mathbf{r}) = (x, -y, \gamma)$. The transformation (6.50) conducts a rotation in the spin space, such that the spin vector of the particle is rotated to point into the direction of the magnetic field vector. The magnetic field vector thereby defines a local quantization axis which in the further will be denoted as the z -axis (for illustration see figure 6.13). We want to point out that the transformation (6.50) holds independently from the

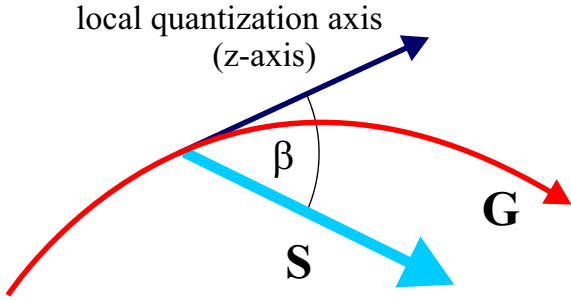


Figure 6.13.: The unitary transformation (6.50) rotates the spin vector into the direction of the local magnetic field. The field vector thereby constitutes a local quantization axis.

dimensionality of the spin space. It is therefore generally applicable and includes equation (6.40) as a special case. Applying U_S to the Hamiltonian (6.29) becomes

$$\begin{aligned}
 U_S^\dagger H_m U_S &= \frac{1}{2} \left[-U_S^\dagger \frac{\partial^2}{\partial \rho^2} U - \frac{1}{\rho} U_S^\dagger \frac{\partial}{\partial \rho} U_S + \frac{(m + U_S^\dagger S_z U)^2}{\rho^2} + S_z |\mathbf{G}(\mathbf{r})| \right] \\
 &= \frac{1}{2} \left[-\frac{\partial^2}{\partial \rho^2} + \left(i2S_y \frac{\cos \beta}{|\mathbf{G}(\mathbf{r})|} - \frac{1}{\rho} \right) \frac{\partial}{\partial \rho} + iS_y \frac{\cos \beta}{|\mathbf{G}(\mathbf{r})|} \left(\frac{1}{\rho} + 2 \frac{\sin \beta}{|\mathbf{G}(\mathbf{r})|} \right) \right. \\
 &\quad \left. + \frac{(m + \cos \beta S_z + \sin \beta S_x)^2}{\rho^2} + S_y^2 \frac{\cos^2 \beta}{|\mathbf{G}(\mathbf{r})|^2} + S_z |\mathbf{G}(\mathbf{r})| \right] \quad (6.51)
 \end{aligned}$$

Here all off-diagonal terms according to equation (6.42) have been taken into account. The coupling term of the spin to the magnetic field has now become proportional to $S_z |\mathbf{G}(\mathbf{r})|$ and is therefore diagonal within the S_z eigenstates. At this point we again want to emphasize that the operator S_z refers to the spin component pointing towards the local magnetic field. In the limit $\rho \ll \gamma$ the coupling term can be approximated up to second order of ρ by

$$S_z |\mathbf{G}(\mathbf{r})| \approx S_z \gamma + S_z \frac{1}{2} \frac{\rho^2}{\gamma}. \quad (6.52)$$

As we deal with quantum states and therefore with delocalized wave functions instead of classical point particles the condition $\rho \ll \gamma$ should be carefully reviewed: We consider the above approxi-

mation to hold for states whose wave function is mainly localized in areas covered by this inequality. As immediately seen from equation (6.52) the term $S_z\gamma$ will dominate the Hamiltonian for a sufficiently large Ioffe field strength. We can therefore consider S_z to be approximately conserved and treat the remaining terms as a perturbation. This is equivalent to assuming that at any spatial point the spin vector is aligned with the magnetic field, which is often referred to as the adiabatic approximation. Projecting the Hamiltonian (6.51) onto a given m_s subspace and considering all terms up to second order in ρ one obtains

$$\begin{aligned} \langle m_s | U_S^\dagger H_m U_S | m_s \rangle &\approx \\ \tilde{H} &= \frac{1}{2} \left[-\frac{\partial^2}{\partial \rho^2} - \frac{1}{\rho} \frac{\partial}{\partial \rho} + \frac{(m + m_s)^2}{\rho^2} + \frac{2 - m_s(m + 2m_s)}{\gamma^2} + m_s\gamma \right. \\ &\quad \left. + \left(\frac{m_s}{2\gamma} - \frac{3 - m_s(\frac{3}{4}m + \frac{5}{2}m_s)}{\gamma^4} \right) \rho^2 \right]. \end{aligned} \quad (6.53)$$

The last term of \tilde{H} provides a harmonic confinement with the trap frequency

$$\omega_{m_s} = \sqrt{\frac{m_s}{2\gamma} - \frac{3 - m_s(\frac{3}{4}m + \frac{5}{2}m_s)}{\gamma^4}}. \quad (6.54)$$

However, here only $m_s = 1$ comes into question as it solely results in a real oscillation frequency with an oscillator length being consistent with the assumption $\rho \ll \gamma$. In this case the eigenenergies of \tilde{H} are those of a two-dimensional isotropic harmonic oscillator being shifted by a constant off-set:

$$\tilde{E}_{Nm} = \frac{\gamma}{2} - \frac{m}{2\gamma^2} + \omega_1 [2N + |m + 1| + 1]. \quad (6.55)$$

The corresponding eigenfunctions read in the initial frame (before the application of U_S)

$$\begin{aligned} |N, m\rangle &= \sqrt{\frac{\omega_1 N!}{\pi(N + |m + 1|)!}} (\sqrt{\omega_1} \rho)^{|m+1|} e^{-\frac{\omega_1 \rho^2}{2}} L_N^{|m+1|} (\omega_1 \rho^2) e^{i(m+1)\phi} \\ &\quad \times \left[\cos^2 \frac{\beta}{2} |1\rangle - \frac{1}{\sqrt{2}} \sin \beta |0\rangle + \sin^2 \frac{\beta}{2} |-1\rangle \right]. \end{aligned} \quad (6.56)$$

In practice one of course does not encounter truly bound states but one rather finds a spectrum of resonances. The bound character of the approximate quantum states (6.56) results from neglecting the coupling between the different local S_z eigenstates. Nevertheless, the above analysis shows that for a sufficiently large Ioffe field, the minimum energy of the system occurs for $m = -1$. This explains the shifted pattern shown in figure 6.9. In table 6.7 we present a comparison of the approximate and the numerically exact energy eigenvalues. The best agreement is found for the lowest energy level in the $m = -1$ subspace. The quality of the approximation decreases with increasing degree of excitation or/and if other m -subspaces are considered. In either case the spatial extension of the atomic resonance wave function increases so that the wave function enters spatial regions where the condition $\rho \ll \gamma$ is violated. The data in table 6.7 also indicate the improvement of the quality of the approximation if larger Ioffe field strengths are considered reminiscent of the spin $\frac{1}{2}$ case.

6.7. Resonances of magnetically trapped alkali metal atoms

The results presented in this chapter can be directly applied to alkali metal atoms being magnetically trapped in a hyperfine state (see also section 5.6). As instructive examples we choose

γ	m		0	1	2	3	4
7	-1	approx.	3.7765	4.3091	4.8416	5.374	5.9068
		exact	3.7726	4.2796	4.7638	5.2286	5.6768
	0	approx.	4.0337	4.5675	5.1012	5.6350	6.1687
		exact	4.0211	4.5170	4.9916	5.4483	5.8893
	+1	approx.	4.2922	4.8271	5.3620	5.8969	6.4318
		exact	4.2663	4.7515	5.2172	5.6660	6.1002
10	-1	approx.	5.2283	5.6750	6.1216	6.5683	7.0149
		exact	5.2262	5.6593	6.0800	6.4893	6.8885
	0	approx.	5.4470	5.8940	6.3410	6.7880	7.2350
		exact	5.4403	5.8672	6.2823	6.6866	7.0813
	+1	approx.	5.6660	6.1133	6.5606	7.0080	7.4553
		exact	5.6525	6.0734	6.4831	6.8826	7.2728

Table 6.7.: Comparison between approximate and numerically exact energy eigenvalues in case of a spin 1 boson. The best agreement is found in the $m = -1$ subspace. The quality of the approximation declines if the degree of excitation or the value of $|m + 1|$ is increased.

	mass [m_e]	g_F	energy unit [neV]	length unit [nm]	E_{gs} [neV]	τ_{gs} [μ s]
${}^6\text{Li}$	10964.67	$\frac{3}{2}$	0.459	121.65	0.61	3.75
${}^7\text{Li}$	12789.55	$\frac{1}{2}$	0.584	100.95	0.76	3.01
${}^{87}\text{Rb}$	155798.23	$\frac{1}{2}$	0.254	43.87	0.33	6.94

Table 6.8.: Mass, g-factor, length and energy unit as well as resonance energy and lifetime of the ground state resonance of ${}^6\text{Li}$ ($2S_{\frac{1}{2}}$, $F = \frac{1}{2}$), ${}^7\text{Li}$ ($2S_{\frac{1}{2}}$, $F = 1$) and ${}^{87}\text{Rb}$ ($5S_{\frac{1}{2}}$, $F = 1$) in a magnetic guide at a gradient $b = 100\frac{T}{m}$.

the species: ${}^6\text{Li}$ ($2S_{\frac{1}{2}}$, $F = \frac{1}{2}$), ${}^7\text{Li}$ ($2S_{\frac{1}{2}}$, $I = \frac{3}{2}$, $F = 1$) and ${}^{87}\text{Rb}$ ($5S_{\frac{1}{2}}$, $I = \frac{3}{2}$, $F = 1$). The corresponding masses and g-factors are provided in table 6.8 where we also present the energy, the length unit as well as the energy E_{gs} and lifetime τ_{gs} of the ground state resonance at a gradient $b = 100\frac{T}{m}$. Using a sideguide configuration such gradient is generated according to equation (2.5) by a current $I = 2A$ and a bias-field strength of $B_B = 6.3 \times 10^{-3}T$. For these parameters we encounter lifetimes which are of the order of μ s. As we have demonstrated the lifetime of trapped states can be significantly prolonged if the atom is prepared in states which carry high angular momentum. In case of ${}^{87}\text{Rb}$ (${}^7\text{Li}$) being prepared in the $m = 20$ subspace at $\gamma = 7$ which corresponds to a Ioffe field strength of $3 \times 10^{-5}T = 0.3G$ one encounters lifetimes of $7782s$ ($3382s$).

6.8. Summary

In this chapter we have presented an investigation on the motion of neutral spin $\frac{1}{2}$ fermions and spin 1 bosons in a Ioffe-Pritchard type trap. After introducing a canonical scaling transformation of the phase space coordinates we have derived an effective two-dimensional Hamiltonian depending on a single parameter γ , i.e. the scaled Ioffe field strength. The energies and decay widths of resonance states of the Schrödinger equation have been calculated by employing the complex scaling method. Utilizing a two-dimensional harmonic oscillator basis we were able to converge hundreds of resonance states.

The analysis of the underlying Hamiltonian revealed a large number of symmetries. In the absence of a homogeneous Ioffe field we have found 16 discrete symmetries of both unitary and anti-unitary character in addition to the conserved quantity $\Lambda_z = L_z - S_z$. A deeper investigation

of the underlying symmetry group revealed a two-fold degeneracy of any energy level. As soon as a Ioffe field is applied only 8 discrete symmetries remain but Λ_z remains conserved. Due to the altered symmetry group the degeneracies are lifted.

We have calculated the resonance energies for several values of the parameter γ and made a comparison to the values obtained by Hinds and Eberlein in ref. [44]. For $\gamma = 0$ (vanishing Ioffe field) the resonance energies and decay widths form a regular pattern in the $E - \Gamma$ plane. An increase of the Ioffe field strength leads to a distorted distribution and the decay widths in general become smaller. Thus the stability of the resonance states increases with growing value of γ . An analysis of the ground state resonance for several γ values has indicated an exponential increase of lifetimes which is within agreement to results obtained by other authors [103]. Furthermore we could show an exponentially increasing lifetime with increasing modulus of the m quantum number. Apparently, with growing $|m|$ the wave functions become localized farther away from the center of the guide where transitions to continuum states take place.

We have illuminated the special class of quasi-bound states which can be approximately described by a scalar radial Schrödinger equation. Its approximate eigenenergies agree very well with the resonance energies yielded by the complex scaling calculation and become exact in the limit of high m quantum numbers. But even for low angular momenta an astonishingly good agreement could be observed for spin $\frac{1}{2}$ particles. For $\gamma = 0$ (without Ioffe field) this is due to the fact that m is half-integer valued which leads to a nonvanishing angular momentum barrier. This prevents the particle from entering the center of the guide. However, the coupling matrix element to the unbound states does only acquire significant values for $\rho \rightarrow 0$ which means the corresponding transitions are strongly inhibited. In the limit of a large Ioffe field strength we have calculated analytical expressions for the resonance energies of both spin $\frac{1}{2}$ and spin 1 particles. For $\gamma \neq 0$ the quasi-bound energies are compared to those obtained from the commonly used (crude) adiabatic approximations. We have shown the presented approach to be in general more accurate and to respect in particular the existing degeneracies.

The results have been applied to the experimentally important case of trapped alkali metal atoms. In particular we have focussed on ^6Li , ^7Li and ^{87}Rb . Here we have considered a magnetic guide generated by a current carrying wire together with a homogeneous bias-field. We have shown that for typical experimental parameter values the ground state energy corresponds to a temperature of a few micro-Kelvin. The lifetime of the resonance states can be extended up to minutes if the atoms are prepared in a high angular momentum state.

Most of the results presented in this chapter are published in refs. [60, 12].

Part III.

Electronic structure of atoms in high gradient magnetic fields

7. Introductory remarks

In part II of this thesis we have studied the dynamics of ground state atoms in magnetic quadrupole fields. Here the internal structure of the atoms was completely neglected. Consequently the atoms were treated as neutral point particles with a certain spin. For stronger fields this description is no more adequate as different internal atomic levels are being coupled.

In the 1980's and the beginning of the 1990's great effort has been put into the investigation of the electronic structure of atoms being exposed to homogeneous magnetic fields of arbitrary strength. This results could be successfully applied to understand the radiation spectra of strongly magnetized white dwarfs. Moreover, the foundations for a deeper understanding of quantum chaos were laid. In contrast to this there exist virtually no investigations on the electronic structure and properties of atoms in inhomogeneous or trapping magnetic field configurations. There was simply no need for such investigations as all such trapping fields could be considered homogeneous over the size of an atom. Nowadays so-called atom chip experiments (see section 2.4) allow for the generation of high gradient magnetic fields which exhibit significant field strength variations over micro-meter length scales. With the surface-mounted microscopic current-carrying structures gradients up to $10^6 \frac{T}{m}$ can be achieved. Within such traps the electronic structure of strongly confined atoms is expected to be significantly altered by the spatially varying field.

This part of the thesis is dedicated to the analysis of the internal structure of electronically excited atoms - in particular Rydberg atoms - which are exposed to magnetic quadrupole fields. Here we will go beyond the point-particle approximation in the sense that we will not only account for the coupling of the magnetic moment to the field but also for the charge-field coupling of the atomic constituents. The major number of today's experiments on ultra cold atoms uses alkali atoms since their level structure allows for the application of efficient cooling methods [75]. Therefore we focus on atoms with a single active electron, only. We assume the motion of the outermost (valence) electron to take place in a Coulomb potential of a single positive point charge, i.e. we assume the nuclear charge to be entirely screened by the inner electron shells. For sufficient highly excited states this should provide a reasonable (approximate) description. We do not account for interactions arising from the non-Coulombic character of the core potential or relativistic effects such as spin-orbit coupling. Furthermore we neglect the coupling of the nuclear and electronic spin, i.e. the hyperfine interaction. Since the latter two interactions drop off as r^{-3} their treatment in terms of perturbation theory should be appropriate. The inclusion of the non-Coulombic nature of the core potential could be done via quantum defect theory and/or core pseudo-potentials which are not considered here.

The presence of an external magnetic field prevents the decoupling of electronic and center of mass (c.m.) motion of the atom. This holds in particular for the case of a homogeneous magnetic field [53, 5, 51, 91] and has also to be expected for an inhomogeneous field. However, c.m. motional effects on the electronic structure become only significant in certain parameter and/or energetic regimes [87, 92, 25]. We take here advantage of the heavy atomic mass compared to the electron mass ($m_A \gg m_e$). In addition we exploit the fact that we are dealing with ultra cold atoms whose c.m. motion takes place on much larger time scales than the electron dynamics, even for highly excited electronic states. In a first approach we consider the atomic core (nucleus) to be fixed in space at the trap center which coincides with the origin of the coordinate system. In this

approximation the Hamiltonian which describes the electronic motion becomes

$$H_C = \frac{1}{2m_e} [\mathbf{p} + e\mathbf{A}(\mathbf{r})]^2 - \frac{e^2}{4\pi\epsilon_0|\mathbf{r}|} + \frac{g_s\mu_B}{\hbar}\mathbf{S} \cdot \mathbf{B}(\mathbf{r}). \quad (7.1)$$

The magnetic field is introduced via the minimal coupling including the vector potential $\mathbf{A}(\mathbf{r})$ thereby providing the kinetic energy in the presence of the field. The third term accounts for the interaction between the spin of the electron and the external field thereby coupling the real-space and spin-space dynamics.

8. Electronic structure of atoms in a three-dimensional quadrupole field

In this chapter we investigate the electronic structure of a Rydberg atom that is exposed to a three-dimensional magnetic quadrupole field in the fixed-nucleus approximation. Thereby we proceed as follows: In section 8.1 we present a Hamiltonian which describes the motion of the outermost (valence-) electron of an alkali atom exposed to the quadrupole field. Here we consider both the interaction of the spatial as well as spin degrees of freedom with the external field. Section 8.2 contains a discussion of the remarkable spin-spatial symmetries of the Hamiltonian. This includes unitary as well as antiunitary symmetries and the related constants of motion. Moreover we discuss the feature of a two-fold degeneracy of each energy level, an effect which is exclusively due to the unique symmetries of the system. In section 8.3 we proceed by outlining our computational approach. Sections 8.4 to 8.8 are dedicated to the discussion of the results obtained by our numerical investigations. We analyze spectral and other properties for low-lying and highly excited states both for weak and strong gradients. Furthermore we present a detailed analysis of the so-called ellipsoidal states which occur in the weak gradient regime. Apart from their exceptional spatial appearance they possess an uncommon angular momentum decomposition and are spatially extremely compact which makes them almost insensitive to the external field. The spin expectation values and in particular the spatial distribution of the spin polarization of excited states are studied and analyzed in detail. Selection rules for electromagnetic transitions as well as their transition strengths and wavelengths are provided. Whenever appropriate a comparison with the case of a homogeneous magnetic field is performed. Finally we investigate in detail the peculiar property of magnetic field-induced permanent electric dipole moments. Section 8.9 contains a summary and an outlook.

8.1. The Hamiltonian

Inserting the two-dimensional quadrupole field (2.1) and its vector potential (2.2) into the Hamiltonian (7.1) yields

$$H_C = -\frac{1}{2}\mathbf{p}^2 - \frac{1}{\sqrt{x^2 + y^2 + z^2}} - bzL_z + \frac{b^2}{2}z^2(x^2 + y^2) + \frac{b}{2}(\sigma_x x + \sigma_y y - 2\sigma_z z). \quad (8.1)$$

Here we have adopted atomic units (see appendix B) together with $g_s = 2$. L_z is the z component of the electronic orbital angular momentum operator, and σ_x , σ_y , σ_z are the Pauli spin matrices ($\mathbf{S} = \frac{1}{2}\boldsymbol{\sigma}$). The third and fourth term of H_C originate from the charge coupling to the external field. The paramagnetic ($\propto b$) or Zeeman term depends - in contrast to the situation in a homogeneous field - not solely on L_z but also linearly on the z -coordinate. The diamagnetic term ($\propto b^2$) represents a quartic oscillator coupling term between the cylindrical coordinates $\rho = \sqrt{x^2 + y^2}$ and z . In a homogeneous field this diamagnetic interaction consists of two pure harmonic oscillators one in x the other in y direction, which results in a confinement perpendicular to the magnetic field [98]. The final term of H_C originates from the coupling of the magnetic moment of the spin of the valence electron to the magnetic field. It depends linearly on the gradient and prevents the factorization of the motions in the spin and spatial degrees of freedom. Thus the corresponding Schrödinger equation is rendered into a spinor equation. In the case of a homogeneous field the spin dynamics can be decoupled from the spatial motion which leads to a scalar Schrödinger equation.

Finally we remark that the Hamiltonian (8.1) possesses a useful scaling property. Performing a canonical scaling transformation $\bar{x}_i = b^{\frac{1}{3}}x_i$ and $\bar{p}_i = b^{-\frac{1}{3}}p_i$ (see also sections 5.1 and 6.1) it becomes

$$b^{-\frac{2}{3}}\bar{H}_C = -\frac{1}{2}\bar{\mathbf{p}}^2 - \frac{\bar{Z}}{\sqrt{\bar{x}^2 + \bar{y}^2 + \bar{z}^2}} - \bar{z}L_z + \frac{1}{2}\bar{z}^2(\bar{x}^2 + \bar{y}^2) + \frac{1}{2}(\sigma_x\bar{x} + \sigma_y\bar{y} - 2\sigma_z\bar{z}) \quad (8.2)$$

with $\bar{Z} = b^{-\frac{1}{3}}$. The parametric dependence on the field gradient is now exclusively included in the Coulomb term. The Hamiltonian therefore does not depend on the field gradient and the nuclear charge number separately. The scaled Hamiltonian describes the motion of an electron in the Coulomb-field of a charge \bar{Z} and a magnetic field with gradient 1. If $b \rightarrow \infty$ the Coulomb term vanishes since $\bar{Z} \rightarrow 0$. In this limit the energy level spacing is expected to scale proportional to $b^{\frac{2}{3}}$.

8.2. Symmetries and conserved quantities

We now perform an analysis of the symmetry properties of the Hamiltonian (8.1) where we discuss the unitary as well as the anti-unitary symmetries and conserved quantities. We will further show how the interplay of the symmetries gives rise to a two-fold degeneracy of any energy level.

For the following investigations it is appropriate to express the Hamiltonian (8.1) in spherical coordinates. It then reads

$$H_S = -\frac{1}{2}\mathbf{p}^2 - \frac{1}{r} + \frac{b^2}{2}r^4 \cos^2\theta \sin^2\theta + \frac{b}{2}r \sin\theta \mathcal{K} - br \cos\theta (L_z + \sigma_z) \quad (8.3)$$

with \mathcal{K} being the matrix

$$\mathcal{K} = \begin{pmatrix} 0 & e^{-i\phi} \\ e^{i\phi} & 0 \end{pmatrix}. \quad (8.4)$$

The rotational invariance of the quadrupole field results in the conservation of the z -component of the total angular momentum ($J_z = L_z + S_z$), i.e. we find $[H_S, J_z] = 0$. Moreover there is a discrete symmetry represented by the unitary operator $P_y\sigma_x P_z$, i.e. $[H_S, P_y\sigma_x P_z] = 0$. Here P_z is the z -parity operator $P_z : z \rightarrow -z$ and P_y the y -parity operator being defined accordingly. Additionally the Hamiltonian possesses two generalized anti-unitary time reversal symmetries namely $T\sigma_x P_z$ and TP_y . Both of them involve the conventional time reversal operator T ($T^2 = 1$) which in the spatial representation, becomes the operation of complex conjugation. By connecting the two anti-unitary operators $T\sigma_x P_z$ and TP_y one receives the unitary operation $P_y\sigma_x P_z$. The operators $T\sigma_x P_z$, TP_y and $P_y\sigma_x P_z$ form an invariant Abelian subgroup. Together with J_z they are subjected to the following (anti-)commutation rules:

$$[J_z, TP_y] = \{J_z, T\sigma_x P_z\} = \{J_z, P_y\sigma_x P_z\} = 0 \quad (8.5)$$

$$[TP_y, T\sigma_x P_z] = [TP_y, P_y\sigma_x P_z] = [P_y\sigma_x P_z, T\sigma_x P_z] = 0 \quad (8.6)$$

Symmetries involving operations that act on both coordinate and spin space form a non-Abelian symmetry group being isomorphic to $C_\infty \otimes C_s$. The conserved quantities J_z and $P_y\sigma_x P_z$ do not commute. Thus one can introduce two sets of eigenfunctions which are classified according to their respective symmetries. The eigenstates of J_z shall be denoted by $|E, m\rangle$ whereas $P_y\sigma_x P_z$ eigenstates have the symbol $|E, \Pi\rangle$ with $\Pi = \pm 1$. Starting from the state $|E, m\rangle$ an eigenstate of $P_y\sigma_x P_z$ can be constructed according to

$$|E, \Pi\rangle = \frac{1}{\sqrt{2}} [|E, m\rangle + \Pi P_y\sigma_x P_z |E, m\rangle]. \quad (8.7)$$

We now demonstrate how the interplay of the above symmetries gives rise to the occurrence of degeneracies in the system: Lets consider a state $|E, m\rangle$ which is an eigenstate of the Hamiltonian

(8.3) with the energy E and of J_z with the half-integer quantum number m . Since $P_y\sigma_xP_z$ commutes with H_S the state $P_y\sigma_xP_z |E, m\rangle$ is also an energy eigenstate with the energy E . If J_z acts on this state one obtains

$$J_z P_y\sigma_xP_z |E, m\rangle = -P_y\sigma_xP_z J_z |E, m\rangle = -m P_y\sigma_xP_z |E, m\rangle.$$

Thus the state $P_y\sigma_xP_z |E, m\rangle$ can be identified by $|E, -m\rangle$. Apparently the states with the eigenvalues m and $-m$ are degenerate. This two-fold degeneracy of each energy level is a remarkable feature since it occurs even if an external magnetic field is present. A similar property known as Kramer's degeneracy is observed for spin $\frac{1}{2}$ systems in the absence of external fields [41].

For an atom in a homogeneous magnetic field oriented along the z -axis the operators L_z , P_z as well as parity P and $T\sigma_zP_y$ form the corresponding set of spatial and time reversal symmetries. They constitute an Abelian symmetry group implying that there are no energy level degeneracies in the homogeneous field.

In concluding this section we have to emphasize that most of the above considerations hold not only for the case of a fixed nucleus in the trap center but also for the full two-body problem. If the nuclear and the electronic motion are both considered the conservation of TP_y , $P_y\sigma_xP_z$ and J_z holds equally if the corresponding quantities are extended to act on both particles (see also part IV of this thesis).

8.3. Numerical treatment

In order to solve the eigenvalue problem of the Hamiltonian (8.1) we employ the linear variational principle. The eigenfunctions of the Schrödinger equation are expanded in a set of spinor orbitals. The calculation of the corresponding expansion coefficients results in a large-scale algebraic eigenvalue equation which is then solved by employing a Krylov space method (for a detailed explanation see chapter 3).

The states $|n, l, m_s = \uparrow, \downarrow\rangle_m$ of the basis set we apply for given m adopts the following form for the upper and lower spinor component, respectively:

$$|n, l, \uparrow\rangle_m = R_n^{(\zeta, k)}(r) Y_l^{m-\frac{1}{2}}(\theta, \phi) |\uparrow\rangle \quad , \quad |n, l, \downarrow\rangle_m = R_{\tilde{n}}^{(\zeta, k)}(r) Y_{\tilde{l}}^{m+\frac{1}{2}}(\theta, \phi) |\downarrow\rangle \quad (8.8)$$

Here $Y_l^m(\theta, \phi)$ denote the spherical harmonics. For fixed m the functions $|n, l, m_s\rangle_m$ are constructed such that the eigenstates of the Schrödinger equation are a priori eigenstates of the J_z operator. The radial part of the orbitals used for the expansion reads

$$R_n^{(\zeta, k)}(r) = \sqrt{\frac{n!}{(n+2k)!}} e^{-\frac{\zeta r}{2}} (\zeta r)^k L_n^{2k}(\zeta r) \quad (8.9)$$

with $L_n^{2k}(r)$ being the Laguerre polynomials. By correctly tuning the parameters k and ζ an optimal convergence behavior in different regions of the spectrum can be gained. The parameter ζ possesses the dimension of an inverse length. It has to be adapted such that $1/\zeta$ corresponds to the typical length scale of the desired wave functions. For given k and ζ the functions $R_n^{(\zeta, k)}(r)$ form a complete set of functions in r -space. They are nonorthogonal which results in an overlap-matrix different from unity and consequently in a generalized eigenvalues problem. The basis set (8.8) is complete in r -, θ - and spin space. Similar basis sets have been employed previously by several other authors [21, 22, 110].

According to section 3.1 an eigenstate $|E, m\rangle$ of the stationary Schrödinger equation can now be expanded in terms of the basis-functions (8.8)

$$|E, m\rangle = \sum_{n=0, l=|m-\frac{1}{2}|}^{n < N, l < L} a_{n, l} |n, l, \uparrow\rangle_m + \sum_{\tilde{n}=0, \tilde{l}=|m+\frac{1}{2}|}^{\tilde{n} < \tilde{N}, \tilde{l} < \tilde{L}} b_{\tilde{n}, \tilde{l}} |n, l, \downarrow\rangle_m \quad (8.10)$$

leading to the generalized spinor eigenvalue problem $\mathcal{H}\mathbf{c} = E\mathcal{S}\mathbf{c}$, where \mathcal{H} and \mathcal{S} are the corresponding matrix representation of the Hamiltonian (8.3) and the overlap matrix, respectively:

$$\mathcal{H} = \langle n, l, m_s | H | n', l', m'_s \rangle_m \quad \mathcal{S} = \langle n, l, m_s | n', l', m'_s \rangle_m \quad (8.11)$$

The vector \mathbf{c} contains the expansion coefficients of (8.10):

$$\mathbf{c} = \begin{pmatrix} a_{n,l} \\ b_{\tilde{n},\tilde{l}} \end{pmatrix} \quad (8.12)$$

The basis set (8.8) allows to analytically calculate the matrix elements of \mathcal{H} and \mathcal{S} . In practise this is done by exploiting recurrence identities for the spherical harmonics and the Laguerre polynomials [1], respectively. The expressions for the matrix elements of the individual parts of the Hamiltonian can be found in [55]. The matrices \mathcal{H} and \mathcal{S} possess a particular sparse appearance, e.g. \mathcal{S} is penta-diagonal which has enabled us to go to large basis set dimensions. In our calculations we have employed basis sets with dimensions up to 17000. We thereby were able to converge several thousand eigenstates and eigenvalues up to energies corresponding to a hydrogen principal quantum number of $n \approx 40$.

8.4. The energy spectrum

We will now be discussing the appearance of the energy spectrum for different field gradients b . Thereby we will see that with increasing gradient the energy spectrum undergoes severe changes. Essentially one can distinguish three regimes which are the weak, the intermediate and the strong gradient regime. Of course, these regimes are not solely determined by the absolute value of the gradient b but also by the degree of excitation of the atom. Thus it is natural to define the weak/strong regime to be the regime, for which the magnetic compared to the Coulomb interaction is weak/strong [33]. To distinguish between the different regimes it is probably the best to consult equation 8.2 that contains the scaled charge \bar{Z} . For $\bar{Z} \gg 1$ the Coulomb force dominates and becomes equal to the strength of the magnetic interaction if \bar{Z} reaches unity. For weak gradients the behavior of the energy levels is dominated by the orbital and spin Zeeman terms both of which depend linearly on the gradient. We find a linear splitting of the degenerate n -multiplets with increasing b . Adjacent n -multiplets do not overlap which makes n an almost good quantum number. In figure 8.1a we show the linear splitting of the $n = 20$ multiplet for the $m = \frac{1}{2}$ subspace.

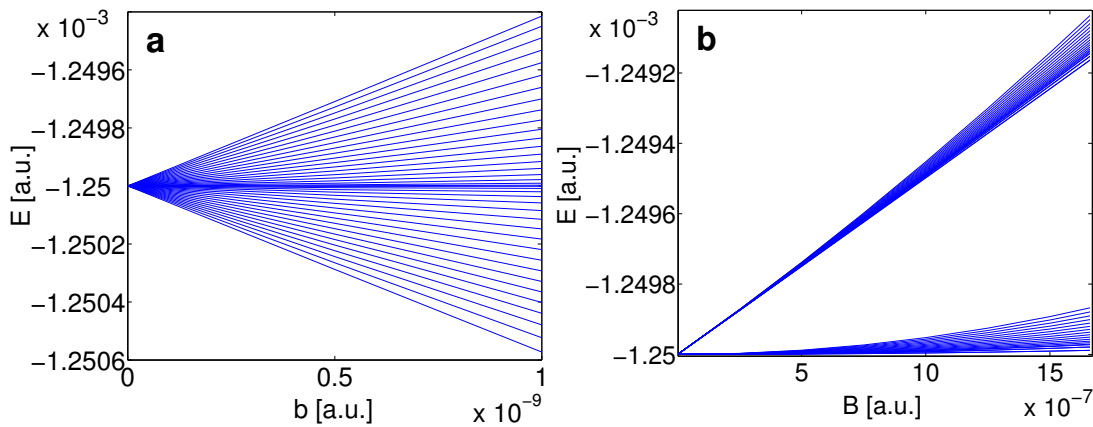


Figure 8.1.: a: Energy level splitting of the $m = \frac{1}{2}$ -states of the $n = 20$ -multiplet in the quadrupole field. b: Splitting of the same energies in a homogeneous field.

As the gradient increases the previously degenerate states split up symmetrically around the zero

field energy. Inside each n -multiplet there is a single state whose energy is barely shifted as the gradient increases. These (ellipsoidal) states exhibit unique features being discussed in section 8.5.

But how does this spectrum compare to the one encountered in a homogeneous field? In contrast to the symmetric splitting, we here find a splitting into two branches (figure 8.1b) belonging to two different orbital angular momentum and spin projections (for fixed m). In a quadrupole field L_z and S_z are not separately conserved and to map the energy levels to a certain spin orientation is impossible.

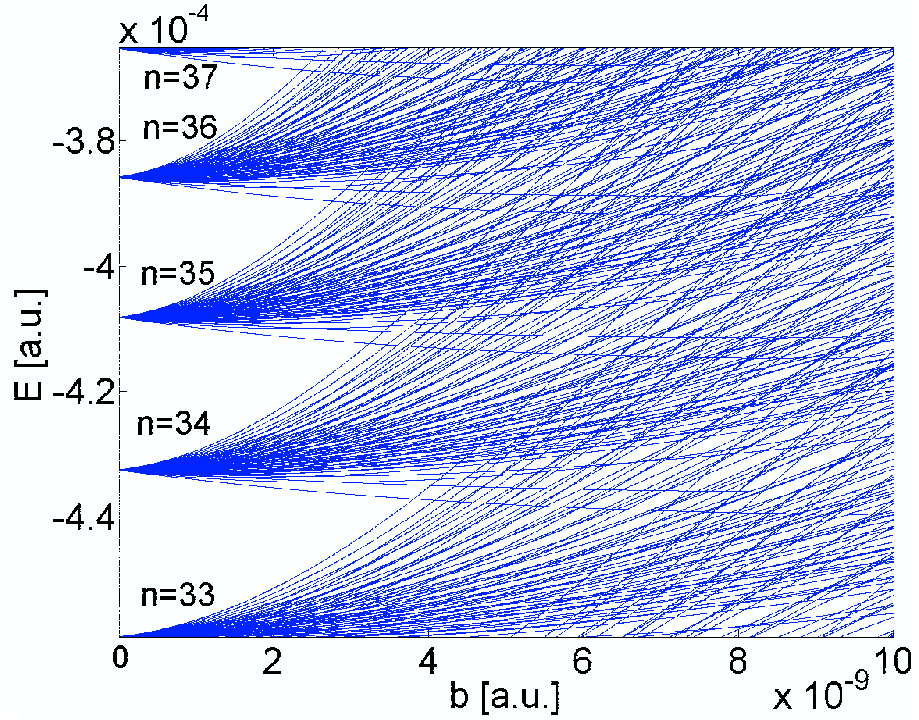


Figure 8.2.: Energy spectrum of the multiplets $n = 33 - 37$ for the states with $m = \pm\frac{1}{2}$. For low gradients the energy levels split almost linearly followed by a transition region where the diamagnetic term becomes increasingly more important. For high gradients different n -multiplets overlap and no symmetries, i.e. approximate quantum numbers, are left.

With increasing gradient the diamagnetic term with its quadratic dependence on b (or B in the homogeneous field) gains importance resulting in a nonlinear behavior of the energy curves. One can show the intra n -manifold mixing regime where different n -multiplets are still energetically well separated but different angular momentum states (l -states) mix to scale as $b \propto n^{-6}$. At even higher gradients we observe mixing of different n -multiplets which leads to the global emergence of avoided crossings. The onset of this inter n -manifold mixing scales according to $b \propto n^{-\frac{11}{2}}$ whereas in the homogeneous field the corresponding scaling is $B \propto n^{-\frac{7}{2}}$. In figure 8.2 we present the energy spectrum in the range of $n = 33$ to $n = 37$ with $m = \pm\frac{1}{2}$ over the gradient interval $0 \leq b \leq 10^{-8}$. For such a degree of excitation the intra n -manifold mixing sets in at $b \approx 5 \cdot 10^{-10}$. Therefore the linear splitting due to the Zeeman-term as shown in figure 8.1 is hardly visible. For $b = 8 \cdot 10^{-9}$ e.g. we are deep inside the inter- n -mixing regime.

8.5. Ellipsoidal states

This section is dedicated to the analysis of a particular class of states - the ellipsoidal states. These states occur exclusively in the $m = \pm\frac{1}{2}$ subspaces and only for gradients where a linear level splitting is observed. Compared to other states inside the same n -multiplet ellipsoidal states exhibit

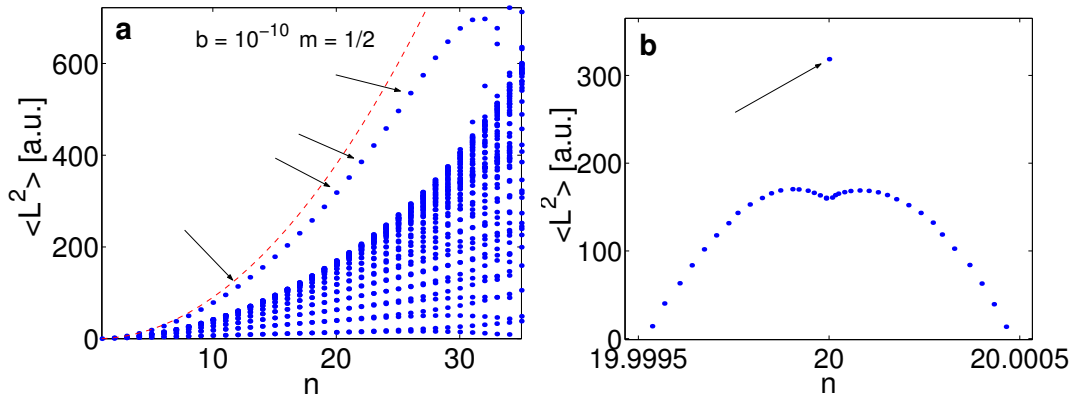


Figure 8.3.: **a:** Expectation value of the squared angular momentum operator L^2 for electronic states obeying $m = \frac{1}{2}$. The maximum achievable value of $\langle L^2 \rangle$ is indicated by the dashed line. The ellipsoidal states (some of them are marked by an arrow) are clearly separated by a gap from the remaining states of a given n -multiplet. **b:** Zoomed view of the $n = 20$ -multiplet. States which suffer a large energy shift exhibit low angular momentum. The angular momentum gradually increases as the corresponding states become less affected by the field. The $\langle L^2 \rangle$ values form a hill-like structure with a dip on its top. The ellipsoidal state is represented by the isolated dot above the dip indicated by an arrow. Its energy is almost the same as in the zero gradient limit.

an extraordinary large mean orbital angular momentum. Figure 8.3a shows the $\langle L^2 \rangle$ expectation value for states in the $m = \frac{1}{2}$ subspace up to a principal quantum number $n = 35$. The magnetic field gradient is $b = 10^{-10}$. The expectation values of states belonging to the same n -multiplet are arranged in vertical lines. This originates from their approximate degeneracy. For $n > 30$ the intra- n -mixing regime where no ellipsoidal states occur is entered. Up to $n = 30$ we find the ellipsoidal states to be located on top of each vertical stack of points clearly separated from the other states by a gap (see also the zoomed view of the $n = 20$ -multiplet which is shown in figure 8.3b). The maximum allowed value of $\langle L^2 \rangle$ for fixed n is given by $\langle L^2 \rangle_{\max} = n(n-1)$ which is indicated by the dashed line. Since $\langle L^2 \rangle$ of the ellipsoidal states are located nearby the dashed line their expansion in terms of angular momentum eigenstates has to contain mainly contributions with large l . We further analyze the ellipsoidal states by calculating their expansion coefficients in

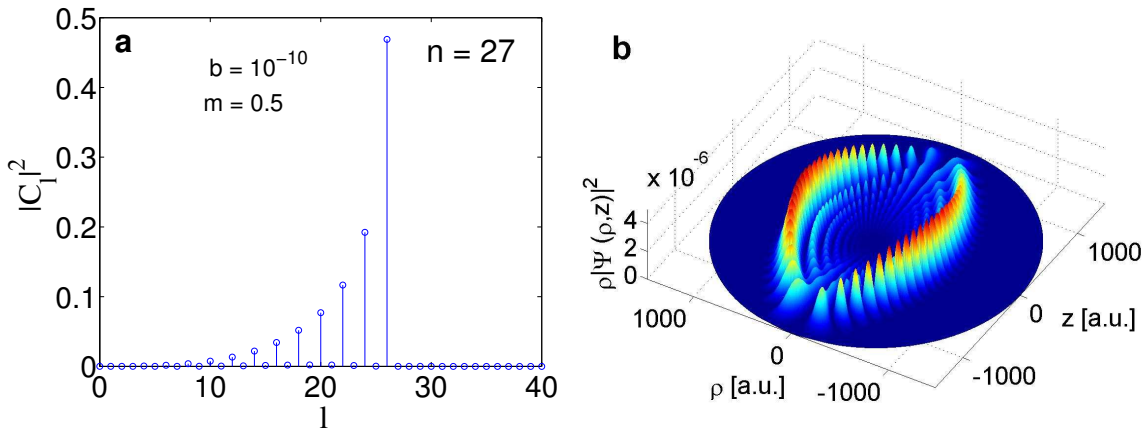


Figure 8.4.: **a:** Expansions coefficients of the $n = 27$ ellipsoidal state in terms of angular momentum eigenstates. Only the even angular momentum states contribute. The contribution of the l states grows exponentially with l . **b:** Spatial distribution of the probability density of the same ellipsoidal state.

terms of angular momentum eigenstates $|l\rangle$:

$$\langle E, m | E, m \rangle = \sum_l \langle E, m | l \rangle \langle l | E, m \rangle = \sum_l |C_l|^2 = 1 \quad (8.13)$$

Figure 8.4a shows the distribution of the coefficients $|C_l|^2$ for the ellipsoidal state of the $n = 27$ multiplet. The contributions of the angular momentum states grow exponentially with increasing l . The maximum angular momentum state contributing possesses the quantum number $l = n - 1 = 26$ which is the highest allowed angular momentum inside a given n subspace. Interestingly one finds the suppression of expansion coefficients $|C_l|^2$ with odd l -values. This turns out to be a generic feature for this class of states. Ellipsoidal states belonging to even n -multiplets contain almost only odd angular momentum contributions and vice versa.

In figure 8.4b we present the spatial probability density $\rho |\Psi(\rho, z)|^2$ (integrated over the azimuthal angle ϕ) of the $n = 27$ ellipsoidal state. The ρ -axis has been extended to the negative half plane. One observes a number of peaks being arranged in concentric ellipses. In order to gain the 3D-shape of the density it has to be rotated around the z -axis. The resulting structure would look like an ellipsoid which gives rise to the designation ellipsoidal state. Although they exhibit high angular momenta ellipsoidal states possess almost no z -component of the angular momentum and are almost completely spin polarized, i.e. $\langle S_z \rangle = \pm \frac{1}{2}$. Moreover, we found them to be relatively compact, i.e. they possess a small spatial extent compared to other states in the same n -multiplet.

At the same time their radial uncertainty $\Delta r = \sqrt{\langle r^2 \rangle - \langle r \rangle^2}$ is small. Hence their wave function is well localized outside the atomic core, i.e. the nucleus or the inner electron shells. For the ellipsoidal state presented in figure 8.4 we find an almost vanishing probability density for $r < 150$. Thus, the properties of such states should not depend on the actual atomic species under consideration. Due to their compact shape they are energetically almost unaffected by the external field i.e. they experience almost no energy shift (see also figure 8.3b). Finally we remark that we did not find similar states to be formed inside an external homogeneous field. Here the $\langle L^2 \rangle$ distribution does not exhibit isolated states. One rather encounters a smooth distribution of angular momenta within a given n -manifold.

8.6. Properties of the electronic spin

8.6.1. Expectation value

For an atom exposed to a homogeneous field the projection of the spin operator onto the field direction is a conserved quantity. Thus, the eigenfunction can be chosen to be eigenfunctions of S_z simultaneously. This means $\langle S_z \rangle$ can only assume either of the two values $\pm \frac{1}{2}$. For atoms in a quadrupole field S_z is not conserved and its expectation value calculated in the J_z eigenstates which can be decomposed according to

$$|E, m\rangle = |u\rangle \left| m_s = \frac{1}{2} \right\rangle + |d\rangle \left| m_s = -\frac{1}{2} \right\rangle \quad (8.14)$$

reads

$$\langle S_z \rangle_{J_z} = \frac{1}{2} [\langle u | u \rangle - \langle d | d \rangle]. \quad (8.15)$$

Figure 8.5 shows the distribution of $\langle S_z \rangle_{J_z}$ for electronic states of the $m = \frac{1}{2}$ subspace as a function of the principal quantum number n . Since S_z is not conserved the values of $\langle S_z \rangle_{J_z}$ are allowed to occupy the entire interval $[-\frac{1}{2}, \frac{1}{2}]$. In figure 8.5a ($b = 10^{-10}$) we find for $n \leq 30$ an even distribution of the expectation values throughout the complete interval. Here the uppermost dots belong to the

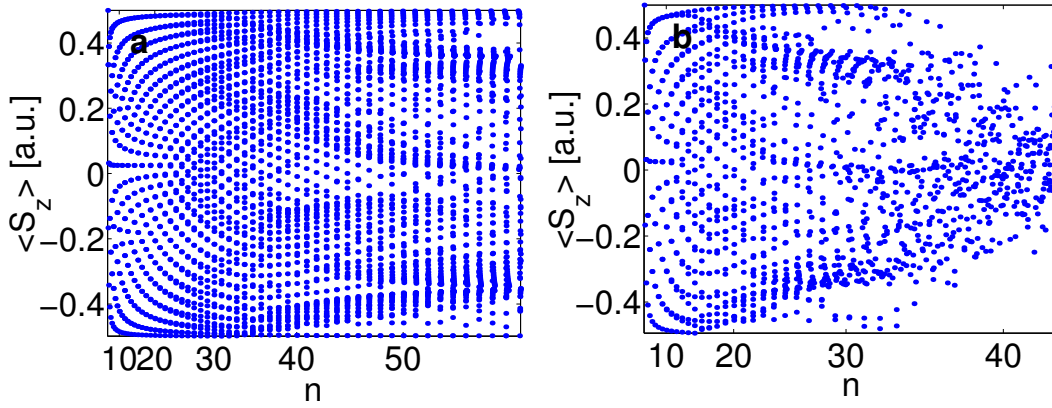


Figure 8.5.: Expectation values of the z -component of the electronic spin operator as a function of the quantum number n for different gradients (**a**: $b = 10^{-10}$, **b**: $b = 10^{-8}$).

ellipsoidal states which possess large mean orbital angular momentum and are almost completely spin polarized (see the previous section 8.5). The states corresponding to the smallest values of $\langle S_z \rangle_{J_z}$ are states that carry little mean orbital angular momentum. At the onset of intra- n -mixing the pattern becomes increasingly distorted. The expectation values agglomerate at -0.35 and 0.35 for $n \geq 50$. For low n the values of $\langle S_z \rangle_{J_z}$ form vertical lines which is a consequence of the approximate degeneracy of the energy levels. When reaching higher degrees of excitation these lines widen. For $b = 10^{-10}$ there is no significant inter- n -mixing up to $n = 60$. Thus, all lines in figure 8.5a are well separated. For larger gradients $b = 10^{-8}$ (figure 8.5b) the above-discussed properties are equally present for low-lying states. However, with increasing excitation energy the inter- n -mixing regime is entered at $n \approx 25$. Here the regular line structure is dissolved and an irregular distribution of $\langle S_z \rangle_{J_z}$ values emerges. The overall distribution narrows, e.g. for $n = 40$ the occupied interval is approximately $[-0.3, 0.3]$.

For $P_y \sigma_x P_z$ -eigenstates we find due to $\{S_z, P_y \sigma_x P_z\} = 0$ a vanishing S_z expectation value: $\langle S_z \rangle_{P_y \sigma_x P_z}^\pm = 0$. Apparently there is no preferred direction for the electronic spin in a state obeying the $P_y \sigma_x P_z$ symmetry.

8.6.2. Spin polarization

As already pointed out the nontrivial coupling of the spin to the spatial degrees of freedom prevents the factorization of the wave function into a spatial and a spin part. Hence, the orientation of the electronic spin is expected to depend on the spatial position of the electron. To study this in more detail we introduce the S_z -polarization $W_S(\mathbf{r})$. For a J_z -eigenstate $|E, m\rangle$ it reads

$$W_S(\mathbf{r}) = \frac{\langle E, m | \vec{r} \rangle S_z \langle \vec{r} | E, m \rangle}{\langle E, m | \vec{r} \rangle \langle \vec{r} | E, m \rangle}. \quad (8.16)$$

In figure 8.6 we present the S_z -polarization of two electronic states. The first one (8.6a) has an effective principal quantum number of $n = 9$ and is located in the $m = \frac{1}{2}$ -subspace. The magnetic field gradient is $b = 10^{-9}$. We observe a complex pattern of domains exhibiting different spin orientation (red: spin up, blue: spin down). If the spin and the spatial part of the wave function factorized as it is the case in a homogeneous field we would encounter a spatially uniform distribution. For small displacements from the coordinate center we observe the domains to form a pattern similar to that of a chess board. With increasing distance from the coordinate center we encounter a transition region where the formation of stripes with different spin orientation sets in. The junctions where four spin domains meet each other coincide with the nodes of the spatial probability density. Our investigation revealed that both the Coulomb interaction and the

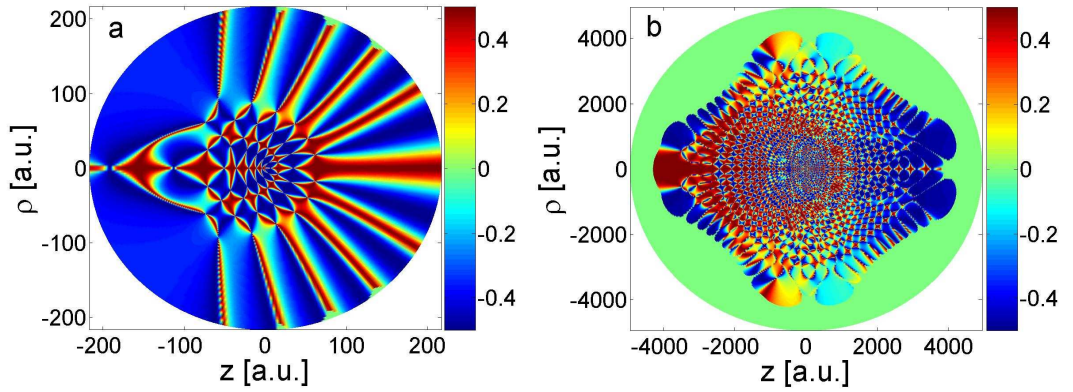


Figure 8.6.: **a:** S_z -polarization of an electronic state whose energy corresponds to an effective principal quantum number of $n = 9$. The state is located in the $m = \frac{1}{2}$ -subspace. The magnetic field gradient is $b = 10^{-9}$. **b:** S_z -polarization of a highly excited state. With an effective quantum number $n = 44.29$ it is located within the inter- n -mixing regime. The values for m and b are the same as in **a**.

spin-Zeeman term are responsible for the formation of the interwoven network of islands exhibiting different spin orientation. The additional presence of the orbital Zeeman and the diamagnetic term only results in a deformation of this network. In figure (8.6a) we show another S_z -polarization but for a much more highly excited state which has an effective principal quantum number of $n = 44.29$. This state is already affected by the inter- n -mixing. The pattern exhibits a more complex structure. This, however, is expected since the number of nodes exhibited by a wave function is determined by the degree of excitation of the corresponding state. Apparently, the distribution of the spin polarized islands for this state is not symmetric: For negative/positive z values a dominance of red/blue colored regions is evident. This feature can be understood by investigating a Hamiltonian that exclusively consists of the spin Zeeman term:

$$H_S = -\boldsymbol{\mu} \cdot \mathbf{B}(\mathbf{r}) = \frac{b}{2}r \begin{pmatrix} -2 \cos \theta & \sin \theta e^{-i\phi} \\ \sin \theta e^{i\phi} & 2 \cos \theta \end{pmatrix} \quad (8.17)$$

Here the complete dynamics takes place in spin space and the spatial coordinates (r, θ, ϕ) enter as parameters, only. The Hamiltonian (8.17) is diagonalized by the transformation $U_1 U_2$ where U_1 and U_2 are defined through equations (5.20) and (5.23), respectively. Its two solutions are

$$\begin{aligned} \Phi_-(r, \theta, \phi) &= U_2^\dagger U_1^\dagger |\uparrow\rangle \\ \Phi_+(r, \theta, \phi) &= U_2^\dagger U_1^\dagger |\downarrow\rangle \end{aligned} \quad (8.18)$$

with $|\uparrow\rangle$ and $|\downarrow\rangle$ being the eigenstates of the spin operator S_z . The corresponding eigenenergies are

$$E_\pm = \mp \frac{1}{2} b r \sqrt{1 + 3 \cos^2 \theta} = \mp |\boldsymbol{\mu}| |\mathbf{B}(\mathbf{r})|. \quad (8.19)$$

These energies correspond to those of a spin oriented parallel (E_-) or antiparallel (E_+) to the magnetic quadrupole field. Constructing the S_z -polarization $W_S^\pm(\mathbf{r})$ of the eigenstates (8.18) yields

$$W_S^\pm(\mathbf{r}) = \pm \frac{1}{2} \cos \beta = \mp \frac{z}{\sqrt{\rho^2 + z^2}} = \mp \frac{\cos \theta}{\sqrt{1 + 3 \cos^2 \theta}} \quad (8.20)$$

with $W_S^+(\mathbf{r})$ being shown in figure 8.7. Both, $W_S^+(\mathbf{r})$ and $W_S^-(\mathbf{r}) = -W_S^+(\mathbf{r})$ neither depend on the radial coordinate nor on the azimuthal angle ϕ . For negative values of z the z -component of the spin is oriented upwards/downwards whereas the opposite orientation is found for positive z values. Around the z -axis there is a transition region with $W_S^\pm(\mathbf{r})$ being close to zero.

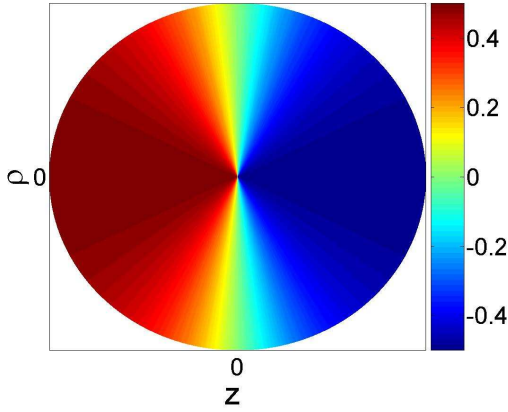


Figure 8.7.: S_z -polarization of the eigenstate $\Phi_+(r, \theta, \phi)$ of the Hamiltonian (8.17). The electronic spin either points antiparallel ($W_S^+(\mathbf{r})$) or parallel ($W_S^-(\mathbf{r}) = -W_S^+(\mathbf{r})$) to the local direction of the field.

This is precisely the behavior we have observed at large r for the S_z -polarization of the highly excited state depicted in figure 8.6b. Apparently in this particular state the electron spin prefers an antiparallel alignment with respect to the external field at large radii which corresponds to $W_S^+(\mathbf{r})$. This situation is to some extent reminiscent of the quasi-bound states which have been discussed in section 5.5. Here, far away from the trap center, the magnetic field interaction dominates the Hamiltonian and the projection of the particles spin on the local direction of the magnetic field is conserved.

8.7. Electric dipole transitions

Let us now investigate electromagnetic transitions between the electronic states in the framework of the dipole approximation. The amplitude for a transition between the initial state $|i\rangle$ and the final state $|f\rangle$ is then given by the squared modulus of the matrix element $\langle i|D|f\rangle$. In the length gauge D takes the forms

$$D_{\sigma^\pm} = \frac{1}{\sqrt{2}}(x \pm iy) = \frac{1}{\sqrt{2}}r \sin \theta e^{\pm i\phi} \quad (8.21)$$

$$D_\pi = z = r \cos \theta \quad (8.22)$$

for σ^\pm - and π -transitions, respectively. The symmetries of the J_z and $P_y\sigma_xP_z$ eigenstates result in certain selection rules:

The evaluation of the transition matrix element for π -transitions $\langle E', m' | r \cos \theta | E, m \rangle$ leads to the selection rule $m' - m = 0$. For σ^\pm -transitions the corresponding matrix element reads $\langle E', m' | r \sin \theta e^{\pm i\phi} | E, m \rangle$ which is only nonzero if $m' - m = \pm 1$. These selection rules are reminiscent of the situation that is encountered in a homogeneous or even in a field-free environment. The transition matrix element for π -transitions between $P_y\sigma_xP_z$ -eigenstates is $\langle E', \Pi' | r \cos \theta | E, \Pi \rangle$ leading to the selection rule $\Pi' \neq \Pi$, i.e. only transitions between states with opposite $P_y\sigma_xP_z$ symmetry are allowed. We were not able to derive a selection rule for the quantum number Π for σ^\pm -transitions between $P_y\sigma_xP_z$ -eigenstates. Our findings are summarized in table 8.1.

We have calculated the amplitudes for transitions from the ground state ($m = \frac{1}{2}$) to several excited states with $m = \frac{1}{2}$ (π -transitions (figure 8.8)) and $m = \frac{3}{2}$ (σ^- -transitions (figure 8.9)). For comparison we also present the transition amplitudes for an atom in a homogeneous magnetic field. The latter are indicated by red lines whereas transitions in the quadrupole field are represented as blue lines. A detailed discussion of electromagnetic transitions in the homogeneous field can be found in [87, 21, 22]. In order to provide a good comparison of the results we have chosen the gradient and the magnetic field strength such that we observe approximately equal splitting of the

transition type	$J_z - \text{states}$ $\Delta m = m' - m$	$P_y \sigma_x P_z - \text{states}$ $\Delta \Pi = \Pi' - \Pi$
π	0	± 2
σ^+	1	-
σ^-	-1	-

Table 8.1.: Selection rules for dipole transitions between J_z -eigenstates and between $P_y \sigma_x P_z$ -eigenstates.

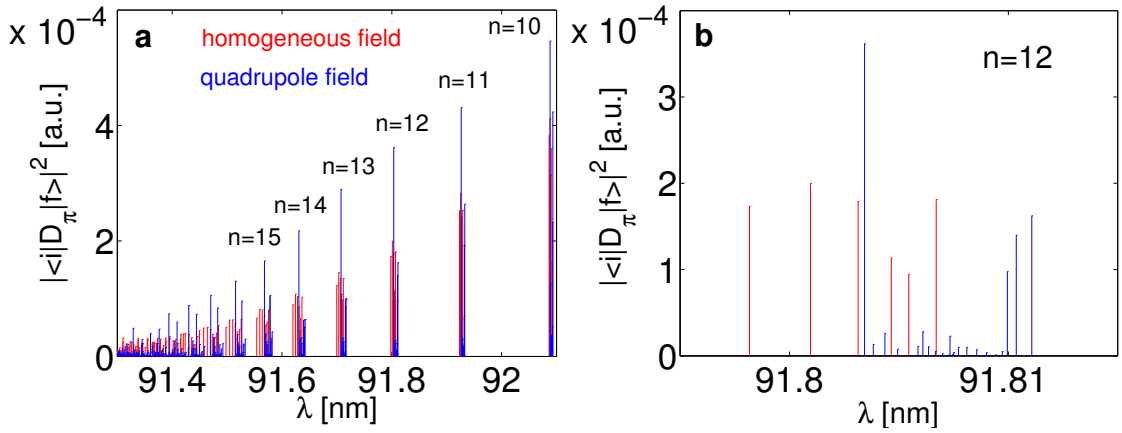


Figure 8.8.: Dipole strengths of $\Delta m = 0$ π -transitions from the ground state to excited levels. Blue lines denote transitions in the quadrupole field whereas transitions in the homogeneous field are indicated by red lines. **a:** The line possessing the largest wavelength belongs to the $n = 1 \rightarrow 10$ transition. **b:** Magnification the $n = 1 \rightarrow 12$ transitions.

n -multiplets with increasing energy. In the present case we have chosen $b = 10^{-7}$ and $B = 10^{-4}$. In figure 8.8a the dipole strengths for π -transitions starting with the $n = 10$ -line are depicted. Up to a certain wavelength (≈ 91.5 nm) neighboring lines are well separated. Transitions with smaller wavelengths involve levels already exhibiting severe inter n -manifold mixing effects, i.e. overlapping of neighboring groups of lines. In figure 8.8b we provide a higher resolution picture of the transitions to the $n = 12$ -manifold in the intra n -mixing regime. In both cases we find each main line to be accompanied by a series of sublines. In the quadrupole field apart from the main line at $\lambda \approx 91.803$ nm one observes four major sublines situated at the outer edge at approximately $\lambda = 91.81$ nm. In the homogeneous field we find a number of sublines being almost equal in height. We note that the subline possessing the maximum strength always belongs to a transition in the quadrupole field. Overall we find a lower number of lines to appear in the homogeneous field than in the quadrupole field. This is owed to additional symmetry properties such as the conservation of z -parity which in the homogeneous field give rise to further selection rules.

In figure 8.9 we present the transitions to states with $m = \frac{3}{2}$ beginning with the transition to the $n = 10$ multiplet. Again the change from the inter to the intra n -mixing regime is observed (figure 8.9a). We find the threshold wavelength at which the overlapping of adjacent groups of lines sets in to be $\lambda \approx 91.5$ nm. Compared to the homogeneous field the transitions in the quadrupole field are systematically shifted towards larger wavelengths. A magnified view of the lines for the $n = 1 \rightarrow 12$ transitions is shown in figure 8.9b. In the homogeneous field each transition to a fixed n -multiplet is dominated by a major line accompanied by a group of significantly weaker sublines. Unlike this we find many transitions of equal strength in the quadrupole field. This is just the opposite to the above-discussed π -transitions. Compared to the homogeneous field the total number of transitions in the quadrupole field is again much larger.

In figure 8.10a-c we present the dipole strengths of π -transitions inside the $m = \frac{1}{2}$ subspace for different values of the gradient b . For comparison the dipole strengths in a homogeneous field

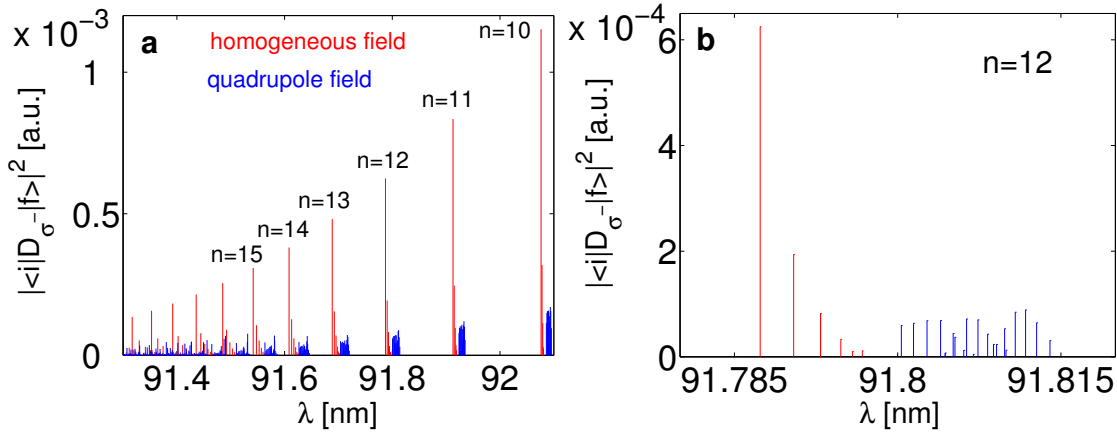


Figure 8.9.: Dipole strengths of $\Delta m = -1$ σ^- transitions (σ^- -transitions) from the ground state to excited levels. Blue lines denote transitions in the quadrupole field whereas transitions in the homogeneous field are indicated by red lines. **a:** The line possessing the smallest wavelength belongs to the $n = 1 \rightarrow 10$ transition. **b:** Magnification of the $n = 1 \rightarrow 12$ transition.

($B = 10^{-5}$) are given as well (figure 8.10d). Starting from large wavelengths one observes a gradual decrease of the dipole strengths as the transition wavelengths decrease. This behavior is also exhibited in the presence of a homogeneous field and also in the field free case. Going to smaller wavelengths a modulation of the dipole strengths (hump) is observed in the quadrupole field whereas no such feature appears in the presence of a homogeneous field. The height and the position of this hump are correlated with the magnitude of the gradient. With increasing gradient it becomes less pronounced and at the same time shifted towards higher wavelengths. Analyzing its position dependence on the gradient b we have found: $b \propto n_{\text{hump}}^{-6}$. This is reminiscent of the scaling law we have derived for the onset of the intra n -manifold mixing regime (see section 8.4). Thus the transition from the weak to the intermediate gradient regime is reflected in an overall spectroscopic signature.

8.8. Magnetic field induced electric dipoles

For an atom in a homogeneous field (and also in the field-free case) parity is a symmetry. Thus, electronic states are not expected to exhibit a permanent electric dipole moment. However, we now show this to be different in the presence of a quadrupole field. From the selection rules derived in the preceding section we deduce for the expectation value of D_{σ^\pm} in the J_z -eigenstates

$$\langle D_{\sigma^\pm} \rangle = \frac{1}{\sqrt{2}} \langle E, m | r \sin \theta e^{\pm i\phi} | E, m \rangle = 0. \quad (8.23)$$

However, the expectation value of D_π is in general nonzero. $\langle D_\pi \rangle$ is shown in figure 8.11 for the two gradients $b = 10^{-10}$ and $b = 10^{-8}$, respectively. Similar to the S_z expectation value we find the electric dipole moments which belong to the almost degenerate states of an n -multiplet to be arranged along vertical lines. Inside a given n -multiplet the dipole moments vary in between an upper and lower bound both of which linearly depend on n . States with a large electric dipole moment emerge from field-free states (with increasing b) that possess small values for the angular momentum and vice versa. The ellipsoidal states exhibit the smallest dipole moment within a given n -multiplet. For $b = 10^{-8}$ and $n > 35$ the distribution of the dipole moments becomes completely irregular. The remarkable occurrence of such state dependent permanent electric dipole moments being induced by the magnetic field is the consequence of an asymmetric charge density distribution induced by the symmetry properties of the quadrupole field. Figure 8.12a exemplarily shows the

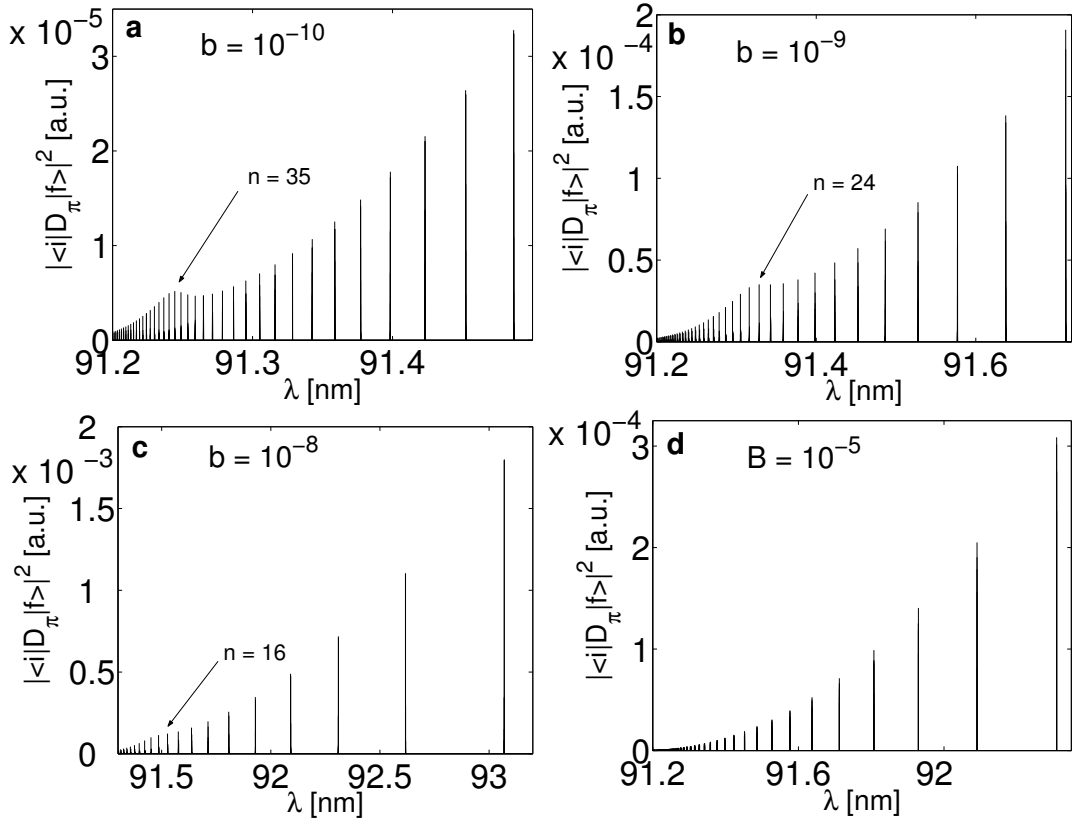


Figure 8.10.: Dipole strengths of π -transitions in the $m = \frac{1}{2}$ subspace for three different gradients b (**a**: $b = 10^{-10}$, **b**: $b = 10^{-9}$, **c**: $b = 10^{-8}$). For comparison the dipole strengths in a homogeneous field (**d**: $B = 10^{-5}$) are shown. At high wavelengths all plots show a gradual decrease of the dipole strength with decreasing transition wavelength. In contrast to the homogeneous field the dipole strengths of transitions in the quadrupole field are modulated when smaller wavelengths are reached. With increasing gradient this structure becomes less pronounced and is shifted towards larger wavelengths.

density distribution of an electronic state inside a quadrupole field. The electronic cloud is almost completely localized in the $z > 0$ half-space which results in a large dipole moment. In contrast to that one finds for states inside a homogeneous field a symmetric charge distribution (see figure 8.12b).

8.9. Summary

In this chapter we have presented a detailed study of the electronic structure of atoms being exposed to a magnetic quadrupole field. We did not take into account the atomic center of mass motion focussing solely on the internal electronic states. We have pursued a one-particle approach in order to describe the dynamics of the valence electron of an excited alkali atom. Here we have considered both the coupling of the electric charge and the magnetic moment (spin) to the field. A spinor-orbital based method to compute the eigenfunctions of the stationary Schrödinger equation has been applied. Utilizing a Sturmian basis we have studied several thousands of excited states over a wide range of gradients. The inhomogeneous character of the quadrupole field results in a coupling of the spatial and spin degrees of freedom. As a consequence of this unique coupling the system is invariant under a number of symmetry operations acting on both degrees of freedom. We have found unitary symmetries relying on the conservation of the total angular momentum J_z and the discrete operation $P_y \sigma_x P_z$. Furthermore we have identified the two anti-unitary generalized time

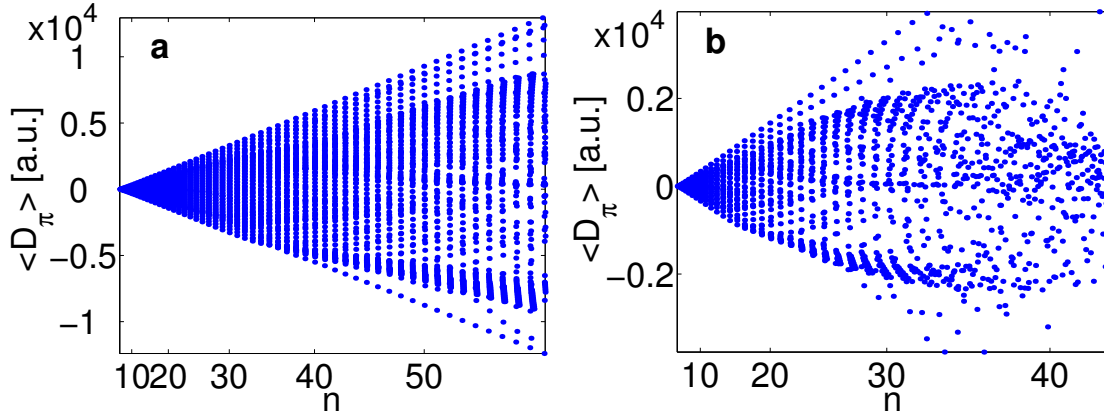


Figure 8.11.: Expectation value of the dipole operator D_π plotted versus the principle quantum number n for different gradients (a: $b = 10^{-10}$, b: $b = 10^{-8}$).

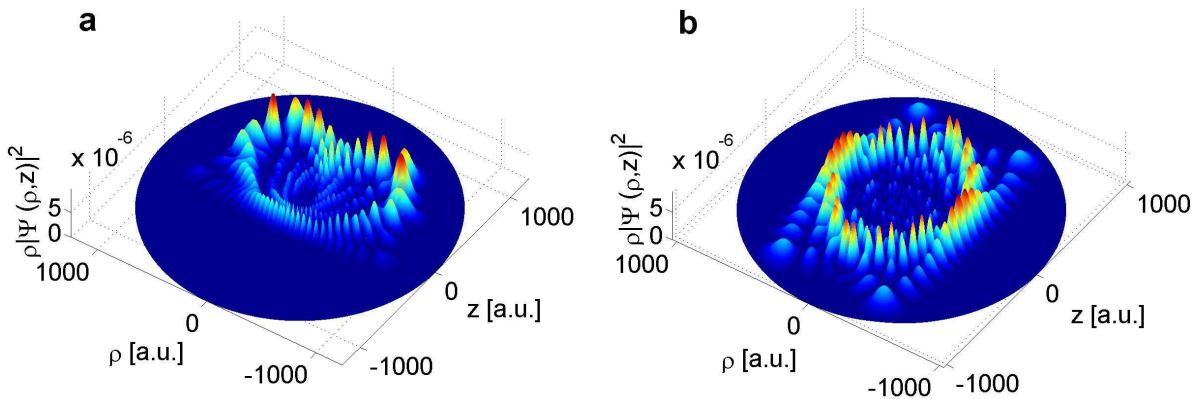


Figure 8.12.: a: Charge distribution of an electronic state in a quadrupole field ($b = 10^{-8}$). The state belongs to the $n = 22$ -multiplet in the $m = \frac{1}{2}$ subspace. The asymmetric charge distribution with respect to the $\rho = 0$ -plane gives rise to a permanent electric dipole moment. b: Charge distribution for an electronic state ($n \approx 22$, $m = \frac{1}{2}$) in a homogeneous field ($B = 10^{-6}$). The electron cloud is mirror symmetric with respect to both the $z = 0$ - and $\rho = 0$ -plane. Thus, no permanent electric dipole moment occurs.

reversal symmetries $T\sigma_x P_z$ and TP_y . We could show the two-fold degeneracy of any energy level which originates from the non-Abelian character of the symmetry group. In the absence of external fields such a degeneracy is well known to occur in spin $\frac{1}{2}$ systems (Kramer's degeneracy).

We have calculated energy spectra up to excitation energies corresponding to a principal quantum number $n \approx 40$. Moreover, an analysis of the distinct characteristics for the weak, intermediate as well as the strong gradient regime has been performed. For weak gradients a linear splitting of the energy levels is observed. For given m the sublevels of an n -multiplet split symmetrically around the zero field energy. In a homogeneous field, however, an asymmetric splitting into only two branches takes place. For larger gradients where adjacent n -manifolds are still separated intra n -manifold mixing is encountered. We have provided scaling relations for the onset of both the intra- and the inter n -manifold mixing in a quadrupole field. Modifications of the energy spectrum especially due to scattering with the inner electron shells have not been considered. Effects relying on the latter can be understood by quantum defect theory [94, 107]. At least for Rydberg states which possess a large angular momentum we do not expect significant changes induced by core scattering processes.

In the linear regime we have discovered the so-called ellipsoidal state. These states exclusively

occur in the $m = \pm\frac{1}{2}$ -subspaces and exhibit unique features such as a large mean orbital angular momentum, spatial compactness and comparably low radial uncertainty. Furthermore they are strongly spin polarized and show almost no energy shift compared to their energy at zero gradient.

Analyzing the electronic spin properties we have found the S_z -expectation values of the electronic states to form a regular pattern at low gradients. At higher gradients or higher excitations, respectively, the regular structure is replaced by a much narrower irregular distribution. For the investigation of the local spin orientation we have introduced the S_z -polarization. For electronic states in the quadrupole field this quantity reveals a rich nodal structure which originates from the unique coupling of the spin and spatial degrees of freedom. The chess-board-like structure consisting of islands with alternating spin orientations at low radii changes to a striped pattern as the radius increases. For Rydberg states we have found a spin polarization effect taking place in the asymptotic region. Here the S_z -polarization exhibits a global dependence on the angle θ . This has been analyzed by studying a Hamiltonian which exclusively describes the coupling of the electronic spin to the magnetic field. By analytically calculating its eigenstates we could reproduce the above mentioned θ -dependence of the S_z -polarization of Rydberg-states for large radii.

In the framework of the dipole approximation we have derived selection rules for both transitions among J_z and $P_y\sigma_xP_z$ eigenstates. We have shown the linearly polarized transitions to take place only between states with the same quantum number m or states with different $P_y\sigma_xP_z$ symmetry. We have also calculated amplitudes of π - as well as σ^- -transitions from the ground state ($m = \frac{1}{2}$) to excited levels lying in the intra and inter n -manifold mixing regime. Additionally a comparison to the case of a homogeneous magnetic field has been performed and significant differences have been outlined. Due to the presence of further selection rules arising from the conservation of z -parity fewer transitions are observed here. Moreover, we have analyzed the dipole strengths for different values of the gradient b . Here we have revealed a modulation of the dipole strengths at the threshold of the weak to the intermediate gradient regime.

By calculating the expectation value of the dipole operator we have found it to be nonzero in general. This is in strong contrast to the situation in the homogeneous field where the conservation of parity prevents the emergence of permanent dipole moments. For low degrees of excitation and low gradients we have observed an almost linear increase of the maximum dipole moment of the n -multiplets. The previously regular pattern becomes increasingly distorted when reaching higher gradients and/or a higher degree of excitation. We have found the nonvanishing dipole moment to be a direct consequence of the symmetry properties of the quadrupole field which force an asymmetric electronic charge distribution with respect to the $x - y$ -plane.

In order to achieve the experimental realization of atoms centered in a quadrupole trap system one could think of two setups. One way is to study extremely excited electronic states ($n > 100$) in macroscopic fields, e.g. produced by coils. Another possibility is to utilize a so-called atom chip (see section 2.4) where current carrying micro-structures can generate high gradient quadrupole fields varying on a μm length scale. Here gradients up to $b = 10^{-10}$ seem to be feasible at the moment. This however should not limit the significance of this work since almost all effects discussed here are not due to the diamagnetic interactions but have their origin in the interplay between the Coulomb and the Zeeman terms. Thus weak gradients should not represent a principle obstacle to experimentally observe the derived properties. Here we want to point out the magnetic field induced permanent electric dipole moments which would potentially find applications in e.g. quantum information processing [70, 49, 18, 28]. In this particular case one could think of exciting the atom up to a certain electronic level in order to obtain a system with tailored dipole moment. This could potentially pave the way to achieve a working two qubit gate which is needed to establish a controlled interaction between two qubits in order to gain a deliberate phase shift. Considering a trapped Rydberg state as a qubit the interaction between two of them can be realized via dipole-dipole interaction. This interaction could be switched on and off on demand by changing the atomic state in the quadrupole field.

Taking into account the finite mass of the nucleus the center of mass (c.m.) and electronic motion do not separate i.e. do not decouple in the presence of a homogeneous magnetic field (see refs. [5, 51, 26]). To enter the regime where the residual coupling becomes important certain parameter values (excitation energy, c.m. energy etc.) have to be addressed. Here a variety of intriguing phenomena which rely on the mixing of the electronic and c.m. motion have been observed. Examples are the classical diffusion of the c.m. due to its coupling to the chaotic internal motion [92], the giant dipole states of moving atoms in magnetic fields [25] as well as the self-ionization process [93, 90, 74] due to energy flow between the c.m. and electronic degrees of freedom. In the current studies we have employed the approximation of an infinitely heavy nucleus i.e. the position of the c.m. is fixed at the center of the quadrupole field. This has been justified with the suppression of c.m. motional effects expected for ultra cold atoms. Nevertheless, a residual coupling is inevitable and will have impact on the electronic structure. We address this point in part IV of this thesis where we develop a theory taking into account both the c.m. and the electronic dynamics.

Most of the results presented in this chapter are published in refs. [64, 62, 65, 59].

9. Electronic structure of atoms in a magnetic guide

In the previous chapter we have examined the electronic quantum states of Rydberg atoms being exposed to a magnetic quadrupole field. Thereby we have discovered remarkable properties such as a nontrivial spin-density and the emergence of magnetic field induced permanent electric dipole moments.

We will now be performing a similar investigation considering an equally important field configuration namely the two-dimensional magnetic quadrupole field which by adding an additional homogeneous Ioffe-field is easily extended to yield a Ioffe-Pritchard trap. Proceeding in a similar manner as in the preceding chapter we present the underlying Hamiltonian in section 9.1. We will show this Hamiltonian to exhibit a wealth of both unitary and anti-unitary symmetries. The uncommonly large symmetry group is analyzed in section 9.2. These symmetries lead to a two-fold degeneracy of any energy level, a feature that turns out to be ubiquitous in quadrupolar magnetic fields. The numerical approach which is employed in order to solve the stationary Schrödinger equation is briefly outlined in section 9.3. Sections 9.4 to 9.8 are dedicated to the discussion of the numerical results: We analyze the electronic energy spectrum for a wide range of field gradients. Furthermore we explore properties of the electronic spin such as spin expectation values and distributions of the spin polarization. Selection rules and dipole strengths of electric dipole transitions between electronic states are calculated as well. In most of the considerations we consider both the two-dimensional quadrupole field as well as the Ioffe-Pritchard trap. Finally we summarize this chapter in section 9.9.

9.1. The Hamiltonian

The two-dimensional quadrupole field and its vector potential are given by the equations (2.4) and (2.6), respectively. Inserting them into the Hamiltonian (7.1) and adopting atomic units (see appendix B) yields

$$H = \frac{1}{2}\mathbf{p}^2 - \frac{1}{\sqrt{x^2 + y^2 + z^2}} + b x y p_z + \frac{b^2}{2} x^2 y^2 + \frac{b}{2} (x \sigma_x - y \sigma_y) \quad (9.1)$$

The first two terms of (9.1) resembles the nonrelativistic hydrogen atom. The third term which is linear with respect to the gradient b replaces the angular Zeeman term which occurs in a homogeneous field. Here the spatial coordinates x and y couple with the linear momentum in z direction. The successive diamagnetic term $\propto b^2$ represents an oscillator coupling term confining the electronic motion in the x and y direction except for the exit channels along the axis. This is to some extent reminiscent to the situation in a homogeneous field. However, there the diamagnetic interaction resembles a two-dimensional harmonic oscillator and consequently the motions in the x and y direction decouple. Finally the fifth term represents the coupling of the electronic spin to the spatial coordinates. It stems from the interaction of its magnetic moment with the field and exhibits a linear dependence on the spatial coordinates and on the gradient b . As for the three-dimensional quadrupole field this term prevents the factorization of the motions in coordinate space and spin space. Finally one should note that the only explicit dependence on the coordinate z is contained in

the Coulomb term. Without this rotationally invariant interaction the system was invariant under translations with respect to the z -coordinate (see for instance the considerations in section 6.1).

Following the treatment of section 8.1 we perform the canonical scaling transformation $\bar{x} = b^{\frac{1}{3}}x$ and $\bar{p} = b^{-\frac{1}{3}}p$ under which the Hamiltonian (9.1) becomes

$$H = b^{-\frac{2}{3}}\bar{H} = \frac{1}{2}\mathbf{p}^2 - \frac{\bar{Z}}{\sqrt{x^2 + y^2 + z^2}} + xyp_z + \frac{1}{2}x^2y^2 + \frac{1}{2}(x\sigma_x - y\sigma_y) \quad (9.2)$$

with $\bar{Z} = b^{-\frac{1}{3}}$. For simplicity we have omitted the bar on top of the phase space variables. This demonstrates that by considering a scaled energy (scaled Hamiltonian) the only free parameter is the scaled Coulomb coupling strength \bar{Z} that depends on the field gradient. The scaled Hamiltonian describes the motion of an electron in the Coulomb-field of an effective charge \bar{Z} and a magnetic quadrupole field with gradient $b = 1$. If $b \rightarrow \infty$ the Coulomb term vanished since $\bar{Z} \rightarrow 0$. In this limit the energy level spacing is expected to scale proportional to $b^{\frac{2}{3}}$.

9.2. Symmetries and degeneracies

This section is dedicated to a detailed analysis of the structure of the Hamiltonian (9.1). After studying its symmetries we will discuss how these symmetries affect the excitation spectrum. As a result of a tedious and elaborate analysis we have discovered 16 (including unity) distinct symmetry operations that leave the Hamiltonian (9.1) invariant. A complete list of them is provided in table 9.1. Each symmetry is composed of a number of elementary operations which are presented in

$\Sigma_x = \sigma_x P_y P_z$	$\Sigma_y = P_x \sigma_y P_z$	$\Sigma_z = P_x P_y \sigma_z$	1
$I_{xy} S_1$	$P_y P_z I_{xy} S_2$	$P_x P_y I_{xy} S_1^*$	$P_x P_z I_{xy} S_2^*$
$T \sigma_x P_z$	$T P_x P_y P_z \sigma_y$	$T P_x \sigma_z$	$T P_y$
$T P_y I_{xy} S_1$	$T P_z I_{xy} S_2$	$T P_x I_{xy} S_1^*$	$T P_x P_y P_z I_{xy} S_2^*$

Table 9.1.: Symmetry operations of the Hamiltonian (9.1). Top part: unitary symmetries. Bottom part: anti-unitary symmetries.

table 9.2. All symmetry operations are either unitary or anti-unitary with the anti-unitary ones

Operator	Operation	Designation
P_{x_i}	$x_i \rightarrow -x_i$	x_i -parity
T	$A \rightarrow A^*$	conventional time reversal
σ_x	$\sigma_y \rightarrow -\sigma_y \quad \sigma_z \rightarrow -\sigma_z$	Pauli spin matrix x
σ_y	$\sigma_x \rightarrow -\sigma_x \quad \sigma_z \rightarrow -\sigma_z$	Pauli spin matrix y
σ_z	$\sigma_x \rightarrow -\sigma_x \quad \sigma_y \rightarrow -\sigma_y$	Pauli spin matrix z
I_{xy}	$x \rightarrow y \quad y \rightarrow x \quad (\phi \rightarrow -\phi + \frac{\pi}{2})$	coordinate exchange
$S_1 = \begin{pmatrix} 0 & 1 \\ -i & 0 \end{pmatrix}$	$\sigma_x \rightarrow -\sigma_y \quad \sigma_y \rightarrow -\sigma_x \quad \sigma_z \rightarrow -\sigma_z$	
$S_2 = \begin{pmatrix} -i & 0 \\ 0 & 1 \end{pmatrix}$	$\sigma_x \rightarrow -\sigma_y \quad \sigma_y \rightarrow \sigma_x \quad \sigma_z \rightarrow \sigma_z$	

Table 9.2.: Set of discrete operations out of which all symmetry operations of the Hamiltonian (9.1) can be composed. Note that S_1 and S_2 are given in a basis where σ_z is diagonal.

involving the conventional time reversal operator T . Although the system looks simple by itself it features a surprising wealth of symmetry properties. The algebra of the underlying symmetry group possesses a complicated structure some features of which are discussed in the following:

The operators Σ_x , Σ_y and Σ_z generate a subgroup obeying the algebra $[\Sigma_i, \Sigma_j] = 2i \epsilon_{ijk} \Sigma_k$ that is reminiscent of angular momentum operators. The individual operators obey $\Sigma_i^2 = 1$. A deeper look into the representation theory of our group reveals a two-fold degeneracy of any energy level similar to those we have encountered during our investigations in chapter 8. The presence of this degeneracy can be shown as follows: The operators Σ_z and $P_y \sigma_x P_z$ obey $\{\Sigma_z, P_y \sigma_x P_z\} = 0$. Let $|E, \pi\rangle$ be an energy eigenstate and at the same time an eigenstate of Σ_z with

$$\Sigma_z |E, \pi\rangle = \pi |E, \pi\rangle \quad (9.3)$$

and $\pi = \pm 1$. Employing the above anti-commutator one obtains

$$\Sigma_z P_y \sigma_x P_z |E, \pi\rangle = -P_y \sigma_x P_z \Sigma_z |E, \pi\rangle = -\pi P_y \sigma_x P_z |E, \pi\rangle \quad (9.4)$$

The state $P_y \sigma_x P_z |E, \pi\rangle$ can be identified with $|E, -\pi\rangle$. Hence, as long as $\pi \neq 0$ ¹ there is always an orthogonal pair of states possessing the same energy namely $|E, \pi\rangle$ and $|E, -\pi\rangle$. We have to emphasize that there are no further degeneracies hidden in the system. In principle one could think of performing the above calculation repeatedly but now substituting $P_y \sigma_x P_z$ by any operator listed in table 9.1 which anti-commutes with Σ_z . It turns out that all of the states generated by this scheme are either superpositions of $|E, \pi\rangle$ and $|E, -\pi\rangle$ or differ only by a phase factor from one of these states.

Out of the 15 nontrivial symmetry operations one can pick several sets of commuting operators. For the following investigation we choose the set $H, \Sigma_z, P_y P_z I_{xy} S_2$. The combination of Σ_z and $P_y P_z I_{xy} S_2$ leads to the additional commuting operator $P_x P_z I_{xy} S_2^*$. We have found the properties:

$$(P_y P_z I_{xy} S_2)^2 = (P_x P_z I_{xy} S_2^*)^2 = -\Sigma_z \quad (9.5)$$

$$(\Sigma_z)^2 = (P_y P_z I_{xy} S_2)^4 = (P_x P_z I_{xy} S_2^*)^4 = 1. \quad (9.6)$$

9.2.1. Degeneracies in the energy spectrum of spin $\frac{1}{2}$ systems in magnetic quadrupole fields

We have now once more observed a two-fold degeneracy in the energy spectrum of a spin system. Usually degeneracies are expected to be lifted in the presence of external fields. However, the occurrence of these two-fold degeneracies seems to be an ubiquitous feature to occur in the presence of quadrupolar magnetic fields. In the following we try to elucidate this phenomenon. Let us assume we have a general spin $\frac{1}{2}$ systems with the following accompanying properties:

1. There are two operators A and B commuting with the Hamiltonian H : $[H, A] = [H, B] = 0$.
2. A and B anti-commute: $\{A, B\} = 0$.
3. A is a hermitian operator. B is an (anti-)unitary operator which can be written as a product $B = RS$ where R and S exclusively act on the real space and the spin space, respectively.
4. The operator S is trace-less: $\text{Tr } S = 0$.

If these conditions are fulfilled any state is doubly degenerate. This is seen as follows. Property 4 immediately leads to $\text{Tr } B = 0$. Hence, we find the nonzero eigenvalues of B to appear pairwise with opposite signs. If now $|E, b\rangle$ is an eigenstate of B and at the same time an energy-eigenstate property 2 implies that

$$BA |E, b\rangle = -AB |E, b\rangle = -bA |E, b\rangle = -b |E, -b\rangle. \quad (9.7)$$

Hence, $|E, b\rangle$ and $A |E, b\rangle = |E, -b\rangle$ are two degenerate energy-eigenstates of the system.

¹Since Σ_z is a unitary operator the case $\pi = 0$ cannot occur.

In the present case the two anti-commuting operators are Σ_z and $P_y\sigma_xP_z$. In the case of a three-dimensional quadrupole field as considered in chapter 8 we have $A = J_z$ and $B = P_y\sigma_xP_z$. In a homogeneous magnetic field the remaining symmetries constitute an Abelian symmetry group leading to exclusively one dimensional irreducible representations i.e. no degeneracies occur. Finally we remark that the reader can find a discussion on degeneracies in spin $\frac{1}{2}$ systems based on the properties of time-reversal operators in ref. [41].

9.2.2. Symmetry properties - eigenstates and expectation values

The operator $P_yP_zI_{xy}S_2$ obeys the eigenvalue relation

$$P_yP_zI_{xy}S_2|\kappa\rangle = \kappa|\kappa\rangle. \quad (9.8)$$

Since

$$|\kappa\rangle = (P_yP_zI_{xy}S_2)^4|\kappa\rangle = \kappa^4|\kappa\rangle \quad (9.9)$$

the eigenvalue κ can adopt the four values ± 1 and $\pm i$. At this point we want to emphasize that $P_yP_zI_{xy}S_2$ is a unitary but nonhermitian operator. We therefore encounter complex eigenvalues. If we apply Σ_z to the states $|\kappa\rangle$ we find by exploiting equation (9.5)

$$\Sigma_z|\kappa = \pm i\rangle = |\kappa = \pm i\rangle \quad (9.10)$$

$$\Sigma_z|\kappa = \pm 1\rangle = -|\kappa = \pm 1\rangle. \quad (9.11)$$

By using the relation

$$(T\sigma_xP_z)(P_yP_zI_{xy}S_2) - i(P_yP_zI_{xy}S_2)(T\sigma_xP_z) = 0 \quad (9.12)$$

one finds the degenerate pairs of states in the $P_yP_zI_{xy}S_2$ -subspaces: $|E, +1\rangle$, $|E, -i\rangle$ and $|E, -1\rangle$, $|E, +i\rangle$. Since nonhermitian operators do not represent physical observables the question on the actual physical meaning of the quantum number κ arises.

We now derive the expectation value of an observable Y in an eigenstate of Σ_z . Assume we have $\{Y, \Sigma_z\} = 0$ and hence

$$\langle E, \pi | Y \Sigma_z | E, \pi \rangle = -\langle E, \pi | \Sigma_z Y | E, \pi \rangle \quad (9.13)$$

$$\pi \langle E, \pi | Y | E, \pi \rangle = -\pi \langle E, \pi | Y | E, \pi \rangle. \quad (9.14)$$

This immediately leads to the result

$$\langle E, \pi | Y | E, \pi \rangle = 0. \quad (9.15)$$

The same arguments hold for an observable Z obeying $\{Z, P_yP_zI_{xy}S_2\} = 0$ in which case we obtain

$$\langle E, \kappa | Z | E, \kappa \rangle = 0. \quad (9.16)$$

We have already shown the states $|E, \pi\rangle$ and $P_y\sigma_xP_z|E, \pi\rangle$ to form a degenerate pair. By superimposing these two states eigenstates of the operator $P_y\sigma_xP_z$ can be constructed:

$$|E, \pm\rangle^{P_y\sigma_xP_z} = \frac{1}{\sqrt{2}} [|E, \pi\rangle \pm P_y\sigma_xP_z |E, \pi\rangle]. \quad (9.17)$$

The corresponding eigenvalue relation is

$$P_y\sigma_xP_z |E, \pm\rangle = \pm |E, \pm\rangle. \quad (9.18)$$

9.2.3. Symmetries in the presence of a Ioffe field

The application of an additional homogeneous magnetic field along the z -direction (Ioffe field) has a dramatic impact on the properties of the system. In particular the symmetry properties are affected. With the magnetic field (2.9) and the vector potential (2.10) of the Ioffe-Pritchard trap the Hamiltonian (7.1) becomes

$$H_I = \frac{1}{2}\mathbf{p}^2 - \frac{1}{\sqrt{x^2 + y^2 + z^2}} + b x y p_z + \frac{b^2}{2} x^2 y^2 + \frac{b}{2} (x \sigma_x - y \sigma_y) + \frac{B_I}{2} (x p_y - y p_x) + \frac{B_I^2}{8} (x^2 + y^2) + \frac{B_I}{2} \sigma_z \quad (9.19)$$

with B_I being the field strength of the Ioffe field. Since both the two-dimensional quadrupole (due to the side guide) and the Ioffe field are perpendicular to each other the homogeneous field terms can simply be added to the Hamiltonian (9.1). We find the well known Zeeman as well as the diamagnetic oscillator term. The coupling of the spin to the Ioffe field leads to a term being proportional to σ_z . The symmetries of H_I are listed in table 9.3. Due to the presence of the

Σ_z	$P_y P_z I_{xy} S_2$	$P_x P_z I_{xy} S_2^*$	1
$T P_x \sigma_z$	$T P_z I_{xy} S_2$	$T P_x P_y P_z I_{xy} S_2^*$	$T P_y$

Table 9.3.: Symmetries of the Hamiltonian (9.19), i.e. side guide with Ioffe field. Top line: unitary symmetries. Bottom line: anti-unitary symmetries.

additional homogeneous field numerous symmetries are lost (see table 9.1 for comparison). The remaining operations obey a non-Abelian algebra. In contrast to the group operations listed in table 9.1 there are no two anti-commuting operators. Hence it is not possible to construct pairs of degenerate energy eigenstates as discussed above. Thus, applying the Ioffe field lifts the degeneracies occurring in the absence of it. Even with a finite Ioffe field the operations Σ_z , $P_y P_z I_{xy} S_2$ and $P_x P_z I_{xy} S_2^*$ together with H_I form a set of commuting operators.

9.3. Numerical treatment

In order to obtain the eigenvalues and eigenfunctions of the Hamiltonians (9.1) and (9.19) particularly for highly excited Rydberg states we adopt once more the linear variational principle. Here the bound state solutions of the Schrödinger equation are expanded in a finite set of square-integrable basis functions. Determining the expansion coefficients is equivalent to solving a generalized eigenvalue problem in case of nonorthogonal basis functions. The latter is done numerically by employing standard linear algebra techniques and routines as outlined in section 3.1.

We are now adopting spherical coordinates as this will be required by the basis set we are going to use. The Hamiltonian (9.1) then reads

$$H = -\frac{1}{2}\Delta_{r,\theta,\phi} - \frac{1}{r} - i b r \sin \phi \cos \phi \left(\sin^2 \theta \cos \theta r \frac{\partial}{\partial r} - \sin^3 \theta \frac{\partial}{\partial \theta} \right) + \frac{b^2}{2} r^4 \sin^4 \theta \sin^2 \phi \cos^2 \phi + \frac{b}{2} r \sin \theta \begin{pmatrix} 0 & e^{i\phi} \\ e^{-i\phi} & 0 \end{pmatrix}. \quad (9.20)$$

With a Ioffe being applied we have to consider the Hamiltonian (9.19) which reads in spherical coordinates

$$H_I = H - i \frac{B_I}{2} \frac{\partial}{\partial \phi} + \frac{B_I^2}{8} r^2 \sin^2 \theta + \frac{B_I}{2} \sigma_z. \quad (9.21)$$

Like in the previous chapter we utilize a Sturmian basis set of the form

$$|n, l, m, m_s\rangle = R_n^{(\zeta, k)}(r) Y_l^m(\theta, \phi) |m_s\rangle. \quad (9.22)$$

These functions form a complete set in real and spin space but are not orthogonal. The angular part is covered by the well-known spherical harmonics $Y_l^m(\theta, \phi)$ whereas the two spinor components are addressed by the spin orbitals $|m_s\rangle = |\uparrow\rangle$ or $|\downarrow\rangle$. For the radial part we employ

$$R_n^{(\zeta, k)}(r) = \sqrt{\frac{n!}{(n+2k)!}} e^{-\frac{\zeta r}{2}} (\zeta r)^k L_n^{2k}(\zeta r) \quad (9.23)$$

with $L_n^{2k}(r)$ being the associated Laguerre polynomials. The parameters k and ζ can be adapted in order to gain an optimal convergence behavior in any spectral region. In particular the nonlinear variational parameter ζ has to be adapted such that it corresponds to the inverse of the characteristic length scale of the desired wave functions.

The general expansion of an energy eigenstate $|E\rangle$ being expanded in a finite set of the basis functions (9.22) reads

$$|E\rangle = \sum_{nlmm_s} c_{nlmm_s} |n, l, m, m_s\rangle. \quad (9.24)$$

Owed to the knowledge of the symmetries we can further specify the appearance of the expansion. In section 9.2 we chose H , Σ_z and $P_y P_z I_{xy} S_2$ to be the set of commuting operators whose eigenfunctions we intend to construct. We now demand $|E\rangle$ to be an eigenstate of $P_y P_z I_{xy} S_2$. Exploiting the relations

$$P_y P_z I_{xy} S_2 Y_l^m |\uparrow\rangle = -i e^{-i\frac{\pi}{2}m} (-1)^l Y_l^m |\uparrow\rangle \quad (9.25)$$

$$P_y P_z I_{xy} S_2 Y_l^m |\downarrow\rangle = e^{-i\frac{\pi}{2}m} (-1)^l Y_l^m |\downarrow\rangle. \quad (9.26)$$

one can construct the following expansions for the four κ -subspaces

$$|E, +1\rangle = \sum_{nlm} [R_n(a_{nlm} Y_{2l+1}^{4m+1} + b_{nlm} Y_{2l}^{4m+3}) |\uparrow\rangle + \bar{R}_n(c_{nlm} Y_{2l+1}^{4m+2} + d_{nlm} Y_{2l}^{4m+4}) |\downarrow\rangle] \quad (9.27)$$

$$|E, -1\rangle = \sum_{nlm} [R_n(a_{nlm} Y_{2l}^{4m+1} + b_{nlm} Y_{2l+1}^{4m+3}) |\uparrow\rangle + \bar{R}_n(c_{nlm} Y_{2l}^{4m+2} + d_{nlm} Y_{2l+1}^{4m+4}) |\downarrow\rangle] \quad (9.28)$$

$$|E, +i\rangle = \sum_{nlm} [R_n(a_{nlm} Y_{2l}^{4m+2} + b_{nlm} Y_{2l+1}^{4m+4}) |\uparrow\rangle + \bar{R}_n(c_{nlm} Y_{2l+1}^{4m+1} + d_{nlm} Y_{2l}^{4m+3}) |\downarrow\rangle] \quad (9.29)$$

$$|E, -i\rangle = \sum_{nlm} [R_n(a_{nlm} Y_{2l+1}^{4m+2} + b_{nlm} Y_{2l}^{4m+4}) |\uparrow\rangle + \bar{R}_n(c_{nlm} Y_{2l}^{4m+1} + d_{nlm} Y_{2l+1}^{4m+3}) |\downarrow\rangle] \quad (9.30)$$

The eigenfunctions (9.27-9.30) are thus a priori eigenfunctions of Σ_z (see equation (9.10) and (9.11)). Due to the structure of the spherical harmonics Y_l^m one has to ensure that $|m| \leq l$. In our calculations the sums run over all valid combinations of $n \leq N$, $l \leq L$ and $m \leq M$ where the maximum indices N , L and M can be set individually. The expansion becomes exact in the limit $M, N, L \rightarrow \infty$.

Performing the linear variational principle with one of the above expansions leads, according to section 3.1, to a generalized eigenvalue problem $\mathcal{H}\mathbf{v} = E\mathcal{S}\mathbf{v}$, where \mathcal{H} and \mathcal{S} are the corresponding matrix representation of the Hamiltonian (9.20) and the overlap matrix, respectively. The expressions for the matrix elements of the individual parts of the Hamiltonian and the overlap matrix can be found in [55].

9.4. Spectral properties

We now analyze the structure of the energy spectrum. With respect to the spectral behavior one can distinguish three regimes: the weak, the intermediate and the strong gradient regime each of which possesses an individual characteristics. The appearance of these regimes is not solely determined by the gradient or the degree of excitation, but by the scaled energy (see discussion in section 9.1). For simplicity we will refer to the gradient as the relevant quantity characterizing the

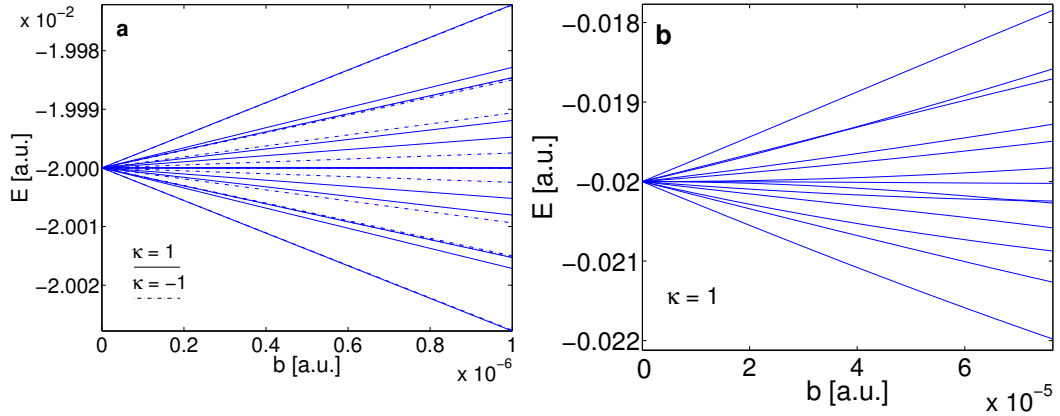


Figure 9.1.: **a:** Splitting of the energy levels belonging to the $n = 5$ multiplet ($\kappa = \pm 1$ -subspace) with increasing gradient. The level structure is dominated by the linear Zeeman term. The splitting is linear and symmetric around zero-free energy ($b = 0$). **b:** Intra n -manifold mixing of the $n = 5$ multiplet in the $\kappa = 1$ -subspace. Due to the increasing dominance of the diamagnetic term the level splitting becomes nonlinear.

different regimes. All figures in this section show energy levels for manifolds belonging to rather small values for n (typically $n = 5 - 7$) and for large gradients (we cover the range $b = 10^{-7} - 10^{-4}$) that are not accessible in the laboratory. This is done for reasons of illustration: Our observations and results equally hold for weaker gradients and higher n -manifolds which however, due to the high level density, are less suited for a graphical representation. In the weak gradient regime the spectral behavior is determined by the linear Zeeman terms. Although the principal quantum number n strictly is not a good quantum number any given level can be assigned to a certain n -multiplet. The levels split symmetrically around the zero-field energy exhibiting the expected linear dependence on b . In figure 9.1a this is exemplarily shown for the $n = 5$ -multiplet.

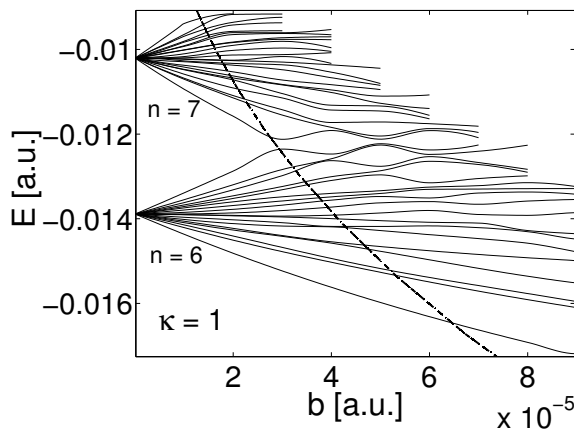


Figure 9.2.: Inter n -manifold mixing between the $n = 6$ - and $n = 7$ -multiplet in the $\kappa = 1$ -subspace. The mixing threshold is indicated by the dashed line. A large number of avoided crossings occur.

The intermediate regime is characterized by the occurrence of intra n -manifold mixing. Although neighboring n -manifolds are still distinguishable the levels now acquire a nonlinear b -dependence

which is due to the increasing importance of the diamagnetic term. sublevels belonging to different angular momenta mix and thus avoided level-crossings appear. The onset of this intermediate regime scales according to $b \propto n^{-6}$. Figure 9.1b shows the regime of intermediate gradients of the $n = 5$ -multiplet. Interestingly we observe here that this nonlinear behavior in the l -mixing regime is very weakly pronounced for an atom in the magnetic guide compared to an atom in a homogeneous magnetic field [33].

As we enter the strong gradient regime adjacent n -manifolds begin to overlap. The spectra are strongly i.e. nonperturbatively influenced by the diamagnetic term. Figure 9.2 shows this inter n -manifold mixing for the $n = 6$ - and $n = 7$ -multiplet where the strong coupling leads to large avoided crossings. The mixing threshold scales according to $b \propto n^{-\frac{11}{2}}$ (indicated by the dashed line in figure 9.2).

9.5. Properties of the electronic spin in the absence of a loffe field

9.5.1. Expectation value

In order to study the mutual influence of coordinate and spin space let us investigate the properties of the electronic spin. The x - and y -components of the spin operator obey $\{\Sigma_z, S_x\} = \{\Sigma_z, S_y\} = 0$. Hence, by using equation (9.15) we arrive at

$$\langle S_x \rangle = \langle S_y \rangle = 0. \quad (9.31)$$

Therefore, only the expectation value of S_z is nonzero in general. This is not obvious since the Hamiltonian (9.20) does not contain an explicit dependence on S_z . Figure 9.3a displays the expec-

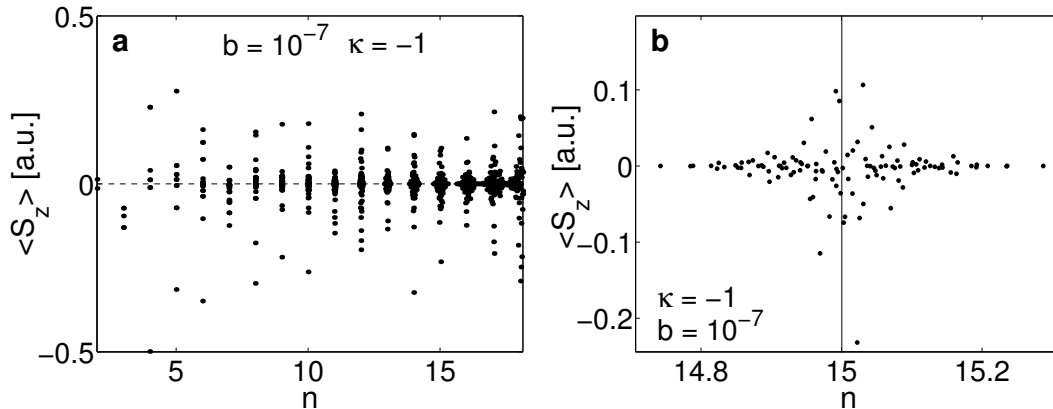


Figure 9.3.: **a:** Expectation value of the z -component of the electronic spin operator for several excited states ($b = 10^{-7}$). **b:** Zoomed view of the $n = 15$ -multiplet. The magnitude of $\langle S_z \rangle$ decreases for states suffering a large energy shift by the external field.

tation value $\langle S_z \rangle$ for several excited states as a function of the principal quantum number n , which serves as an energy label. The expectation values are arranged along vertical lines each of which belongs to a certain n -multiplet. With increasing degree of excitation these lines widen and begin to overlap as the inter n -mixing threshold is surpassed. A zoomed view of the $n = 15$ -multiplet is shown in figure 9.3b. We find states experiencing a large energy shift due to the external field to possess a small S_z expectation value. For the states shown in this figure $\langle S_z \rangle$ vanishes for $n > 15.2$ and $n < 14.8$.

9.5.2. Spin polarization

We now study the relative alignment of the electronic spin and the magnetic field. This is done by extending the spin polarization defined by equation (8.16). Instead of only considering the

z -component of the spin operator we now define the spin polarization of a two-component spinor

$$|\Psi\rangle = |u\rangle \left| m_s = \frac{1}{2} \right\rangle + |d\rangle \left| m_s = -\frac{1}{2} \right\rangle \quad (9.32)$$

by

$$\begin{aligned} W_{SB}(\mathbf{r}) &= \frac{\langle \Psi | \mathbf{r} \rangle \langle \mathbf{r} | \mathbf{S} \cdot \mathbf{B} | \mathbf{r} \rangle \langle \mathbf{r} | \Psi \rangle}{|\mathbf{S}| |\mathbf{B}| |\langle \Psi | \mathbf{r} \rangle|^2} = \frac{\langle \Psi | \mathbf{r} \rangle (\sigma_x \cos \phi - \sigma_y \sin \phi) \langle \mathbf{r} | \Psi \rangle}{|\langle \mathbf{r} | u \rangle|^2 + |\langle \mathbf{r} | d \rangle|^2} \\ &= 2 \frac{\text{Re} [u^*(\mathbf{r}) d(\mathbf{r}) e^{i\phi}]}{|u(\mathbf{r})|^2 + |d(\mathbf{r})|^2} = \langle \cos \gamma \rangle (\mathbf{r}) \end{aligned} \quad (9.33)$$

$W_{SB}(\mathbf{r})$ describes the spatially varying alignment of the spin vector relative to the local direction of the magnetic quadrupole field. $W_{SB}(\mathbf{r}) = 1$ indicates the spin to be oriented parallel to the field whereas we find antiparallel alignment if $W_{SB}(\mathbf{r}) = -1$. According to equation (9.33) $W_{SB}(\mathbf{r})$ can be interpreted as the local expectation value of the cosine of the angle γ between \mathbf{S} and \mathbf{B} . Since in a homogeneous field the projection of the spin onto the field direction is conserved $W_{SB}(\mathbf{r})$ would either be $+1$ or -1 throughout the whole space. In the two-dimensional quadrupole field, however, we expect a much richer structure resulting from the coupling of the coordinate and the spin degrees of freedom. In figure 9.4 we present three tomographic cuts of the spin polarization

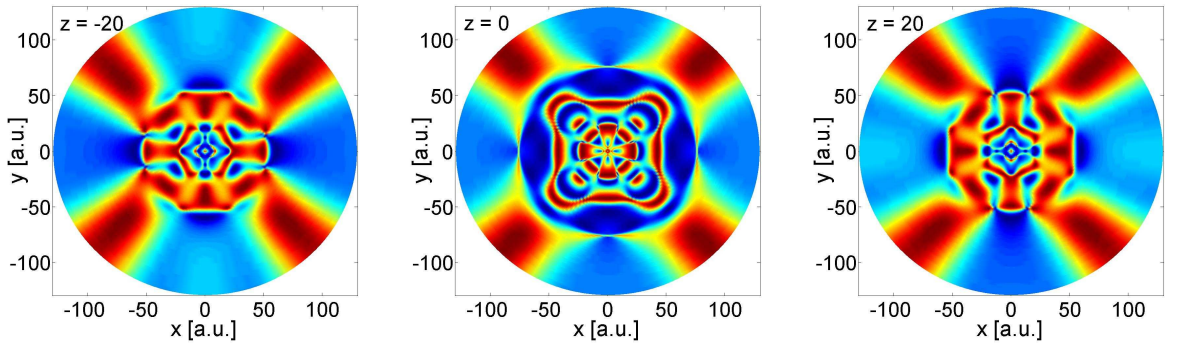


Figure 9.4.: Tomographic cuts through the spin polarization $W_{SB}(\mathbf{r})$ of the 83rd excited state. The state belongs to the $n = 8$ multiplet within the $\kappa = 1$ -subspace ($b = 10^{-7}$). The cuts are made at $z = \pm 20$ and $z = 0$. Positive and negative values are indicated red and blue, respectively. We observe a rich pattern of different spin polarizations around the origin. From $\rho \approx 60$ on the nodal structure is replaced by a regular striped pattern varying periodically with the azimuthal angle ϕ .

$W_{SB}(\mathbf{r})$ of the 83rd excited state in the $\kappa = 1$ -subspace. In the vicinity of the coordinate center we observe a large number of nodes. From $\rho \approx 60$ on this complex nodal structure changes to a smooth regular pattern exhibiting a periodicity with respect to the azimuthal angle ϕ . Here $W_{SB}(\mathbf{r})$ becomes almost independent of the z -coordinate. This feature seems to be induced mainly by the magnetic interaction which is invariant under translations along z . One can identify four sectors reminiscent of the quadrupolar structure of the magnetic field of the guides. In the present case we apparently have a anti-parallel alignment in the $x = 0$ - and $y = 0$ -plane and a parallel one between these planes. The densities are invariant under the operations $P_x P_y$ and $P_z I_{xy} S_2$ whose actions are equivalent to those of Σ_z and $P_y P_z I_{xy} S_2$ when acting on real and scalar quantities.

9.6. Electric dipole transitions in the absence of a Ioffe field

We now consider electromagnetic transitions between electronic states in the framework of the dipole approximation. The transition amplitude between the initial state $|i\rangle$ and the final state $|f\rangle$

is then given by the squared modulus of the matrix element $\langle i | \mathbf{D} | f \rangle$. In the length gauge \mathbf{D} takes the forms

$$D_{\sigma^\pm} = \frac{1}{\sqrt{2}}(x \pm iy) = \frac{1}{\sqrt{2}}r \sin \theta e^{\pm i\phi} \quad (9.34)$$

$$D_\pi = z = r \cos \theta \quad (9.35)$$

for σ^\pm - and π -transitions, respectively. Exploiting the symmetry properties of the $P_y P_z I_{xy} S_2$ -eigenstates one finds

$$\langle E, \kappa | (P_y P_z I_{xy} S_2)^\dagger z P_y P_z I_{xy} S_2 | E', \kappa' \rangle = \kappa^* \kappa' \langle E, \kappa | z | E', \kappa' \rangle = - \langle E, \kappa | z | E', \kappa' \rangle \quad (9.36)$$

which leads to the expression

$$(\kappa^* \kappa' + 1) \langle E, \kappa | z | E', \kappa' \rangle = 0. \quad (9.37)$$

Here we have used $\langle E, \kappa | (P_y P_z I_{xy} S_2)^\dagger = \langle \kappa | \kappa^*$. Apparently the matrix element for π -transitions can only be nonzero for the following combinations of κ and κ' :

$$\pi : (\kappa, \kappa') = (1, -1), (-1, 1), (i, -i), (-i, i) \quad (9.38)$$

The above calculation shows also that the expectation value of the z -coordinate vanishes in any of the eigenstate $|E, \kappa\rangle$ i.e. we have $\langle E, \kappa | z | E, \kappa \rangle = 0$. Conducting a similar calculation one obtains for the selection rules of σ^\pm -transition:

$$\sigma^+ : (\kappa, \kappa') = (i, 1), (1, -i), (-1, i), (-i, -1) \quad (9.39)$$

$$\sigma^- : (\kappa, \kappa') = (-i, 1), (1, i), (-1, -i), (i, -1). \quad (9.40)$$

In figure 9.5 a schematic view of the allowed dipole transitions between different κ -subspaces is

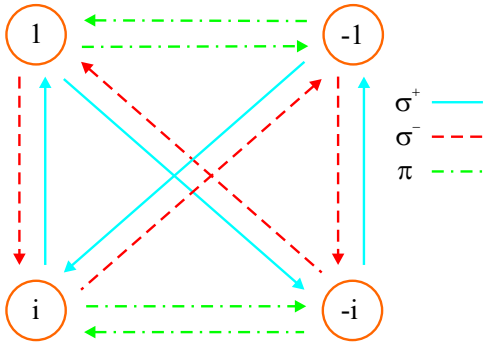


Figure 9.5.: Graphical representation of allowed dipole transitions between the different κ -subspaces. The arrows point from κ to κ' .

depicted.

By using the numerically computed electronic eigenstates we have calculated the dipole strengths for transitions from the ground state to excited states. Figure 9.6 shows the data which we obtained for π -transitions among the $\kappa = 1$ - and $\kappa' = -1$ -subspace. In figure 9.6a we observe a general decrease of the dipole strengths with decreasing transition wavelengths. However, the decrease is not monotonous as it was in the case of a homogeneous or a three-dimensional quadrupole field [62]. One rather finds a modulation on top of the transition amplitudes. For instance the $n = 8$ -, $n = 10$ - and $n = 12$ -multiplet exhibit smaller dipole strengths than both of their neighbors. Figure 9.6b shows a magnified view of the $n = 1 \rightarrow 12$ transition line. Its structure is dominated by two

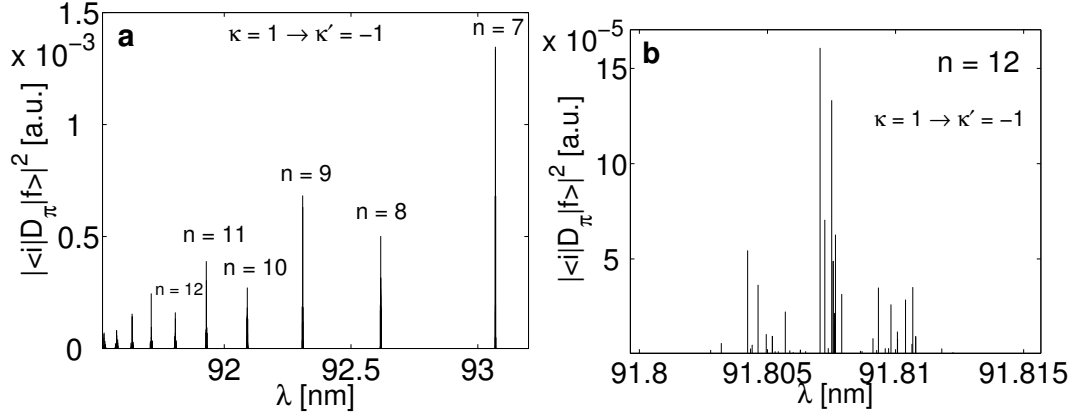


Figure 9.6.: **a:** Dipole strengths for π -transition from the ground state of the $\kappa = 1$ -subspace to excited states belonging to the $\kappa = -1$ -subspace ($b = 10^{-7}$). The line with the smallest transition wavelength belongs to the $n = 1 \rightarrow 7$ -transition. **b:** Zoomed view of the line belonging to the transition to the $n = 12$ -multiplet. The line center is dominated by two sublines. The two bunches located at its right- and left-hand side possess a significantly lower dipole strength.

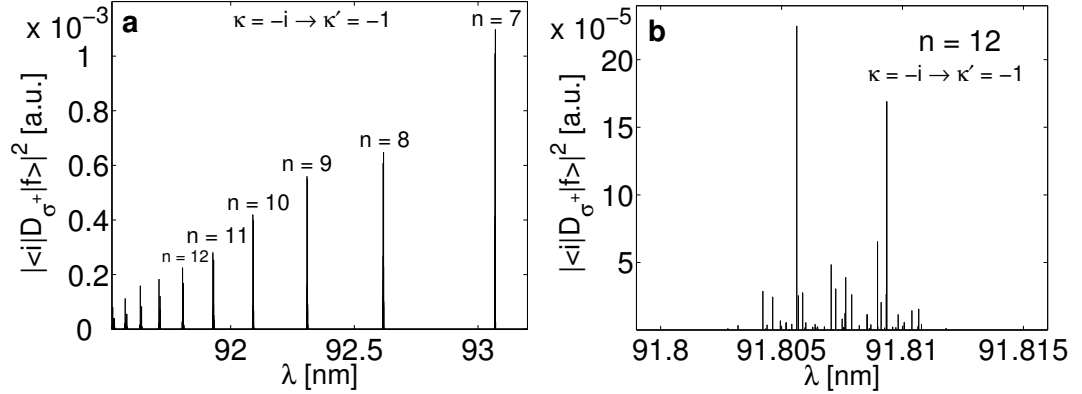


Figure 9.7.: **a:** Dipole strengths for σ^+ -transition from the ground state of the $\kappa = -i$ -subspace to excited states belonging to the $\kappa = -1$ -subspace ($b = 10^{-7}$). The line with the smallest wavelength λ belongs to the $n = 1 \rightarrow 7$ -transition. **b:** Zoomed view of the line belonging to the transition to the $n = 12$ -multiplet. The line consists of three bunches each of which possesses numerous of sublines. The line is dominated by two sublines one of each located in the left and right hand side bunch.

sublines located in the line center. The central bunch is almost symmetrically accompanied by two bunches of sublines located for smaller and larger wavelength, respectively.

Also for σ^+ -transitions the dipole strengths decrease systematically with decreasing wavelength (figure 9.7a). In the magnified view (figure 9.7b) one sees the line to consist of three bunches of sublines. There are two dominating sublines which are located in the two outer bunches rather than in the central one.

9.7. Properties of the electronic spin in the presence of a Ioffe field

9.7.1. The expectation value of S_z

As discussed in section 9.1 an additionally applied homogeneous field leads to changes of the symmetry properties of the system. Thus, apart from the lifting of the degeneracies also a significant influence on the electronic spin and the transition amplitudes has to be expected.

Apparently there is a critical radius ρ_c at which both fields are equal in strength. For a given

gradient b and homogeneous field strength B_I it is given by $\rho_c = \frac{B_I}{b}$. Considering that for electronic states we have $\langle \rho \rangle \approx \langle r \rangle \propto n^2$ we expect states with

$$n_c = \sqrt{\frac{B_I}{b}} \quad (9.41)$$

to be equally affected by both fields. Hence, the structure of states with $n \ll n_c$ or $n \gg n_c$ should be dominated by the homogeneous field or the quadrupole field, respectively.

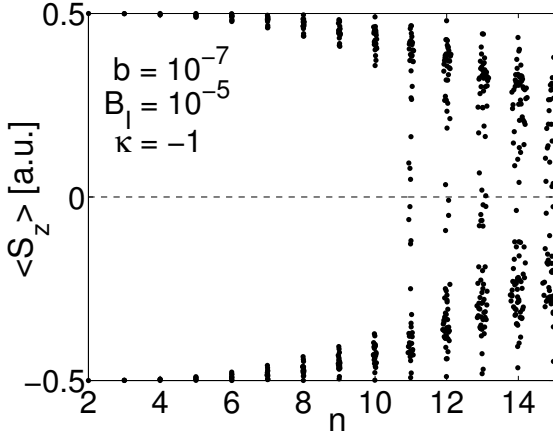


Figure 9.8.: Expectation values of the z -component of the electronic spin for a Ioffe field strength ($B_I = 10^{-5}$) and a gradient of $b = 10^{-7}$. At low degree of excitation the homogeneous field dominates the electronic states. In this region S_z becomes an approximate constant of motion admitting $\langle S_z \rangle$ to possess only one of the two possible values $\pm \frac{1}{2}$. States lying above the critical principal quantum number n_c become increasingly dominated by the quadrupole field. Consequently the expectation values tend towards $\langle S_z \rangle = 0$.

Figure 9.8 shows the expectation values of S_z for a gradient $b = 10^{-7}$ and a homogeneous field strength $B_I = 10^{-5}$. This yields the critical principal quantum number $n_c = 10$. Indeed one finds for $n \ll 10$ the expected dominance of the homogeneous field. In this region $\langle S_z \rangle$ is approximately restricted to one of the two values $\pm \frac{1}{2}$. This is due to the fact that S_z becomes an approximate constant of motion. For $n > 10$ we observe the expectation values to move towards zero which is expected from the results shown in figure 9.3. We have to remark that since the symmetry Σ_z persists the expectation values of S_x and S_y vanish even for a finite strength of the homogeneous field.

9.7.2. Spin polarization

Not only the spin expectation value but also the spin polarization suffers significant changes if a Ioffe field is switched on. For a sufficiently high field strength or low degree of excitation ($n < n_c$), respectively, the structure of the electronic states is dominated by the Ioffe field. Here the spin is expected to be aligned with the homogeneous field. Since $W_{SB}(\mathbf{r})$ describes the projection of the electronic spin onto the direction of the quadrupole field which is perpendicular to the Ioffe field one expects $W_{SB}(\mathbf{r})$ to be approximately zero in this domain. Figure 9.9 shows $W_{SB}(\mathbf{r})$ for the state which has been already presented in figure 9.4 but for a Ioffe field strength of $B_I = 10^{-5}$. The state is located inside the $n = 8$ multiplet which lies below the critical quantum number $n_c = 10$. Thus the state's structure should be predominantly determined by the Ioffe field. As expected from the discussion above we observe large greenish regions indicating $W_{SB}(\mathbf{r}) = 0$. The geometry of the quadrupole field is barely recognized for the cut made at $z = 0$. Unlike in figure 9.4 there are only small regions exhibiting a well-defined spin orientation that is dominated by the magnetic guide, i.e either $W_{SB}(\mathbf{r}) = -1$ or $W_{SB}(\mathbf{r}) = 1$.

9.8. Electric dipole transitions for in the presence of a Ioffe field

Figure 9.10a shows the dipole strengths for π -transitions from the ground state in the $\kappa = 1$ -subspace to various states in the $\kappa = -1$ -subspace. Compared to the $B_I = 0$ case the dipole

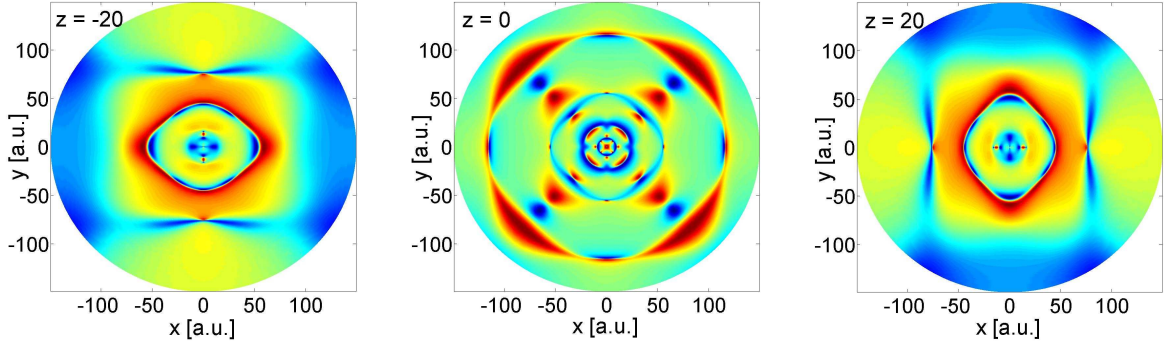


Figure 9.9.: Tomographic cuts through the spin polarization $W_{SB}(\mathbf{r})$ (defined by equation (9.33)) of the 83rd excited state for a Ioffe field strength of $B_I = 10^{-5}$. The state belongs to the $n = 8$ multiplet in the $\kappa = 1$ -subspace ($b = 10^{-7}$). The cuts are made at $z = \pm 20$ and $z = 0$. Positive and negative values are indicated by red and blue, respectively. One observes large greenish domains which indicate $W_{SB}(\mathbf{r}) \approx 0$.

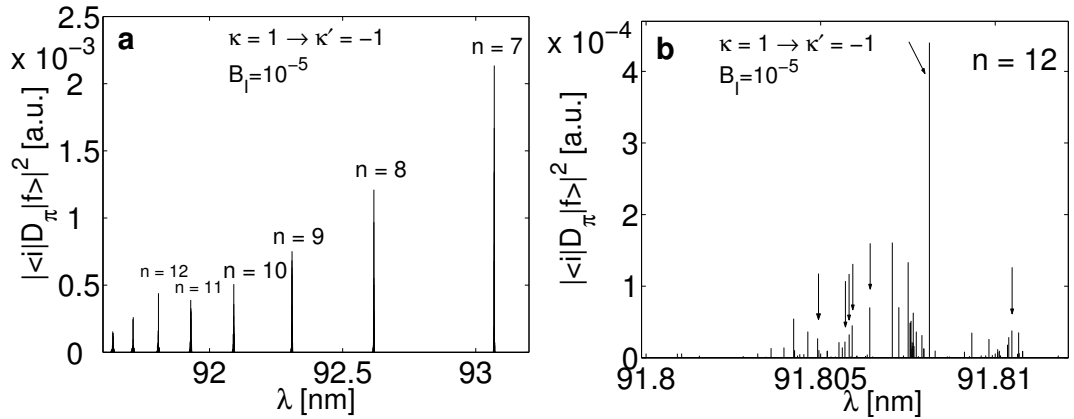


Figure 9.10.: **a:** Dipole strengths for π -transition from the ground state of the $\kappa = 1$ -subspace to excited states belonging to the $\kappa = -1$ -subspace ($b = 10^{-7}$ and $B_I = 10^{-5}$). The line with the smallest wavelength λ belongs to the $n = 1 \rightarrow 7$ -transition. **b:** Zoomed view of the line associated with the transition to the $n = 12$ -multiplet. Several additional lines appear at finite homogeneous field strength (some are marked by an arrow). The line center is dominated by a single subline emerging from a transition which is induced by the external homogeneous field.

strengths have increased by approximately 70%. The transition strengths increase with increasing transition wavelengths. Again there seems to occur some kind of modulation as already seen in figure 9.6a but being less pronounced here. In the present case the $n = 12$ -transition exhibits a larger transition amplitude than the neighbored transitions. In figure 9.10b we present a magnified view of the line associated with the $n = 12$ -transition. Due to the presence of the homogeneous field a number of additional lines appear some of which are marked by an arrow. In contrast to the $B_I = 0$ case the $n = 12$ line is dominated by a single subline originating from a transition that is only permitted in the presence of the homogeneous field.

9.9. Summary

We have studied the electronic quantum states of an highly excited atom inside in a magnetic guide. The motion of the valence electron has been described by an effective one-body approach. Both the coupling of the spatial degrees of freedom (para- and diamagnetism) as well as the spin degrees of freedom to the external field have been taken into account. The linear variational principle has been used to solve the stationary Schrödinger equation: Employing a Sturmian basis set enabled

us to converge a large number of electronic states.

A thorough inspection of the Hamiltonian has yielded an amazingly large number of symmetries involving both the spin and spatial degrees of freedom: We have found 16 symmetry operations of both unitary and anti-unitary character. This has allowed for a classification of the electronic eigenstates with respect to a complete set of commuting constants of motion. The latter has involved the hermitian Σ_z -operator which is a combined spin and parity operator and the unitary but nonhermitian operator $P_y P_z I_{xy} S_2$ which involves parity and permutation operators. Employing specific anti-commuting operators of this symmetry group we could prove the two-fold degeneracy of each energy level. This feature has shown to be generic for spin $\frac{1}{2}$ systems exhibiting certain symmetry properties. We have discussed how the symmetries are affected if an additional homogeneous magnetic field is applied in order to obtain a Ioffe-Pritchard type trap. In this case only 8 symmetry operations remain including Σ_z , $P_y P_z I_{xy} S_2$ and $P_x P_z I_{xy} S_2^*$.

The calculated spectra have been investigated up to energies corresponding to a principal quantum number of $n \approx 15$. In the low gradient regime degenerate n -manifolds split up symmetrically around the zero field energy. For the intra- n -mixing regime only a very weak restructuring takes place inside each n -multiplet, i.e. we observe only a minor nonlinear behavior of the energies on the gradient. For even higher gradients the inter- n -mixing takes place where states belonging to adjacent multiplets begin to mix and avoided crossings dominate the spectrum. Scaling relations for the onset of both, the inter- and the intra- n -mixing have been provided.

Effects due to the coupling of the spin and spatial degrees of freedom have been studied in detail. An analysis of the spin-field orientation has been undertaken by examining the appearance the spin polarization. The electronic states in the magnetic guide $W_{SB}(\mathbf{r})$ reveal a rich structure which does not happen inside a uniform magnetic field. Moreover an analysis of the S_z expectation value has been performed. It has been shown that states being energetically strongly affected by the presence of the magnetic guide possess a small expectation value of S_z .

We have derived selection rules for the quantum number κ belonging to the $P_y P_z I_{xy} S_2$ symmetry operator for linear as well as circular polarized dipole transitions. Wave lengths and dipole strengths from the ground state to Rydberg levels were analyzed. In particular for π transitions we have found a global modulation of the transition amplitudes. The impact of the presence of an additional homogeneous magnetic field (Ioffe field) on several relevant quantities has been studied. This includes the S_z -expectation values and the electric dipole transition amplitudes.

Let us now comment on the approach chosen in the present chapter. Neglecting the fine and hyperfine structure of the atom as well as omitting the influence of the core scattering events represent, at least for certain species and regimes (high excitations !), certainly a good approximation to the true physical system. Another approximation is the fact that we centered the nucleus at the minimum of the field configuration. This is suggested by our assumption that we have ultracold atoms with an extremely small kinetic center of mass (c.m.) energy in tight traps leading to a well-localized atomic c.m. Nevertheless, it is expected that the c.m. motion blurs the effects occurring for an atom with a fixed nucleus. Beyond this, it is well-known that already in the presence of a homogeneous magnetic field the c.m. and electronic motions of atoms do not separate i.e. they perform an intimately coupled motion [5, 51, 91, 92, 25]. Then the immediate question arises how this coupling might look like in our inhomogeneous field configuration and in particular what its impact on the overall electronic motion is. These questions will be partly answered in the next part of this thesis where we present a discussion on the combined dynamics of the electronic and the c.m. system.

Most of the results presented in this chapter are published in ref. [63].

Part IV.

Coupled electronic and center of mass dynamics of Rydberg atoms in an inhomogeneous magnetic field

10. Quantum states of ultracold electronically excited atoms in a magnetic quadrupole trap

10.1. Introductory remarks

On our way to gain understanding of the dynamics of atoms in inhomogeneous magnetic fields we have so far passed two milestones. We have explored both the resonance spectrum of ground state atoms as well as the electronic structure of highly excited atoms in the fixed-nucleus approximation. Now it is about time to put these pieces together and to obtain the full picture of a moving Rydberg atom inside a field.

Certainly one question that immediately arises is how the electronic dynamics couples to that of the center of mass (c.m) and vice versa. A separation of these two subsystems is certainly not achievable by simple means as this happens not even in the case of a homogeneous magnetic field [92, 26]. Compared to ground state atoms Rydberg atoms possess a rich internal structure that finds its manifestation in an extremely high dimensional manifold of electronic states - any n -manifold consists of $2n^2$ substates. It is this complexity which gives rise to a number of remarkable effects. In Rydberg gases for instance one observes strong long-range interactions which are based on multipole interactions of the electronic clouds [15]. This mechanism is not present in gases of ground state atoms where only short-ranged interactions are present. Hence the interaction strength of spatially separated atoms can in principle be tuned by changing their degree of excitation. This makes such systems possible candidates for the implementation of quantum information processing schemes [70, 88]. However, a prerequisite for the controlled interaction of two highly excited atoms is the ability to confine their motion to a given spatial region by using external fields. Dutta *et al.* have investigated the possibility of trapping such atoms in standing-wave light fields [27]. By employing a Born-Oppenheimer type approximation the authors could demonstrate the possibility of forming an optical lattice for Rydberg atoms. A different approach has been pursued by Hyafil *et al.* who propose a long time coherence preserving trap architecture utilizing static and time-dependent electric fields [47]. Apart from optical and electric fields there is also the alternative to consider magnetic fields as they are widely used to trap ultracold ground state atoms. Very recently magnetic trapping of cold Rydberg atoms has been experimentally demonstrated [38, 20]. So far all theoretical considerations assume a classical treatment of the atomic center of mass degrees of freedom. To our knowledge the question of trapping electronically excited atoms in the ultracold regime with their c.m. motion also being quantized has not been addressed theoretically. Magnetic trapping might be advantageous since there are no trap losses due to photon scattering as there are for optical traps.

In the present part of this thesis we establish a method to describe the complete quantized motion of a Rydberg atom being exposed to an inhomogeneous magnetic field (quadrupole field) and analyze the properties of the emerging quantum states. In detail we proceed as follows: In section 10.2 we present the Hamiltonian describing an atom which is exposed to a linear external magnetic field. By employing a two-body approximation we establish the interactions of the c.m. and electronic degrees of freedom with the external magnetic field. In section 10.3 we specifically turn to three-dimensional magnetic quadrupole field. We provide a symmetry analysis of the Hamiltonian and perform a scaling transformation which removes all but one parameter from the equation of motion. From section 10.4 on we exclusively focus on electronically highly excited

(Rydberg-) atoms. To this end the interaction between the valence electron and the remaining core is assumed to be of pure Coulomb character. By estimating the energy scales of the system we demonstrate that magnetic field induced couplings between adjacent n -manifolds can be neglected for certain magnetic field gradients and degrees of electronic excitation. The Hamiltonian is then solved in the framework of an adiabatic approximation which is thoroughly discussed in section 10.5. Here we also analyze the typical appearance of the adiabatic energy surfaces. In this context we discuss under what conditions trapped states of the c.m. motion can be achieved. The properties of these states are examined in section 10.6. We present the energy spectrum and study the properties of the c.m. quantum states such as various expectation values and radiative decay rates. We will also show that under certain conditions the radial extension of the electronic wave function can exceed that of the c.m. motion. We conclude and summarize our findings in section 10.7.

10.2. The Hamiltonian of an excited atom exposed in a linear magnetic field configuration

Like in the previous chapters focus on alkali metal atoms as they are the most frequently used species to experimentally study ultracold atomic physics. To a good approximation they can be modeled by a two-body approach in which the mutual interaction of the valence electron (particle 1) and the remaining core (particle 2) is accounted for by an effective potential. This interaction potential is assumed to depend on the spatial coordinates of the two particles such that $V(\mathbf{r}_1, \mathbf{r}_2) = V(\mathbf{r}_1 - \mathbf{r}_2)$. It consists of a short range part accounting for electron-core scattering and adopts pure Coulombic character for large separations of the two particles. After including the coupling to the external magnetic field the Hamiltonian of such modeled atom reads

$$H_{2\text{body}} = \frac{1}{2M_1} [\mathbf{p}_1 - q_1 \mathbf{A}(\mathbf{r}_1)]^2 + \frac{1}{2M_2} [\mathbf{p}_2 - q_2 \mathbf{A}(\mathbf{r}_2)]^2 + V(\mathbf{r}_1 - \mathbf{r}_2) - \boldsymbol{\mu}_1 \cdot \mathbf{B}(\mathbf{r}_1) - \boldsymbol{\mu}_2 \cdot \mathbf{B}(\mathbf{r}_2). \quad (10.1)$$

Here $\mathbf{A}(\mathbf{r}_i)$ and $\mathbf{B}(\mathbf{r}_i)$ are the vector potential and the inhomogeneous magnetic field, respectively. Now we require $\mathbf{B}(\mathbf{r})$ to satisfy the following two conditions: it be linear, i.e. $\mathbf{B}(\mathbf{r}_1 + \mathbf{r}_2) = \mathbf{B}(\mathbf{r}_1) + \mathbf{B}(\mathbf{r}_2)$, and shall obey the homogeneity condition $\mathbf{B}(\alpha \mathbf{r}_i) = \alpha \mathbf{B}(\mathbf{r}_i)$. Additionally we require $\nabla \times \mathbf{B}(\mathbf{r}) = 0$ and $\nabla \cdot \mathbf{B}(\mathbf{r}) = 0$ which are simply Maxwell's equations in a source-free region in space. In this case a vector potential of $\mathbf{B}(\mathbf{r})$ obeying the Coulomb-gauge $\nabla \cdot \mathbf{A}(\mathbf{r}) = 0$ is according to appendix A given by

$$\mathbf{A}(\mathbf{r}) = \frac{1}{3} \mathbf{B}(\mathbf{r}) \times \mathbf{r}. \quad (10.2)$$

The previous condition gives rise to the identity

$$\mathbf{A}(\mathbf{r}_i) \cdot \mathbf{p}_i = \frac{1}{3} \mathbf{L}_i \cdot \mathbf{B}(\mathbf{r}_i). \quad (10.3)$$

which represents the coupling of the orbital angular momentum \mathbf{L}_i of a charged particle to the external magnetic field. These so-called Zeeman terms are reminiscent of those which emerge in a homogeneous magnetic field. We assume here that the diamagnetic terms of the Hamiltonian (10.1) which are proportional to $\mathbf{A}^2(\mathbf{r}_i)$ can be neglected. This assumption is valid for a broad range of excitation energies as well as typical laboratory field configurations (see also section 10.4 for a discussion of the range of validity of this approximation). Utilizing the identity (10.3) and neglecting the diamagnetic coupling terms the Hamiltonian (10.1) acquires the following shape

$$H_{\text{lin}} = \frac{1}{2M_1} \mathbf{p}_1^2 + \frac{1}{2M_2} \mathbf{p}_2^2 + \frac{e}{3M_1} \mathbf{L}_1 \cdot \mathbf{B}(\mathbf{r}_1) - \frac{e}{3M_2} \mathbf{L}_2 \cdot \mathbf{B}(\mathbf{r}_2) + V(\mathbf{r}_1 - \mathbf{r}_2) - \boldsymbol{\mu}_1 \cdot \mathbf{B}(\mathbf{r}_1) - \boldsymbol{\mu}_2 \cdot \mathbf{B}(\mathbf{r}_2). \quad (10.4)$$

Here we have taken into account that both particles carry the same amount of charge e but with opposite signs. Since the interaction potential depends only on the relative coordinate vector \mathbf{r} of the two particles it is natural to introduce relative and c.m. coordinates \mathbf{R} : $\mathbf{r}_1 = \mathbf{R} + \frac{M_2}{M}\mathbf{r}$ and $\mathbf{r}_2 = \mathbf{R} - \frac{M_1}{M}\mathbf{r}$ with the total mass $M = M_1 + M_2$. The single-particle angular momenta transform according to

$$\begin{aligned}\mathbf{L}_1 &= \frac{M_1}{M}\mathbf{L}_R + \frac{M_2}{M}\mathbf{L}_r + \mathbf{R} \times \mathbf{p} + \frac{M_1M_2}{M^2}\mathbf{r} \times \mathbf{P} \\ \mathbf{L}_2 &= \frac{M_2}{M}\mathbf{L}_R + \frac{M_1}{M}\mathbf{L}_r - \mathbf{R} \times \mathbf{p} - \frac{M_1M_2}{M^2}\mathbf{r} \times \mathbf{P}.\end{aligned}\quad (10.5)$$

Here (\mathbf{p}, \mathbf{r}) and (\mathbf{P}, \mathbf{R}) form two sets of conjugate variables. This gives rise to the Hamiltonian

$$\begin{aligned}H_{\text{lin}} &= \frac{\mathbf{p}^2}{2m} + \frac{\mathbf{P}^2}{2M} + V(\mathbf{r}) + \left[-\frac{e}{3M} \left(\frac{M_1}{M_2} - \frac{M_2}{M_1} \right) \mathbf{L}_r - \boldsymbol{\mu}_1 - \boldsymbol{\mu}_2 \right] \cdot \mathbf{B}(\mathbf{R}) \\ &+ \left[\frac{e}{3M} \mathbf{L}_R + \frac{e}{3M^2} \left(\frac{M_2^2}{M_1} + \frac{M_1^2}{M_2} \right) \mathbf{L}_r - \frac{M_2}{M} \boldsymbol{\mu}_1 + \frac{M_1}{M} \boldsymbol{\mu}_2 \right] \cdot \mathbf{B}(\mathbf{r}) \\ &+ \frac{e}{3m} \mathbf{B}(\mathbf{R}) \times \mathbf{R} \cdot \mathbf{p} + \frac{e}{3} \frac{M_2 - M_1}{M_1M_2} \mathbf{B}(\mathbf{r}) \times \mathbf{R} \cdot \mathbf{p} \\ &+ \frac{e}{3M} \mathbf{B}(\mathbf{R}) \times \mathbf{r} \cdot \mathbf{P} + \frac{e}{3} \frac{M_2 - M_1}{M^2} \mathbf{B}(\mathbf{r}) \times \mathbf{r} \cdot \mathbf{P}\end{aligned}\quad (10.6)$$

with m being the reduced mass. If no external field was present the introduction of the new coordinates would decouple the c.m. and relative motions. However, the presence of the external field prevents this separation leading to field induced coupling terms. The latter cannot be eliminated but it is possible to somewhat simplify them by applying the unitary transformation

$$U_1 = \exp \left[i \frac{e}{3} (\mathbf{B}(\mathbf{r}) \times \mathbf{R} \cdot \mathbf{r} + \mathbf{B}(\mathbf{R}) \times \mathbf{r} \cdot \mathbf{R}) \right]. \quad (10.7)$$

We want to emphasize here that $U_1 = 1$ for a homogeneous field $\mathbf{B}(\mathbf{r}) = \mathbf{B}$. After the application of U_1 we arrive at

$$\begin{aligned}U_1^\dagger H_{\text{lin}} U_1 &= \frac{\mathbf{p}^2}{2m} + U_1^\dagger V(\mathbf{r}) U_1 + \left[\frac{e}{3} \left(\frac{1}{m} - \frac{3}{M} \right) \mathbf{L}_r - \frac{M_2}{M} \boldsymbol{\mu}_1 + \frac{M_1}{M} \boldsymbol{\mu}_2 \right] \cdot \mathbf{B}(\mathbf{r}) \\ &+ \frac{\mathbf{P}^2}{2M} - \left[\frac{2e}{3M_2} \mathbf{L}_r + \boldsymbol{\mu}_1 + \boldsymbol{\mu}_2 \right] \cdot \mathbf{B}(\mathbf{R}) + \frac{e}{3} \frac{3M_2 + M_1}{M_1M_2} \mathbf{p} \times \mathbf{B}(\mathbf{r}) \cdot \mathbf{R} \\ &+ \frac{e}{M} \mathbf{B}(\mathbf{R}) \times \mathbf{r} \cdot \mathbf{P} - \frac{2e}{3} \frac{M_1}{M^2} \mathbf{B}(\mathbf{r}) \times \mathbf{r} \cdot \mathbf{P}.\end{aligned}\quad (10.8)$$

At this point we want to remark that the potential $V(\mathbf{r})$, apart from depending on the radial coordinate \mathbf{r} can also contain the angular momentum \mathbf{L}_r and the spin operator \mathbf{S} . Thus it does not necessarily commute with the transformation U_1 . In the Hamiltonian (10.8) we again have dropped all terms that contain the magnetic field strength quadratically. In the following we employ another approximation exploiting the fact that the nuclear mass M_2 is much larger than the electronic mass M_1 . Keeping only magnetic field dependent terms of the order M_1^{-1} we find

$$\begin{aligned}H_{\text{ap}} &= \frac{\mathbf{p}^2}{2M_1} + U_1^\dagger V(\mathbf{r}) U_1 + \left[\frac{e}{3M_1} \mathbf{L}_r - \boldsymbol{\mu}_1 \right] \cdot \mathbf{B}(\mathbf{r}) + \frac{\mathbf{P}^2}{2M_2} - [\boldsymbol{\mu}_1 + \boldsymbol{\mu}_2] \cdot \mathbf{B}(\mathbf{R}) \\ &+ \frac{e}{M_1} \mathbf{p} \times \mathbf{B}(\mathbf{r}) \cdot \mathbf{R}.\end{aligned}\quad (10.9)$$

Although $\boldsymbol{\mu}_2$ is proportional to M_2^{-1} we will not drop the corresponding term at this stage. Its the only term containing the nuclear spin and is thus necessary for a proper analysis of the symmetry

properties. Eventually this term decides upon whether we deal with a boson or fermion. The individual terms of H_{ap} can be interpreted as follows: The first three terms represent the Hamiltonian of an electron in an inhomogeneous magnetic field orbiting around a fixed nucleus (see part III of this thesis). The two successive terms involving the c.m. variables describe the dynamics of a neutral point-like particle carrying the magnetic moment $\boldsymbol{\mu}_1 + \boldsymbol{\mu}_2$ inside a magnetic field. Such systems have been thoroughly explored in part II of this thesis. The last term, which is induced by the motion of the atom in the field, couples the c.m. to the electronic motion.

10.3. The magnetic quadrupole field: Hamiltonian and symmetries

Up to this point we did not refer to a particular magnetic field configuration. We now focus on the three-dimensional magnetic quadrupole field given by equation (2.1). Apparently this field is linear in the spatial coordinates and meets the requirements of section 10.2. By employing atomic units (see appendix B) and inserting equation (2.1) the Hamiltonian (10.9) becomes

$$\begin{aligned} H_Q &= H_A + \frac{\mathbf{P}^2}{2M_2} - bzL_z + \mathbf{B}(\mathbf{r}) \times \mathbf{R} \cdot \mathbf{p} + \mathbf{B}(\mathbf{r} + \mathbf{R}) \cdot \mathbf{S} + \frac{g_K}{M_2} \mathbf{B}(\mathbf{R}) \cdot \boldsymbol{\Sigma} \\ &= H_A + \frac{\mathbf{P}^2}{2M_2} + b[-zL_z + (2Yz + Zy)p_x - (2Xz + Zx)p_y + (xY - Xy)p_z] \\ &\quad + b[(x + X)S_x + (y + Y)S_y - 2(z + Z)S_z] + \frac{g_K b}{M_2} [X\Sigma_x + Y\Sigma_y - 2Z\Sigma_z]. \end{aligned} \quad (10.10)$$

Here we have abbreviated the Hamiltonian of the field free atom by $H_A = \frac{\mathbf{p}^2}{2} + U_1^\dagger V(\mathbf{r})U_1$. The spin operators of the electron and the nucleus are denoted as \mathbf{S} and $\boldsymbol{\Sigma}$, respectively. They are related to the corresponding magnetic moments according to

$$\boldsymbol{\mu}_1 = -\mathbf{S} \quad \text{and} \quad \boldsymbol{\mu}_2 = -\frac{eg_K}{2M_2} \boldsymbol{\Sigma}. \quad (10.11)$$

Here g_K is the g -factor of the nuclear spin. We will keep the nuclear spin term until after we have finished our investigations regarding the symmetries of the Hamiltonian (10.10).

10.3.1. Symmetries and degeneracies

The Hamiltonian (10.10) commutes with the z -component of the total angular momentum $J_z = L_z + L_Z + S_z + \Sigma_z$, i.e. $[H_Q, J_z] = 0$. This conservation of J_z is a consequence of the rotational invariance of the system around the z -axis also encountered in chapters 5 and 8. Additionally H_Q commutes with the operator $K = e^{i\pi\Sigma_x} P_Y P_Z e^{i\pi S_x} P_y P_z$ where P_Z, P_Y, P_z and P_y are parity operations. Here the upper and lower case indices refer to the c.m. and electronic (relative) coordinates, respectively. The operators K and $J_z = L_Z + L_z + S_z + \Sigma_z$ anti-commute, i.e. $\{K, J_z\} = 0$. This fact leads directly to the conclusion that there are degeneracies in the energy spectrum of the system. Proceeding similarly as in the previous chapters this is shown as follows:

Suppose $|E, m_J\rangle$ to be an energy eigenstate of the Hamiltonian H_Q and at the same time an eigenstate of J_z with the quantum number m_J . Using the anti-commutator $\{K, J_z\} = 0$ one finds

$$J_z K |E, m_J\rangle = -K J_z |E, m_J\rangle = -m_J K |E, m_J\rangle \quad (10.12)$$

Thus the state $K |E, m_J\rangle$ can be identified with $|E, -m_J\rangle$. Hence, except for $m_J \neq 0$ which can only occur in bosonic systems, these states form a degenerate pair [14].

10.3.2. Unitary and scaling transformations

Now knowing that J_z constitutes a conserved quantity it is of immediate interest to transform the Hamiltonian H_Q such that J_z appears as a canonical momentum. This way we can eliminate its canonical coordinate and will hence be in position to replace J_z by the corresponding quantum number m_J [14]. Let us first change the coordinate system as follows. For the relative motion we introduce spherical coordinates $\mathbf{r} \rightarrow (r, \theta, \phi)$ whereas for the c.m. motion cylindrical coordinates are employed, i.e. $\mathbf{R} \rightarrow (\rho, \Phi, Z)$. Applying the unitary transformation

$$U_2 = e^{-i[L_z + S_z + \Sigma_z]\Phi} \quad (10.13)$$

the Hamiltonian (10.10) is transformed into

$$\begin{aligned} U_2^\dagger H_Q U_2 &= U_2^\dagger H_A U_2 - \frac{1}{2M_2} \left[\partial_\rho^2 + \frac{1}{\rho} \partial_\rho + \partial_Z^2 - \frac{1}{\rho^2} \bar{T}_{\text{ang}} \right] \\ &\quad + bH_e + b[\boldsymbol{\mu} - \boldsymbol{\mu}_2] \cdot \mathbf{G}(\rho, Z) - \frac{3}{2} b\rho (zp_y + yp_z) \end{aligned} \quad (10.14)$$

with

$$\begin{aligned} H_e &= -zL_z + b^{-1} \mathbf{S} \cdot \mathbf{B}(\mathbf{r}) \\ &= -r \cos \theta L_z + r \sin \theta \cos \phi S_x + r \sin \theta \sin \phi S_y - 2r \cos \theta S_z \end{aligned} \quad (10.15)$$

$$\bar{T}_{\text{ang}} = (L_Z - L_z - S_z - \Sigma_z)^2 \quad (10.16)$$

and the magnetic moment $\boldsymbol{\mu} = \frac{1}{2} [\mathbf{L} + 2\mathbf{S}]$ coupling to the magnetic field $b\mathbf{G}(\rho, Z) = b(\rho, 0, -2Z)$. The transformation U_2 has removed the dependence of the c.m. motion on the azimuthal angle Φ . Thus the operator L_Z constitutes a conserved quantity in the transformed frame, i.e. $[L_Z, U_2^\dagger H_Q U_2] = 0$. With

$$U_2^\dagger J_z U_2 = L_Z \quad (10.17)$$

one easily observes that L_Z is nothing but the transformed z -component of the total angular momentum. Consequently L_Z can be replaced by the quantum number m_J .

To arrive at our final working Hamiltonian we neglect the coupling of the nuclear spin to the magnetic field, which is consistent with the approximations done previously. Taking into account the coupling of the nuclear spin to the field would lead to a negligibly small splitting of the energy levels into $2\sigma + 1$ sublevels with σ being the nuclear spin quantum number. Now that such a splitting is absent we will encounter further - trivial - degeneracies in the system. They arise from the different nuclear spin orientations being now energetically equivalent. By construction the resultant Hamiltonian commutes with Σ_z and each of the nuclear spin subspaces can be considered separately. This way we can replace Σ_z by its quantum number m_σ . For brevity we introduce the new quantum number $m_T = m_J - m_\sigma$.

As a next step we simplify the structure of the c.m. kinetic energy: The Hamiltonian $U_2^\dagger H_Q U_2$ gives rise to the stationary Schrödinger equation $U_2^\dagger H_Q U_2 |\Psi\rangle = E |\Psi\rangle$. By choosing $|\Psi\rangle = \rho^{-\frac{1}{2}} |\Phi\rangle$ we arrive at a new Hamiltonian H_F satisfying $H_F |\Phi\rangle = E |\Phi\rangle$. It reads

$$\begin{aligned} H_F &= U_2^\dagger H_A U_2 - \frac{1}{2M_2} [\partial_\rho^2 + \partial_Z^2 - \rho^{-2} T_{\text{ang}}] + bH_e + b\boldsymbol{\mu} \cdot \mathbf{G}(\rho, Z) \\ &\quad - \frac{3}{2} b\rho (zp_y + yp_z) \end{aligned} \quad (10.18)$$

with

$$T_{\text{ang}} = (L_Z - L_z - \Sigma_z - S_z)^2 - \frac{1}{4}. \quad (10.19)$$

Finally we introduce a scaling transformation for the c.m. coordinates which reads $\mathbf{P} \rightarrow \gamma^{\frac{1}{3}}\mathbf{P}$, $\mathbf{R} \rightarrow \gamma^{-\frac{1}{3}}\mathbf{R}$ with $\gamma = bM_2$. For the scaled Hamiltonian we get

$$\begin{aligned} H = M_2\gamma^{-\frac{2}{3}}H_F &= M_2\gamma^{-\frac{2}{3}}H_A - \frac{1}{2}[\partial_\rho^2 + \partial_Z^2 - \rho^{-2}T_{\text{ang}}] \\ &+ \gamma^{\frac{1}{3}}H_e + \boldsymbol{\mu} \cdot \mathbf{G}(\rho, Z) - \frac{3}{2}\rho(zp_y + yp_z). \end{aligned} \quad (10.20)$$

As from now we will refer to these scaled coordinates unless stated otherwise.

10.4. Moving Rydberg atoms in the magnetic quadrupole field

In order to solve the Schrödinger equation belonging to the Hamiltonian (10.20) an explicit form of the interaction potential $V(\mathbf{r})$ has to be provided. Here we consider the most simple case of a pure Coulomb-potential $V(\mathbf{r}) = V(r) = -\frac{1}{r}$ without accounting for relativistic corrections such as spin-orbit interaction, whose corresponding terms would be proportional to r^{-3} . For large angular momenta l which we will focus on in the following study one finds $\langle r^{-3} \rangle \propto n^{-6}$ [11] which would yield a negligibly small energy shift for sufficiently high degrees of electronic excitation. Equally, effects due to the nonhydrogenic character of the core can be neglected for high angular momentum states [61].

With having specified the interaction potential we now discuss the typical energy scales of the system: For all laboratory fields and typical nuclear masses one finds $\gamma = bM_2 \ll 1$. Thus the Hamiltonian (10.20) to zeroth order is dominated by the field-free electronic energy $M_2\gamma^{-\frac{2}{3}}H_A$. The structure of the energy spectrum of H_A is well known: The levels are arranged in highly degenerate n -multiplets. We now assume the quadrupole field not to cause a significant coupling between the n -multiplets, i.e. the inter n -manifold mixing is negligible. This approximation holds if the energetic separation between adjacent n -multiplets ΔE_A is much larger than the energy E_{zee} (Zeeman energy) contributed by the linear magnetic field terms, i.e. $\Delta E_A \gg E_{\text{zee}}$. By estimating $E_{\text{zee}} \approx b \langle \mathbf{r} \rangle \approx bn^2$ one obtains the condition $b \ll n^{-5}$. We now have to check whether this result is compatible with our initial approximation to neglect all quadratic magnetic field terms. We verify this by comparing the Zeeman energy E_{zee} with the diamagnetic energy $E_{\text{dia}} \approx b^2n^8$ (see also ref. [64]) contributed by the quadratic field terms, which yields $b \ll n^{-6}$. Hence, both approximations are compatible.

Assuming the latter inequality holds, each of the degenerate n -manifolds can be considered separately. An approximate Hamiltonian is obtained by projecting the full Hamiltonian (10.20) onto a given set of states covering an entire n -manifold. Such a subspace is spanned by the hydrogenic eigenfunctions $|\alpha\rangle = |n, l, m_l, m_s\rangle$ which in the spatial representation read

$$\langle \mathbf{r} | n, l, m_l, m_s \rangle = \frac{2}{n^2} \sqrt{\frac{(n-l-1)!}{(l+n)!}} \left(\frac{2r}{n}\right)^l e^{-\frac{r}{n}} L_{n-l-1}^{2l+1} \left(\frac{2r}{n}\right) Y_l^{m_l}(\theta, \phi) |m_s\rangle. \quad (10.21)$$

Here the functions $L_n^l(r)$ and $Y_l^{m_l}(\theta, \phi)$ are the associated Laguerre polynomials and spherical harmonics, respectively. The states $|m_s\rangle$ are the usual two-component spinors accounting for the electronic spin state. For a fixed principal quantum number n the states $|\alpha\rangle$ obey $H_A|\alpha\rangle = E_A^n|\alpha\rangle$. The quantum numbers l , m_l and m_s are those of the squared orbital angular momentum of the relative (electronic) motion \mathbf{L}_r^2 , its z -component L_z and the one of the electronic spin S_z , respectively. In a given n -subspace the Hamiltonian (10.20) becomes

$$\begin{aligned} [H]_{\alpha\alpha'} &= M_2\gamma^{-\frac{2}{3}}[H_A]_{\alpha\alpha'} - \frac{1}{2}[\partial_\rho^2 + \partial_Z^2] \delta_{\alpha\alpha'} + \frac{1}{2}\rho^{-2}[T_{\text{ang}}]_{\alpha\alpha'} + \gamma^{\frac{1}{3}}[H_e]_{\alpha\alpha'} + [\boldsymbol{\mu} \cdot \mathbf{G}(\rho, Z)]_{\alpha\alpha'} \\ &- \frac{3}{2}\rho[zp_y + yp_z]_{\alpha\alpha'} \end{aligned} \quad (10.22)$$

where the last term can be rewritten as $yp_z + zp_y = -i[yz, H_A]$. Apparently all matrix elements of this operator vanish since

$$[zp_y + yp_z]_{\alpha\alpha'} = -i \langle \alpha | [yz, H_A] | \alpha' \rangle = -i(E_A^n - E_A^n) \langle \alpha | yz | \alpha' \rangle = 0. \quad (10.23)$$

In the following we will drop the term $M_2\gamma^{-\frac{2}{3}}H_A$ yielding only a constant off-set for the total energy, namely $E_A^n = \frac{M_2}{2n^2\gamma^{\frac{2}{3}}}$. Finally, the Schrödinger equation belonging to the Hamiltonian (10.22) describes the multi-channel quantum dynamics of the c.m. where the coupling between the (electronic) channels is induced by the external inhomogeneous field. Keeping in mind that all subsequent considerations incorporate only a single n -subspace we will omit in the following the indices of the matrices/operators. The Hamiltonian then acquires the form:

$$H = -\frac{1}{2} [\partial_\rho^2 + \partial_Z^2 - \rho^{-2}T_{\text{ang}}] + \gamma^{\frac{1}{3}}H_e + \boldsymbol{\mu} \cdot \mathbf{G}(\rho, Z). \quad (10.24)$$

Here the first term represents the kinetic energy of the c.m. It is followed by a term describing the internal (electronic) dynamics of the atom. The last term represents the coupling of the magnetic moment $\boldsymbol{\mu}$, which is composed of the electronic orbital angular momentum and spin operators, to the scaled magnetic field $\mathbf{G}(\rho, Z)$.

The matrix elements that are required for assembling the Hamiltonian (10.24) were calculated by using numerical algorithms provided by the NAG library. Fortunately, the matrix elements factorize so that the radial and angular integrations can be carried out independently. In order to calculate the radial matrix elements we have employed an adaptive quadrature based on the Gauss 7-point and Kronrod 15-point rules over a semi-infinite interval. The integration over the azimuthal angle θ was performed by using an adaptive quadrature method being particularly suited for oscillating functions (Gauss 30-point and Kronrod 61-point).

10.5. The adiabatic approximation

To solve the Schrödinger equation belonging to the Hamiltonian (10.24) we pursue an adiabatic approach. We assume the motion of the (Rydberg) electron to be much faster than the one of the ultracold c.m. motion. While the c.m. is slowly moving through the inhomogeneous field the electronic dynamics is adapting rapidly to the surrounding magnetic field. We now rewrite the Hamiltonian according to

$$H = T + V(\rho, Z; \gamma, n) \quad (10.25)$$

where T is the sum of the radial and axial kinetic energy

$$T = -\frac{1}{2} [\partial_\rho^2 + \partial_Z^2] \quad (10.26)$$

and $V(\rho, Z; \gamma, n)$ designates the potential matrix

$$V(\rho, Z; \gamma, n) = \gamma^{\frac{1}{3}}H_e + \frac{1}{2}\rho^{-2}T_{\text{ang}} + \boldsymbol{\mu} \cdot \mathbf{G}(\rho, Z). \quad (10.27)$$

At first we diagonalize the potential matrix $V(\rho, Z; \gamma, n)$ by employing a spatially dependent unitary transformation $U = U(\rho, Z; \gamma, n)$:

$$U^\dagger V(\rho, Z; \gamma, n) U = E(\rho, Z; \gamma, n) \quad (10.28)$$

The column vectors of U are the normalized vector representations of the electronic eigenstates $|\chi_\kappa^n(\mathbf{r}); \mathbf{R}\rangle$ at fixed c.m. position. These column vectors are denoted by \mathbf{U}_κ . Their components read

$$[\mathbf{U}_\kappa]_\alpha = U_{\alpha\kappa} = \langle \alpha | \chi_\kappa^n(\mathbf{r}); \mathbf{R} \rangle. \quad (10.29)$$

Here the multi index α adopts all the $2n^2$ combinations of the indices l , m_l and m_s of an n -manifold. By diagonalizing $V(\rho, Z; \gamma, n)$ one obtains the adiabatic potential energy curves $E(\rho, Z; \gamma, n)$ which depend parametrically on the c.m. coordinates ρ and Z . Applying the transformation U to the total Hamiltonian (10.25) yields

$$U^\dagger H U = U^\dagger T U + U^\dagger V(\rho, Z; \gamma, n) U = T + E(\rho, Z; \gamma, n) + \Delta T = H_{\text{ad}} + \Delta T \quad (10.30)$$

with the adiabatic Hamiltonian H_{ad} and the nonadiabatic coupling matrix

$$\Delta T = -\frac{1}{2} U^\dagger \left[2 \frac{\partial U}{\partial \rho} \partial_\rho + 2 \frac{\partial U}{\partial Z} \partial_Z + \frac{\partial^2 U}{\partial \rho^2} + \frac{\partial^2 U}{\partial Z^2} \right]. \quad (10.31)$$

In the adiabatic approximation these nonadiabatic coupling elements are neglected. The total wave function of the system is then obtained as a product of the electronic, the c.m. state and the eigenstates of Σ_z and $L_Z = U_2 J_z U_2^\dagger$

$$|\Psi_{\kappa\nu}^n(\mathbf{r}, \mathbf{R}), m_J, m_\sigma\rangle = |\chi_\kappa^n(\mathbf{r}); \mathbf{R}\rangle |\Phi_\nu^n(\mathbf{R})\rangle |m_J\rangle |m_\sigma\rangle \quad (10.32)$$

with $|m_J\rangle = \frac{1}{\sqrt{2\pi}} e^{im_J\Phi}$. This gives rise to the adiabatic Schrödinger equation for the c.m. motion

$$H_{\text{ad}} |\Phi_\nu^n(\mathbf{R})\rangle = [T + E_\kappa(\rho, Z; \gamma, n)] |\Phi_\nu^n(\mathbf{R})\rangle = \varepsilon_\nu |\Phi_\nu^n(\mathbf{R})\rangle \quad (10.33)$$

whose solutions $|\Phi_\nu^n(\mathbf{R})\rangle$ are the adiabatic c.m. wave functions. In equation (10.32) the index κ

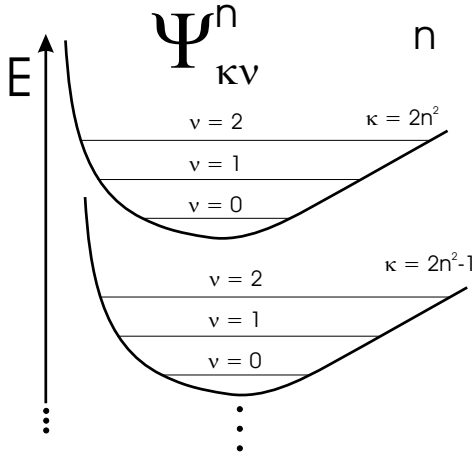


Figure 10.1.: Term symbol of the adiabatic quantum states. The index κ labels the $2n^2$ energy surfaces in a given n -subspace for fixed γ and m_T . By convention the energetically highest surfaces is labelled by $\kappa = 2n^2$. The index ν labels the c.m. quantum states in the energy surface defined by κ and n .

labels the adiabatic energy surface whereas ν denotes the degree of excitation of the c.m. state (see figure 10.1).

Having obtained the adiabatic states and therefore knowing the structure of U the elements of the nonadiabatic coupling matrix (10.31) can be explicitly calculated employing the expressions

$$\left(U^\dagger \frac{\partial U}{\partial X} \right)_{\kappa'\kappa} = \mathbf{U}_{\kappa'}^\dagger \frac{\partial \mathbf{U}_\kappa}{\partial X} = \langle \chi_{\kappa'}^n(\mathbf{r}); \mathbf{R} | \frac{\partial}{\partial X} | \chi_\kappa^n(\mathbf{r}); \mathbf{R} \rangle = \frac{1}{E_\kappa - E_{\kappa'}} \mathbf{U}_{\kappa'}^\dagger \frac{\partial H}{\partial X} \mathbf{U}_\kappa \quad (10.34)$$

$$\left(U^\dagger \frac{\partial^2 U}{\partial X^2} \right)_{\kappa'\kappa} = \langle \chi_{\kappa'}^n(\mathbf{r}); \mathbf{R} | \frac{\partial^2}{\partial X^2} | \chi_\kappa^n(\mathbf{r}); \mathbf{R} \rangle \quad (10.35)$$

$$= \frac{1}{E_\kappa - E_{\kappa'}} \left[\mathbf{U}_{\kappa'}^\dagger \frac{\partial^2 H}{\partial X^2} \mathbf{U}_\kappa + \sum_{\kappa''} \frac{2}{E_\kappa - E_{\kappa''}} \left(\mathbf{U}_{\kappa'}^\dagger \frac{\partial H}{\partial X} \mathbf{U}_{\kappa''} \right) \left(\mathbf{U}_{\kappa''}^\dagger \frac{\partial H}{\partial X} \mathbf{U}_\kappa \right) - \frac{\partial E_\kappa}{\partial X} \frac{2}{E_\kappa - E_{\kappa'}} \mathbf{U}_{\kappa'}^\dagger \frac{\partial H}{\partial X} \mathbf{U}_\kappa \right]$$

with X being a placeholder for the coordinates ρ and Z , respectively. Consequently nonadiabatic transitions can be neglected if

$$\left| \frac{\langle \chi_{\kappa'}^n(\mathbf{r}); \mathbf{R} | \frac{\partial H}{\partial X} | \chi_{\kappa}^n(\mathbf{r}); \mathbf{R} \rangle}{E_{\kappa'} - E_{\kappa}} \right| \ll 1 \quad \text{and} \quad \left| \frac{\langle \chi_{\kappa'}^n(\mathbf{r}); \mathbf{R} | \frac{\partial^2 H}{\partial X^2} | \chi_{\kappa}^n(\mathbf{r}); \mathbf{R} \rangle}{E_{\kappa'} - E_{\kappa}} \right| \ll 1. \quad (10.36)$$

Provided that the matrix elements $\langle \chi_{\kappa'}^n(\mathbf{r}); \mathbf{R} | \frac{\partial H}{\partial X} | \chi_{\kappa}^n(\mathbf{r}); \mathbf{R} \rangle$ and $\langle \chi_{\kappa'}^n(\mathbf{r}); \mathbf{R} | \frac{\partial^2 H}{\partial X^2} | \chi_{\kappa}^n(\mathbf{r}); \mathbf{R} \rangle$ are well-behaved the energy denominator of the formulae (10.34) and (10.35) indicates that nonadiabatic transitions between the adiabatic energy surfaces are highly likely to occur in the vicinity of avoided crossings. In figure 10.2 we present the typical appearance of an intersection $E(\rho, Z; \gamma, n)$ through

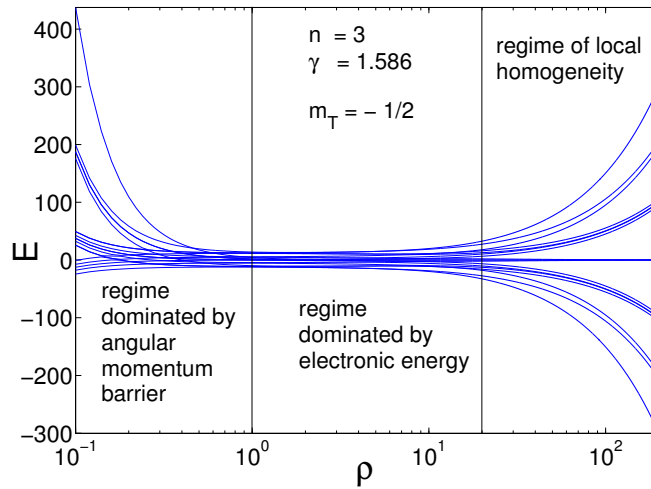


Figure 10.2.: Intersection at $Z = 0$ through the adiabatic potential energy surfaces of the $n = 3$ -multiplet. One can distinguish three regimes: In the angular momentum dominated regime all energy surfaces except for the lowest one exhibit a ρ^{-2} -dependence. It is followed by a regime dominated by the electronic energy. For large values of ρ one clearly recognizes the Zeeman-splitting indicating the limit of local homogeneity. All quantities are given in scaled units, i.e. energies in units of $M_2 \gamma^{-\frac{2}{3}}$ and lengths in units of $\gamma^{-\frac{1}{3}}$.

the adiabatic potential energy surfaces. For reasons of illustration we have chosen the $n = 3$ multiplet and the value $\gamma = 1.586$ which is beyond the regime accessible by laboratory experiments. However, this example provides us with some useful insights into the general structure of the energy surfaces holding in particular also for Rydberg states. For small ρ , i.e. in the vicinity of the center of the field, the angular momentum barrier $\rho^{-2} T_{\text{ang}}$ dominates the potential matrix (10.27). Here we observe a splitting into a number of grouped components. Moving away from the trap center we first encounter a regime where the adiabatic energy surfaces are determined by the electronic energy due to H_e . In even further distance from the field center the so-called limit of local homogeneity is reached. Here the coupling to the magnetic field is mainly established by the various electronic angular momentum and spin orientations of the Rydberg atom. The energy surfaces group into $2n + 1$ branches. In the following we provide a more detailed discussion of the individual regimes.

10.5.1. The angular momentum barrier and the avoided crossings near the Z -axis

In the vicinity of the trap center ($Z \rightarrow 0, \rho \rightarrow 0$) the potential matrix (10.27) can be roughly approximated by

$$V(\rho, Z; \gamma, n) = \frac{1}{2\rho^2} T_{\text{ang}} = \frac{1}{2\rho^2} \left[(m_T - L_z - S_z)^2 - \frac{1}{4} \right]. \quad (10.37)$$

with $m_T = m_J - m_\sigma$ as defined previously. Replacing L_z and S_z by their respective quantum numbers m_l and m_s we find the following analytic expression for the adiabatic potential surfaces:

$$E(\rho, Z; \gamma, n) = E(\rho, m_l, m_s) = \frac{1}{2\rho^2} \left[(m_T - m_l - m_s)^2 - \frac{1}{4} \right]. \quad (10.38)$$

Since $m_l \in [-n+1, -n+2, \dots, n-2, n-1]$ and $m_s = \pm\frac{1}{2}$ there is only a limited number ζ of possible values which can be assumed by $(m_T - m_l - m_s)^2$ provided that m_T is fixed. One finds

$$\zeta = \begin{cases} 2n & |m_T| \geq n - \frac{1}{2} \\ 2n - ||m_T| - n + \frac{1}{2}| - \alpha_s & |m_T| < n - \frac{1}{2} \end{cases}. \quad (10.39)$$

Here α_s is equal to $\frac{1}{2}$ if the quantum number m_T is integer and zero otherwise. Thus for $\rho \rightarrow 0$ one finds a splitting of the energy surfaces into ζ branches. For bosons the numerator of equation (10.38) can become zero. In this particular case there is no angular momentum barrier and hence no ρ^{-2} -dependence visible. This feature is striking at the lowest branch in figure 10.2. If we now

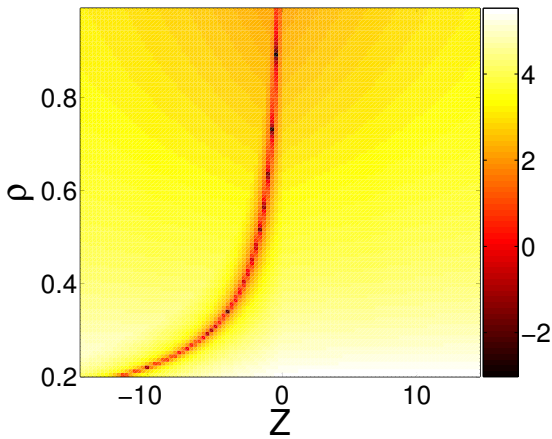


Figure 10.3.: Energetic separation ($\delta = E_{\kappa'}(\rho, Z; \gamma, n) - E_{\kappa}(\rho, Z; \gamma, n)$) of the two uppermost potential surfaces ($\kappa' = 2 \cdot 10^2$, $\kappa = 2 \cdot 10^2 - 1$). The plot shows $\log(|\delta|)$ for $n = 10$, $\gamma = 1.59 \times 10^{-7}$, $m_T = 0.5$. The (avoided) crossing in the negative Z -half plane is clearly visible. In order to ensure the applicability of the adiabatic approximation the c.m. motion has to be kept away from the Z -axis. All quantities are given in scaled units, i.e. energies in units of $M_2\gamma^{-\frac{2}{3}}$ and lengths in units of $\gamma^{-\frac{1}{3}}$.

consider the c.m. motion parallel to the Z axis for small values of ρ the potential matrix is still diagonal in the L_z and S_z basis function yielding the potential curves:

$$E(\rho, m_l, m_s) = \frac{1}{2\rho^2} \left[(m_T - m_l - m_s)^2 - \frac{1}{4} \right] - Z [m_l + 2m_s]. \quad (10.40)$$

For $Z > 0$ and $m_T \geq 0$ the uppermost $\kappa = 2n^2$ energy surface is apparently found in the $m_l = -(n-1)$ and $m_s = -\frac{1}{2}$ subspace. For $Z < 0$ the situation is somewhat different. For large negative Z the energetically highest potential curve is defined through $m_l = n-1$ and $m_s = \frac{1}{2}$. Hence there has to occur at least one (avoided) crossing when going from large negative to large positive values of Z . This is illustrated in figure 10.3 where we present the energetic separation of the two uppermost potential surfaces $\delta = E_{\kappa'}(\rho, Z; \gamma, n) - E_{\kappa}(\rho, Z; \gamma, n)$. Following the same line of argument it can be shown that for negative values of m_T the avoided crossing is found in the positive Z -half-plane. Since the occurrence of such avoided crossings is inevitable the adiabatic approximation necessarily breaks down in the vicinity of the Z -axis. Thus adiabatic c.m. states must not penetrate this central region.

10.5.2. The regime of local homogeneity

For $Z, \rho \gg 1$, i.e. the c.m. being located far away from the center of the quadrupole field, the potential matrix (10.27) can be approximately written as

$$V(\rho, Z, \gamma, n) = \boldsymbol{\mu} \cdot \mathbf{G}(\rho, Z). \quad (10.41)$$

This is feasible since H_e is constant whereas the influence of $\boldsymbol{\mu} \cdot \mathbf{G}(\rho, Z)$ grows with increasing displacement from the trap center. After applying the unitary transformation

$$U_r = e^{-i(L_y + S_y)\beta} \quad (10.42)$$

with $\sin \beta = \rho |\mathbf{G}(\rho, Z)|^{-1}$ and $\cos \beta = -2Z |\mathbf{G}(\rho, Z)|^{-1}$ one finds

$$U_r^\dagger V(\rho, Z, \gamma, n) U_r = \frac{1}{2} [L_z + 2S_z] \sqrt{\rho^2 + 4Z^2}. \quad (10.43)$$

Thus, the adiabatic potential curves evaluate to

$$E(\rho, Z, \gamma, n) = E(\rho, Z, m_l, m_s) = \frac{1}{2} [m_l + 2m_s] \sqrt{\rho^2 + 4Z^2} \quad (10.44)$$

with m_l and m_s being the respective eigenvalues of L_z and S_z . The possible combinations of the two eigenvalues yield $2n + 1$ energy surfaces. The transformation U_r rotates the electronic spin and orbital angular momentum such that they are parallel to the local direction of the magnetic field. Thus the operators L_z and S_z are not identical to the ones referred to in the previous section but are here related to the local quantization axis defined by the direction of the local magnetic field.

Since we now have an analytical expression for the unitary transformation which diagonalizes the potential matrix the off-diagonal elements of the kinetic energy operator can be calculated analytically:

$$\begin{aligned} \Delta T = & -\frac{1}{2} \left[i \frac{L_y + S_y}{|\mathbf{G}(\rho, Z)|} [2 \cos \beta \partial_\rho + 4 \sin \beta \partial_Z] + 6i \frac{L_y + S_y}{|\mathbf{G}(\rho, Z)|^2} \sin \beta \cos \beta \right. \\ & \left. + \frac{(L_y + S_y)^2}{|\mathbf{G}(\rho, Z)|^2} (1 + 3 \sin^2 \beta) \right] \end{aligned} \quad (10.45)$$

All terms in equation (10.45) involve inverse powers of the modulus of the scaled magnetic field $\mathbf{G}(\rho, Z)$ and therefore vanish for large distances from the trap center. Thus in the regime of local homogeneity - where $Z, \rho \gg 1$ is required - nonadiabatic transitions between the adiabatic energy surfaces can be safely neglected.

10.5.3. The regime being dominated by the electronic energy

In the potential matrix (10.27) the electronic energy is represented by the term $\gamma^{\frac{1}{3}} H_e$. As already shown its energetic contribution can be estimated by $E_e \approx n^2 \gamma^{\frac{1}{3}}$ which should not obscure the fact, that E_e depends on the individual states of an n -manifold. Thus the influence of the electronic energy on the potential surface strongly depends on the value of γ and the degree of electronic excitation. If E_e is of the order of one or larger the occurrence of a more or less pronounced electronic energy dominated regime is expected. On the other hand the angular momentum barrier grows dramatically for small ρ and the magnetic interaction becomes dominant for large values of ρ and Z . Thus, if at all the electronic energy can only dominate close to $Z = 0$ and for values of ρ being of the order of one. The spectrum of H_e is two-fold degenerate. Thus the energy surfaces tend to arrange pairwise in the spatial regions where H_e is dominant. Consequently nonadiabatic couplings and transitions among the adiabatic energy surfaces are supposed to be highly likely, i.e. ubiquitous in this regime. A detailed analysis of the structure of H_e can be found in chapter 8.

10.6. Quantized center of mass motion

According to the above discussion the adiabatic approximation is applicable if the c.m. motion takes place sufficiently far away from the axis of the quadrupole trap. This can be achieved by

increasing the value of the quantum number m_T which effectively pushes the angular momentum barrier towards larger values of ρ . Additionally the influence of the internal (electronic) Hamiltonian has to be suppressed. Fortunately the influence of $\gamma^{\frac{1}{3}}H_e$ can be controlled rather easily. As it does not depend on the c.m. coordinates but solely on the electronic state considered, this term can only become dominant in-between the regime dominated by the angular momentum barrier and the regime where the limit of local homogeneity is established. Here the part of the potential matrix $V(\rho, Z; \gamma, n)$ which depends on the c.m. coordinates becomes minimal. This minimal energy has to be much larger than the energy E_e which is associated to the internal atomic motion in order to suppress the influence of $\gamma^{\frac{1}{3}}H_e$. Our goal in the following is twofold. First we want to establish

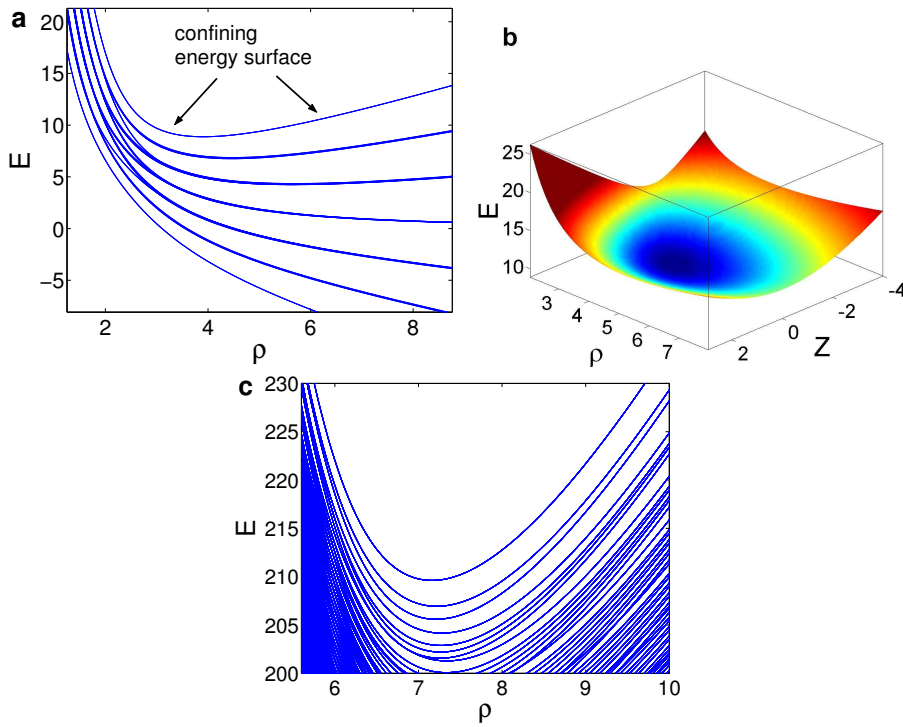


Figure 10.4.: **a:** Intersection $E(\rho, Z = -0.5; \gamma, n)$ through the complete $n = 3$ -manifold ($\gamma = 1.59 \times 10^{-6}$ and $m_T = 9.5$). The energetically uppermost $\kappa = 2n^2$ surface is well isolated from other surfaces and possesses a pronounced minimum. **b:** Energetically highest adiabatic energy surface for the same set of parameters. The well-pronounced minimum of this particular potential surface is found at $(\rho_0, Z_0) = (3.95, -0.50)$. **c:** In higher n -manifolds the number of energy surfaces increases. But still the uppermost energy surface is isolated from the others below and exhibits a pronounced minimum being capable of trapping c.m. states. The intersection shown is made for the following set of parameters: $Z = -1.64$, $n = 39$, $m_T = 84.5$, $\gamma = 1.59 \times 10^{-10}$. All quantities are given in scaled units, i.e. energies in units of $M_2\gamma^{-\frac{2}{3}}$ and lengths in units of $\gamma^{-\frac{1}{3}}$.

the existence of confined c.m. states. We will show that trapping of the c.m. motion is possible thereby arriving at quantized c.m. states. Thereafter we will demonstrate the beautiful interplay of the c.m. and electronic motion in the quadrupole field focussing on states for which both the c.m. and electronic wave functions are of similar size.

As a first example let us consider the cut through the $n = 3$ energy surfaces which is presented in figure 10.4a. Only a subset of the surfaces shown can provide complete confinement of the c.m. motion. To our opinion the uppermost potential energy surface ($\kappa = 2n^2$) which is depicted in figure 10.4b is suited best for this purpose. It possesses a pronounced minimum and - unlike others - it is well isolated from neighboring surfaces in the vicinity of its minimum which is located at $(\rho_0, Z_0) = (3.95, -0.50)$. In the local homogeneity limit the separation of the $\kappa = 2n^2$ and

$\kappa = 2n^2 - 1$ surface increases as $\frac{1}{2}\sqrt{\rho^2 + 4Z^2}$. Here the second and third surface are found to become approximately degenerate which is expected to lead to nonadiabatic transitions. For comparison we present in figure 10.4c an intersection through a set of energy surfaces belonging to the highly excited $n = 39$ multiplet. Here all features already shown for $n = 3$ are equally present. However, due to the large number of electronic states ($2n^2$) the electronic structure becomes more complex.

10.6.1. Confined quantum states of the center of mass motion

The quantized c.m. state are obtained by solving the eigenvalue problem of the adiabatic Hamiltonian which is defined through equation (10.30). Since the potential surfaces are already given on a two-dimensional grid we employ a grid-based method to find the eigenvalues and wave functions. The fundamentals of this procedure are briefly outlined in section 3.3.

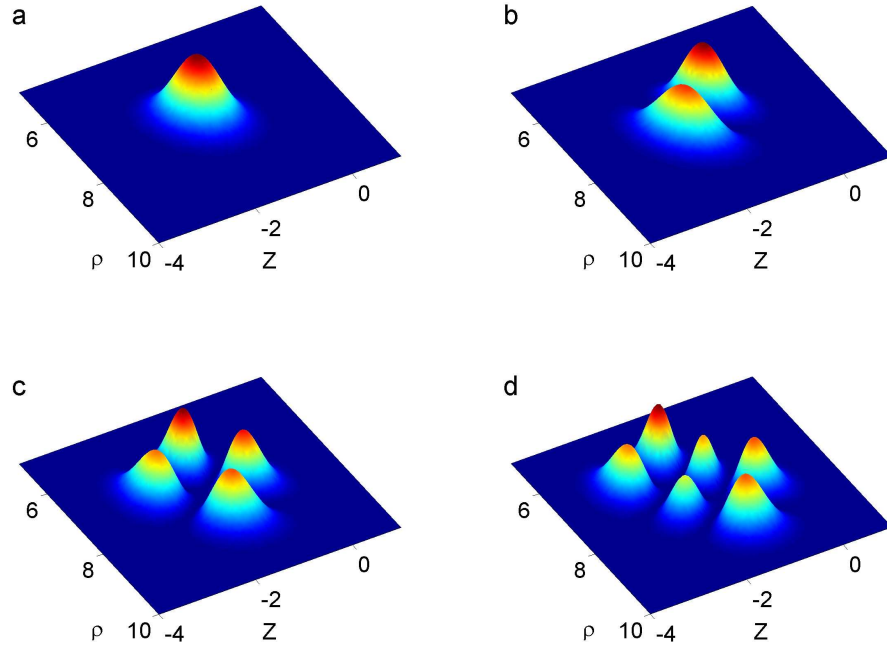


Figure 10.5.: Ground state ($\varepsilon_0 = 3.494$) **a**, second ($\varepsilon_2 = 7.860$) **b**, fourth ($\varepsilon_4 = 10.300$) **c** and seventh ($\varepsilon_7 = 12.739$) **d** excited state of the quantized c.m. motion in the $\kappa = 2 \times n^2$ -th potential surface in the $n = 39$ multiplet ($\gamma = 1.586 \times 10^{-10}$, $m_T = 84.5$). This corresponds to a ^{87}Rb atom in a quadrupole field with a gradient $b = 10^{-15} = 4.44 \frac{T}{m}$. All lengths are given in units of $\gamma^{-\frac{1}{3}}$.

In figure 10.5 we present the probability density of a few c.m. quantum states which are found in the energetically highest energy surface of the $n = 39$ multiplet ($\kappa = 2 \times 39^2$). The values of γ and m_T are 1.586×10^{-10} and $m_T = 84.5$, respectively, which in case of a ^{87}Rb atom translates to a gradient of $b = 10^{-15} = 4.44 \frac{T}{m}$. We will mostly refer to the latter set of values since the ^{87}Rb atom is used by many experiments and a gradient $4.44 \frac{T}{m}$ is easily realizable even by a macroscopic setup such as anti-Helmholtz coils (see chapter 2). In table 10.1 we present the energies of the c.m. quantum numbers for various combinations of the parameters n , m_T and γ . The typical 'trap frequency' of the confined c.m. states can be estimated by $\nu_{\text{trap}} = \gamma^{\frac{2}{3}} M_2^{-1}$. Using the term 'trap frequency' shall not obscure the fact that the confining energy surfaces in general are strongly anharmonic. To provide an example we present the Taylor expansion of the potential surface giving

n	m_T	γ	ν_{trap} [kHz]	ε_0	ε_1	ε_2	ε_3	ε_4	ε_5	ε_6
19	± 24.5	$1.586 \cdot 10^{-8}$	266.5	4.065	6.281	8.399	8.793	10.467	11.045	12.440
25	± 59.5	$1.586 \cdot 10^{-9}$	57.4	2.866	4.952	6.310	7.035	8.368	9.115	9.618
35	± 64.5	$1.586 \cdot 10^{-10}$	12.4	3.666	6.108	8.306	8.571	10.696	11.047	12.718
38	± 84.5	$1.586 \cdot 10^{-10}$	12.4	3.394	5.824	7.621	8.254	10.028	10.684	11.704
39	± 84.5	$1.586 \cdot 10^{-10}$	12.4	3.494	5.960	7.860	8.427	10.300	10.895	12.064

Table 10.1.: Ground state energy and the first six excited energies for selected parameters n , m_T and γ . A constant energy off-set corresponding to the minimum of the respective energy surface has been subtracted. The frequency unit $\nu_{\text{trap}} = \gamma^{\frac{2}{3}} M_2^{-1}$ for ^{87}Rb is also provided. The strongly varying level spacing results from the anharmonicity of the confining energy surface (see equation (10.47)).

rise to the states presented in figure 10.5. Up to fourth order it reads

$$E(\rho, Z) = \sum_{i,j=0}^4 c_{mn} (Z - Z_0)^m (\rho - \rho_0)^n \quad (10.46)$$

with the coefficient matrix

$$c_{mn} = \begin{pmatrix} 209.621 & -0.125 & 10.293 & -2.329 & -0.204 \\ -0.582 & 0 & 3.439 & -1.009 & 0 \\ 3.046 & -0.785 & 1.047 & 0 & 0 \\ 0.275 & 0.994 & 0 & 0 & 0 \\ -0.161 & 0 & 0 & 0 & 0 \end{pmatrix} \quad (10.47)$$

and $(Z_0, \rho_0) = (-1.6, 7.2)$. The surface has been aligned with the principal axes which are defined by the eigenvectors of the Hessian matrix. In figure (10.6) we illustrate the quality of this approx-

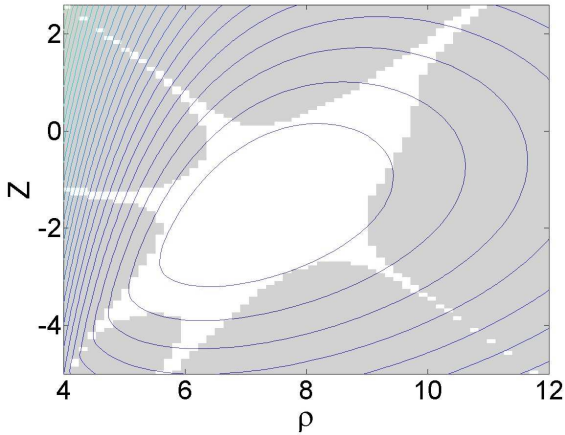


Figure 10.6.: Quality of the Taylor expansion (10.47). In the highlighted region the agreement with the exact result is better than 1%. The contourlines also show the distinct anharmonicity and anisotropy of the potential surface.

imation. In the light region the relative discrepancy of the approximated potential surface with respect to the exact one is less than 1%. Thus for calculating the c.m. ground state both surfaces should yield almost equal results.

In case of ^{87}Rb the 'trap frequency' ν_{trap} can range from 10 kHz (at a gradient $b \approx 1 \frac{T}{m}$) to 10 MHz ($b = 10^5 \frac{T}{m}$). For the realization of the latter gradients, microstructures such as atom chips (see section 2.4), seem to be the most promising tool rather than macroscopic setups. However, while dealing with such high gradients the validity of the relations $b \ll n^{-6}$ has to be ensured.

10.6.2. Properties of the combined quantized center of mass and Rydberg states

We are now going to analyze the properties of the fully quantized states, i.e. of the combined external (c.m.) and internal (electronic) motions. We exclusively focus on a regime where the influence of the electronic Hamiltonian $\gamma^{\frac{1}{3}}H_e$ is negligible, i.e. comparatively small gradients b and high quantum numbers m_T . We first analyze the radial extension of the electronic $\langle r \rangle$ and the c.m. $\langle R \rangle$ wave functions. The corresponding expectation values are calculated according to

$$\langle R \rangle = \left\langle \sqrt{(\rho - \langle \rho \rangle)^2 + (Z - \langle Z \rangle)^2} \right\rangle = \langle \Phi_\nu^n(\mathbf{R}) | \sqrt{(\rho - \langle \rho \rangle)^2 + (Z - \langle Z \rangle)^2} | \Phi_\nu^n(\mathbf{R}) \rangle \quad (10.48)$$

$$\langle r \rangle = \langle \Phi_\nu^n(\mathbf{R}) | \langle \chi_\kappa^n(\mathbf{r}); \mathbf{R} | r | \chi_\kappa^n(\mathbf{r}); \mathbf{R} \rangle | \Phi_\nu^n(\mathbf{R}) \rangle. \quad (10.49)$$

In figure 10.7a we present $\langle r \rangle$ and $\langle R \rangle$ for the 10 lowest c.m. states in the uppermost potential

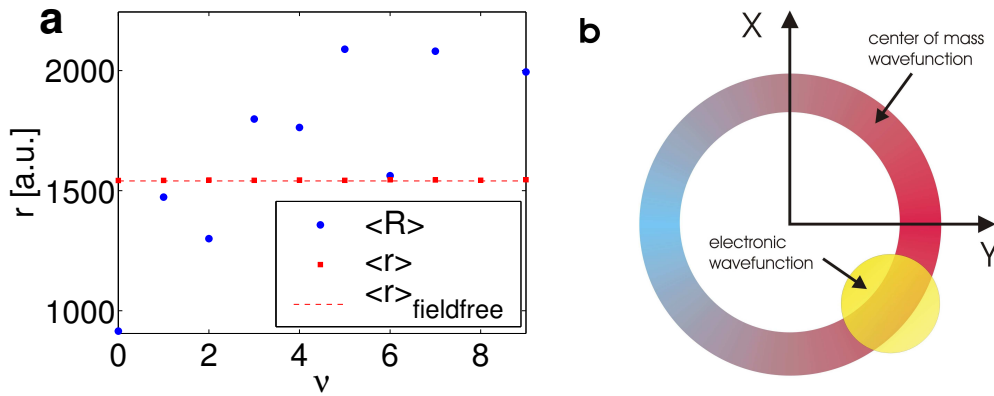


Figure 10.7.: **a:** Expectation values of the radial coordinate of the c.m. states $\langle R \rangle$ and the electronic wave function $\langle r \rangle$ of the ν -th excited c.m. state in the uppermost potential curve with $n = 39$, $\gamma = 1.586 \times 10^{-10}$ and $m_T = 84.5$. The radial expectation value for the field free case is indicated by the dashed line. **b:** Schematic view of the proportions of the electronic and c.m. wave function for the c.m. ground state. The radial extension of the electronic cloud exceeds that of the c.m. wave function.

curve ($\kappa = 2n^2$) defined by the parameters $n = 39$, $\gamma = 1.586 \times 10^{-10}$ and $m_T = 84.5$. Remarkably, $\langle R \rangle$ and $\langle r \rangle$ are of the same order of magnitude. The radial extension of the electronic wave function remains virtually unchanged at a mean value of $\langle \bar{r} \rangle = 1543.8 a.u.$. This value barely differs from the field free result $\langle r \rangle_{\text{fieldfree}} = 1540.5 a.u.$ (see dashed line in figure 10.7a) which is calculated by assuming the electron to occupy the maximum orbital angular momentum state, i.e. $l = n - 1$. This finding suggests that the uppermost potential surface is formed by the electronic states with highest orbital angular momentum in a given n -subspace. The smallness of the discrepancy between $\langle \bar{r} \rangle$ and $\langle r \rangle_{\text{fieldfree}}$ indicates that for the given set of parameters the electronic cloud suffers almost no global deformation from the external magnetic field. Unlike $\langle r \rangle$ the radial extension of the c.m. wave function increases with increasing degree of excitation. Most interestingly the ground state as well as the first and second excited state possess a radial extension which lies below that of the electronic wave function. For the ground state, for instance, one finds a ratio of $\langle r \rangle / \langle R \rangle = 1.69$. This corroborates the statement that our Rydberg atoms cannot be considered to be point like. A schematic view of the proportions is presented in figure 10.7b. The c.m. wave function is localized in concentric tubes around the z -axis, whereas the electronic state possesses approximately a spherical symmetry and is superimposed on the c.m. motion in the tubes. The mere fact that $\langle r \rangle$ deviates only little from its field-free value suggests that the squared electronic angular momentum L_r^2 is approximately conserved. Calculating the commutator with the Hamiltonian (10.24) by employing the relation

$$[L_r^2, \mathbf{r}] = 2\mathbf{r} + 2i\mathbf{r} \times \mathbf{L}_r \quad (10.50)$$

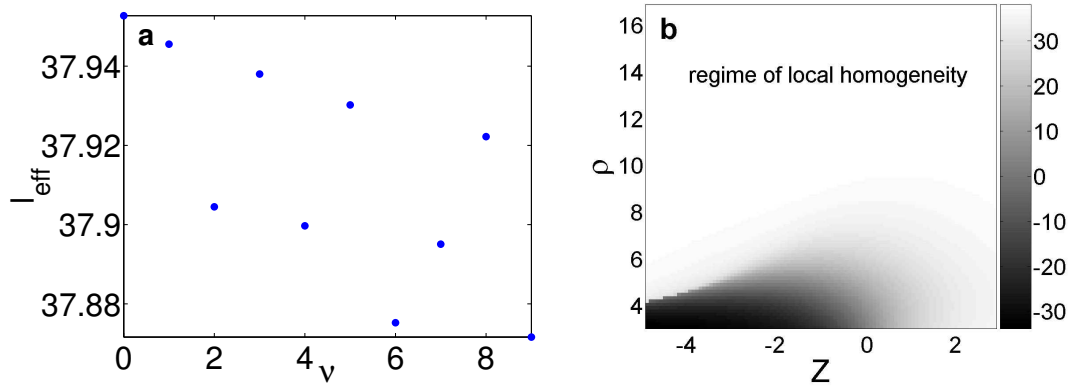


Figure 10.8.: **a:** Effective quantum number $l_{\text{eff}} = \sqrt{\langle L_r^2 \rangle + \frac{1}{4}} - \frac{1}{2}$ of the square electronic angular momentum. The data are calculated for $(n = 39, m_T = 84.5, \gamma = 1.586 \times 10^{-10})$. In the field free case a maximal value of $l = n - 1 = 38$ is expected. The small deviation from this value indicate an approximate conservation of L_r^2 . The admixture of lower l states increases for higher excitations of the c.m. motion. **b:** Projection of the electronic angular momentum onto the magnetic field vector. Once the region of local homogeneity is reached the projection remains at a constant value of $\Lambda(\rho, Z) = n - 1 = 38$. All lengths are given in units of $\gamma^{-\frac{1}{3}}$.

yields

$$[L_r^2, H] = \gamma^{\frac{1}{3}} [L_r^2, H_e] = 2\gamma^{\frac{1}{3}} \{H_e - i[xL_y - yL_x]L_z + i\mathbf{S} \cdot \mathbf{B}(\mathbf{r} \times \mathbf{L}_r)\}. \quad (10.51)$$

Hence if γ tends to zero L_r^2 will constitute a conserved quantity and consequently l will be a good quantum number. For finite but small γ L_r^2 remains approximately conserved. Interestingly only the electronic Hamiltonian $\gamma^{\frac{1}{3}}H_e$ contributes to the above commutator. Thus the conservation of L_r^2 should be more manifest in spatial regions where the influence of $\gamma^{\frac{1}{3}}H_e$ is small. In figure 10.8a we present the effective electronic angular momentum quantum number $l_{\text{eff}} = \sqrt{\langle L_r^2 \rangle + \frac{1}{4}} - \frac{1}{2}$ of the first ten c.m. states. The data points lie below $l = n - 1 = 38$ which is the highest possible value that can be assumed by $\langle L_r^2 \rangle$. This indicates mixing with lower angular momentum states. Whereas the c.m. ground state exhibits smaller l -mixing effects the admixture of lower l states increases for a higher degree of excitation.

Apart from its absolute value it is also interesting to analyze the orientation of the electronic angular momentum vector in space. In figure 10.8b we present the local expectation value of the projection of \mathbf{L}_r onto the local magnetic field direction defined by the vector $\frac{\mathbf{B}(\mathbf{R})}{|\mathbf{B}(\mathbf{R})|}$. Accounting for the correct transformation of this observable one finds

$$\begin{aligned} \Lambda(\rho, Z) &= \left\langle U_2^\dagger \left[\mathbf{L}_r \cdot \frac{\mathbf{B}(\mathbf{R})}{|\mathbf{B}(\mathbf{R})|} \right] U_2 \right\rangle \\ &= \left\langle \mathbf{L}_r \cdot \frac{\mathbf{G}(\mathbf{R})}{|\mathbf{G}(\mathbf{R})|} \right\rangle = \langle \chi_\kappa^n(\mathbf{r}); \mathbf{R} | \mathbf{L}_r \cdot \frac{\mathbf{G}(\mathbf{R})}{|\mathbf{G}(\mathbf{R})|} | \chi_\kappa^n(\mathbf{r}); \mathbf{R} \rangle. \end{aligned} \quad (10.52)$$

Near the magnetic field axis $\Lambda(\rho, Z)$ is varying strongly whereas it remains virtually constant for large values of ρ . In the latter case one finds $\Lambda(\rho, Z) = n - 1 = 38$. This is precisely the value which is expected to be assumed by the $\kappa = 2n^2$ energy surface according to the discussion of the regime of local homogeneity in section 10.5.2, i.e. the angular momentum is aligned with the field. In this sense the angular momentum of the electronic wave function of the confined ultracold Rydberg states maps or probes the local direction of the field.

In section 8.8 we have seen that once an atom is exposed to the three-dimensional quadrupole field it can develop large permanent electric dipole moments. We now analyze whether a similar

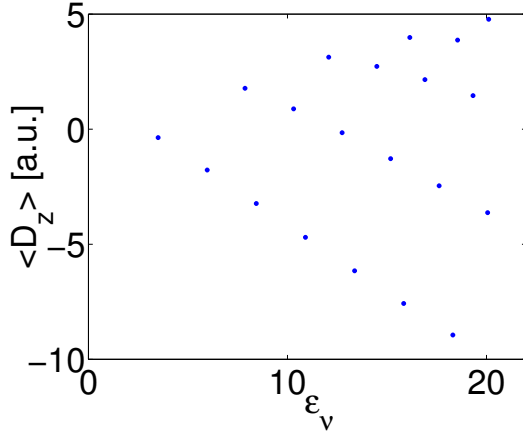


Figure 10.9.: Electric dipole moment $\langle z \rangle$ plotted against the energy of the 20 lowest c.m. states in the $n = 39$ multiplet ($m_T = 84.5$, $\gamma = 1.586 \times 10^{-10}$). $\langle D_z \rangle$ increases systematically with increasing c.m. energy ϵ_ν .

feature is found in the present system. For this purpose we calculate the expectation value of the z -component of the dipole operator $\mathbf{D} = \mathbf{r}$. The data for the 20 lowest c.m. states in the $n = 39$ multiplet ($m_T = 84.5$, $\gamma = 1.586 \times 10^{-10}$) is presented in figure 10.9. Whereas the c.m. ground state exhibits almost no electric dipole moment we find $\langle D_z \rangle$ to systematically increase with the c.m. energy ϵ_ν . Compared to the dipole moments which were observed in section 8.8 the present results are four orders smaller in magnitude. This is simply a consequence of the small field gradient which does not severely alter the atomic structure. In this context we have already seen the angular momentum of the electronic states not to be significantly mixed by the magnetic field. Thus it is not surprising to observe only small dipole moments as their emergence solely relies on the mixing of parity eigenstates. The latter, of course, do not exhibit any permanent dipole moment.

10.6.3. Radiative decay of trapped atoms

In the framework of the dipole approximation the likelihood of an electronic transition between the initial state $|i\rangle$ and a final state $|f\rangle$ is proportional to the square of the dipole matrix element

$$D_{i \rightarrow f}^e = \langle i | \mathbf{e} \cdot \mathbf{D} | f \rangle. \quad (10.53)$$

Depending on the polarization of the emitted / absorbed light this unit vector \mathbf{e} becomes $\mathbf{e} = \mathbf{e}_z$ for linear polarized light (π -transition) or $\mathbf{e} = \frac{1}{\sqrt{2}}(\mathbf{e}_x \pm i\mathbf{e}_y) = \mathbf{e}_\pm$ for circular polarized light (σ^\pm -transition). The unit vectors \mathbf{e}_k span a Cartesian coordinate system with the direction of \mathbf{e}_z being defined by the symmetry axis of the quadrupole trap. Once having evaluated the dipole matrix element the decay rate Γ of the transition is obtained via

$$\Gamma = \frac{4}{3} \frac{\omega^3}{c^3} |D_{i \rightarrow f}^e|^2 \quad (10.54)$$

with ω being the transition frequency. When calculating transitions between two of the states (10.32) one has to transform the dipole operator to the frame where $L_Z = U_2^\dagger J_z U_2$ is conserved. Thus the dipole matrix elements between the ν' -th c.m. state in the κ' -th energy surface to the ν -th c.m. state in the κ -th energy surface reads

$$\begin{aligned} D_{n'\kappa'\nu' \rightarrow n\kappa\nu}^e &= \left\langle \Psi_{\kappa'\nu'}^{n'}(\mathbf{r}, \mathbf{R}), m'_{\kappa'}, m'_{\sigma} \left| U_2^\dagger \mathbf{e} \cdot \mathbf{D} U_2 \right| \Psi_{\kappa\nu}^n(\mathbf{r}, \mathbf{R}), m_J, m_\sigma \right\rangle \\ &= \left\langle \Phi_{\nu'}^{n'}(\mathbf{R}) \left| \langle m'_J \right| \left\langle \chi_{\kappa'}^{n'}(\mathbf{r}); \mathbf{R} \left| U_2^\dagger \mathbf{e} \cdot \mathbf{D} U_2 \right| \chi_{\kappa}^n(\mathbf{r}); \mathbf{R} \right\rangle |m_J\rangle \left| \Phi_{\nu}^n(\mathbf{R}) \right\rangle \langle m'_{\sigma} | m_\sigma \rangle \\ &= \left\langle \Phi_{\nu'}^{n'}(\mathbf{R}) \left| \langle m'_J \right| D_{n'\kappa'\nu' \rightarrow n\kappa\nu}^e(\mathbf{R}) |m_J\rangle \left| \Phi_{\nu}^n(\mathbf{R}) \right\rangle \delta_{m'_{\sigma} m_\sigma} \right. \end{aligned} \quad (10.55)$$

with the electronic transition dipole moment

$$D_{n'\kappa'n\kappa}^e(\mathbf{R}) = \left\langle \chi_{\kappa'}^{n'}(\mathbf{r}); \mathbf{R} \mid U_2^\dagger \mathbf{e} \cdot \mathbf{D} U_2 \mid \chi_{\kappa}^n(\mathbf{r}); \mathbf{R} \right\rangle. \quad (10.56)$$

From equation (10.55) one immediately finds the selection rule $m'_\sigma = m_\sigma$, i.e. no change of the nuclear spin projection is allowed. Investigating the structure of $U_2^\dagger \mathbf{e} \cdot \mathbf{D} U_2$ one finds $m'_J = m_J$ for π -transitions and $m'_J = m_J \pm 1$ for σ^\pm -transitions. In figure 10.10 we present the decay rate of a ^{87}Rb

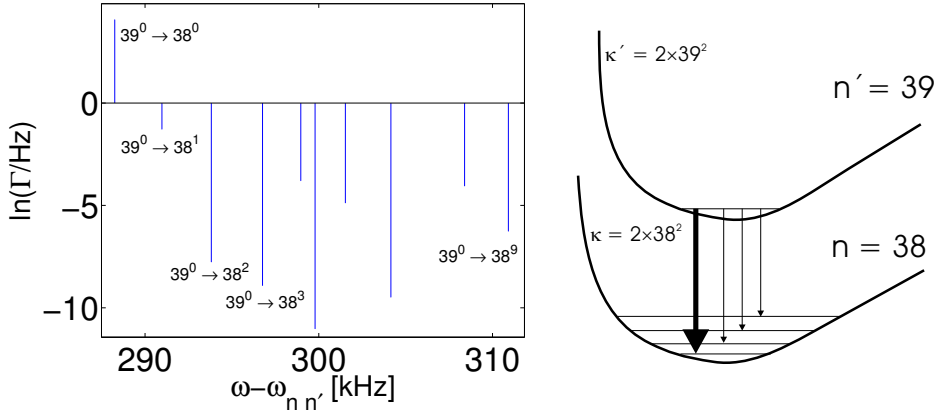


Figure 10.10.: Transition frequencies ω and decay rates Γ (in units of Hz - logarithmic representation) for π -transitions ($n' = 39 \rightarrow n = 38$, $\kappa' = 2 \times 39^2 \rightarrow \kappa = 2 \times 38^2$, $\nu' = 0 \rightarrow \nu$). For labelling the individual transitions we use the symbol $n'^{\nu'} \rightarrow n^\nu$. The data shown corresponds to a ^{87}Rb atom with $m_T = 84.5$ and a magnetic gradient $b = 4.44 \frac{T}{m}$. The frequency off-set $\omega_{n n'}$ is equal to the field-free transition frequency $n' = 39 \rightarrow n = 38$. All transitions except for $39^0 \rightarrow 38^0$ are strongly suppressed.

atom undergoing the π -transition ($n' = 39 \rightarrow n = 38$, $\kappa' = 2 \times 39^2 \rightarrow \kappa = 2 \times 38^2$, $\nu' = 0 \rightarrow \nu$) for $m_T = 84.5$ and $b = 4.44 \frac{T}{m}$. The transitions are labeled according to $n'^{\nu'} \rightarrow n^\nu$. Only the $39^0 \rightarrow 38^0$ transition constitutes a significant decay channel whereas all other transitions are highly suppressed. The reason for this is twofold. First, the electronic transition dipole moment $D_{n'\kappa'n\kappa}^e(\mathbf{R})$ does not significantly vary in the spatial region where the c.m. wave functions are located. Additionally both energy surfaces possess a similar shape resulting in similarly shaped c.m. wave functions which obey $\left| \langle \Phi_{\nu'}^{n'}(\mathbf{R}) \mid \Phi_{\nu}^n(\mathbf{R}) \rangle \right|^2 \approx \delta_{\nu'\nu}$. Hence ν can be regarded as an approximate quantum number. Thus the total decay rate for π -transitions is approximately

$$\Gamma_\pi = \frac{4}{3} \frac{\omega^3}{c^3} \left| D_{39,2 \times 39^2, 0 \rightarrow 38, 2 \times 38^2, 0}^{e_z} \right|^2 \quad (10.57)$$

which yields $58.82s^{-1}$. Together with the approximate circular transition rates ($\Gamma_{\sigma^+} = 29.70s^{-1}$ and $\Gamma_{\sigma^-} = 29.82s^{-1}$) one obtains the total decay rate $\Gamma = 118.34s^{-1}$. This is in very good agreement to the field-free result (which relies on the conservation of \mathbf{L}_r^2) being $\Gamma_{\text{fieldfree}} = 121.34s^{-1}$. The latter can be calculated analytically [50]:

$$\Gamma(n, n-1) = \frac{2}{3} \left(\frac{\alpha}{n} \right)^5 c^2 \left[\frac{n^{2n+1} (n-1)^{2n-2}}{(n-1/2)^{4n-1}} \right]. \quad (10.58)$$

Here α is the fine-structure constant. For high n this formula can be approximated by

$$\Gamma(n, n-1) \approx \frac{2}{3} \left(\frac{\alpha}{n} \right)^5 c^2 \quad (10.59)$$

Hence, the higher the degree of electronic excitation the more stable the atom becomes with respect to the radiative decay.

In order to have trapped states the oscillation frequency ν_{trap} of the c.m. motion has to be much greater than the decay rate Γ of the electronic state. By estimating $\nu_{\text{trap}} \approx \frac{\gamma^{\frac{2}{3}}}{M_2} = \left(\frac{b^2}{M_2}\right)^{\frac{1}{3}}$ one therefore has to obey the inequality

$$\frac{2c^2}{3} \left(\frac{\alpha}{n}\right)^5 \left(\frac{M_2}{b^2}\right)^{\frac{1}{3}} \ll 1. \quad (10.60)$$

For the $n' = 39 \rightarrow n = 38$ transition discussed here this ratio is smaller than 2×10^{-3} . Hence the atom performs more than 500 oscillations before decaying into the adjacent lower n -manifold.

10.7. Summary

In this chapter we have presented an investigation of the motion of an ultracold electronically excited (Rydberg-)atom exposed to an external magnetic quadrupole field. First we have established an atomic Hamiltonian which is valid for an arbitrary linear magnetic field configuration. The Rydberg atom has been modeled by employing a two-body approximation. Here we did not account for relativistic effects such as spin-orbit coupling and/or effects arising from the non-Coulombic character of the atomic core potential. By performing a coordinate dependent unitary transformation we were able to simplify the magnetic field induced couplings between the c.m. and the relative motion, significantly. A thorough symmetry analysis has been undertaken revealing the remarkable occurrence of a two-fold degeneracy of the energy spectrum. For solving the stationary Schrödinger equation of the Hamiltonian we have pursued an adiabatic approach. Here the electronic motion is assumed to take place on much faster timescales than the c.m. motion, justifying an approximate decoupling, i.e. an adiabatic separation, of the external (c.m.) and internal (electronic) degrees of freedom. By estimating the energy scales we found it to be appropriate to focus on a single n -manifold, i.e. magnetic field induced couplings of adjacent n -manifolds have been neglected. This approximation is justified as long as $bn^5 \ll 1$ - a condition which is easily satisfiable in experiments. The Hamiltonian is then represented in a set of hydrogenic wave functions spanning a given n -manifold.

By diagonalizing the resultant potential matrix the adiabatic potential surfaces have been obtained. Analyzing the shape of these potential surfaces we have identified three different regimes each of which exhibits unique characteristics. For small displacements from the trap center the overall structure is dominated by the angular momentum barrier. The potential energy surfaces group in branches whose shape is determined by the local value of the electronic orbital angular momentum projection onto the z -axis. Moving further outwards the influence of the angular momentum barrier diminishes rapidly. Here the internal dynamics of the atom determines the shape of the energy surfaces. Due to the symmetry properties of the internal Hamiltonian avoided level crossings and therefore nonadiabatic transition are likely to occur in this region. Fortunately, this effect can be controlled by choosing appropriate parameters. Finally, for large displacements of the trap center the limit of local homogeneity is established. Here the projection of the electronic spin as well as the orbital angular momentum constitute approximately conserved quantities. This results in a Zeeman-like splitting of the energy surfaces.

In order to achieve our goal of retrieving trapped c.m. states, we found the uppermost potential surface in a given n -multiplet to be best suited for this purpose. For sufficiently high values of the quantum number m_T this surface provides a pronounced minimum and is also energetically well-isolated from adjacent (lower) surfaces. We have calculated the adiabatic c.m. states in the uppermost energy surfaces for a number of different parameter sets. The corresponding energy eigenvalues have been provided.

In particular we have focused on the case $n = 39$, $\gamma = 1.586 \times 10^{-6}$ and $m_T = 84.5$. For this set of parameters a thorough analysis of the properties of the c.m. states has been performed. The

parameters are chosen such that the influence of the internal Hamiltonian H_e is negligible. We have found the radial extension of the electronic wave function to be comparable or even exceed the size of the c.m. wave function. This strongly indicates that such atoms cannot be considered point-like. Here both the electronic and the c.m. are equal partners of a combined quantum state. We have further analyzed the orbital electronic angular momentum of the confined states and demonstrated \mathbf{L}_r^2 to constitute an approximately conserved quantity. Calculating the projection of \mathbf{L}_r onto the local direction of the magnetic field the onset of the regime of local homogeneity is demonstrated.

Finally, the issue of radiative decay has been addressed. By calculating the decay rates it has been demonstrated that electromagnetic transitions connect mainly states with the same vibrational quantum number ν . Selection rules for the quantum number m_J have been provided. Moreover, we have shown that transition rates calculated for the field free case provide an excellent approximation to the exact results. For our particular set of parameters we have estimated the atom to perform about 500 oscillations in the confining energy surface before decaying into the next lower n -manifold.

The present investigation shows that there are no principle obstacles in order to realize trapped c.m. states of atoms being excited to Rydberg states. We have shown that in macroscopic field configurations trapped states are achievable if the total angular momentum is sufficiently high. This requirement is necessary for the quadrupole field, which possesses a point of zero field at its origin. However, this might be obsolete for other trap/field configurations. However, also in its present form the system has the potential to offer a number of interesting features. Besides the issue of trapping - on which the focus of this work has been set here - there is certainly a plethora of beautiful effects to study which arise from the coupled electronic and c.m. dynamics.

Most of the results presented in this chapter are published in refs. [57, 58].

11. Conclusion and outlook

In order to conclude this thesis we want to give a summary of its main points as well as an outlook to future work:

We have first considered the quantum dynamics of alkali metal atoms being in their electronic ground state in typical magnetic quadrupole traps. To a good approximation the details of the internal structure of such atoms can be neglected. Eventually they can be treated as neutral particles that carry a certain total spin which is determined by their fine-structure state. For both, the three-dimensional quadrupole field as well as the Ioffe-Pritchard trap, we have performed a thorough symmetry analysis considering the cases of spin $\frac{1}{2}$ and 1 particles. This was followed by a careful inspection of the resonance spectrum. In both cases we could show a larger amount of angular momentum to stabilize the atomic states with respect to decay from the trap. In the limit of large angular momenta we were even able to establish an approximative analytical description of the quantum states. These so-called quasi-bound states represent an extremely good approximation to very long-lived resonance states. The quality of the quasi-bound approximation has been tested against the commonly used adiabatic approach and has found to be more accurate. In case of the Ioffe-Pritchard trap the stabilizing action of an additionally applied Ioffe field has been verified. For a large Ioffe field we have demonstrated the ground state to be more stable than the next few excited states. This is of potential experimental use since such system would automatically 'cool' to the ground state over a sufficiently long period of time.

After having discussed ground state atoms we have turned to the investigation of the quantum dynamics of highly excited atoms, so-called Rydberg atoms. For their description we have employed an approach where the interaction of the single valence electron and the remaining core are accounted for by a two-body potential. For the latter the most simple case - a Coulomb potential - has been chosen. In a first approach we have considered the atomic core to be placed in the minimum of the magnetic field. Even in this simple approximation we have observed a number of remarkable effects. This is mainly the consequence of the nontrivial coupling between real-space and spin-space dynamics which is evoked by the inhomogeneous field. After the obligatory symmetry analysis we have discussed the energy spectrum, properties of the electronic spin and electromagnetic transitions. In the three-dimensional quadrupole field we have identified so-called ellipsoidal states that are spatially compact and almost energetically unaffected by the field. Moreover, we have explored the spatial dependence of the spin orientation. Thereby we have encountered a polarization effect that occurs for large degrees of electronic excitation. By investigating electromagnetic transitions we have identified a spectral signature that occurs when the intra n -mixing regime is entered. The most striking thing, however, was the observation of permanent electric dipole moments that are induced by the three-dimensional quadrupole field. In the case of a Ioffe-Pritchard trap we have found a discrete symmetry that gives rise to four separated subspaces which are characterized by a complex-valued quantum number. In the course of this symmetry analysis we have generally discussed the occurrence of a two-fold degeneracies in the spectrum of spin particles being exposed to magnetic quadrupole fields. The spatially dependent spin-field orientation as well as the spin expectation value has been discussed in the absence and in the presence of a Ioffe field. We have presented selection rules for electromagnetic transitions and have shown a larger number of transition lines to occur if a Ioffe field is present.

In the next step we have given up the fixed-nucleus approximation. In order to describe the coupled quantum dynamics of the atomic core and the active electron we have pursued an adiabatic

approach. We have significantly simplified the Hamiltonian by applying a unitary transformation which has removed several coupling terms between the internal and external atomic dynamics. The presented method is applicable for any linear magnetic field configuration. In particular we have studied the case of a three-dimensional quadrupole field. We have thereby focussed on gradients which are experimentally accessible even by the utilization of macroscopic field-generating structures. For sufficiently large angular momenta we have shown the existence of adiabatic potential curves which possess a pronounced minimum. This gives rise to bound adiabatic center of mass quantum states whose dynamics and properties have been discussed. We have demonstrated that the spatial extension of the center of mass quantum state can be smaller than that of the electronic wave function. This finding confirms that such Rydberg atoms even in fields with moderate gradients cannot be considered point-like. Albeit this fact the internal atomic structure suffers comparatively little modification. The square of the electronic orbital angular momentum constitutes an approximate constant of motion and the electromagnetic decay rate coincides almost with the field-free value. Comparing this decay rate to the typical oscillation frequency we have found the atom to perform several hundreds of oscillations before decaying radiatively. Thus magnetic trapping of ultracold and electronically excited atoms has been shown to be possible.

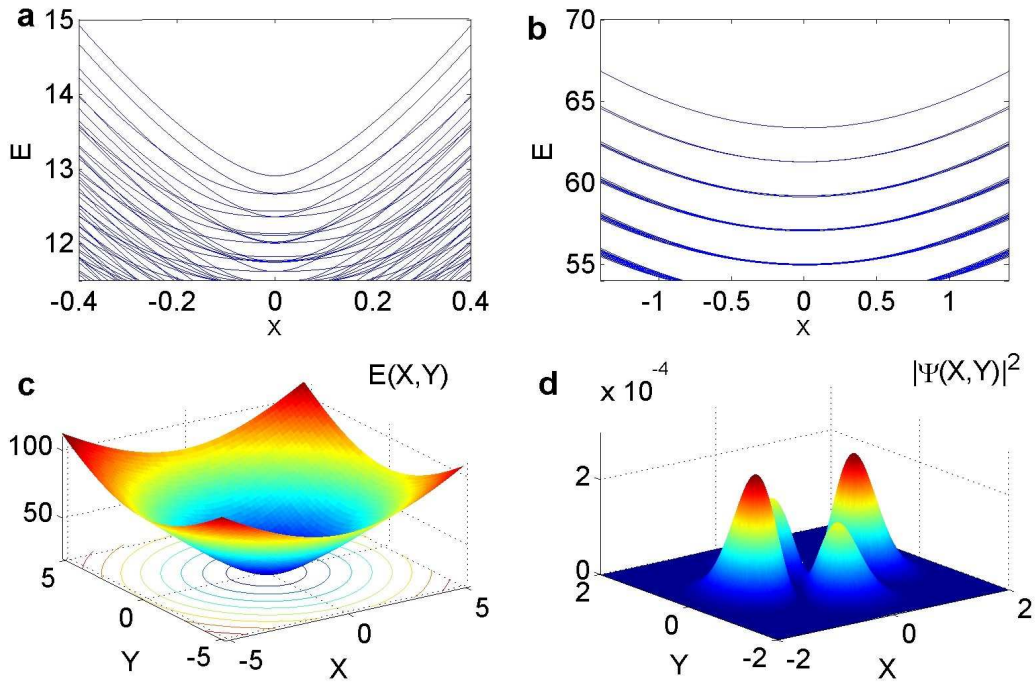


Figure 11.1: **a:** Intersection through the energy surfaces of the $n = 30$ manifold for a gradient of $b = 20 \frac{T}{m}$ and a Ioffe field strength of $B_I = 10^{-6} T$ along $Y = 0$. Due to the translational symmetry along the Z -axis a two-dimensional description of the system is sufficient. The uppermost surface provides an approximately harmonic confinement and is clearly separated from the next lower ones. The lower lying surfaces show a number of avoided crossings. **b:** Same plot as in **a** but with the Ioffe field strength increased to $B_I = 10^{-5} T$. The surfaces are now grouped in submanifolds whose mutual energetic distance is proportional to the Ioffe field strength. **c:** Uppermost energy surface in the $n = 30$ subspace for $B_I = 10^{-6} T$ and $b = 10 \frac{T}{m}$. An approximately harmonic confinement in the $X - Y$ -plane is achieved. **d:** Fourth excited c.m. quantum state in the energy surface presented in **c**. All lengths and energies are given in scaled units. Courtesy of Bernd Hezel.

An obvious drawback of the presented trapping scheme is the necessity to put a sufficiently large amount of angular momentum into the system. One possible way to overcome this is to superimpose a homogeneous electric field [95]. This will presumably result in a larger separation of adjacent potential energy surfaces and thereby inhibit nonadiabatic transitions even for low total

angular momenta. However, the most promising approach is probably to focus on a Ioffe-Pritchard type trap [43]. As we have already observed for ground state atoms its homogeneous Ioffe field is expected to suppress nonadiabatic transitions dramatically. Investigations regarding this setup are currently underway (some preliminary data is shown in figure 11.1).

A (meta-)stable trap for ultracold Rydberg atoms is a cornerstone for the exploration of interacting Rydberg gases in a well-controlled environment. The findings presented in this thesis strongly indicate that the same magnetic fields that confine the motion of ground state atoms can also be used to trap Rydberg atoms. This suggests that a trapped Rydberg gases can be simply achieved by laser excitation of atoms from an ultracold trapped gas of ground state atoms.

A. Vector potential of a magnetic field in a source-free region

When considering the behavior of charged particles (with charge q) being exposed to a magnetic field $\mathbf{B}(\mathbf{r})$ the charge-field interaction is usually introduced via the minimal coupling: $\mathbf{p} \rightarrow \mathbf{p} - q\mathbf{A}(\mathbf{r})$. Here $\mathbf{A}(\mathbf{r})$ is the vector potential of the field $\mathbf{B}(\mathbf{r})$ obeying $\mathbf{A}(\mathbf{r}) = \nabla \times \mathbf{B}(\mathbf{r})$. In this appendix we outline a way to obtain the vector potential of an arbitrary magnetic field in a source-free region without the necessity of performing an integration.

According to Maxwell's equations such field obeys $\nabla \cdot \mathbf{B}(\mathbf{r}) = 0$. Calculating the curl of the quantity $\boldsymbol{\alpha} = \mathbf{B}(\mathbf{r}) \times \mathbf{r}$ yields

$$\nabla \times \boldsymbol{\alpha} = \mathbf{r} \cdot \nabla \mathbf{B}(\mathbf{r}) - \mathbf{B}(\mathbf{r}) \cdot \nabla \mathbf{r} + \mathbf{B}(\mathbf{r}) \nabla \cdot \mathbf{r} - \mathbf{r} \nabla \cdot \mathbf{B}(\mathbf{r}) \quad (\text{A.1})$$

Using $(\mathbf{r} \cdot \nabla \mathbf{B}(\mathbf{r}))_k = \sum_i x_i \partial_i B_k$, $\nabla \cdot \mathbf{r} = 3$ and $\mathbf{r} = \sum_i x_i \mathbf{e}_i$ the cartesian vector components of equation (A.1) read

$$(\nabla \times \boldsymbol{\alpha})_k = \sum_i x_i \partial_i B_k - \sum_i B_i \partial_k x_i \partial_i B_k x_i + 3B_k = \sum_i x_i \partial_i B_k + 2B_k. \quad (\text{A.2})$$

Suppose the vector components of $\mathbf{B}(\mathbf{r})$ to satisfy the partial differential equation

$$\sum_i x_i \partial_i B_k = \gamma B_k. \quad (\text{A.3})$$

In this case one obtains

$$(\nabla \times \boldsymbol{\alpha})_k = \gamma B_k + 2B_k \quad (\text{A.4})$$

and the vector potential thus evaluates to

$$\mathbf{A}(\mathbf{r}) = \frac{\boldsymbol{\alpha}}{2 + \gamma} = \frac{\mathbf{B}(\mathbf{r}) \times \mathbf{r}}{2 + \gamma}. \quad (\text{A.5})$$

However, this equation only holds if the magnetic field $\mathbf{B}(\mathbf{r})$ obeys the condition (A.3). In order to find a more general expression we consider in the following a magnetic field with the cartesian components $B_k^{lmn}(\mathbf{r}) = b_k^{lmn} x_1^l x_2^m x_3^n$ and insert it into equation (A.3). This yields

$$\begin{aligned} \sum_i x_i \partial_i B_k^{lmn}(\mathbf{r}) &= b_k^{lmn} \sum_i x_i \partial_i x_1^l x_2^m x_3^n = b_k^{lmn} (l + m + n) x_1^l x_2^m x_3^n \\ &= (l + m + n) B_k^{lmn}(\mathbf{r}) = \gamma B_k^{lmn}(\mathbf{r}) \end{aligned} \quad (\text{A.6})$$

and correspondingly the vector potential becomes

$$\mathbf{A}^{lmn}(\mathbf{r}) = \frac{\mathbf{B}^{lmn}(\mathbf{r}) \times \mathbf{r}}{2 + l + m + n}. \quad (\text{A.7})$$

The Taylor series expansion of a general magnetic field around $\mathbf{r} = 0$ is given by

$$\mathbf{B}(\mathbf{r}) = \sum_{lmn} \mathbf{B}^{lmn}(\mathbf{r}) = \sum_{lmn} \sum_k b_k^{lmn} \mathbf{e}_k x_1^l x_2^m x_3^n = \sum_{lmn} \frac{\partial_1^l \partial_2^m \partial_3^n \mathbf{B}(\mathbf{r}) |_{\mathbf{r}=0}}{l! m! n!} x_1^l x_2^m x_3^n. \quad (\text{A.8})$$

Apparently the vector potential of this field can be expressed as

$$\mathbf{A}(\mathbf{r}) = \sum_{lmn} \mathbf{A}^{lmn}(\mathbf{r}) = \sum_{nlm} \frac{x_1^l x_2^m x_3^n}{2 + l + m + n} \left[\frac{\partial_1^l \partial_2^m \partial_3^n \mathbf{B}(\mathbf{r}) |_{\mathbf{r}=0}}{l!m!n!} \right] \times \mathbf{r}. \quad (\text{A.9})$$

Thus we have found an expression for a vector potential of an arbitrary magnetic field that can be expanded in a Taylor series. If $\nabla \times \mathbf{B}^{lmn}(\mathbf{r}) = 0$ for any choice of l, m, n the vector potential satisfies the Coulomb-gauge condition, i.e. $\nabla \cdot \mathbf{A}(\mathbf{r}) = 0$.

B. Atomic Units

	Système International d'Unités	atomic units
mass	$m_e = 9.10953 \times 10^{-31} \text{ kg}$	1
length	$a = \frac{4\pi\epsilon_0\hbar^2}{m_e e^2} = 0.52918 \times 10^{-10} \text{ m}$	1
charge	$e = 1.60219 \times 10^{-19} \text{ C}$	1
angular momentum	$\hbar = 1.05457 \times 10^{-34} \text{ Js}$	1
energy	$E_{\text{Ryd}} = \frac{m_e e^4}{32\pi^2 \epsilon_0^2 \hbar^2} = 21.78961 \times 10^{-19} \text{ J}$	$\frac{1}{2}$
magnetic field strength	$\alpha^2 \frac{m_e^2 c^2}{e\hbar} = 2.35051 \times 10^5 \text{ T}$	1
magnetic field gradient	$\alpha^2 \frac{m_e^2 c^2}{e\hbar a} = 4.44181 \times 10^{15} \frac{\text{T}}{\text{m}}$	1
time	$\frac{\hbar}{E_{\text{Ryd}}} = 4.83978 \times 10^{-17} \text{ s}$	2
momentum	$\frac{m_e E_{\text{Ryd}} a}{\hbar} = 9.96032 \times 10^{-25} \frac{\text{kg m}}{\text{s}}$	$\frac{1}{2}$
electric field	$\frac{E_{\text{Ryd}}}{e a} = 2.56999 \times 10^{11} \frac{\text{V}}{\text{m}}$	$\frac{1}{2}$

C. Matricelements

C.1. Spin $\frac{1}{2}$ Fermions in a magnetic guide - cartesian basis set

The matrix elements of the Hamiltonian (6.17) have been calculated in the cartesian basis functions of a two-dimensional harmonic oscillator. We have represented the momentum and spatial variables in terms of annihilation and creation operators whose action on the energy eigenstates is know [98]. The resulting matrix representation of the Hamiltonian in case of a spin $\frac{1}{2}$ particle reads:

$$\begin{aligned}
\langle k', n', m'_s | H(\theta) | k, n, m_s \rangle = & \\
& -\frac{\omega_x}{4} e^{-i2\theta} \left[\sqrt{k(k-1)} \delta_{k',k-2} - (2k+1) \delta_{k',k} + \sqrt{(k+1)(k+2)} \delta_{k',k+2} \right] \delta_{n',n} \delta_{m'_s, m_s} \quad (C.1) \\
& -\frac{\omega_y}{4} e^{-i2\theta} \left[\sqrt{n(n-1)} \delta_{n',n-2} - (2n+1) \delta_{n',n} + \sqrt{(n+1)(n+2)} \delta_{n',n+2} \right] \delta_{k',k} \delta_{m'_s, m_s} \\
& + \frac{e^{i\theta}}{4\sqrt{2\omega_x}} \left[\sqrt{k} \delta_{k',k-1} + \sqrt{k+1} \delta_{k',k+1} \right] \times [\delta_{m'_s, m_s+1} + \delta_{m'_s, m_s-1}] \delta_{n',n} \\
& - \frac{i e^{i\theta}}{4\sqrt{2\omega_x}} \left[\sqrt{n} \delta_{n',n-1} + \sqrt{n+1} \delta_{n',n+1} \right] \times [\delta_{m'_s, m_s+1} - \delta_{m'_s, m_s-1}] \delta_{k',k} \\
& + \frac{\gamma}{4} (-1)^{m_s - \frac{1}{2}} \delta_{n',n} \delta_{k',k} \delta_{m'_s, m_s}.
\end{aligned}$$

C.2. Spin 1 Bosons in a magnetic guide - cylindrical basis set

The matrix elements of the Hamiltonian (6.30) can be calculated analytically by exploiting the recurrence relations of the associated Laguerre polynomials [1, 86]. The matrix reads

$$\begin{aligned}
& \langle n, m_s, m | H_m(\theta) | n', m'_s, m \rangle \\
& = \frac{1}{2} \left[e^{-i2\theta} \rho_0^{-2} \left[(2n + |m + m_s| + 1) \delta_{n,n'} + \sqrt{(n+1)(n + |m + m_s| + 1)} \delta_{n,n'-1} \right. \right. \\
& \quad \left. \left. + \sqrt{n(n + |m + m_s|)} \delta_{n,n'+1} \right] \delta_{m_s, m'_s} \quad (C.2) \\
& \quad + e^{i\theta} \rho_0 [\delta_{m_s, m_s+1} + \delta_{m_s, m_s-1}] \times \left[\sqrt{n + |m| + \Theta([m_s + m'_s] m)} \delta_{n,n'} \right. \\
& \quad \left. - \sqrt{n + M_1(m_s, m'_s)} M_2(n, n', m_s, m'_s) (\delta_{n,n'+1} + \delta_{n,n'-1}) \right] \\
& \quad \left. + \gamma m_s \delta_{n,n'} \delta_{m_s, m'_s} \right]
\end{aligned}$$

with

$$M_1(m_s, m'_s) = \frac{1}{2} + (|m_s| - |m'_s|) (\Theta([m_s + m'_s] m) - \frac{1}{2}) \quad (C.3)$$

$$M_2(n, n', m_s, m'_s) = \frac{1}{2} + (n' - n) (|m_s| - |m'_s|) (\Theta([m_s + m'_s] m) - \frac{1}{2}) \quad (C.4)$$

and $\Theta(x)$ being the Heavyside step function.

D. Danksagung

- Mein Dank gilt meinem Betreuer Prof. **Peter Schmelcher** für all die Jahre voller fruchtbarer Zusammenarbeit.
- Weiterhin möchte ich Prof. **Jörg Schmiedmayer** danken, der mir die Möglichkeit gegeben zu hat, mich in seiner experimentellen Arbeitsgruppe zu entfalten, deren offene und lockere Atmosphäre ich stets sehr geschätzt habe.
- Ich möchte mich bei Prof. **Jochen Schirmer** für die Erstellung des Zweitgutachtens zu dieser Arbeit bedanken.
- Mein ausdrücklicher Dank gilt der **Quantenoptikgruppe** für die legendären und vielen gewonnenen Parties und die Fülle an Freizeitaktivitäten.

Vielen Dank

- **Albrecht** (Frisbee) **Haase**
 - **Peter** (en ce moment à Paris) **Krüger**
 - **Thorsten** (qui a déjà quitté Paris) **Schumm**
 - **Sebastian** (Standfußballer) **Hofferberth**
 - **Christian** (Jever) **Hock**
 - **Stephan** (Mack - down-under) **Wildermuth**
 - **Daniel** (Kollego) **Gallego**
 - **Stephan** (Feuerlöscher) **Schneider**
 - **Björn Hessmo**
 - **Frau Willig**
 - **Sönke** (Sonk) **Groth**
 - **Mauritz** (radio frequency) **Andersson**
 - **Ulrich** (Uli) **Schmidt**
 - **Bernd** (erklär mal) **Hezel**
 - **Florian** (Mop - High tower) **Lenz**.
- Ich danke meinen **Eltern** für den mir gebotenen Rückhalt und ihre Unterstützung.
 - Danke **Alexandra**, für alles.

Bibliography

- [1] M. Abramowitz and A. Stegun. *Handbook of mathematical functions*. Dover Publications Inc. New York, 5 edition, 1968.
- [2] O.-A. Al-Hujaj and P. Schmelcher. Helium in superstrong magnetic fields. *Phys. Rev. A*, 67:023403, 2003.
- [3] O.-A. Al-Hujaj and P. Schmelcher. Beryllium in strong magnetic fields. *Phys. Rev. A*, 70:023411, 2004.
- [4] O.-A. Al-Hujaj and P. Schmelcher. Lithium in strong magnetic fields. *Phys. Rev. A*, 70:033411, 2004.
- [5] J. E. Avron, I. W. Herbst, and B. Simon. Separation of center of mass in homogeneous magnetic fields. *Ann. Phys. (N.Y.)*, 114:431, 1978.
- [6] M. A. Baranov, K. Osterloh, and M. Lewenstein. Fractional quantum Hall states in ultracold rapidly rotating dipolar fermi gases. *Phys. Rev. Lett.*, 94:070404, 2005.
- [7] W. Becken and P. Schmelcher. Electromagnetic transitions of the helium atom in strong magnetic fields. *Phys. Rev. A*, 65:033416, 2002.
- [8] W. Becken, P. Schmelcher, and F. K. Diakonov. The helium atom in a strong magnetic field. *J. Phys. B*, 32:1557, 1999.
- [9] K. Berg-Sorensen, M.M. Burns, J.A. Golovchenko, and L. Veestergard-Hau. Waveguide for cold atoms: Spin-1 magnetic particles and a filamentary current. *Phys. Rev. A*, 53:1653, 1996.
- [10] T.H. Bergeman, P. McNicholl, J. Kycia, H. Metcalf, and N.L. Balazs. Quantized motion of atoms in a quadrupole magnetostatic trap. *J. Opt. Soc. Am. B*, 6:2249, 1989.
- [11] H. A. Bethe and E. Salpeter. *Quantum Mechanics of One- and Two-Electron Atoms*. New York Plenum, 1977.
- [12] J. Bill, M. Trappe, I. Lesanovsky, and P. Schmelcher. Resonant quantum dynamics of neutral spin 1 bosons in a magnetic guide. *to appear in Phys. Rev. A*, 2006.
- [13] R. Blümel and K. Dietrich. Quantum states of neutrons bound in the magnetic field of a rectilinear current. *Phys. Rev. A*, 43:22, 1991.
- [14] H. Bock, I. Lesanovsky, and P. Schmelcher. Neutral two-body systems in inhomogeneous magnetic fields: the quadrupole configuration. *J. Phys. B: At. Mol. Phys.*, 38:893, 2005.
- [15] C. Boisseau, I. Simbotin, and R. Côté. Macrodimers: Ultralong range Rydberg molecules. *Phys. Rev. Lett.*, 88:133004, 2003.
- [16] V. Bretin, S. Stock, Y. Seurin, and J. Dalibard. Fast rotation of a Bose-Einstein condensate. *Phys. Rev. Lett.*, 92:050403, 2004.

- [17] J.P. Burke, C.H. Greene, and B.D. Esry. Multichannel spectrum of neutral particles trapped by a wire. *Phys. Rev. A*, 54:3225, 1996.
- [18] T. Calarco, E.A. Hinds, D. Jaksch, J. Schmiedmayer, J.I. Cirac, and P. Zoller. Quantum gates with neutral atoms: Controlling collisional interactions in time-dependent traps. *Phys. Rev. A*, 61:022304, 2000.
- [19] L.S. Cederbaum, K.C. Kulander, and N.H. March, editors. *Atoms and Molecules in Intense Fields*, volume Structure and Bonding 86 p. 27. Springer Heidelberg, 1997.
- [20] J.-H. Choi, J. R. Guest, A. P. Povilus, E. Hansis, and G. Raithel. Magnetic trapping of long-lived cold Rydberg atoms. *Phys. Rev. Lett.*, 95:243001, 2005.
- [21] C.W. Clark and K.T. Taylor. The quadratic zeeman effect in hydrogen Rydberg series. *J. Phys. B: At. Mol. Phys.*, 13:L737, 1980.
- [22] C.W. Clark and K.T. Taylor. The quadratic zeeman effect in hydrogen Rydberg series: application of sturmian functions. *J. Phys. B: At. Mol. Phys.*, 15:1175, 1982.
- [23] K. B. Davis, M.-O. Mewes, M. R. Andrews, N. J. van Druten, D. S. Durfee, D. M. Kurn, and W. Ketterle. Bose-Einstein condensation in a gas of sodium atoms. *Phys. Rev. Lett.*, 75:3969, 1995.
- [24] James W. Demmel, Stanley C. Eisenstat, John R. Gilbert, Xiaoye S. Li, and Joseph W. H. Liu. A supernodal approach to sparse partial pivoting. *SIAM J. Matrix Analysis and Applications*, 20(3):720–755, 1999.
- [25] O. Dippel, P. Schmelcher, and L. S. Cederbaum. Charged anisotropic harmonic oscillator and the hydrogen atom in crossed fields. *Phys. Rev. A*, 49:4415, 1994.
- [26] O. Dippel, P. Schmelcher, and L.S. Cederbaum. Charged anisotropic harmonic oscillator and the hydrogen atom in crossed fields. *Phys. Rev. A*, 49:4415, 1994.
- [27] S.K. Dutta, J R. Guest, D. Feldbaum, A. Walz-Flannigan, and G. Raithel. Ponderomotive optical lattice for Rydberg atoms. *Phys. Rev. Lett.*, 85:5551, 2000.
- [28] K. Eckert, J. Mompert, X.X. Yi, J. Schliemann, D. Bruß, G. Birkl, and M. Lewenstein. Quantum computing in optical microtraps based on the motional states of neutral atoms. *Phys. Rev. A*, 66:042317, 2002.
- [29] J. R. Ensher, D. S. Jin, M. R. Matthews, C. E. Wieman, and E. A. Cornell. Bose-Einstein condensation in a dilute gas: Measurement of energy and ground-state occupation. *Phys. Rev. Lett.*, 77:4984, 1996.
- [30] S.M. Farooqi, D. Tong, S. Krishnan, J. Stanojevic, Y.P. Zhang, J.R. Ensher, A.S. Estrin, C. Boisseau, R. Côté, E.E. Eyler, and P.L. Gould. Long-range molecular resonances in a cold Rydberg gas. *Phys. Rev. Lett.*, 91:183002, 2003.
- [31] R. Folman, P. Krüger, J. Denschlag, C. Henkel, and J. Schmiedmayer. Macroscopic atom optics: From wires to an atom chip. *Adv. At. Mol. Opt. Phys.*, 48:263, 2002.
- [32] H. Friedrich and B. Eckard, editors. *Lecture Notes in Physics - Classical, Semiclassical and Quantum Dynamics in Atoms*, volume 485. Springer Heidelberg, 1997.
- [33] H. Friedrich and D. Wintgen. The hydrogen atom in a uniform magnetic field an example of chaos. *Phys. Rep.*, 183:37, 1989.

- [34] T.F. Gallagher. *Rydberg Atoms*. Cambridge University Press, 1994.
- [35] D. Gallego Garcia. Dipolfallen in Atomchipexperimenten. Universität Heidelberg, 2005.
- [36] C.H. Greene, A.S. Dickinson, and H.R. Sadeghpour. Creation of polar and nonpolar ultra-long-range Rydberg molecules. *Phys. Rev. Lett.*, 85:2458, 2000.
- [37] Markus Greiner, Olaf Mandel, Tilman Esslinger, Theodor W. Hänsch, and Immanuel Bloch. Quantum phase transition from a superfluid to a Mott insulator in a gas of ultracold atoms. *Nature*, 415:39, 2002.
- [38] J.R. Guest, J.-H. Choi, E. Hansis, A. P. Povilus, and G. Raithel. Laser cooling and magnetic trapping at several tesla. *Phys. Rev. Lett.*, 94:073003, 2005.
- [39] J.R. Guest, J.H. Choi, and G. Raithel. Decay rates of high- $|m|$ Rydberg states in strong magnetic fields. *Phys. Rev. A*, 68:022509, 2003.
- [40] J.R. Guest and G. Raithel. High- $|m|$ Rydberg states in strong magnetic fields. *Phys. Rev. A*, 68:052502, 2003.
- [41] F. Haake. *Quantum Signatures of Chaos*. Springer, 2001.
- [42] L. Vestergaard Hau, J.A. Golovchenko, and Michael M. Burns. Supersymmetry and the binding of a magnetic atom to a filamentary current. *Phys. Rev. Lett.*, 75:1426, 1995.
- [43] B. Hezel. Diploma Thesis: Rydberg atoms in a Ioffe-Pritchard trap. Universität Heidelberg, 2006.
- [44] E.A. Hinds and C. Eberlein. Erratum: Quantum propagation of neutral atoms in a magnetic quadrupole guide. *Phys. Rev. A*, 64:039902(E), 2000.
- [45] E.A. Hinds and C. Eberlein. Quantum propagation of neutral atoms in a magnetic quadrupole guide. *Phys. Rev. A*, 61:033614, 2000.
- [46] A. Holle, G. Wiebusch, J. Main, K.H. Welge, G. Zeller, G. Wunner, T. Ertl, and H. Ruder. Theoretical and experimental spectra in the transition from regularity to irregularity. *Z. Phys. D*, 5:279, 1987.
- [47] P. Hyafil, J. Mozley, A. Perrin, J. Tailleur, G. Nogues, M. Brune, J. M. Raimond, and S. Haroche. Coherence-preserving trap architecture for long-term control of giant Ryberg atoms. *Phys. Rev. Lett.*, 93:103001, 2004.
- [48] C.H. Iu, G.R. Welch, M.M. Kash, D. Kleppner, D. Delande, and J.C. Gay. Diamagnetic Rydberg atom: Confrontation of calculated and observed spectra. *Phys. Rev. Lett.*, 66:145, 1991.
- [49] D. Jaksch, H.-J. Briegel, J.I. Cirac, C. W. Gardiner, and P. Zoller. Entanglement of atoms via cold controlled collisions. *Phys. Rev. Lett.*, 82:1975, 1999.
- [50] U.D. Jentschura, E.-O. Le Bigot, J. Evers, P. J. Mohr, and C.H. Keitel. Relativistic and radiative energy shifts for Rydberg states. *J. Phys. B: At. Mol. Phys.*, 38:S97, 2005.
- [51] B. R. Johnson, J. O. Hirschfelder, and K. H. Yang. Interaction of atoms, molecules, and ions with constant electric and magnetic fields. *Rev. Mod. Physics*, 55:109, 1983.

- [52] P. Krüger, X. Luo, M. W. Klein, K. Brugger, A. Haase, S. Wildermuth, S. Groth, I. Bar-Joseph, R. Folman, and J. Schmiedmayer. Trapping and manipulating neutral atoms with electrostatic fields. *Phys. Rev. Lett.*, 91:233201, 2003.
- [53] W. E. Lamb. Fine structure of the hydrogen atom. III. *Phys. Rev.*, 85:259, 1959.
- [54] P. J. Leo, C. J. Williams, and P. S. Julienne. Collision properties of ultracold Cs-133 atoms. *Phys. Rev. Lett.*, 85:2721, 2000.
- [55] I. Lesanovsky. Diploma Thesis: Rydberg-Atome in magnetischen Quadrupolfallen. Universität Heidelberg, 2003.
- [56] I. Lesanovsky and P. Schmelcher. Spectral properties and lifetimes of neutral spin-1/2 fermions in a magnetic guide. *Phys. Rev. A*, 70:063604, 2004.
- [57] I. Lesanovsky and P. Schmelcher. Magnetic trapping of ultracold Rydberg atoms. *Phys. Rev. Lett.*, 95:053001, 2005.
- [58] I. Lesanovsky and P. Schmelcher. Quantum states of ultracold electronically excited atoms in a magnetic quadrupole trap. *Phys. Rev. A*, 72:053410, 2005.
- [59] I. Lesanovsky and P. Schmelcher. Selected aspects of the quantum dynamics and electronic structure of atoms in magnetic microtraps. *Eur. Phys. J. D*, 35:31, 2005.
- [60] I. Lesanovsky and P. Schmelcher. Spectral properties and lifetimes of neutral fermions and bosons in a magnetic quadrupole trap. *Phys. Rev. A*, 71:032510, 2005.
- [61] I. Lesanovsky, P. Schmelcher, and H. Sadeghpour. Ultra long-range Rydberg molecules exposed to a magnetic field. *J. Phys. B: At. Mol. Phys.*, 39:L69, 2006.
- [62] I. Lesanovsky, J. Schmiedmayer, and P. Schmelcher. Electronic structure of atoms in magnetic quadrupole traps. *Phys. Rev. A*, 69:053405, 2004.
- [63] I. Lesanovsky, J. Schmiedmayer, and P. Schmelcher. Rydberg atoms in a magnetic guide. *Phys. Rev. A*, 70:043409, 2004.
- [64] I. Lesanovsky, J. Schmiedmayer, and P. Schmelcher. Rydberg atoms in magnetic quadrupole traps. *Europhys. Lett.*, 65, 2004.
- [65] I. Lesanovsky, J. Schmiedmayer, and P. Schmelcher. Rydberg atoms in a magnetic quadrupole field. *J. Phys. B: At. Mol. Phys.*, 38:S151, 2005.
- [66] I. Lesanovsky, T. Schumm, S. Hofferberth, L. M. Andersson, P. Krüger, and J. Schmiedmayer. Adiabatic radio frequency potentials for the coherent manipulation of matter waves. *Phys. Rev. A*, 73:033619, 2005.
- [67] W. Li, M. W. Noel, M. P. Robinson, P. J. Tanner, T. F. Gallagher, D. Comparat, B. Laburthe Tolra, N. Vanhaecke, T. Vogt, N. Zahzam, P. Pillet, and D. A. Tate. Evolution dynamics of a dense frozen Rydberg gas to plasma. *Phys. Rev. A*, 70:042713, 2004.
- [68] W. Li, P. J. Tanner, and T. F. Gallagher. Dipole-dipole excitation and ionization in an ultracold gas of Rydberg atoms. *Phys. Rev. Lett.*, 94:173001, 2005.
- [69] T. C. Liebisch, A. Reinhard, P. R. Berman, and G. Raithel. Atom counting statistics in ensembles of interacting Rydberg atoms. *Phys. Rev. Lett.*, 95:253002, 2005.

- [70] M.D. Lukin, M. Fleischhauer, and R. Côté. Dipole blockade and quantum information processing in mesoscopic atomic ensembles. *Phys. Rev. Lett.*, 87:037901, 2001.
- [71] E. A. Manykin, M. I. Ozhovan, and P. P. Poluektov. *Sov. Phys. JETP*, 57:256, 1983.
- [72] M. Marinescu, J. F. Babb, and A. Dalgarno. Long-range potentials including retardation for the interaction of two alkali-metal atoms. *Phys. Rev. A*, 50:003096, 1994.
- [73] M. Marinescu and L. You. Controlling atom-atom interaction at ultralow temperatures by dc electric fields. *Phys. Rev. Lett.*, 81:4596, 1998.
- [74] V.S. Melezhik and P. Schmelcher. Quantum energy flow in atomic ions moving in magnetic fields. *Phys. Rev. Lett.*, 84:1870, 2000.
- [75] H.J. Metcalf and P. van der Straten. *Laser Cooling and Trapping*. Springer New York, 1999.
- [76] N. Moiseyev. Quantum theory of resonances: calculating energies, widths and cross-sections by complex scaling. *Phys. Rep.*, 302:212, 1998.
- [77] I. Mourachko, D. Comparat, F. de Tomasi, A. Fioretti, P. Nosbaum, V. M. Akulin, and P. Pillet. Many-body effects in a frozen Rydberg gas. *Phys. Rev. Lett.*, 80:253, 1998.
- [78] R. G. Newton. *Scattering theory of waves and particles*. Springer, 1982.
- [79] C. J. Pethick and H. Smith. *Bose-Einstein Condensation in dilute gases*. Cambridge University Press, 2002.
- [80] T. Pohl, T. Pattard, and J.M. Rost. Plasma formation from ultracold Rydberg gas. *Phys. Rev. A*, 68:010703(R), 2003.
- [81] T. Pohl, T. Pattard, and J.M. Rost. Coulomb crystallization in expanding laser-cooled neutral plasmas. *Phys. Rev. Lett.*, 92:155003, 2004.
- [82] R.M. Potvliege and V. Zehnle. Complex scaling calculation of the decaying quantum-propagation modes of neutral atoms in a magnetic guide. *Phys. Rev. A*, 63:025601, 2001.
- [83] W. H. Press, B. P. Flannery, S. A. Teukolsky, and W. T. Vetterling. *Numerical Recipes in C : The Art of Scientific Computing*, volume 2. Cambridge University Press, 1992.
- [84] C. A. Regal, M. Greiner, and D. S. Jin. Observation of resonance condensation of fermionic atom pairs. *Phys. Rev. Lett.*, 92:040403, 2004.
- [85] J. Reichel. Microchip traps and Bose-Einstein condensation. *Appl. Phys. B*, 74:469, 2002.
- [86] Wolfram research. The Wolfram function site. <http://functions.wolfram.com>.
- [87] H. Ruder. *Atoms in Strong Magnetic Fields*. Springer Berlin, 1992.
- [88] I.I. Ryabtsev, D.B. Tretyakov, and I.I. Beterov. Applicability of Rydberg atoms to quantum computers. *J. Phys. B: At. Mol. Phys.*, 38:S421, 2005.
- [89] M. Schäfer, M. Andrist, H. Schmutz, F. Lewen, G. Winnewisser, and F. Merkt. A 240.380 GHz millimetre wave source for very high resolution spectroscopy of high Rydberg states. *J. Phys. B: At. Mol. Opt. Phys.*, 39:831, 2006.
- [90] P. Schmelcher. Interaction of the collective and electronic motion of atomic ions in magnetic fields. *Phys. Rev. A*, 52:130, 1995.

- [91] P. Schmelcher, L. S. Cederbaum, and U. Kappes. *Conceptual Trends in Quantum Chemistry*. Kluwer Academic Publishers, 1994.
- [92] P. Schmelcher and L.S. Cederbaum. On chaos in unbounded phase space. *Phys. Lett. A*, 164:305, 1992.
- [93] P. Schmelcher and L.S. Cederbaum. Classical self-ionization of fast atomic ions in magnetic fields. *Phys. Rev. Lett.*, 74:662, 1995.
- [94] P. Schmelcher and W. Schweizer, editors. *Atoms and Molecules in Strong External Fields*. Plenum Press New York, 1998.
- [95] U. Schmidt. Diploma Thesis: Rydberg atoms in a magnetic quadrupole trap superimposed by an electric field. Universität Heidelberg.
- [96] F. Schreck, L. Khaykovich, K. L. Corwin, G. Ferrari, T. Bourdel, J. Cubizolles, and C. Salomon. Quasipure Bose-Einstein condensate immersed in a Fermi Sea. *Phys. Rev. Lett.*, 87:080403, 2001.
- [97] T. Schumm, S. Hofferberth, L. M. Andersson, S. Wildermuth, S. Groth, I. Bar-Joseph, J. Schmiedmayer, and P. Krüger. Matter-wave interferometry in a double well on an atom chip. *Nature Physics*, 1:57, 2005.
- [98] F. Schwabl. *Quantenmechanik I*. Springer Berlin, 6 edition, 2004.
- [99] J. D. Section. *Classical Electrodynamics*. John Wiley and Sons, 3 edition, 1998.
- [100] K. Singer, M. Reetz-Lamour, T. Amthor, L. Gustavo Marcassa, and M. Weidemüller. Suppression of excitation and spectral broadening induced by interactions in a cold gas of Rydberg atoms. *Phys. Rev. Lett.*, 93:163001, 2004.
- [101] D.C. Sorensen. *Parallel numerical algorithms - Implicitly restarted Arnoldi/Lanczos methods for large scale eigenvalue calculations*. Kluwer Dordrecht, 1995.
- [102] S. Stock, Z. Hadzibabic, B. Battelier, M. Cheneau, and J. Dalibard. Observation of phase defects in quasi-two-dimensional bose-einstein condensates. *Phys. Rev. Lett.*, 95:190403, 2005.
- [103] C.V. Sukumar and D.M. Brink. Spin-flip transitions in a magnetic trap. *Phys. Rev. A*, 56:2451, 1997.
- [104] R. Svensson and L. Holmlid. Electronic Raman processes in Rydbergmatter of Cs: Circular Rydberg States in Cs and Cs+. *Phys. Rev. Lett.*, 83:1739, 1999.
- [105] A. Szabo and N. S. Ostlund. *Modern Quantum Chemistry: Introduction to Advanced Electronic Structure Theory*. Dover, 1996.
- [106] D. Tong, S.M. Farooqi, J. Stanojevic, S. Krishnan, Y.P. Zhang, R. Côté, E.E. Eyler, and P.L. Gould. Local blockade of Rydberg excitation in an ultracold gas. *Phys. Rev. Lett.*, 93:063001, 2001.
- [107] Q. Wang and C.H. Greene. Parameter-dependent multichannel Rydberg spectra. *Phys. Rev. A*, 44:1874, 1991.
- [108] S. Wildermuth, S. Hofferberth, I. Lesanovsky, S. Groth, I. Bar-Joseph, P. Krüger, and J. Schmiedmayer. Sensing electric and magnetic fields with Bose-Einstein condensates. *arXiv/cond-mat*, page 0512520, 2005.

-
- [109] S. Wildermuth, S. Hofferberth, I. Lesanovsky, E. Haller, L.M. Andersson, Sönke Groth, I. Bar-Joseph, P. Krüger, and J. Schmiedmayer. Microscopic magnetic-field imaging. *Nature*, 435:440, 2005.
- [110] G. Wunner, M. Kost, and H. Ruder. “Circular” states of Rydberg atoms in strong magnetic fields. *Phys. Rev. A*, 33:1444, 1986.